

CHEMICAL
RESEARCH,
DEVELOPMENT &
ENGINEERING
CENTER

CRDEC-SP-026

PROCEEDINGS OF THE 1989 SCIENTIFIC CONFERENCE
ON OBSCURATION AND AEROSOL RESEARCH

AD-A229 946

Elmer H. Engquist
Deborah A. Clark

BATTELLE - EDGEWOOD OPERATIONS
Edgewood, MD 21040

August 1990

DTIC
ELECTE
DEC 03 1990
S E D

DISTRIBUTION STATEMENT A
Approved for public release
Distribution Unlimited

U.S. ARMY
ARMAMENT
MUNITIONS
CHEMICAL COMMAND



Disclaimer

The findings in this report are not to be construed as an official Department of the Army position unless so designated by other authorizing documents.

Distribution Statement

Approved for public release; distribution is unlimited.

REPORT DOCUMENTATION PAGE

Form Approved
OMB No. 0704-0188

Public reporting burden for this collection of information is estimated to average 1 hour per response, including the time for reviewing instructions, searching existing data sources, gathering and maintaining the data needed, and completing and reviewing the collection of information. Send comments regarding this burden estimate or any other aspect of this collection of information, including suggestions for reducing this burden, to Washington Headquarters Services, Directorate for Information Operations and Reports, 1215 Jefferson Davis Highway, Suite 1204, Arlington, VA 22202-4302, and to the Office of Management and Budget, Paperwork Reduction Project (0704-0188), Washington, DC 20503.

1. AGENCY USE ONLY (Leave blank)	2. REPORT DATE 1990 August	3. REPORT TYPE AND DATES COVERED Final, 89 Jun - 89 Jun	
4. TITLE AND SUBTITLE Proceedings of the 1989 Scientific Conference on Obscuration and Aerosol Research		5. FUNDING NUMBERS PR-1C161102A71A	
6. AUTHOR(S) Compiled by Engquist, Elmer H., and Clark, Deborah A.			
7. PERFORMING ORGANIZATION NAME(S) AND ADDRESS(ES) Battelle - Edgewood Operations 2113 Emmorton Park Road, Suite 200 Edgewood, MD 21040		8. PERFORMING ORGANIZATION REPORT NUMBER CRDEC-SP-026	
9. SPONSORING/MONITORING AGENCY NAME(S) AND ADDRESS(ES) CDR, CRDEC, ATTN: SMCCR-RSP-B, APG, MD 21010-5423		10. SPONSORING/MONITORING AGENCY REPORT NUMBER	
11. SUPPLEMENTARY NOTES POC: E. Stuebing, SMCCR-RSP-B, (301) 671-3089			
12a. DISTRIBUTION/AVAILABILITY STATEMENT Approved for public release; distribution is unlimited.		12b. DISTRIBUTION CODE	
13. ABSTRACT (Maximum 200 words) In this report, 22 papers presented at the 1989 Scientific Conference on Obscuration and Aerosol Research are included under the headings of Physical and Chemical Properties of Aerosols, Aerosol Characterization Methods, and Optical Properties of Aerosols. <i>Keywords: Aerosols, obscuration, optical properties, Physical properties, chemical properties, (JS)</i>			
14. SUBJECT TERMS Obscurants Aerosols Extinction Transmission Obscuration Aerosol Absorption Infrared Scattering Sizing Smoke (continued on page 2)			15. NUMBER OF PAGES 311
			16. PRICE CODE
17. SECURITY CLASSIFICATION OF REPORT UNCLASSIFIED	18. SECURITY CLASSIFICATION OF THIS PAGE UNCLASSIFIED	19. SECURITY CLASSIFICATION OF ABSTRACT UNCLASSIFIED	20. LIMITATION OF ABSTRACT UL

A

14. SUBJECT TERMS (continued)

Electromagnetic scattering
Millimeter wave radiation
Submillimeter wave radiation
Visible radiation
Electromagnetic waves
Spherical particles
Mie scattering
Rayleigh scattering
Raman scattering
Concentration sampling
Particle dynamics
Diffusive mixing
Aerosol growth
Nucleation
Smoke generation
Aerosol generation
Photoionization
Conductivity
Chemical characterization
Phosphorus smoke
Fluorescence
Aerosol clusters
Spheres
Cylinders
Rough particles
Irregular particles
Nonspherical particles
Particle aggregates
Particle chains
Infrared emission
Cooperative scattering
Dependent scattering
Multiple scattering
Radiative transfer
Coagulation
Condensation
Liquid drop
Drop growth
Fog oil smoke
Diesel oil smoke
Particle mechanics
Atmospheric optics
Atmospheric dispersion
Cloud dynamics
Scavenging
Aerosol collectors
Aerosol elimination
Aerosol characterization
Particle sizing
Hygroscopic smokes
Particle size distribution
Particle orientation distribution
Optical constants
Optical properties
Anomalous diffraction
Attenuated total reflection
Reflection spectroscopy
ATR
Far-infrared
Refractive index
Index of refraction
Inversion
Inversion techniques
Gypsum
Natural minerals
Minerals
Metal
Metallic particles
Powdered minerals
Complex refractive index
Effective media
High energy laser
Particles
Aerosol particles
SERS
Surface enhanced Raman scattering
Dielectric particles
Conducting particles
Cylindrical particles
Fibers
Conducting fibers
Gas-aerosol reactions
Transport phenomena
Aerosol measurement
Spheroids
Laser pulses
Optical pulses
Pulse propagation
Clouds
Laser
Radiation transport
Fourier analysis
Plume mechanics
Light
Plumes
Properties

PREFACE

The 1989 U.S. Army Chemical Research, Development and Engineering Center Scientific Conference on Obscuration and Aerosol Research was held 27 - 30 June 1989 at the Edgewood Area Conference Center of Aberdeen Proving Ground, Maryland. The Conference is held annually, the last full week in June, under the direction of Dr. Edward Steubing, Research Area Coordinator, Aerosol Science. This report was authorized under project number 1C161102A71A, Research CW/CB Defense.

The Conference is an informal forum for scientific exchange and stimulation among investigators in the wide variety of disciplines required for aerosol research including a description of an obscuring aerosol and its effects. The participants develop some familiarity with the U.S. Army aerosol and obscuration science research programs and also become personally acquainted with the other investigators and their research interests and capabilities. Each attendee is invited to present any aspect of a topic of interest and may make last minute changes or alterations in his presentation as the flow of ideas in the Conference develops.

While all participants in the Conference are invited to submit papers for the proceedings of the Conference, each investigator, who is funded by the U.S. Army Research Program, is requested to provide one or more written papers that document specifically the progress made in his funded effort in the previous year and indicating future directions. Also, the papers for the proceedings are collected in the Fall to allow time for the fresh ideas that arise at the Conference to be incorporated. Therefore, while the papers in these proceedings tend to closely correspond to what was presented at the Conference, there is not an exact correspondence.

The reader will find the items relating to the Conference itself, photographs, the list of attendees, and the agenda in the appendixes following the papers and in the indexes pertaining to them.

The use of trade names or manufacturers' names in this report does not constitute an official endorsement of any commercial products. This report may not be cited for purposes of advertisement.

Reproduction of this document in whole or in part is prohibited except with permission of the Commander, U.S. Army Chemical Research, Development and Engineering Center, ATTN: SMCCR-SPS-T, Aberdeen Proving Ground, Maryland 21010-5423. However, the Defense Technical Information Center and the National Technical Information Service are authorized to reproduce this document for U.S. Government purposes.

This report has been approved for release to the public.



Accession For	
DTIC GRAB	<input checked="" type="checkbox"/>
DTIC TAB	<input type="checkbox"/>
Unannounced	<input type="checkbox"/>
Justification	
By _____	
Distribution/	
Availability Codes	
Dist	Avail and/or Special
A-1	

BLANK

PROPERTY OF THE U.S. GOVERNMENT	
CLASSIFIED BY	DATE
EXEMPT FROM GDS	EXEMPTION CODE
DECLASSIFICATION AUTHORITY	
DATE OF REVIEW	
APPROVED FOR DECLASSIFICATION	
DATE OF DECLASSIFICATION	
REASON FOR DECLASSIFICATION	
APPROVED BY	
DATE	

CONTENTS

I. AEROSOL DYNAMICS	9
ANALYSIS OF THE FLUCTUATIONS OF OBSCURATION THROUGH A GROUND LEVEL AEROSOL SOURCE	9
M. Poreh, A. Hadad, J.E. Cermak	
DISPERSION/REACTION MODEL OF AEROSOL FILTRATION BY POROUS FILTERS	15
M. Shapiro, H. Brenner	
EXPERIMENTAL STUDIES OF AEROSOL DYNAMICS IN REACTING SYSTEMS	25
R.C. Flagan	
II. AEROSOL CHARACTERIZATION	35
A MICROPARTICLE ELECTROMETER FOR REPEATED CHARGE EXCHANGE MEASUREMENTS BETWEEN A MICROPARTICLE AND A SURFACE	35
L.M. Folan, S. Arnold	
AN APPROACH TO THE ULTIMATE DETECTION LIMIT BY FLUORESCENCE MEASUREMENTS IN MICRODROPLETS	45
W.B. Whitten, J.M. Ramsey, S. Arnold, B.V. Bronk	
PARTICLE CHARACTERIZATION IN SONIC VELOCITY IMPACTORS	51
B. Jurcik, J. Brock	
PROBING THE STRUCTURE OF THE CORNEA OF THE EYE WITH LIGHT SCATTERING	57
R.A. Farrell, R.L. McCally, D.E. Freund	
RELATIONSHIP OF GROWTH CONDITIONS AND CONSEQUENT BACTERIAL SIZE TO THE S34/S11 ANGULAR SCATTERING PATTERN FOR BACTERIA	87
B.V. Bronk, W.P. Van de Merwe, D.R. Huffman, M. Stanley	
III. NONLINEAR EFFECTS AT HIGH ENERGY	97
COMPARISON BETWEEN THEORY AND EXPERIMENT FOR LASER-INDUCED PLASMA AND SHOCK WAVES IN DROPLETS	97
J. Carls, J. Brock	

MICRON-SIZED DROPLETS IRRADIATED WITH A PULSED CO ₂ LASER: MEASUREMENTS OF EXPLOSION AND BREAKDOWN THRESHOLDS	107
A. Biswas, B.S. Park, R.L. Armstrong, R.G. Pinnick, J.D. Pendleton, S.G. Jennings, G. Fernandez	
MOMENT SIMULATION OF AEROSOL EVAPORATION	115
Y. Seo, J. Brock	
NONLINEAR EFFECTS OF EXCIMER LASER INTERACTION WITH WATER DROPLETS	121
D.R. Alexander, J.P. Barton, S.A. Schaub, G. Holtmeier	
NONLINEAR LASER - DROPLET INTERACTIONS: STIMULATED RAMAN SCATTERING	135
A. Biswas, H. Latifi, R.L. Armstrong, R.G. Pinnick	
 IV. OPTICAL PROPERTIES OF AEROSOLS	 143
A FINITE ELEMENT APPROACH TO ABSORPTION AND SCATTERING OF ELECTROMAGNETIC RADIATION BY PARTICLES	143
L. Liebman, J. Brock	
ABSORPTION MEASUREMENTS USING AN INTEGRATING CAVITY	149
R.M. Pope, E.S. Fry, R.L. Montgomery	
AN ASYMPTOTIC EXPANSION FOR HANKEL FUNCTIONS WITH COMPLEX INDEX WITH APPLICATIONS	159
D.K. Cohoon	
ELECTROMAGNETIC FIELD CALCULATIONS FOR A TIGHTLY-FOCUSED LASER BEAM INCIDENT UPON A SPHERICAL PARTICLE	175
J.P. Barton, D.R. Alexander, S.A. Schaub	
ELECTROMAGNETIC SCATTERING AND DEPOLARIZATION ACROSS ROUGH SURFACE - FULL WAVE SOLUTIONS	199
E. Bahar, G. Huang	
HOMOTOPY AS AN ELECTROMAGNETIC DESIGN METHOD APPLIED TO A PERFECT CONDUCTOR COVERED WITH BIANISOTROPIC COATINGS HAVING NONTRIVIAALLY DISPERSIVE MAGNETIC PROPERTIES	211
D.K. Cohoon, R.M. Purcell	
MORPHOLOGY DEPENDENT RESONANCES OF TWO DISSIMILAR COOPERATIVELY SCATTERING SPHERES	249
K.A. Fuller	
SCATTERING OF FEMTOSECOND LASER PULSES	259
W.E. White, C. Wang, E.S. Fry	

UNIQUENESS OF SOLUTIONS OF ELECTROMAGNETIC INTERACTION PROBLEMS ASSOCIATED WITH SCATTERING BY A BIANISOTROPIC BODIES COVERED WITH IMPEDANCE SHEETS AND HOMOTOPY D.K. Cohoon	277
--	-----

INDEXES FOR THESE PROCEEDINGS

A. INDEX OF AUTHORS	293
B. INDEX OF AUTHORS' ORGANIZATIONS	295

APPENDIXES FOR THESE PROCEEDINGS

A. PHOTOGRAPH OF 1989 CONFERENCE ATTENDEES	297
B. LIST OF 1989 ATTENDEES	299
C. CONFERENCE AGENDA	307

BLANK

PROCEEDINGS
OF THE 1989 SCIENTIFIC CONFERENCE
ON OBSCURATION AND AEROSOL RESEARCH

I. AEROSOL DYNAMICS

ANALYSIS OF THE FLUCTUATIONS OF OBSCURATION THROUGH A
GROUND LEVEL AEROSOL SOURCE

M. Poreh and A. Hadad
Technion, Israel Institute of Technology
Haifa, 32000, Israel

J. E. Cermak
Colorado State University
Ft. Collins, Colorado 80523

RECENT PUBLICATIONS, SUBMITTALS FOR PUBLICATION AND PRESENTATIONS:

- A) M. Poreh and J. E. Cermak, "Experimental Study of Aerosol Plume Dynamics, Part I: Wind-tunnel Study of Diffusion and Deposition of Particles with Appreciable Settling Velocities," Annual Progress Report to CRDC, CER86-87MP-JEC1, September 1986.
- B) M. Poreh and J. E. Cermak, "Experimental Study of Aerosol Plume Dynamics, Part II: Wind-tunnel Study of Buoyant Horizontal Emissions," Annual Progress Report to CRDC, CER86-87MP-JEC5, November 1986.
- C) M. Poreh and J. E. Cermak, "Experimental Study of Aerosol Plume Dynamics, Part III: Wind-tunnel Simulation of Vertical Concentration Fluctuations," Annual Progress Report to CRDC, CER87-88MP-JEC4, December 1987.
- D) M. Poreh and J. E. Cermak, "'Lift-off' of Buoyant Horizontal Plumes," Proceedings of the Eighth Symposium on Turbulence and Diffusion, AMS, San Diego, CA, 25-29 April 1988.

ABSTRACT

It is shown that the classical "fluctuating-plume model" (Gifford, 1959) cannot describe the fluctuations of obscuration by an aerosol plume from a ground level source, which had been measured in a simulated small-scale wind-tunnel physical model. A modified semi-empirical analytical model, which is shown to be in very good agreement with the measurements, is presented.

INTRODUCTION

Obscuration by aerosol plumes is related to the integral of their concentration along the line of vision. A novel IR/CO₂ system for measuring the fluctuations of such integrals in small-scale wind-tunnel models has been developed (Poreh and Cermak, 1987, 1988a, 1988b). The method was used to measure the fluctuations of the vertical integrated concentration in an aerosol plume from a point source at ground level as it is carried downwind (the x direction). The measurements indicate that the relative probability, $P(\alpha)$, that the obscuration exceeds the mean obscuration value by a factor of α , at a given point downwind in the range $300 \text{ m} < x < 1200 \text{ m}$, is a function of the lateral off-center location y/σ_T , where σ_T is the characteristic mean plume-width parameter, and is independent of x. The curves in Figures 1-3 show the measured values of $P(\alpha)$

at different values of y/σ_T . The values of x in the figures denote the distances downwind from the source in the model.

It is of considerable theoretical and practical interest to find theoretical or semi-empirical models which will describe $P(\alpha)$.

SUMMARY OF THE RESULTS

The classical fluctuating-plume model of Gifford (1959) assumes that the concentration fluctuations are produced by a meandering instantaneous plume. The dimensions of the instantaneous plume σ_{yI} and σ_{zI} , for a given flow, are constants for each value of x . Using the continuity equation it can be shown that the ratio of the maximum concentrations of the mean plume and of the instantaneous plume, at a constant velocity field, is given in this model, by

$$C_{\max}/C_{I \max} = \sigma_I/\sigma_T = m(x). \quad (1)$$

The values of $P(\alpha)$ according to this model, calculated for the centerline of the plume ($y/\sigma_T = 0$) for different values of m , are plotted in Figure 4. Comparison with Figure 1 shows that the model cannot describe the measurements in a satisfactory manner.

Since in reality, σ_{yI} at a given x is not a constant but fluctuates considerably, it was decided to examine what would be the effect of letting the values of the width (σ_{iy}) and of the maximum concentration ($C_{i \max}$) in the model fluctuate (lower case indices are used to distinguish this case from the previous one). The mean concentration field and its statistical properties can in this case be calculated by weighted integrations over all the subsets which have the same σ_{iy} and $C_{i \max}$. Such a calculation requires, however, that assumptions be made regarding the correlation between σ_{iy} , $C_{i \max}$, σ_{iz} and σ_t , for all the subsets and regarding the probability of their occurrence. For the sake of simplicity, it has been decided to use as simple a model as possible. Accordingly, it was assumed that the product $\sigma_{iy}C_{i \max} = \text{constant}$, as in Equation (1), and also that $\sigma_{iz} = \text{constant}$, although the continuity equation requires only that the mean of the product $\sigma_{iy}\sigma_{iz}C_{i \max} = \text{constant}$. It was further assumed that the values of σ_t of all the subsets are the same and are equal to σ_T , as the mean field obtained by averaging the Gaussian concentration distributions of the subsets would be Gaussian, as observed in the experiments, only if this assumption is made. Accordingly, each subset in the model satisfies the equation,

$$C_{t \max}/C_{i \max} = \sigma_{iy}/\sigma_T = m. \quad (2)$$

Now, the value of m , at each x , was assumed to fluctuate in the range $0 < m < 1$ and its pdf was assumed to be described by a Beta function, Beta (\underline{m} , s^2), where \underline{m} is the mean value of m and s^2 is its variance.

Using this model, the shapes of $P(\alpha)$ for $\underline{m} = 0.60$ and $s^2 = 0.15$, which had been chosen by trial and error, were plotted in Figures 1-3 (triangular symbols). It is seen from these figures that although the calculated values of P deviate

at some regions from the experimental measurements, the general agreement between all the measurements and the model is surprisingly good.

This agreement does not imply, of course, that the physical model used to describe the fluctuations of the properties of the instantaneous plume is correct. Different models with different distributions of m may give similar results. However, since $P(\alpha)$ is in good agreement with the measurements, the results enable one to calculate the mean value of any function of the fluctuations.

The results suggest that the structure of the instantaneous plume could be investigated in greater detail by using the newly developed experimental method. Previous theoretical work and experimental work suggest, for example, that the structure of the fluctuating plume in homogeneous turbulence varies with the distance downwind from the source (Batchelor, 1952; Nappo, 1979, 1980, 1983). It is therefore expected that the observed plume similarity for the shear flow and boundary conditions reported herein is not universal, and it is of interest to determine experimentally its limitations. Development of a more accurate modified fluctuation model, which would be based on more detailed measurements of the properties of the instantaneous plume in shear flows, is also desired. Also, the new experimental method makes it possible to obtain a clearer understanding of the nature of plume fluctuations in homogeneous turbulence, which is also of considerable theoretical and practical value.

PLANNED FUTURE STUDIES

An improved IR/CO₂ system is being assembled for collecting more accurate data of obscuration fluctuations. It is planned to measure the dynamic properties of obscuration by plumes for different conditions of atmospheric stability. Characteristics of plume meandering and concentration fluctuations will be investigated.

REFERENCES

1. Batchelor, G. K. (1952), "Diffusion in a Field of Homogeneous Turbulence-II. The Relative Motion of Particles," Proc. Cambridge Phys. Soc., Vol. 48, pp. 345-362.
2. Gifford, F. G. (1959), "Statistical Properties of a Fluctuating Plume Dispersion Model," Adv. Geophysics, Vol. 6, pp. 117-138.
3. Nappo, C. J. (1979), "Relative and Single Particle Diffusion Estimates Determined from Smoke Plume Photographs," Fourth Symposium on Turbulence, Diffusion and Air Pollution, (Amer. Meteorol. Soc., Boston, MA), pp. 46-47.
4. Nappo, C. J. (1980), "Atmospheric Turbulence and Diffusion Estimates Derived from Observations of a Smoke Plume," Atmos. Environ., Vol. 15, pp. 541-547.
5. Nappo, C. J. (1983), "Turbulence Parameters Derived from Smoke-Plume Photoanalysis," Preprints Sixth Symposium on Turbulence and Diffusion, AMS, pp. 329-332.

6. Poreh, M. and J. E. Cermak (1987), "Experimental Study of Aerosol Plume Dynamics, Part III: Wind-tunnel Simulation of Vertical Concentration Fluctuations," Annual Progress Report to CRDC, CER87-88MP-JEC4, December.
7. Poreh, M. and J. E. Cermak (1988a), "Wind-tunnel Simulation of Obscuration Fluctuations by Aerosol Plumes," Proceeding of the 1988 CRDC Conference on Obscuration and Aerosol Research, Aberdeen Proving Ground, MO.
8. Poreh, M. and J. E. Cermak (1988b), "Instrumentation for Measuring Fluctuations of Horizontally and Vertically Integrated Concentrations in Wind-tunnel Plumes," Fourth International Workshop on Wind and Water Tunnel Modeling, Karlsruhe, West Germany, October.

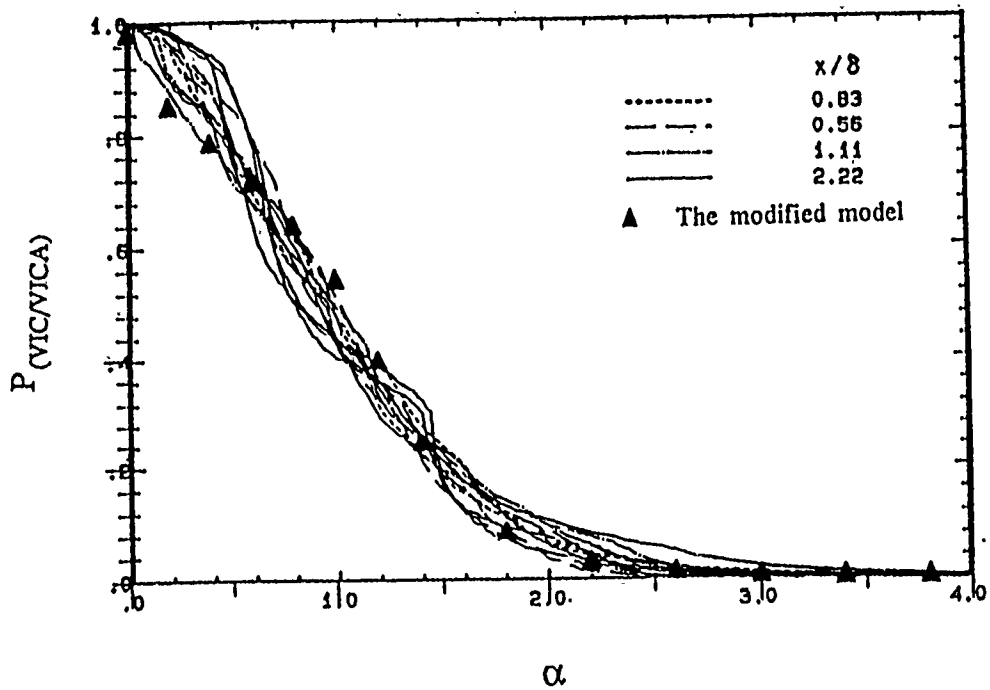


FIGURE 1. THE PROBABILITY THAT VIC/VICA EXCEEDS α AT $y/\sigma_T = 0$. The lines are calculated from the measurements. The \blacktriangle are calculated using the modified model for $B(0.6, 0.15)$.

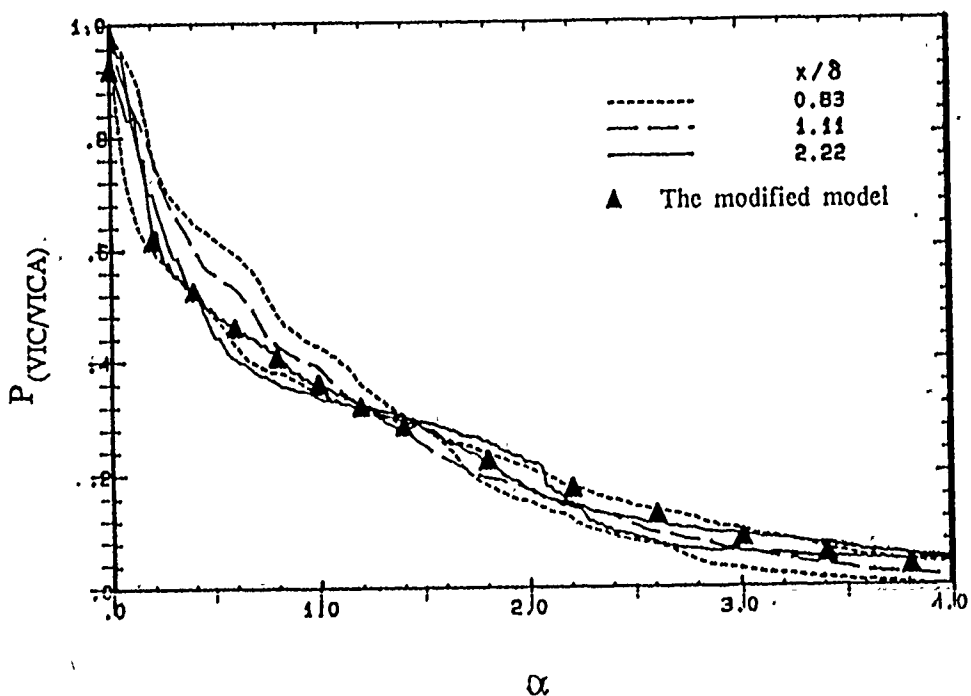


FIGURE 2. THE PROBABILITY THAT VIC/VICA EXCEEDS α AT $y/\sigma_T = 1.22$. The lines are calculated from the measurements. The \blacktriangle are calculated using the modified model for $B(0.6, 0.15)$.

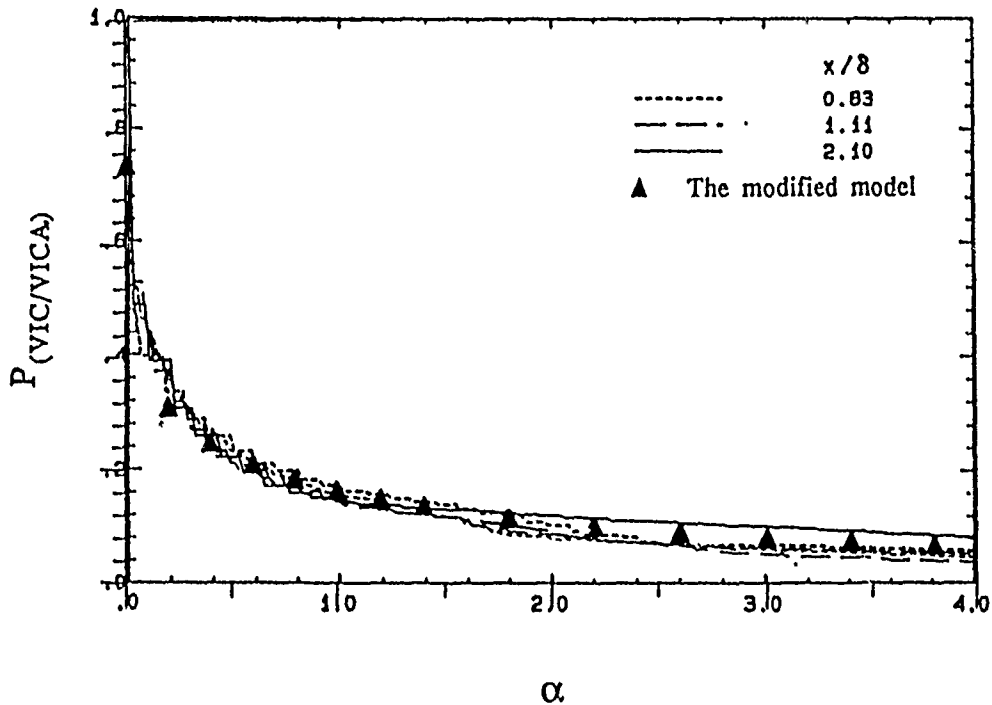


FIGURE 3. THE PROBABILITY THAT VIC/VICA EXCEEDS α AT $y/\sigma_T = 2.34$. The lines are calculated from the measurements. The \blacktriangle are calculated using the modified model for $B(0.6, 0.15)$.

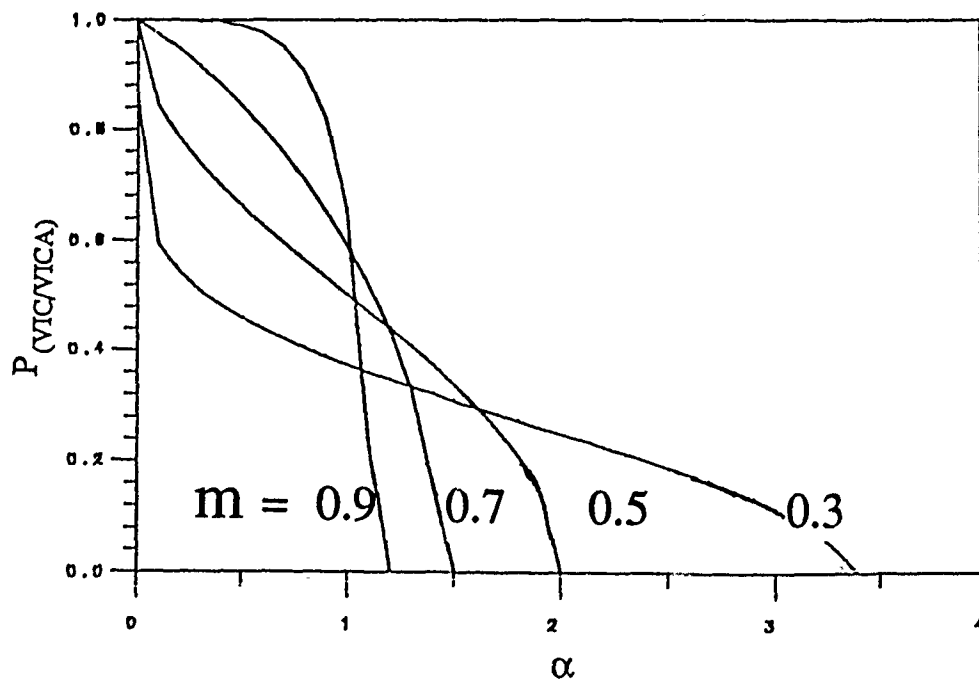


FIGURE 4. THE PROBABILITY THAT VIC/VICA EXCEEDS α AT $y/\sigma_T = 0$ according to the fluctuating-plume model for different values of m .

**DISPERSION/REACTION MODEL OF AEROSOL
FILTRATION BY POROUS FILTERS**

Michael Shapiro

Faculty of Mechanical Engineering
Technion-Israel Institute of Technology
Haifa 32000, Israel

and

Howard Brenner

Department of Chemical Engineering
Massachusetts Institute of Technology
Cambridge, MA 02139

RECENT PUBLICATIONS, SUBMITTALS FOR PUBLICATION AND PRESENTATIONS:

A) M. Shapiro and H. Brenner, "Dispersion/Reaction Model of Aerosol Collection by Porous Filters," *Proceedings of the 1986 CRDEC Scientific Conference on Obscuration and Aerosol Research*, R.H. Kohl, Ed. (This is a preliminary publication of the research results reported *in extenso* in publication B of this list.)

B) M. Shapiro and H. Brenner, "Dispersion/Reaction Model of Aerosol Collection by Porous Filters," *Journal of Aerosol Science* **20**, No. 1 (1990).

C) M. Shapiro, H. Brenner and D. C. Guell, "Accumulation and Transport of Brownian Particles at Solid Surfaces: Aerosol and Hydrosol Deposition Processes," *Journal of Colloid and Interface Science*. (Accepted in September 1989 for publication.)

D) M. Shapiro and H. Brenner, "Dispersion and Deposition of Aerosol Particles in Porous Filters." Presentation made at the *European Aerosol Conference*, Vienna, Austria, September 18-23 (1989).

ABSTRACT

Characteristic filtration lengths of fibrous filters collecting diffusional submicrometer aerosols are computed by a finite element method on the basis of the dispersion/reaction filtration model. The calculated data are compared with known theoretical and experimental results, with good agreement. Future calculations will include interceptional and gravitational aerosol collection mechanisms.

This study is concerned with the collection of submicrometer aerosol particles by porous filters, primarily fibrous and granular. A porous filter is composed of a matrix of small elements -- collectors, possessing various (usually irregular) shapes and sizes. The filter efficiency η is defined in terms of the respective inlet and outlet aerosol particle concentrations, P_{in} and P_{out} , as

$$\eta = 1 - P_{out}/P_{in} \quad (1)$$

η is the principal experimentally measurable parameter of engineering interest, whose determination for given aerosol particle properties and filtration operating parameters lies at the focus of various theoretical approaches. Classical filtration theory (Pich, 1966; Davies, 1973; Dorman, 1973) treats this problem on the basis of several *ad hoc* assumptions. Filter microstructure is characterized by specifying a unit bed element (UBE), within which the detailed velocity and external force fields are calculated. To calculate the aerosol collection rate achieved by such a single UBE, the convective-diffusive aerosol microtransport problem is formulated within one UBE while imposing an *ad hoc* boundary condition specifying a *uniform* inlet aerosol concentration at its upstream boundary. As a result, a so-called unit bed efficiency η_c is calculated.

In order to cumulatively sum the aerosol collection rates over all such collector elements comprising the bed, and thus calculate the *total* filter efficiency η , yet other *ad hoc* assumptions have to be invoked pertaining to the filter-bed structure and spatial aerosol concentration distribution existing within the filter bed interstices. As a result, the following formula was proposed, correlating the total and single-element efficiencies:

$$\eta = 1 - \exp(-\alpha\eta_c L/a), \quad (2)$$

where L is the filter thickness and a the collector size. The exact nature of the nondimensional porosity-dependent coefficient α is controversial. In many cases the choice of α was simply phenomenologically dictated so as to effect a better correlation of the theory with experimental data obtained for selected aerosols.

Our contribution describes a novel approach to the problem of diffusion-controlled aerosol filtration processes in porous filters. While utilizing the conventional microscale description of aerosol transport and deposition processes accepted in classical filtration theory, it explicitly avoids *ad hoc* summation of the respective collection rates characterizing each individual UBE; nor does it even utilize the concept of unit bed efficiency. Rather than formulate the microscale aerosol filtration problem within the one representative UBE, the present theory begins with a comparable description of the aerosol transport and collection processes *within the entire porous filter bed*. Accordingly, instead of the artificial (indeed, physically incorrect) boundary conditions imposed upon the aerosol concentration field between neighboring UBEs (as is currently done in existing theories), our more physically realistic model imposes conditions of continuity of aerosol concentration and flux across adjacent faces separating contiguous UBEs.

The proposed scheme ultimately describes the filter bed at a Darcy, rather than interstitial scale; as such, the bed is viewed at the former level of description as being a homogeneous convective-diffusive-'reactive' *continuum*, possessing uniform (i.e. position-independent) phenomenological transport coefficients characterizing each of these three transport and deposition mechanisms. These macrotransport coefficients consist respectively of the aerosol's Darcy-scale mean velocity vector \bar{U}^* , dispersion dyadic \bar{D}^* and volumetric deposition-rate scalar coefficient \bar{K}^* . They are demonstrated to be independent of the macroscale filter geometry, and can be rigorously calculated (Shapiro and Brenner, 1988; see also Ref. B) by employing generalized Taylor dispersion phenomena theory.

The sequential process of calculating the total filtration efficiency via the proposed model may be described as follows: After a precise physico-mathematical formulation of the aerosol microtransport and deposition processes in the *entire* spatially periodic (model of the) filter bed, the three Darcy-scale transport coefficients are explicitly calculated (while introducing no *ad hoc* assumptions, such as is done in the classical theory). These Darcy-scale coefficients are subsequently used to describe the gross, coarse-scale filtration process at a continuum level. Solution of the coarse-scale transport and reaction problem thereby posed immediately yields the total filtration efficiency [without utilizing *ad hoc* formulas of the type displayed above in Eq. (2)]. In particular, in many practically important cases the filter efficiency is shown to have the following form:

$$\eta = 1 - \exp(-L/l_f), \quad (3)$$

with $l_f = \bar{U}^*/\bar{K}^*$ (and $\bar{U}^* = |\bar{U}^*|$ the scalar aerosol particle mean speed) the characteristic filtration length, first introduced by Leers (1957). In contrast with the comparable *ad hoc* formula (2) employed in the classical filtration theory, the validity of Eq. (3) may be explicitly substantiated.

Calculation of the Darcy-scale aerosol transport and deposition coefficients, and from them the characteristic filtration length, constitutes the main objective of the present research. Our analysis assumes that the filter bed possesses a spatially-periodic structure (Fig. 1); that is, the filter microscale geometry may be described by the single unit cell indefinitely reproduced in three directions to fill all of space. A locally disordered unit cell microstructure (as in Fig. 1) may, if desired, be chosen to adequately approximate situations prevailing in real filters.

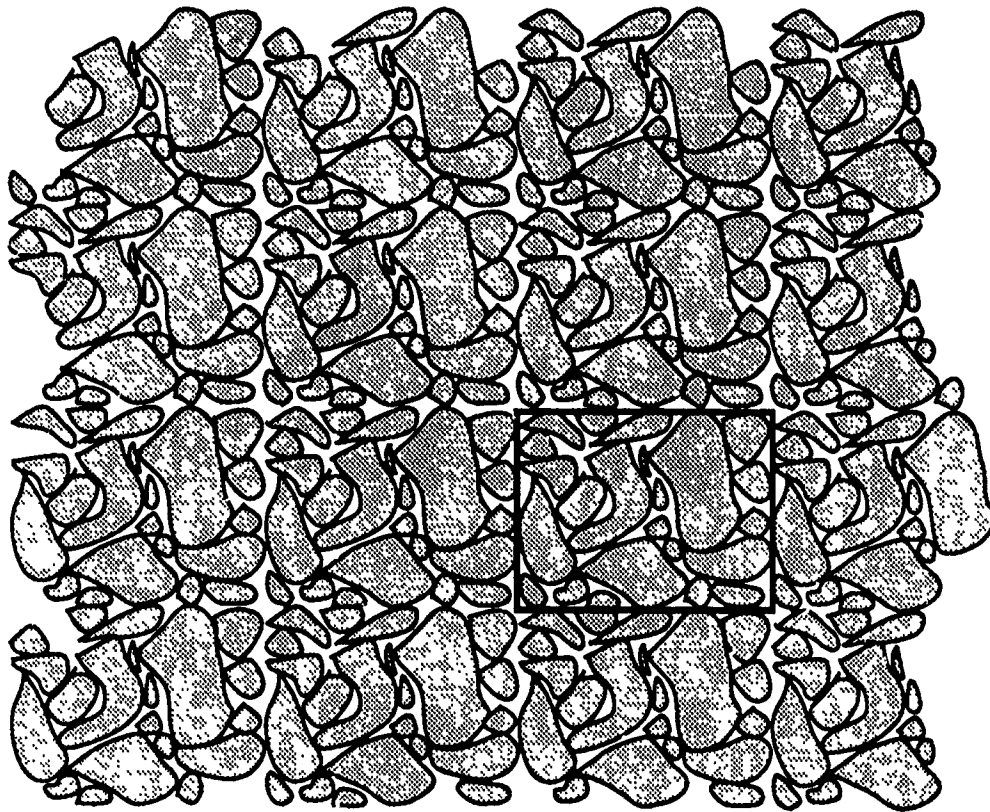


Figure 1. Spatially periodic model of a porous filter.
A typical unit cell is indicated by the square box.

The spatially-periodic model of the filter bed possesses several advantages. First, since the microscale geometry of the entire filter is known, the aerosol transport and deposition process may be exhaustively described by a well posed physicomathematical problem, formulated throughout the entire interstitial region of the effectively infinite filter bed. On the other hand, owing to the geometrical and physicochemical indistinguishability of the unit cells, the information necessary for determination of the Darcy-scale phenomenological coefficients is embodied in a *single unit cell* of the spatially periodic structure, within which cell the detailed calculations of these coefficients were actually performed.

The Darcy-scale aerosol transport and deposition coefficients were evaluated first for several simple arrays of circular cylinders (Fig. 2): square (staggered) and hexagonal. More complicated structures were modelled by bi-disperse arrays.

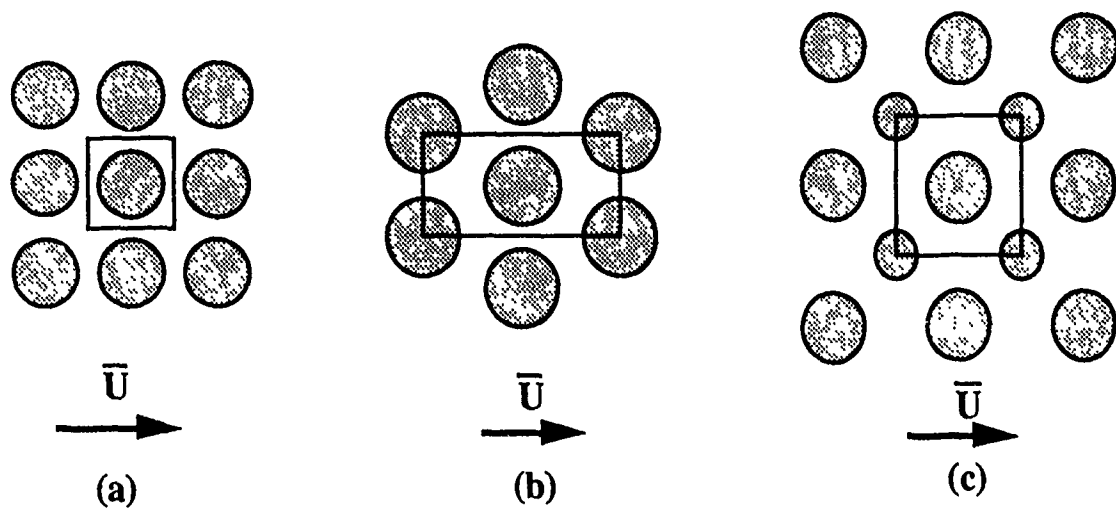


Figure 2. Spatially periodic arrays of cylinders used in calculations:
 (a) Square; (b) Hexagonal; (c) Bi-disperse.

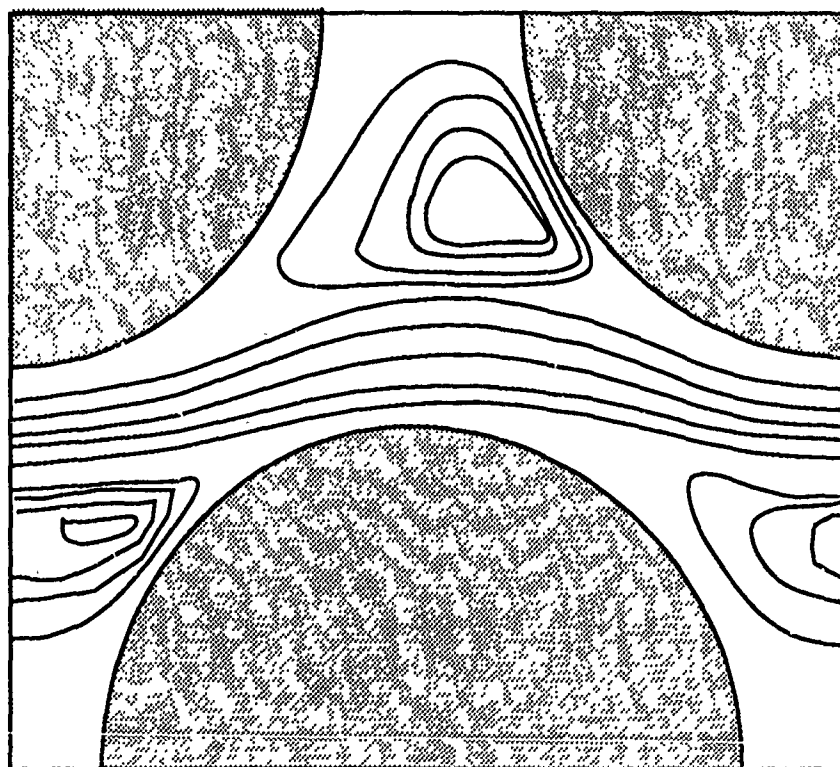


Figure 3. Microscale flow field within the hexagonal array
 (porosity=0.4, $Re=165$).

At the first step the spatially periodic interstitial flow field existing within the filter bed was calculated both for zero and nonzero characteristic microscale Reynolds numbers Re . All calculations were performed using finite element techniques. A typical result of these calculations is shown in Fig. 3 for a hexagonal array (porosity=0.4; $Re=165$). As a result of such calculations the array permeability as well as the Darcy-scale pressure gradient across the filter were evaluated (Edwards *et al.*, 1989).

Next, the Darcy-scale aerosol transport and deposition coefficients were calculated. This was done by solving several eigenvalue problems formulated within the unit cell for the convective-diffusive partial differential operator; subject to a zero particle concentration boundary condition on the collector surface(s) within the cell. The proposed model describes the diffusional and interceptional aerosol collection mechanisms, as well as the influences of externally applied forces, if any (gravitational, electrostatic, etc.). First, however, the external forces and the interception were assumed negligible. In this case, for given bed geometry and Reynolds number, the Darcy-scale aerosol transport and deposition coefficients depend only upon the microscale Peclet number $Pe = 2\bar{U}a/D$ and bed porosity, with \bar{U} the mean interstitial air velocity, a the bed cylinder radius and D the diffusivity of the aerosol particle.

At the next step the concentration distribution within the filter bed was calculated for several values of the microscale Peclet number. It was found that for low Pe numbers, of order unity (for which case the convective and diffusive particle transport mechanisms are comparable everywhere within the unit cell), that particle deposition on the collector surfaces reduces the aerosol concentration in the bulk, i.e. far from the collectors, where the local, interstitial air velocity is higher. As a result, the effective *averaged* aerosol speed \bar{U}^* is less than the comparable mean interstitial air speed \bar{U} within the filter bed.

A different situation was found to prevail in the large Peclet number case, for which circumstances a thin diffusional boundary layer exists proximate to the collector, upon whose surface(s) particle deposition occurs. Aerosol concentrations within this thin layer, where the local, interstitial air velocity is low, are depleted due to particle removal, whereas the bulk concentration remains virtually unchanged. As a result, the major portion of the aerosol is transported within the bulk region by the faster moving streamlines. Consequently, for large Peclet numbers the average aerosol particle velocity \bar{U}^* is greater than the mean air flow velocity \bar{U} within the filter. Since the large Peclet number regime usually prevails in the filtration of submicrometer aerosols, it may generally be concluded that the phenomenon of enhanced mean aerosol velocity obtains for most filtration operating conditions. A more extensive discussion, including graphical presentations of the functional dependences of the three Darcy-scale aerosol transport and deposition coefficients upon filtration parameters, is presented in a forthcoming contribution (Shapiro *et al.*, 1990).

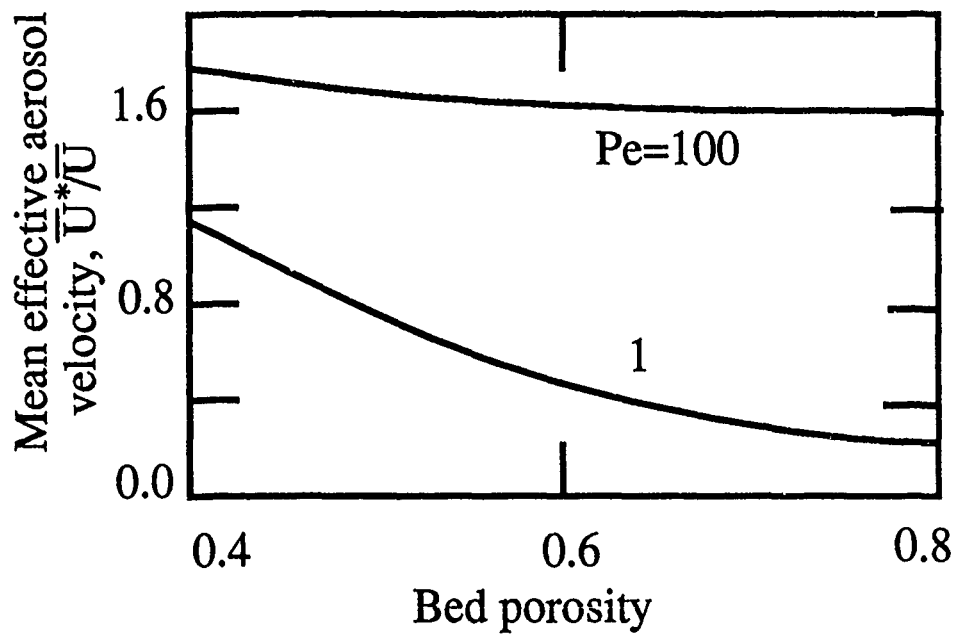


Figure 4. Mean Darcy-scale aerosol interstitial speed vs bed porosity.

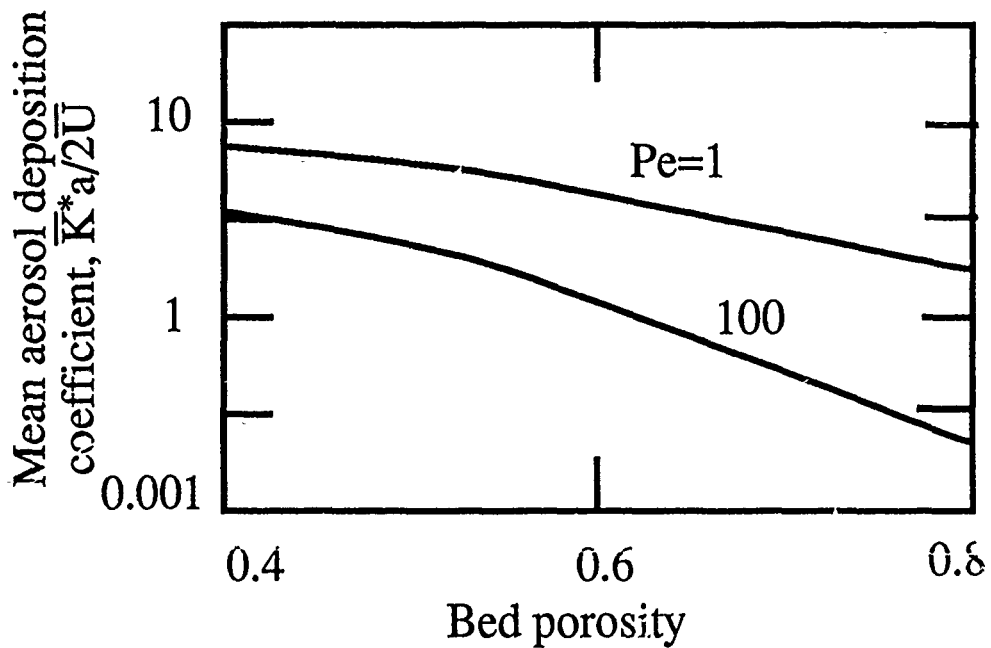


Figure 5. Darcy-scale aerosol deposition-rate coefficient vs bed porosity.

The trends discussed above are shown in Fig.4, where the Darcy-scale aerosol velocity normalized by the mean air velocity \bar{U} is plotted vs bed porosity for $Pe = 1$ and 100 . As may be seen, the effect of the increasing bed porosity is to diminish the difference between the large and small Peclet number Darcy-scale aerosol velocities. For high porosity fibrous filters, where the porosity exceeds 0.9 , the effect of Pe upon \bar{U}^* is negligible. However, the effect of Peclet number is certainly significant for packed granular filters, where the porosity may be as low as 0.35 .

Figure 5 shows the dependence of the Darcy-scale aerosol deposition-rate coefficient upon bed porosity. As may be seen, the value of \bar{K}^* is largely determined by the Peclet number, while the effect of increasing porosity is to decrease the effective aerosol deposition-rate coefficient for all Peclet numbers. This implies that coarser particles and more loosely packed filters possess smaller values of \bar{K}^* than do their opposite members.

Figure 6 compares the characteristic filtration length l_f of fibrous filters (characterized by a porosity of 0.85 and collecting $0.1 \mu\text{m}$ latex polystyrene aerosols) calculated by the present theory

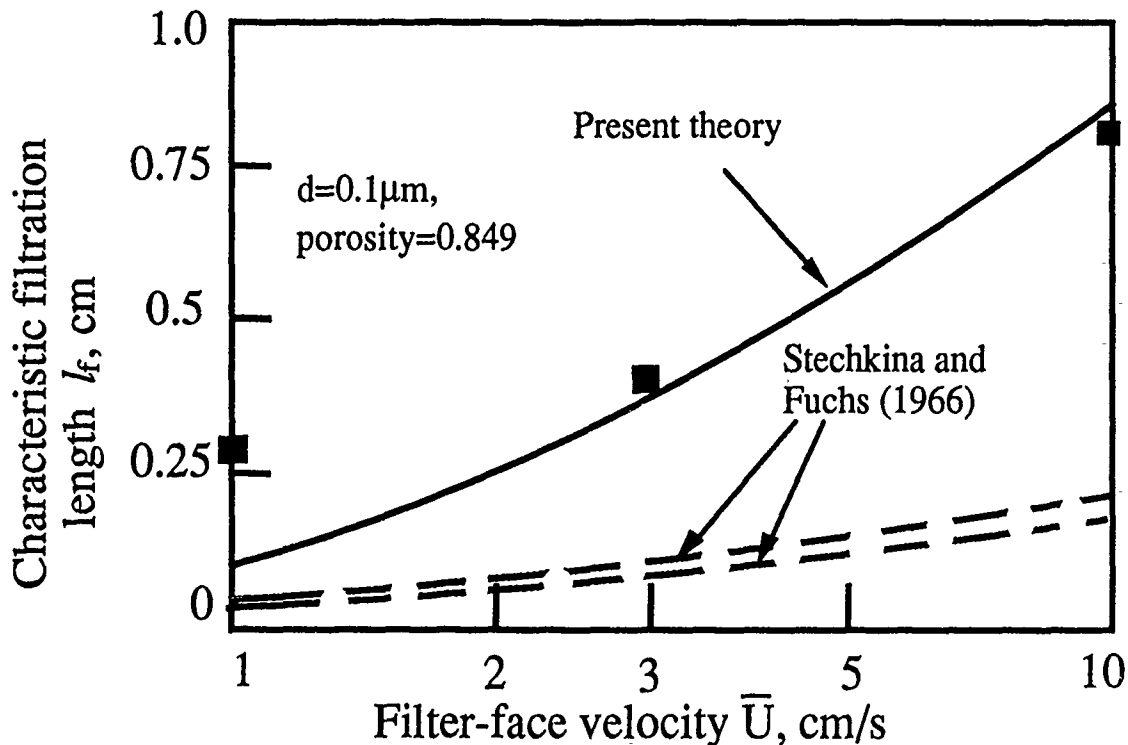


Figure 6. Comparison between the calculated data and previous results for $0.1 \mu\text{m}$ aerosol particles.

■ - Experimental (Lee, 1977);

Upper dashed line - correlation of Davies (1973);

Lower dashed line - correlation of Lee and Liu (1977).

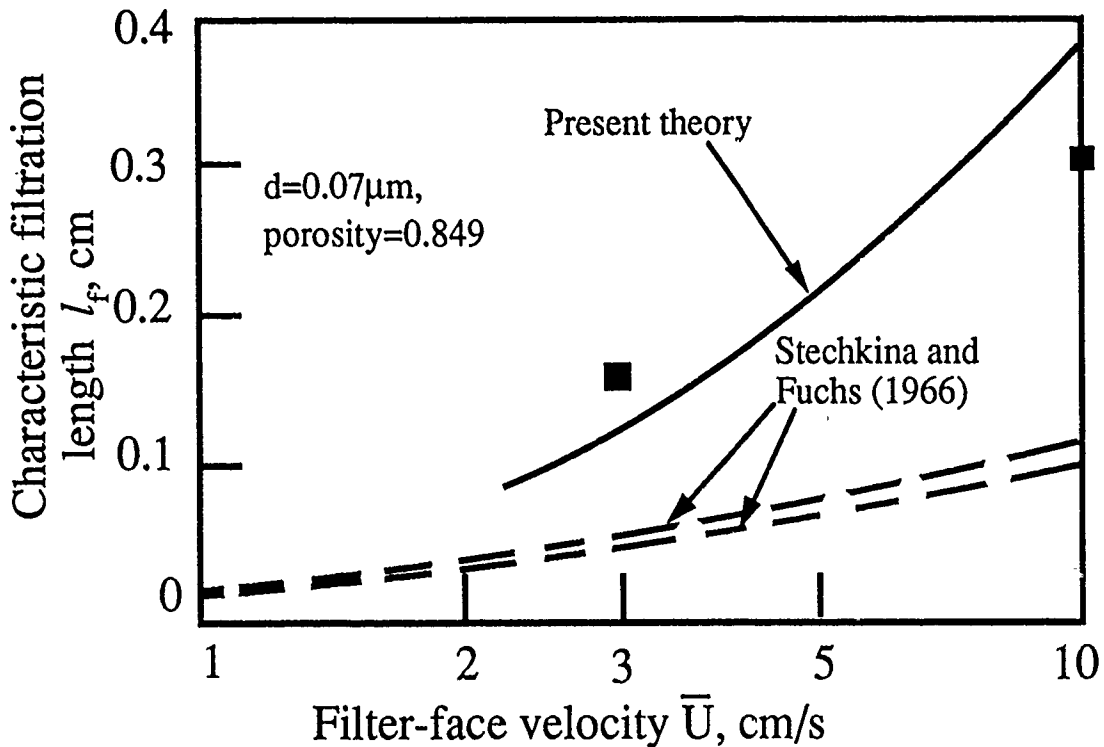


Figure 7. Comparison between the calculated data and previous results for $0.07\mu\text{m}$ aerosol particles. For legend see Figure 6.

(solid line) with the existing theory of Stechkina and Fuchs (1966) (dashed lines). Because of the ambiguity existing in the formula correlating the single-element and total filter efficiencies, two dashed curves appear in the figure -- one obtained using the correlation of Davies (1973), and the other of Lee and Liu (1982). Included also are experimental results of Lee (1977), obtained for fibrous Darcon filters. The theory of Stechkina and Fuchs significantly underestimates the characteristic filtration length and hence overestimates the filtration efficiency. Our model, however, displays satisfactory agreement with the data. The same conclusion may be drawn from Fig. 7, which displays a similar comparison for aerosol particles possessing diameters of $0.07\mu\text{m}$.

Conclusions. The proposed dispersion/reaction model of aerosol transport and deposition in porous media constitutes a novel fundamental contribution to the theory of submicron aerosol filtration by porous filter beds. Principally, it eliminates the need for many of the *ad hoc* assumptions present in the classical theory.

Instead of the misleading concept of a unit-bed efficiency, we introduce naturally three Darcy-scale phenomenological aerosol macrotransport coefficients, whose values we then rigorously calculate. These coefficients constitute physically objective, experimentally accessible

joint properties of the aerosol and porous medium, in terms of which the characteristic filtration length and the filtration efficiency are easily determined. Indeed, finite element computations of these coarse-scale transport coefficients characterizing diffusional aerosol particles in two-dimensional spatially-periodic models of fibrous media yielded values of the characteristic filtration length in good agreement with the available experimental data of Lee (1977).

LITERATURE CITED

- C.N. Davies. *Air Filtration*. Academic Press, London (1973).
- R.G. Dorman. *Dust Control and Air Cleaning*. Pergamon Press, Oxford (1966)
- D.A. Edwards, M. Shapiro, P. Bar-Yoseph and M. Shapira. The effect of Reynolds number upon the permeability of spatially-periodic arrays of cylinders. Submitted to *Physics of Fluids* (1989).
- K.W. Lee, *Filtration of submicrometer aerosols by fibrous filters*. Ph. D. Thesis. University of Minnesota, Minneapolis (1977).
- K.W. Lee and B.Y.H. Liu. Theoretical study of aerosol filtration by fibrous filters. *Aerosol Sci. and Technol.* **1**, 147 (1982).
- R. Leers. Die Abscheidung von Schwebstoffen in Faserfiltern. *Staub.* **17**, 402 (1957).
- J. Pich. Theory of aerosol filtration by fibrous and membrane filters, In *Aerosol Science*, (C. N. Davies, Ed.) Academic Press, London (1966).
- M. Shapiro and H. Brenner. Dispersion of a chemically reactive solute in a spatially periodic model of a porous medium. *Chem. Eng. Sci.* **43**, 512 (1988).
- M. Shapiro and H. Brenner. Theoretical investigation of aerosol collection in fibrous filters by the dispersion reaction model. (In preparation).
- I.B. Stechkina and N.A. Fuchs. Studies on fibrous filters I. Calculation of diffusional deposition of particles in fibrous filters. *Ann. Occup. Hyg.* **9**, 59 (1966).

Experimental Studies of Aerosol Dynamics in Reacting Systems

Richard C. Flagan
Division of Engineering and Applied Science
California Institute of Technology
Pasadena, CA 91125

Abstract

New techniques make possible rapid, high resolution measurements of fine particle size distributions. These methods have been applied to the study of the formation or growth of particles by atmospheric photochemical reactions. Direct observations of nucleation bursts are shown, including multiple nucleation events in a single reacting system and in systems involving multiple reactants.

Introduction

Gas phase chemical reactions frequently produce condensible vapors, leading to the formation and growth of aerosol particles. Particles may be formed by homogeneous nucleation, or the vapors may condense onto previously generated particles. Surface reactions of noncondensable species may also contribute to particle growth. Particle size also increases due to Brownian coagulation. The theoretical description of aerosol dynamics has advanced dramatically in recent years, making possible the simulation of the chemical dynamics of multi-component aerosol systems.

The technology for following the dynamics of rapidly changing aerosols has lagged behind the theoretical developments. In a recent study performed at Caltech, Stern et al. (1989) used a commonly used electrical mobility sizing system, the TSI Model 3030 Electrical Aerosol Analyzer, to follow the dynamics of secondary aerosols in photochemical oxidation of aromatic hydrocarbons. Conclusions from that study were (i) the EAA does not have the size range or resolution needed for quantitative interpretation; and (ii) faster response than the 5 to 8 minutes typically required for EAA size distribution measurements is needed to follow the rapid changes due to nucleation in the simulated atmospheric chemistry.

Advances in measurement technology approach the present predictive capability. Methods for making high resolution particle size distribution measurements have been available for a number of years, but these techniques have seen relatively little use in the study of time-varying aerosols due to the long times required for such measurements. Recent improvements in electrical mobility size distribution analysis make it possible to follow rapidly changing aerosols. This paper will present results obtained using state of the art aerosol measurement methods in studies of aerosol formation in the atmospheric photochemical oxidation reactions.

Experimental Methods

Studies of aerosol formation and evolution are conducted at Caltech using the Teflon reactor illustrated in Fig.1. The reactor is a Teflon balloon with a volume of approximately 60 m^3 when fully inflated. The reactor is located on the roof of the Keck Laboratories at Caltech, and utilizes sunlight to drive the photochemical reactions. The reactor is operated in two modes: (i) single bag mode; and (ii) dual bag mode in which the chamber is divided into two chambers of roughly equal volume. The former mode offers the largest volume for long duration experiments or to minimize wall effects. The dual-bag mode allows simultaneous experiments to be performed to observe directly the impact of varying a single parameter such as the initial hydrocarbon concentration or the quantity of particles present in the chamber at the beginning of the experiment.

The experimental operation consists of filling the chamber with air that has been cleaned by passing it through a series of packed bed scrubbers. The filling and subsequent addition of reactants to the chamber is performed with the chamber covered to eliminate photochemical reactions. The reactants consist of selected hydrocarbon species, nitrogen oxides, and, in some experiments, sulfur dioxide or ammonia. In some experiments an aerosol of fine particles is added to the reactant mix to probe the influence of pre-existing aerosol on the formation and growth of new particles. After filling the chamber, some time is allowed for the reactants to mix. The photochemical reactions are initiated by uncovering the chamber. The smog chamber is operated as a batch reactor. A number of gas analyzers are used to follow the progress of the gas phase reactions. Aerosol instrumentation is used to probe the formation of condensed phase reaction products.

Two series of experiments were performed in collaboration with Georg Reischl and his coworkers from the University of Vienna to probe the dynamics of ultrafine particles produced when photochemical reactions lead to homogeneous nucleation. Aerosol measurements were made with TSI differential mobility classifiers with TSI clean room condensation nuclei counters used as detectors, and with the Electrical Mobility Spectrometer (EMS) developed at the University of Vienna by Reischl and coworkers. Both of these instruments are based upon electrical mobility analysis wherein charged particles are classified according to their mobility in an electric field. Measurements of the number concentration within a narrow increment of mobility are made at a sequence of field strengths to determine the size distribution. Because the smog chamber is a batch reactor, and the measurements of different sizes are made sequentially, only transients slower than the scan period can be followed with conventional use of these instruments. Hence, we have sought alternate modes of operation that would allow fast transients to be followed.

The EMS utilizes a new mobility classifier design and a highly sensitive electrometer (detection limit of approximately 3×10^{-17} amps) to facilitate particle size distribution measurements to sizes as small as 3 nm diameter (Reischl, 1987). With this instrument, 30 point particle size distributions can be measured in 8 minutes. The TSI

instrument combination can measure particles as small as about 10 nm although the counting efficiency drops dramatically below 20 nm diameter (Wang and Flagan, 1989). The time required to measure a particle size distribution depends on the resolution sought, and can range from 8 minutes to more than an hour in conventional operation.

Parallel measurements of the concentrations of particles in a number of size intervals have been used at Caltech to overcome the time resolution limitations of mobility size distribution analysis. In these experiments, several mobility classifiers were operated in parallel to measure the time variation in the concentrations of particles of several sizes. In this way, the minimum resolvable time was reduced from several minutes to a few seconds. A new approach to mobility analysis was then developed that allows complete size distributions to be measured in as little as 30 seconds. With these measurement systems the dynamics of homogeneous nucleation in photochemical reactions has been probed experimentally.

Results

Dimethyl sulfide (DMS, CH_3SCH_3) and dimethyl disulfide (DMDS, CH_3SSCH_3) are biogenically released sulfur species that are thought to be important in determining the sulfate levels in the clean troposphere. Photochemical oxidation of these compounds leads to the formation of two condensible species, sulfuric acid (H_2SO_4), and methane sulfonic acid ($\text{CH}_3\text{SO}_3\text{H}$). The vapor pressures of these species are sufficiently different that they can be expected to cause quite distinct particle formation patterns. These have been probed in smog chamber studies using mobility analyzers set to measure the time variation in the concentrations of particles of several sizes, with the EMS used to measure particles in the 3 to 100 nm size range, and the DMA-CNC instruments measuring particles as large as 200 nm. Figure 2 shows the results for an experiment with no initial seed particles. Just a few minutes into the experiment, large numbers of 10 nm particles are formed. These rapidly disappear as the particles grow to larger sizes. A wave of particle formation is seen to propagate through particle size space.

The behavior becomes more complicated when there are particles present before the reactions begin. Nuclei coagulate with seed particles, so the number concentrations decrease more rapidly than in unseeded experiments. As the number of nuclei decreases, so does the ability of the nuclei to scavenge condensible vapors and suppress additional nucleation. This leads to oscillations in the number concentrations in seeded experiments as shown in Fig. 3.

It is important to note that the time scales characteristic of these dynamic features of aerosols produced by gas phase reactions could not be resolved using conventional aerosol measurement methods. To resolve size distribution evolution during such transients, greatly accelerated instruments are needed. An analysis of the differential mobility analyzer operation reveals that most of the time required to make a size distribution measurement is consumed waiting for the concentration to reach a steady state after changing the field

strength. This limitation has been overcome by replacing the step-wise measurements with a continuous ramp of the field strength (Wang and Flagan, 1989). All particles then migrate through a time-varying electric field, but, for any particle entrance time, only particles whose mobilities fall within a narrow range will reach the sample extraction slot on the collection rod. By using the continuously varying field strength, the delay between measurements is eliminated entirely. A complete high resolution size distribution scan can be made in 30 to 80 seconds. With this Scanning Electrical Mobility Spectrometer (SEMS), the dynamics of fine particle evolution in reacting systems can be followed with unprecedented time resolution.

Figure 4 shows a series of size distribution measurements made in a smog chamber study of the photochemical oxidation of 1-octene and SO₂. A large number of particles were formed only 8 minutes after uncovering the chamber. The fine nuclei then grew primarily by condensation, causing the size distribution to narrow as the particles grew. An hour after this initial nucleation burst, at 1:20 into the experiment, a second nucleation burst occurred, again forming a large number of particles in the 10 to 20 nm size range. The resulting size distribution was bimodal. Both modes continued to grow through the remaining hour of the experiment. Similar experiments without SO₂ did not form particles early in the experiment. Thus, the first burst of nucleation can be attributed to the sulfur dioxide reactions and is likely the result of sulfuric acid nucleation. The second nucleation burst appears to be the result of the hydrocarbon/NO_x reactions. Hence, one would expect that the compositions of the particles in the two modes of the size distribution might differ significantly. The particles formed early are composed of the material that was responsible for that nucleation, probably H₂SO₄, and material that condensed on the nuclei later, a mix of H₂SO₄, water, and hydrocarbon species. The particles formed in the second burst of nucleation would contain only those condensable species that are present late in the reaction process.

Theoretical considerations

The theoretical description of the complex chemical dynamics of aerosols in reacting systems have advanced considerably in recent years. Numerous codes have been developed to describe the evolution of the particle size distribution function. For the experiments described above, the primary physical processes that are active are nucleation and condensation. Due to the relatively low number concentrations produced during the nucleation bursts, coagulation is not particularly important, so it may not be necessary to treat coagulation to describe these experiments. The nature of the experiments makes it critical that the distribution of composition with particle size be followed in order that the size dependent solution thermodynamics can be correctly treated. At present, the multi-component sectional code MAEROS written by Gelbard is the primary tool for the study of aerosols whose composition changes with time. The sectional representation of the general dynamic equation for aerosols is subject to numerical diffusion when condensational growth is important, so further improvements are needed. The narrow size distributions

observed in the smog chamber experiments are the result of condensational growth. Accurate simulation of the dynamics of multicomponent aerosols will clearly require further improvements in the aerosol dynamics codes.

Conclusions

Recent advances in electrical mobility size distribution analysis makes it possible to follow the dynamics of fine particle formation and evolution with heretofore unachievable time and size resolution. Measurements of aerosol formation have been made during photochemical reactions under simulated atmospheric conditions. Transient phenomena that would not previously been measurable have been recorded in considerable detail. These include oscillations in the formation and growth of aerosols in experiments in which particles were present before reaction was initiated, and multiple bursts of nucleation in systems with multiple reactants. The observed oscillations had sufficiently high characteristic frequencies that they would only appear as noise in conventional measurements.

A comprehensive understanding of the chemical dynamics of aerosols requires further advances. Ideally, the time variation of the chemical composition with size would be followed with similar time resolution to that achieved in this study in the measurement of particle size distributions. This might be accomplished by interfacing chemical detection systems to mobility analyzers. Present mobility analysis is limited to particles smaller than about 0.2 μm in diameter because of the large number of multiply charged particles at larger sizes. This difficulty may be overcome to some extent through the inversion of the raw size distribution data, in effect correcting for the non-ideal instrument response functions. Since particles in larger than 0.2 μm are so important to the effects of aerosols, improved instrumentation is needed for larger particles as well. Again, knowledge of the composition-size distribution in this size regime will be critical to the understanding of the sources and effects of the aerosols.

Acknowledgements

This research was supported by the Coordinating Research Council.

References

- Gelbard, F., Tambour, Y., and Seinfeld, J.H. (1980) *J. Colloid Interface Sci.* **78**, 485.
- Reischl, G. (1987) University of Vienna, Institute for Experimental Physics, *private communication*.
- Stern, J.E., Flagan, R.C., and Seinfeld, J.H. (1989) "Aerosol Dynamics in Atmospheric Aromatic Photooxidation," *Aerosol Sci. Technol.* **10**, 515-534.
- Wang, S. C., and Flagan, R. C. (1989) "The Scanning Electrical Mobility Spectrometer," *submitted to Aerosol Science and Technology*.

Figure Captions

Figure 1. Schematic of the Teflon smog chamber reactor facility at Caltech.

Figure 2. Time variations in particle concentrations at different times in the photochemical oxidation of dimethyl disulfide with no seed particles present. (a) 4.86 nm and 10.9 nm particles; (b) 20.2 nm and 49.9 nm particles; (c) 71.3 nm, 97.8 nm, 148 nm, and 205 nm particles.

Figure 3. Oscillations in the concentration of 3.4 nm nuclei late in the photochemical oxidation of dimethyl disulfide. Data obtained with the University of Vienna Electrical Mobility Spectrometer continuously monitoring a fixed mobility interval.

Figure 4. Particle evolution in photochemical oxidation of 1-octene in the presence of SO_2 . Initial burst of nucleation occurred at 8 minutes into the experiment. A second nucleation burst occurred 1 hour 11 minutes after uncovering the chamber. After the second nucleation burst, both modes of the resulting bimodal distribution continued to grow.

OUTDOOR SMOG CHAMBER FACILITY

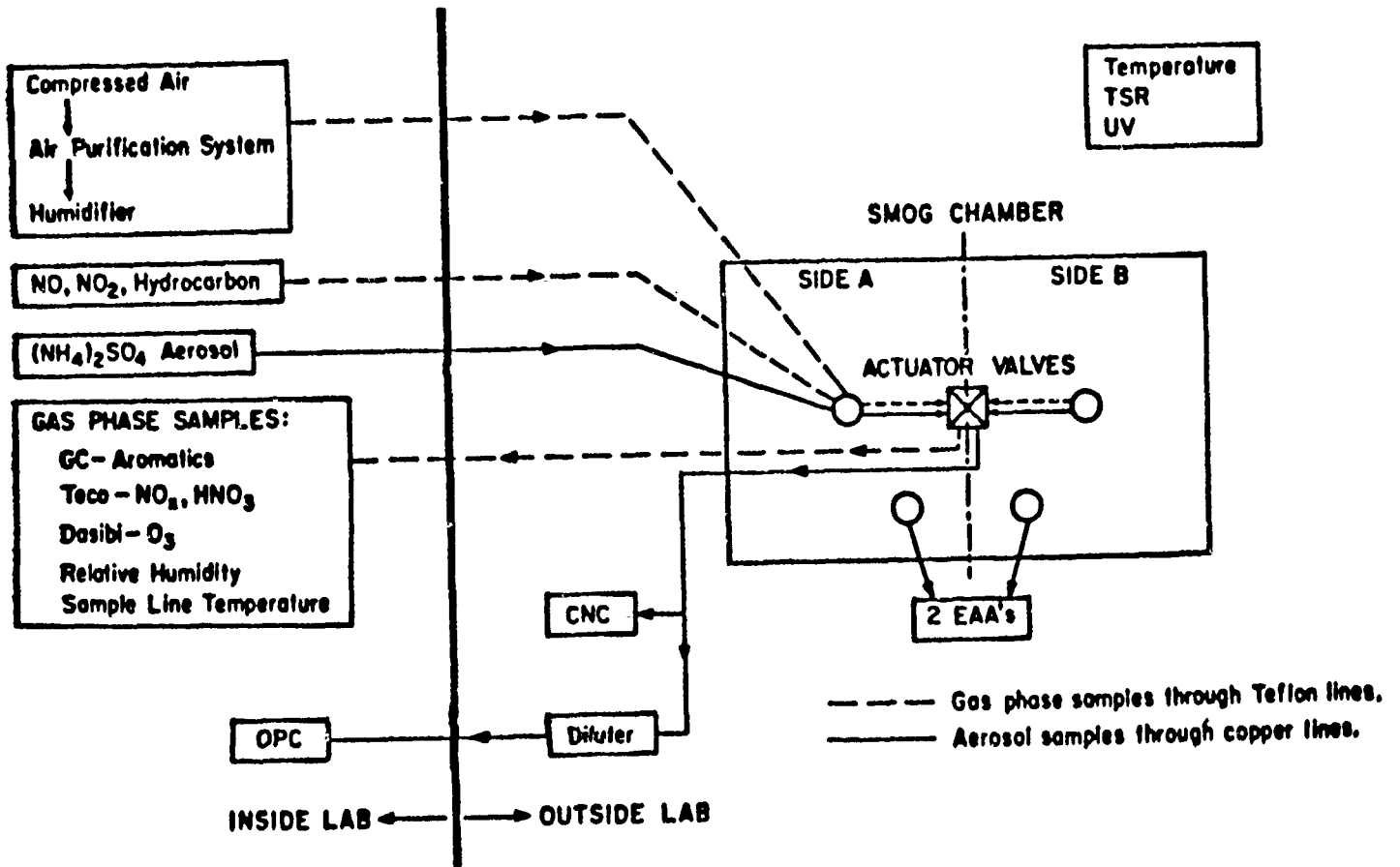


Figure 1. Schematic of the Teflon smog chamber reactor facility at Caltech.

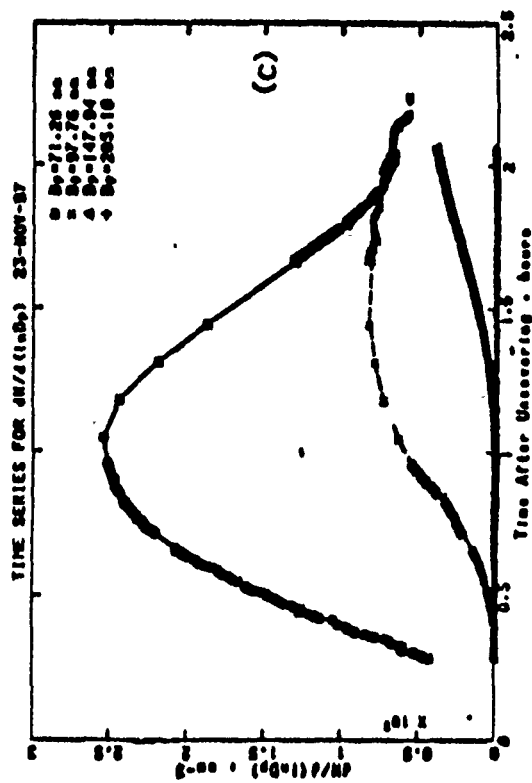
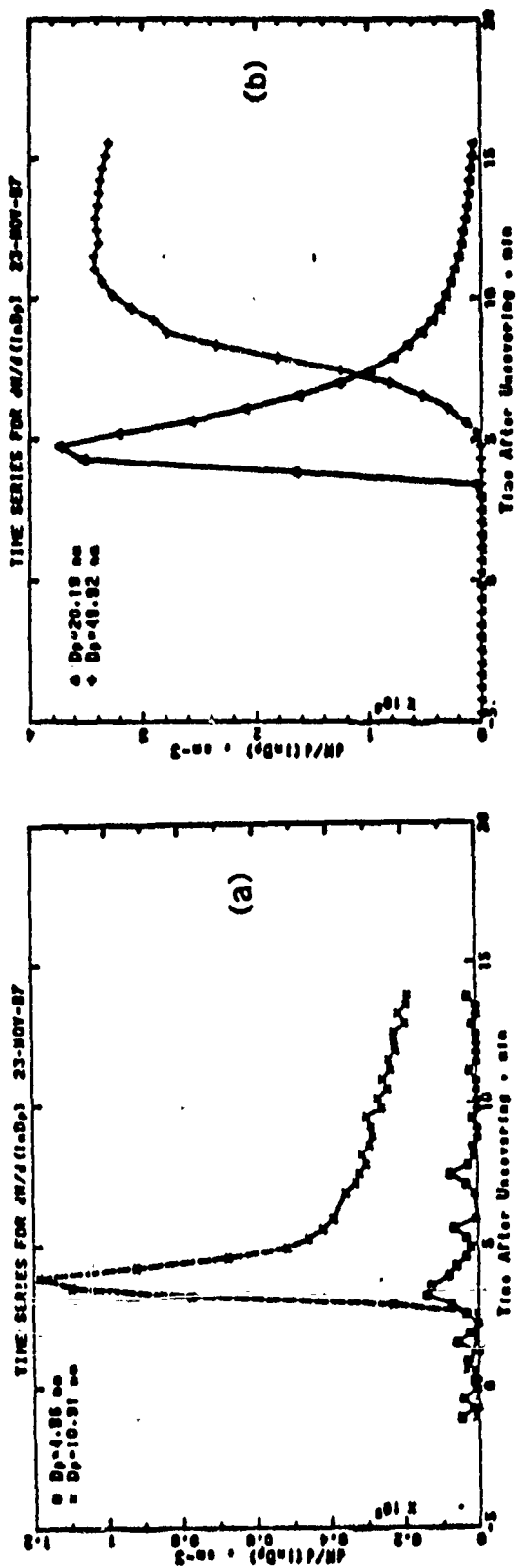


Figure 2. Time variations in particle concentrations at different times in the photochemical oxidation of dimethyl disulfide with no seed particles present. (a) 4.86 nm and 10.9 nm particles; (b) 20.2 nm and 49.9 nm particles; (c) 71.3 nm, 97.8 nm, 148 nm, and 205 nm particles.

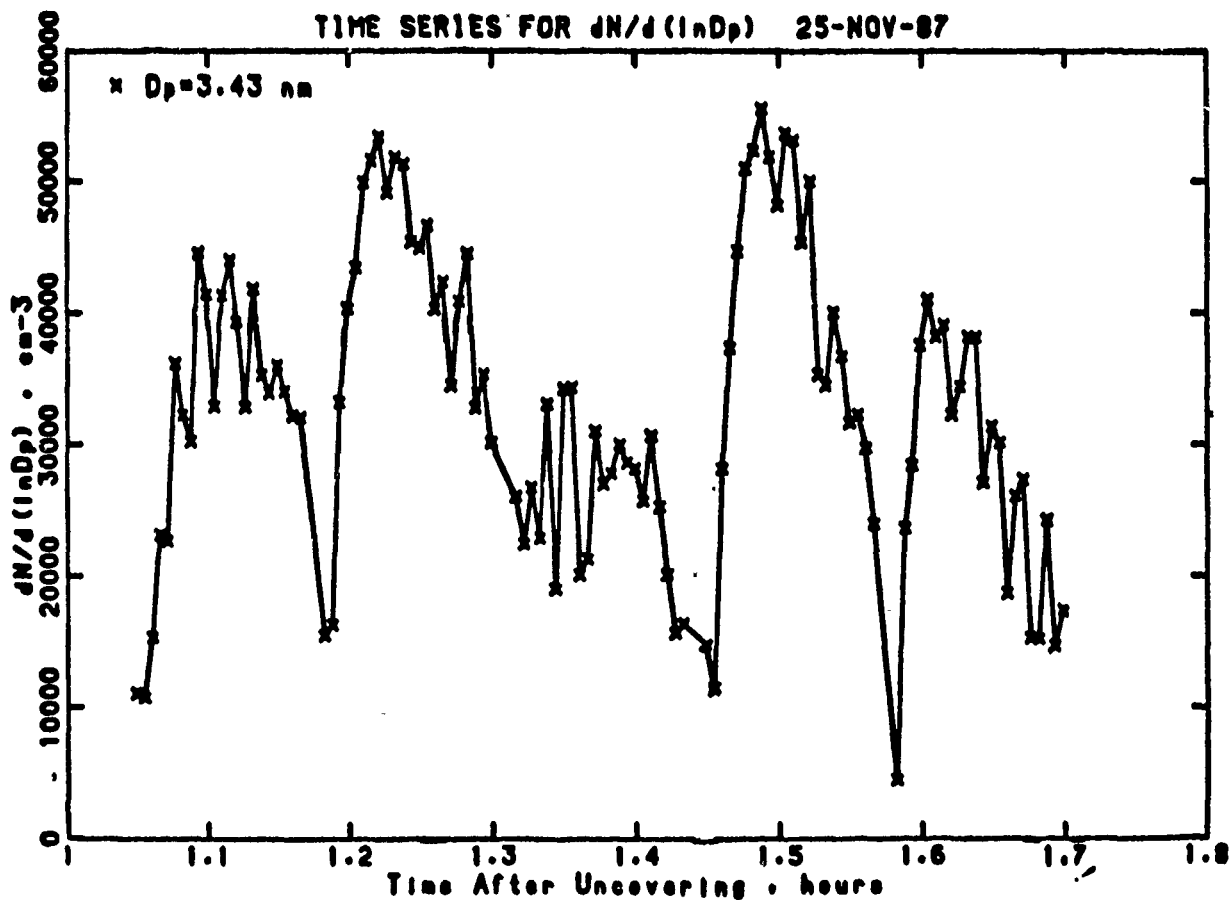


Figure 3. Oscillations in the concentration of 3.4 nm nuclei late in the photochemical oxidation of dimethyl disulfide. Data obtained with the University of Vienna Electrical Mobility Spectrometer continuously monitoring a fixed mobility interval.

$[NO]_0 = 2.104 \text{ ppm}$
 $[NO_2]_0 = 0.073 \text{ ppm}$
 $[1\text{-Octene}]_0 = 1.4 \text{ ppm}$
 $[SO_2]_0 = 0.003 \text{ ppm}$

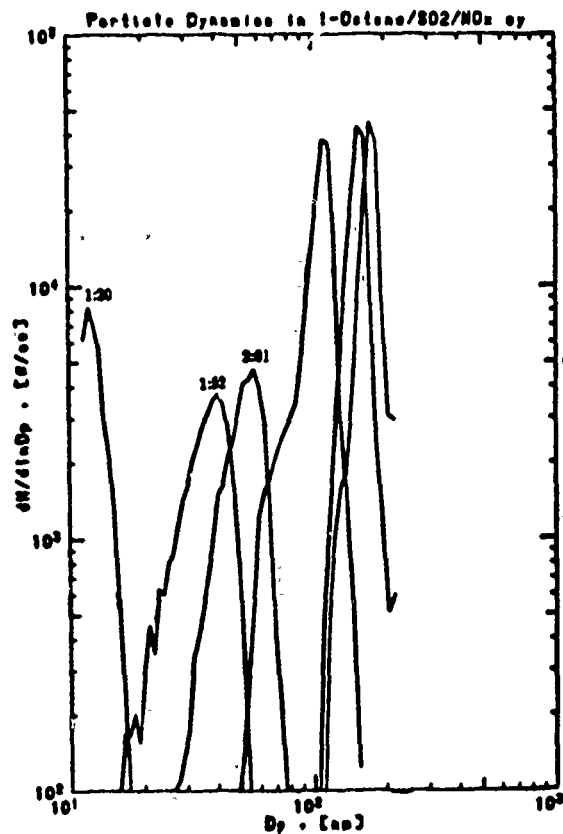
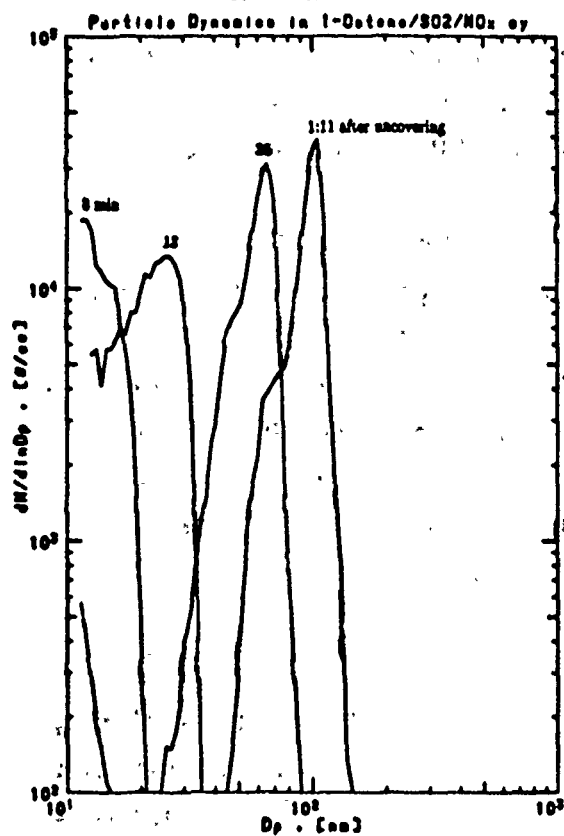


Figure 4. Particle evolution in photochemical oxidation of 1-octene in the presence of SO₂. Initial burst of nucleation occurred at 8 minutes into the experiment. A second nucleation burst occurred 1 hour 11 minutes after uncovering the chamber. After the second nucleation burst, both modes of the resulting bimodal distribution continued to grow.

II. AEROSOL CHARACTERIZATION

A Microparticle Electrometer for Repeated Charge Exchange Measurements between a Microparticle and a Surface

L.M. Folan and S. Arnold
Microparticle Photophysics Laboratory (MP³L)
Department of Physics
Polytechnic University
333 Jay St., Brooklyn, N.Y. 11201

RECENT PUBLICATIONS, SUBMITTALS FOR PUBLICATION AND PRESENTATIONS

- A) L.M. Folan and S. Arnold, "A Levitation-based Electrometer for Repeated Charge Exchange Measurements between Individual Micron Sized Particles and a Surface", 63rd Colloid and Surface Science Symposium, University of Washington, Seattle, June 21, 1989.
- B) L.M. Folan, S. Arnold, T.R. O'Keeffe, D.E. Spock, L.B. Schein and A.Z. Diaz, "A Microparticle Electrometer for Repeated Charge Exchange Measurements between a Microparticle and a Surface", J. Electrostat. (accepted, Sept., 1989).
- C) L.M. Folan and S. Arnold, "A Microparticle Electrometer for Determination of Charge Exchange", 1989 CRDEC Conference on Obscuration and Aerosol Research, June 26-30, 1989
- D) S. Arnold and L.M. Folan, "Tribo-Electricity", Weber Symposium on Electron Transport in Solids, Weber Institute, Polytechnic University, December 16, 1988.

ABSTRACT

We present a new electrometer for the purpose of performing repeated contact charging experiments between a single microparticle and a metal surface. The electrometer is based on an electrodynamic levitator-trap and has a leakage current of 10^{-23} A. The electrometer is applied to the study of the charging of polystyrene-DVB copolymer particles on Ni. We find that contact charging is not inhibited in a "dry" N₂ atmosphere relative to ambient air. It is unlikely that ionic transfer is responsible for contact charging in this system. In addition through a combination of gravimetric and light scattering measurements we have determined both the amount of water accreted in a humid atmosphere and have concluded that this water is principally distributed throughout the particle bulk.

Recently there has been a great deal of interest in charge transfer processes associated with microparticles at surfaces[1,2]. In most experiments involving micron size particles charge transfer is measured on a statistical basis by allowing a continuous stream of particles to reflect off a surface and into a Faraday cup, where the accumulated charge is measured[3,4]. Since no two particles are precisely alike in either size and/or morphology it is advantageous, from a scientific standpoint, to repeat measurements on a given particle over an extended period. In addition, because of the possible importance of deep trap states in insulators one would like to allow a particle to rest on a surface for a controllable period before determining the amount of charge transferred. In what follows we describe an electrometer with which one can experiment on a single micron size particle over an extended period. Aside from the ability to make repeated contacts, this new approach has a low enough leakage rate ($\sim 10^{-23}$ A) that one has the time in between contact events in which to change the immediate environment. One particular application is the determination of the effect which ambient air has on charge transfer. By bringing a particle in and out of vacuum between charge transfer events one can ask specific questions such as the effect of relative humidity on the charge transfer process. It has been hypothesized by several authors that ionic transfer can be an important mechanism in contact charging, if so one would expect ambient humidity to play a central role. The microparticle electrometer will be applied to testing this hypothesis for the specific case of a polystyrene-DVB copolymer particle on Ni.

The basic idea behind the Microparticle Electrometer is the use of Electrostatic Levitation as a means for isolating a particle in between contact events and measuring the exchanged charge. The basic working equation is that of Millikan,

$$q = mg/E, \quad (1)$$

where mg is the weight of the particle and E is the levitating field. In practice one merely has to measure the inverse electrostatic potential $1/V_{dc}$ between the electrodes, and so long as the mass does not change, this number is proportional to the charge. The difficulty with charge exchange measurements is not the accuracy with which charge can be measured (i.e., the state of charge of a single particle is easily measured in such an apparatus with one electron accuracy[5]), but the problem of a) contacting a surface, b) removing the particle from the surface, and c) recapturing the particle for re-analysis of its

charge. In addition, to best interpret the experimental effect, the particle should make contact and be removed without using an external field. A reasonable means for removing a particle is through the use of a mechanical impulse. However, considering the level of acceleration needed to accomplish this ($\sim 10^4g$) the resulting velocity makes recapture a difficult prospect in a conventional Millikan capacitor. To overcome this limitation of traditional electrostatic levitation we have added an additional time varying potential which creates an electrodynamic trap.

A schematic of the Microparticle Electrometer is shown in Fig.1.

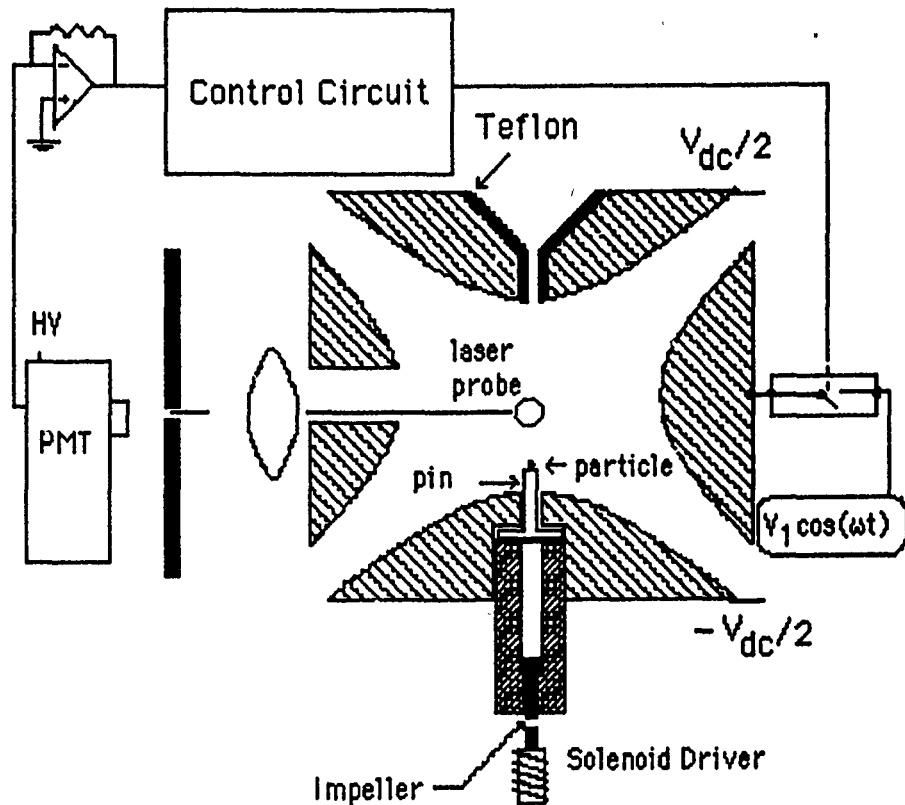


Fig.1 Microparticle Electrometer for Charge Exchange Measurements.

The basic levitator-trap(LT) in Fig.1 consists of three electrodes; top and bottom hyperboloids of revolution and a hyperbolic torus[6]. For the current discussion we will ignore the pin in the bottom. A precharged polystyrene-DVB copolymer particle formed by rubbing a relatively neutral polystyrene microsphere against a teflon surface with a

teflon wand is allowed to fall through the center hole in the top hyperbolic electrode. The alternating field $E_{ac}(r)\cos(\omega t)$ is what distinguishes the Microparticle Electrometer from the Millikan capacitor. The particle executes rapid oscillations in the presence of this field. Since these oscillations occur in a field having a gradient, a time averaged force is produced[7]. For the limit of small and rapid oscillations it can be shown that this force is given by[8]

$$\langle E_{ac} \rangle_t = -[q^2 b(\omega)] \nabla [E_{ac}^2], \quad (2)$$

where q is the charge of the particle, and $b(\omega)$ is a positive frequency dependent function. Thus the particle moves toward a minimum in the square of the field, E_{ac}^2 . For the apparatus in Fig.1, the fact that the alternating potential is azimuthally symmetric about the vertical axis and has a horizontal mirror plane intersecting the center guarantees that E_{ac} is zero at the center, although E_{ac}^2 grows in all directions away from the center. Thus $\langle E_{ac} \rangle_t$ traps the particle. In the absence of gravity the particle would simply remain at the center, however, in the presence of gravity the particle is pulled below center and oscillates with its center of oscillation at a displacement such that $\langle E_{ac} \rangle_t$ balances gravity. It should be noted that the force $\langle E_{ac} \rangle_t$ is proportional to q^2 which allows particles to be trapped independent of the sign of charge. In addition the trapping force is large enough for the particle to be contained while the chamber encasing the electrometer is pumped down from atmospheric pressure to $\sim 10^{-3}$ Torr in less than 1/2 hr. Aside from $\langle E_{ac} \rangle_t$ an additional levitating force E_{dc} is produced by utilizing the dc power supply, V_{dc} . This force enables the particle to be pulled to the center of the levitator-trap where oscillations stop and Eqn.1 applies. Now that the details of the levitator have been described we next focus on the methodology for performing the charge exchange experiments.

In Fig.1 the particle is shown sitting on a pin which is at the potential of the bottom electrode. For our experiments this pin was polished Pt or Ni. During the initial levitation phase the particle's charge to mass ratio was measured by adjusting V_{dc} to

balance and applying Eqn.1. The particle was placed near the center of the pin by allowing it to fall under gravity after being levitated at the center of the LT; at the time of contact no external field was present (i.e., both the ac and dc potentials are zero). Contact was maintained until the particle was driven off the pin by using an impulsive mechanical force. This single impulse was formed by using a solenoid driver to shoot an impeller toward the bottom of the pin. Since the impeller was trimmed in order to be slightly smaller in mass than the pin, it recoiled on impact. In this way the primary impulse was given to the pin and not to the LT. The particle was driven from the pin in the absence of an external field. As the particle ascended a few millimeters it entered the region of a focussed laser beam where light scattering by the particle was used to activate the alternating trapping potential. The particle was then rebalanced by adjusting V_{dc} and its new charge to mass ratio was calculated. The entire cycle was repeated as many as thirty times.

Fig.2a shows a typical result for contact charging between a polystyrene-DVB copolymer particle 11μ in radius and a polished Ni pin in ambient laboratory air. The particle has an initial negative charge of $-2.7 \mu\text{C/gm}$. After 10 contacts this charge is seen to increase to $-3.15 \mu\text{C/gm}$; charge is exchanged on average by $-0.045 \mu\text{C/gm}$ per "contact" (i.e. considering the size of the particle this represents an exchange of ~ 1500 electronic charges). After these points were taken the chamber was evacuated to $\sim 10^{-3}$ Torr with the particle levitated. The vacuum was held for 4 hours after which the chamber was backfilled with purified N_2 to 760 mm Hg. Charge exchange experiments were then performed as shown in the second segment of data in Fig.2b. Here the charge is seen to further increase from $-3.15 \mu\text{C/gm}$ to $-3.80 \mu\text{C/gm}$ for another 10 contacts; charge is exchanged on average by $-0.065 \mu\text{C/gm}$ per "contact". It appears that going from a lab atmosphere to a relatively dry N_2 atmosphere does not inhibit the charge exchange process : this is the opposite of what one would expect if the charge transfer was ionic in origin. In fact the charge transfer process may be improved. To further test these tentative conclusions the chamber was once again evacuated while the particle was levitated. This time the evacuation to 10^{-3} Torr was carried out for 24hr. At the end of this procedure the chamber was once again backfilled with N_2 to 760mm Hg. The next ten "contacts" (i.e. "contact" 21 to 30 inc., Fig.2c) revealed an ever increasing charge from

-3.90 $\mu\text{C/gm}$ to -4.70 $\mu\text{C/gm}$; charge is exchanged on average by -0.080 $\mu\text{C/gm}$ per "contact". This last result is consistent with our previous findings. The experiment was subsequently terminated with the loss of the particle.

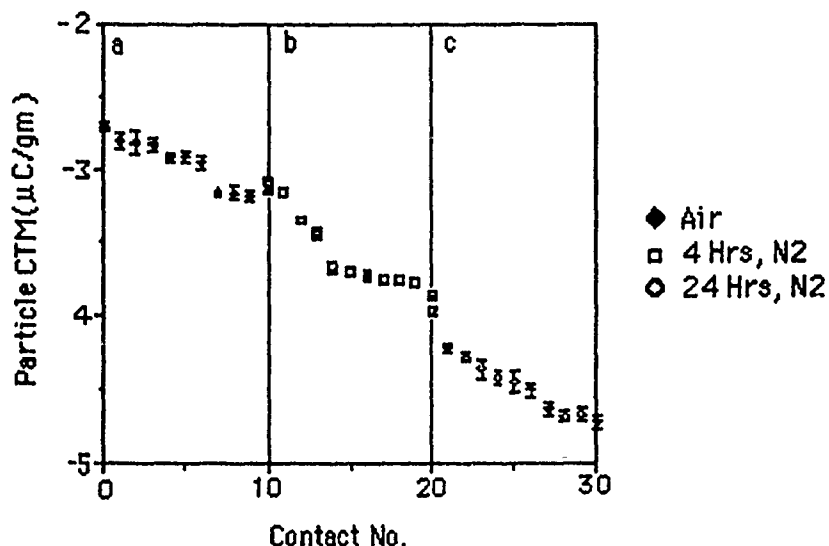


Fig.2. Charge exchange measurements between a polystyrene-DVB copolymer particle and a Ni pin.

It is interesting to note that the variations in charge exchange from one contact to the next as demonstrated in Fig.2 appear to be far from that expected from Poisson statistics. Since the particle is likely to change its angular orientation from one contact to the next, "patch" effects associated with surface states may explain this behavior.

Effects associated with water will depend on its ability to be adsorbed by the particle. Thus an attempt was made to measure water adsorption on a levitated particle by operating the levitator as a pico-balance[9]. In this mode one monitors adsorption by continuously measuring the levitation voltage as the particle accretes vapor. Specifically the chamber was first evacuated to 10^{-3} Torr with a particle (polystyrene-DVB copolymer, 10μ in diameter) levitated and vapor was bleed in up to a relative humidity of 80% (as monitored by a capacitive monometer). Fig.3 shows the results. We see that the particle

takes on 0.25% water at 80%RH, and this accretion is in proportion to the humidity. It is not possible through this gravimetric means to know whether the water stays on the surface or distributes throughout the bulk. However, it is possible by utilizing elastic light scattering to obtain an answer to this question.

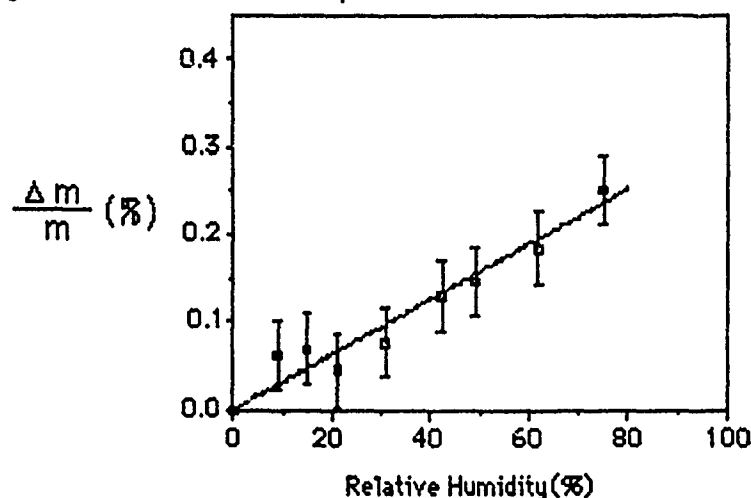


Fig.3 Measured mass of a Polystyrene DVB copolymer Microparticle (~10 μ diam.) vs. Relative Humidity.

By utilizing a dye laser we excited the natural electromagnetic modes of a particle. This vector wave excitation allows us to excite both TE and TM type resonances. If the water resides principally on the surface we expect through a self-consistent electromagnetic calculation that both the TE and TM modes will shift toward longer wavelengths and that the TM mode will have a shift in excess of the TE mode by about 30%. On the other hand if the water goes uniformly into the bulk we expect no differential shift between the TE and TM modes. This new technique is termed Resonant Ellipsometry.[10] The measured shift in the TM optical resonance of the particle as a function of relative humidity is shown in Fig.4. Since we were more sensitive to the resonant shift than the mass, measurements of the shift could be started below 10%RH. Above this point the measurements show a linear shift of the resonant mode with additional water concentration. Thus, one can expect to be able to extrapolate the mass data down to 10%RH in a linear fashion. The difference between the TE and TM mode

shift was measured at 90%RH and found to be considerably below the 30% level predicted for isolated water on the particle surface. In addition the expected overall shift of the TM mode as shown in Fig.4 is only half of what would have been expected for surface isolated water on the basis of the added mass. Therefore we believe that the water does not form an interface at the particle surface; our measurements are consistent with water going primarily into the bulk.

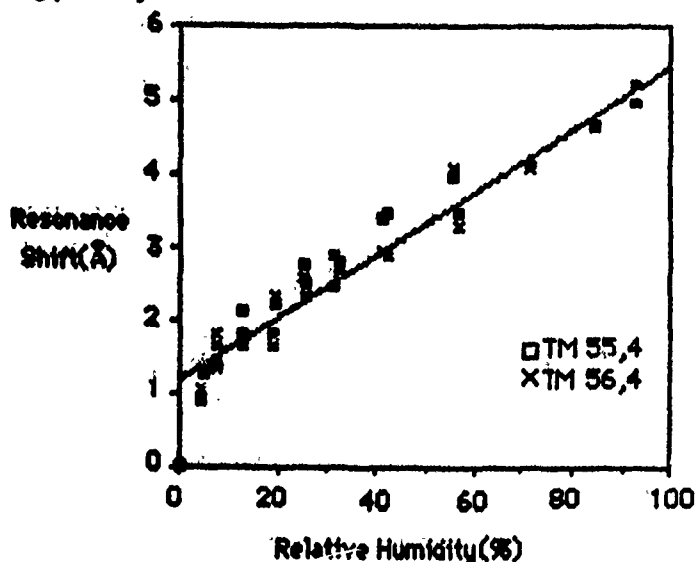


Fig.4 Shift in natural electromagnetic resonance versus relative humidity for a polystyrene-DVB copolymer particle approx. 10μ in diameter.

Surfactant free particles were obtained from Polysciences. These solution polymerized polystyrene particles (approximately 15μ in diameter) had been cleaned by ion exchange. Water uptake was 1/4 to 1/3 of that found for the surfactant covered particles. A comparison of the mass uptake measured by the balance principle with the shift in resonances in light scattering indicated once again that the mass uptake was principally in bulk.

In conclusion we have demonstrated that it is possible to perform repeated contact charging experiments using an individual microparticle, and have developed a microparticle electrometer for this purpose. We find that in the case of polystyrene-DVB copolymer particles on Ni that contact charging is not inhibited in a "dry" atmosphere

relative to ambient air; it is unlikely that ionic transfer is responsible for contact charging in this system. In addition through a combination of gravimetric and light scattering measurements we have determined both the amount of water accreted in a humid atmosphere and have concluded that this water is principally distributed throughout the bulk of the particles.

We are grateful for support from IBM and the Chemical Research Development and Engineering Center of the Army for this work.

REFERENCES

1. L.B. Schein, Electrophotography and Development Physics, (Springer-Verlag, Berlin 1988), Chap.4.
2. D.M. Burland and L.B. Schein, Physics of Electrophotography, Physics Today **39**, 46(1986).
3. W. John, G. Reischl and W. Devor, Charge Transfer to Metal Surfaces from Bouncing Aerosol Particles, J. Aerosol Sci. **11**, 115(1980).
4. N. Masui and Y. Murata, Electrification of Polymer Particles by Impact on a Metal Plate, Jpn. J. Appl. Phys. **22**, 1057(1983).
5. S. Arnold, Determination of Particle Mass and Charge by One Electron Differentials, J. Aerosol Sci., **10**, 49-53(1979).
6. R.F. Weurker, R.F. Shelton, and R.V. Langmuir, Electrodynamic Containment of Charged Particles, J. Appl. Phys., **30**, 342-349(1959).
7. L.D. Landau, and E.M. Lifshitz, Mechanics (Addison-Wesley, New York, 1960), P93.
8. S. Arnold, The Spectroscopy of Single Micron Sized Particles, in Optical Effects Associated with Small Particles, P.W. Barber and R.K. Chang, eds. (World Scientific, Teaneck, N. J., 1988), Chap.2.
9. E.J. Davis, Single Aerocolloidal Particle Instrumentation and Measurement, in Surface and Colloid Science Vol.14, Ed. by Egon Matijevic (Plenum Press, New York, 1987), pp 1-81.
10. L.M. Folan and S. Arnold, Distribution of Adsorbed Molecules within a Microparticle by Resonant Ellipsometry, in preparation.

BLANK

AN APPROACH TO THE ULTIMATE DETECTION LIMIT
BY FLUORESCENCE MEASUREMENTS IN MICRODROPLETS

W. B. Whitten, J. M. Ramsey
Oak Ridge National Laboratory
Oak Ridge, Tennessee 37831

S. Arnold
Polytechnic Institute of New York
Brooklyn, NY 11201

B. V. Bronk
U. S. Army CRDEC
Aberdeen, MD 20101

RECENT PUBLICATIONS, SUBMITTALS FOR PUBLICATION, AND PRESENTATIONS

A) J. M. Ramsey and W. B. Whitten, "Looking for Single Molecules in Small Droplets", to be presented at American Chemical Society, Miami, Fla., Sept. 12, 1989.

ABSTRACT

The sensitivity of fluorescence measurements is usually limited by background signal due to solvent fluorescence and Raman scattering. We are exploring the use of levitated microdroplets as a sampling technique for ultrasensitive fluorescence measurements. The background signal from a droplet with picoliter volume is comparable to the emission signal from a very small number of fluorescing molecules. We report the results of our initial experiments to determine the detection limit of rhodamine-6G by this technique. In future work, we hope to improve the photon collection efficiency and obtain further reductions in background signal to improve the limit of detection.

The detection of molecules by laser-excited fluorescence is extremely sensitive because a molecule can undergo many excitation-emission cycles before undergoing photochemical degradation. For example, for rhodamine-6G, (R-6G), the fluorescence lifetime is in excess of 10^5 cycles(1). The fraction of emitted photons collected and converted to countable pulses can be as high as 10^{-3} , although 10^{-4} is more readily attainable. Thus, sufficient photons are emitted for single molecules to be detectable. The detection limits for molecules in solution have been limited by the background signal from Raman scattering and fluorescence from the solvent. This background has effectively restricted the detectable concentration to about 10^{-13} molar. Over the past decade, advances in detection have all been made by reducing the measurement volume and/or increasing the measuring time.

We have plotted in Figure 1 the detection limits from several investigations reported in the literature(2-7). The results appear in chronological order from Diebold and Zare(2) in 1977 at the upper right to Nguyen et al.(7) in 1987 at the lower left. All of the data shown are for measurements on flowing streams so we have plotted on the abscissa the volume passing through the laser beam in 1 second except for the left-most point. The integration time for this latter measurement was 180 μ s. It is easily seen that if the concentration sensitivity of 10^{-13} molar can be maintained for a 10-micron droplet, volume 0.5 pl, a detection limit below one molecule should be attainable. The present experiments are designed to test this hypothesis.

We first estimated the signal-to-noise ratio that might be attained for a single R-6G molecule in a water droplet. The experimental conditions were assumed to be identical to those of Nguyen et al.(6) except for the sample configuration, now a droplet instead of a flowing stream. They achieved a sample fluorescence rate of 1.2×10^4 photocounts/s per R-6G molecule with a background rate, primarily due to Raman scattering, of 1.7×10^5 counts/s from a 0.6-pl probe volume. The statistical noise from the background should be the square root of the background count rate. The laser irradiance was 0.7×10^6 W/cm². We have plotted the Raman background noise versus droplet diameter in Figure 2, together with the fluorescence signal from a single R-6G molecule. We have also included an estimate of the noise due to Mie scattering of the incident laser beam, with the assumption that this scattered light can be selectively attenuated by 10^{12} . It is evident from Figure 2 that single molecule detection should be possible for droplets approximately 10 microns in diameter or smaller.

A block diagram of our experimental arrangement is shown in Figure 3. Droplets of R-6G in glycerol-water are levitated in a spherical void electrodynamic trap(8) and excited by the horizontally-polarized beam from an argon-ion laser, 514-nm wavelength. The fluorescence from the droplet is collected by a GRIN lens and 20X microscope objective, spatially filtered, and directed through several optical filters to a cooled C31034 photomultiplier tube. The filter stack consists of a vertical polarizer, an interference filter - Omega 575 DF 26 (center wavelength and bandwidth in nm) and two Corning CS 3-67 filters. The aperture stop helps to reduce Raman scattering from the atmosphere surrounding the droplet. Photon pulses from the photomultiplier are amplified and counted on a computer.

Our best results to date are shown in Figure 4. The droplet was a 5×10^{-6} -molar solution of R-6G in glycerol originally diluted 10:1 with water. After formation from a Uniphoton Systems piezoelectric pipette, the droplet was suspended in the trap, with most of the water evaporating. We estimate the droplet diameter to have been 20 microns after the water loss from measurements of the voltages at the onset of parametric oscillations in the trap(9). When the excitation was initiated, the fluorescence from the 12×10^6 R-6G molecules present was 4.0×10^6 counts/s. The sample rapidly photolyzed, with the count rate eventually stabilizing at about 200 counts/s, with a variance of 700 counts²/s². The slow fluctuations in background are structural variations as the particle diameter continues to decrease due to evaporation.

We can estimate a detection limit from the data presented above. At the peak signal intensity, 600 molecules would give a fluorescence intensity equal to the background signal we observe (peak count rate was 0.33 counts/s per R-6G molecule). For a statistical determination, we should use the background noise. If the structural variations in the background cannot be anticipated, the noise will be the square root of the total variance, or 80 molecules. On the other hand, if the time-variation of the larger fluctuations can be calculated from the background when the sample is known to have been photolyzed, then it would be appropriate to consider the noise to be the square root of the background itself, or about 40 molecules in this case. The detection limit is usually calculated for a signal-to-noise ratio of 2. We would therefore consider our present sensitivity to be in the 10^2 to 10^3 range.

The background signal appears to be mostly due to Raman scattering and fluorescence from the glycerol solvent. Some improvement in sensitivity could be expected from a change to a solvent with lower Raman cross section. Our extrapolated concentration for a detection of 10^2 molecules is 4×10^{-11} molar, still considerably higher than the sensitivity in flowing streams with water as a solvent. The background signal can be further reduced by measuring smaller droplets. An improved photon collection would reduce the relative background fluctuations. We are also considering the use of two-photon excitation which should shift the spectral range of the Mie and Raman scattering far from the wavelength range of sample emission. Photomultipliers are available with very high quantum efficiencies in the blue region that are almost blind in the near infrared. Thus it should be easier to separate the sample emission from the background. All of these possibilities will be explored in our future work.

REFERENCES

1. E. P. Ippen, C. V. Shank, and A. Dienes, IEEE J. Quantum Electron. OE-7, 178 (1971).
2. G. J. Diebold and R. N. Zare, Science 196, 1439 (1977).
3. T. A. Kelly and G. D. Christian, Anal. Chem. 53, 2110 (1981).
4. N. J. Dovichi, J. C. Martin, J. H. Jett, and R. A. Keller, Science 219, 845 (1983).
5. N. J. Dovichi, J. C. Martin, J. H. Jett, M. Trkula, and R. A. Keller, Anal. Chem. 56, 348 (1984).
6. D. C. Nguyen, R. A. Keller, and M. Trkula, J. Opt. Soc. Am. B-4, 138 (1987).
7. D. C. Nguyen, R. A. Keller, J. H. Jett, and J. C. Martin, Anal. Chem. 59, 2158 (1987).
8. S. Arnold and L. M. Folan, Rev. Sci. Instrum. 58, 1732 (1987).
9. E. J. Davis, Langmuir 1, 379 (1985).

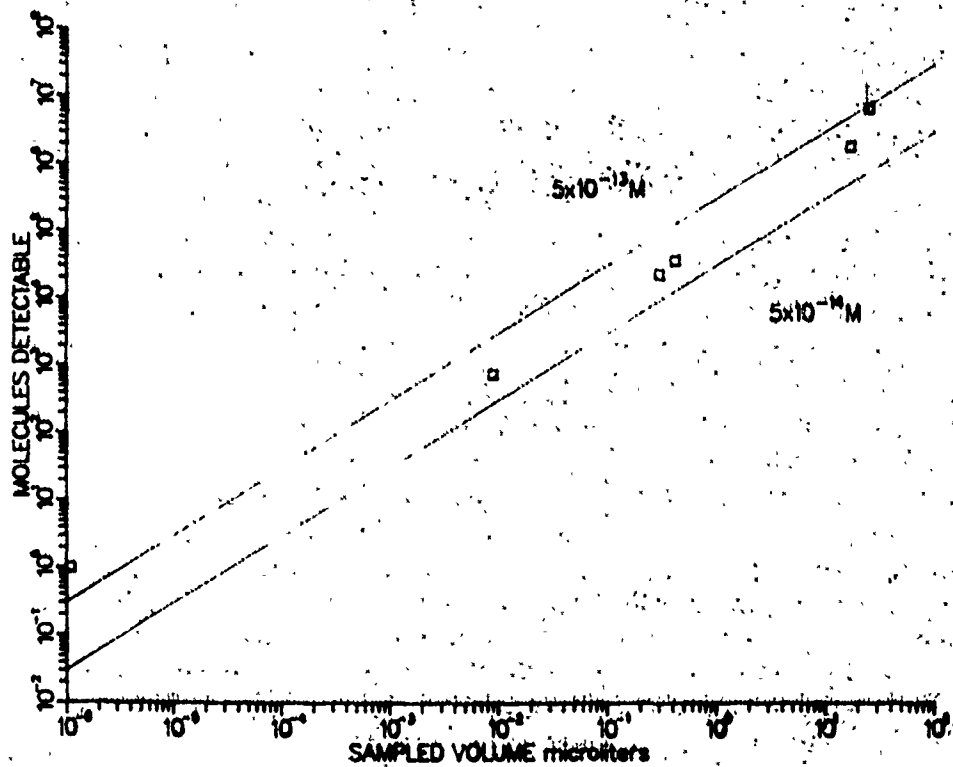


Figure 1. Historical summary of the number of molecules that can be detected versus the volume sampled during the integration time.

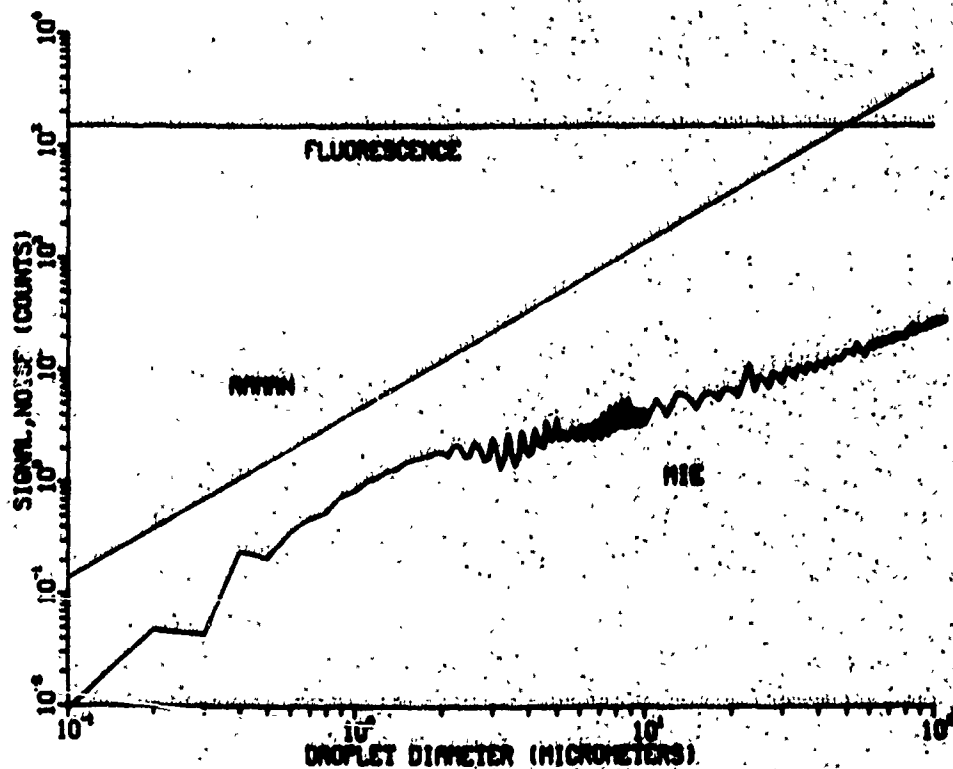


Figure 2. Fluorescence signal from one rhodamine-6G molecule and square root of Raman and Mie scattering backgrounds versus droplet diameter.

BLANK

PARTICLE CHARACTERIZATION IN SONIC VELOCITY IMPACTORS

B. Jurcik and J. Brock
Chemical Engineering Department
University of Texas, Austin, Texas 78712

RECENT PUBLICATIONS, SUBMITTALS FOR PUBLICATION AND PRESENTATIONS

1. J. Carls and J. Brock, "Propagation of laser breakdown and detonation waves in transparent droplets", *Optics Letters* 13 273 (1988).
2. J. Brock, D. Zehavi, and P. Kuhn, "Binary aerosol formation in a laminar coaxial jet", *J. Aerosol Sci.* 4 462 (1988).
3. J. Carls and J. Brock, "Explosive vaporization of single droplets by lasers: comparison of models with experiments" *Optics Letters* 13 919 (1988)
4. J. Carls, G. Moncivais and J. Brock, "Time resolved Raman spectroscopy from optically levitated reacting droplets", *Proceedings of the 1988 CRDEC Scientific Conference on Obscuration and Aerosol Research*, CRDEC, U. S. Army, 1989
5. J. Carls, G. Moncivais and J. Brock, "Time resolved Raman spectroscopy from reacting, optically levitated microdroplets", Submitted for publication.
6. B. Jurcik and J. Brock, "Particle formation in shocked flows", *Proceedings of the 1988 CRDEC Scientific Conference on Obscuration and Aerosol Research*, CRDEC, U. S. Army, 1989
7. J. Carls and J. Brock, "High energy laser-particle interactions", *Proceedings of the 1988 CRDEC Scientific Conference on Obscuration and Aerosol Research*, CRDEC, U. S. Army, 1989
8. Y. Chen, J. Brock, and I. Trachtenberg, "Aerosol jet etching", *Aerosol Sci. Tech.*, In Press 1989
9. B. Jurcik and J. Brock, "A study of low pressure impaction processes", *J. Aerosol Science* 20, 560, 1989.
10. J. Carls, Y. Seo and J. Brock, "Laser-induced breakout and detonation waves in droplets: II. Model", Submitted for publication, 1989.
11. Y. Seo and J. Brock, "Distributions for moment simulation of aerosol evaporation", Submitted for publication, 1989.
12. B. Jurcik and J. Brock, "The theory of sonic impactors", Submitted for publication, 1989
13. J. Carls and J. Brock, "The effect of laser pulse frequency and amplitude modulation on energy absorption in ionized shocks", Submitted for publication, 1989.
14. J. Brock, "Aerosol dynamics", Chemical Engineering Seminar, Tokyo Institute of Technology, November 1988.
15. J. Brock, "Aerosol filtration", Chemical Engineering Seminar, Tokyo Institute of Technology, November, 1988.
16. J. Brock, "Advances in aerosol technology", Japan Chemical Engineering Society Lecture, Tokyo, December 1988.
17. J. Brock, "Laser-particle interactions", Invited Lecture, Institute of Chemistry and Physics (RIKEN), Wako, Japan, November 1988.
18. J. Brock, "Aerosol jet etching", Chemical Engineering Seminar, Kanazawa University, Kanazawa, Japan, November 1988.
19. J. Brock, "Aerosols and the environment", U.N.E.S.C.O. Lecture, Tokyo, Japan, December 1988.
20. L. Liebmann and J. Brock, "A finite element approach to laser-droplet interactions", 1989 CRDEC Scientific Conference on Obscuration and Aerosol Research, Aberdeen Proving Ground (Edgewood), Maryland, June 1989.
21. B. Jurcik and J. Brock, "Aerosol plumes: dispersion and characterization", 1989 CRDEC Scientific Conference on Obscuration and Aerosol Research, Aberdeen Proving Ground (Edgewood), Maryland, June 1989.
22. J. Carls and J. Brock, "Studies in nonlinear response of microparticles to laser radiation", 1989 CRDEC Scientific Conference on Obscuration and Aerosol Research, Aberdeen Proving Ground (Edgewood), Maryland, June 1989.
23. J. Carls and J. Brock (presented by M. Sitariski), "The response of single microparticles to high energy laser radiation", 20th Annual Meeting of the Fine Particle Society, Boston, Mass., August 1989.

ABSTRACT

Sonic velocity impactor stages are particularly useful devices for classifying and collecting stable particles smaller than ~ 200 nm. -- particularly when subsequent testing for unusual physico-chemical or biological properties may be necessary. In this presentation, we give comparison between experiment and theory for such stages. The theory presented involves numerical solution of the gas dynamic equations using the FEM - FCT method and subsequent solution of the Lagrangian equations of motion for particle trajectories. Comparisons between experiment and this theory are satisfactory, showing that our model describes very well the physical system. The effects on particle collection efficiency of the jet to plate distance S/D , and the pressure ratio are explored.

INTRODUCTION

Impactor stages in which the velocity at the nozzle exit is sonic have been used for a number of years for the aerodynamic size separation of small aerosol particles. In sonic stages the collection of small particles is enhanced in two ways 1) the aerosol particles have large axial velocities at the nozzle exit and therefore significant directed momenta and 2) the downstream pressure (P_{∞}) can be much less than the upstream stagnation pressure (P_0) increasing the particle Knudsen number so the drag force is reduced relative to the continuum value. In this way extremely fine particles ($D_p < 50$ nm, Hering et al. 1979) can be collected in an impactor stage. This makes the use of sonic velocity impactor stages attractive for classification and collection of particles (stable to evaporation) for $D_p < 200$ nm. The design and analysis of sonic velocity impactor stages is complicated, however, since the fluid dynamics of an impinging jet in this regime exhibits a complicated shock structure and the pressure, temperature and density of the carrier gas varies with position.

In order to understand the effects of the operating parameters of sonic velocity impactor stages a model was developed to predict particle collection efficiencies. This paper describes our simulation method and presents some results. First, a brief description of the model for the impinging jet and particle collection efficiency is given. Then some results obtained with this model are given and compared with experimental results.

MODEL DESCRIPTION

In this work the gas flow field of an impinging sonic jet is calculated first. Then with the assumption that the particles are passive contaminants, particle trajectories are calculated using the gas flow field and the Lagrangian equations of motion for individual particles. It is further assumed that all non-continuum effects are confined to the interaction of the gas with particles. This general approach has been used previously for efficiency calculations in incompressible flow impactors (Rader and Marple, 1985), compressible flow impactors (Flagan, 1981), and virtual impactors (Marple and Chien, 1980).

The physical system to be described along with the shock structure of an impinging jet is shown in figure 1. Gas at stagnation conditions P_0, T_0, ρ_0 is accelerated through the nozzle where the gas conditions (P_e, T_e, ρ_e) are set by assuming isentropic flow in the nozzle and sonic velocity at the nozzle exit. The exiting gas then expands to a supersonic velocity to the standoff shock where it recompresses and expands radially. More information about the physics of impinging jets is given in Jurcik et al. (1989), Powell (1988) and Kalghatgi and Hunt (1976).

The equations used to describe the impinging jet are the Navier-Stokes equations written in conservative form neglecting diffusive effects. The ideal gas law with constant heat capacity ratio is used for the equation of state. These equations are:

$$\frac{\partial \rho}{\partial t} + \frac{1}{r} \frac{\partial \rho v_r}{\partial r} + \frac{\partial \rho v_z}{\partial z} = 0 \quad (1)$$

$$\frac{\partial \rho v_r}{\partial t} + \frac{1}{r} \frac{\partial \rho v_r^2}{\partial r} + \frac{\partial \rho v_z v_r}{\partial z} + \Lambda \frac{\partial P}{\partial r} = 0 \quad (2)$$

$$\frac{\partial \rho v_z}{\partial t} + \frac{1}{r} \frac{\partial \rho v_r v_z}{\partial r} + \frac{\partial \rho v_z^2}{\partial z} + \Lambda \frac{\partial P}{\partial z} = 0 \quad (3)$$

$$\frac{\partial \rho E}{\partial t} + \frac{1}{r} \frac{\partial v_r (\rho E + P)}{\partial r} + \frac{\partial v_z (\rho E + P)}{\partial z} = 0 \quad (4)$$

$$A = \frac{(P_e/P_\infty)}{\gamma (P/P_\infty)^2} M_{exit}^2 \quad P = (\gamma - 1) \rho E + \frac{1}{2A} (\rho v_r^2 + \rho v_z^2)$$

All variables in these equations are nondimensional and defined as follows:

$$\rho = \frac{\hat{\rho}}{\rho_\infty} \quad v_r = \frac{\hat{v}_r}{v_{z_\infty}} \quad v_z = \frac{\hat{v}_z}{v_{z_\infty}} \quad E = \frac{\hat{E}}{P_\infty / \rho_\infty}$$

$$P = \frac{\hat{P}}{P_\infty} \quad r = \frac{\hat{R}}{D} \quad z = \frac{\hat{Z}}{D} \quad \text{exit} = \frac{\hat{v}_{z_\infty}}{D}$$

where the hatted quantities are dimensional. In all the simulations given here the exit Mach number was set equal to 1.0, and the heat capacity ratio was set at 1.4. The density ratio (ρ_e/ρ_∞) was set at $1.2(P_e/P_\infty)$ so that $T_0 = T_\infty$. Therefore, two parameters S/D and P_e/P_∞ (or P_0/P_∞) specify the conditions to simulate the gas flow field in a sonic velocity impactor stage. These equations are solved by the FEM - FCT method (Finite Element Method - Flux Corrected Transport) Lohner et al. (1987), Lohner et al. (1984), and Morgan et al. (1986).

With the calculated gas flow field, particle trajectories were determined by integrating Lagrangian equations of motion for the particle trajectories. These equations are (Fuchs, 1978)

$$\frac{d v_{z_p}}{dt} = \frac{3}{4} C_d (v_z - v_{z_p}) |(\mathbf{V}_0 - \mathbf{V}_p)| \frac{\rho \rho_\infty}{\rho_p} \quad (5)$$

$$\frac{d v_{r_p}}{dt} = \frac{3}{4} C_d (v_r - v_{r_p}) |(\mathbf{V}_0 - \mathbf{V}_p)| \frac{\rho \rho_\infty}{\rho_p} \quad (6)$$

$$\frac{dr}{dt} = v_{r_p} \quad (7)$$

$$\frac{dz}{dt} = v_{z_p} \quad (8)$$

$$\text{at } t=0: v_{z_p} = 1; v_{r_p} = 0; r = r_{start}; z = 0$$

where the subscript p denotes a particle property and C_d is the drag coefficient, which is a function of Mach and Knudsen numbers.

RESULTS

In numerical simulations it is vital to verify the solution procedure by either comparing with analytical solutions or experimental results. Here we compare with experimental results due to the lack of analytical solutions for axisymmetric supersonic flows. Figure 2 shows a comparison of calculated and measured pressures on the flat plate on the axis for a fixed value of S/D at various pressure ratios. The experimental data shown are taken from Biswas and Flagan (1984). As can be seen from figure the predicted pressures compare favorably with those measured. In this figure $P_{flat\ plate}$ is the pressure at the stagnation point, and $\chi = P_\infty/P_0$.

Since there are few explicit experimental data available in the literature on impinging jets for this comparison, a direct simulation of impactor stages was carried out to determine how well particle collection efficiencies are calculated. One of the impactor stages simulated corresponds to stage 8 of the low pressure impactor designed by Hering et al. (1979). This impactor stage was operated with $P_0 = 50$ Torr, $P_{\infty} = 8$ Torr, $D = 0.14$ cm, $S = 0.07$ cm, and $\rho_p = 1.46$ gm/cm³ (therefore $P_e/P_{\infty} = 3.30$ and $S/D = 0.5$). The results of our simulation are shown in figure 3. For a set of as yet unpublished data, another series of simulation results are shown in figure 4. In this figure the diameter of 50% collection efficiency for a NaCl aerosol ($\rho_p = 2.163$) is plotted versus the parameter S/D . In these simulations $P_0/P_{\infty} = 400$ ($P_e/P_{\infty} = 211.3$), and the upstream stagnation conditions are air at atmospheric pressure and $T_0 = 300$ K. The diameter of the nozzle is $D = 0.027$ cm. As can be seen from figures 3 and 4 the numerical model results compare well with the experimental ones. This gives us confidence that the model is representing the physical system accurately.

Notice that in figure 4 the diameter of 50% collection efficiency decreases as the parameter S/D increases. This behavior is fundamentally different from that seen in incompressible impactors where as S/D is increased the diameter of 50% collection efficiency increases. This unusual behavior is due to the increased velocity of the particle from rapid acceleration immediately upstream of the standoff shock and the reduced pressure in the stagnation point region as S/D increases (i. e. see figure 2). The reduction in pressure in the stagnation point region reduces the drag force the particle experiences so that particle impaction is enhanced.

Some results for constant parameter S/D and several pressure ratios are shown in figure 5. In this figure the pressure ratio is defined as $= P_0/P_{\infty}$, $S/D = 0.8$, nozzle diameter = 0.1 cm, and the density of the aerosol particles = 1.0 gm/cm³. Notice that for $2.86 < P_0/P_{\infty} < 5.0$ the curves coalesce onto one curve. This implies that for an $S/D = 0.8$ in this pressure ratio range the diameter of 50% collection depends only on the upstream stagnation conditions and is insensitive to the downstream pressure. Notice also that there is not a great difference between the pressure ratio = 400 case and pressure ratio = 10 case. This could imply that as the pressure ratio increases the diameter of 50% collection efficiency reaches some limiting value and becomes insensitive to pressure ratio.

ACKNOWLEDGMENT

This work was supported under NSF Grant CBT-8812516 and partially by contract DAAA15-86-K-0015 from US Army CRDEC.

REFERENCES

- Biswas, P., and Flagan, R. C. (1984) *Environ. Sci. and Tech.* 18, 611.
- Flagan, R. C. (1981) *J. Colloid and Interface Sci.* 87, 291.
- Fuchs, N. A. (1978) In *Fundamentals of Aerosol Science*, Shaw, D. T. (ed), Wiley and Sons, N. Y., 1-83.
- Hering, S. V., Friedlander, S. K., Collins, J. J., and Richards, L. W. (1979) *Environ. Sci. and Tech.* 13, 184.
- Jurcik, B. J. Jr., Brock, J. R., Trachtenberg, I. (1989) To appear in *J. Aerosol Sci.*
- Kalghatgi, G. T., and B. L. Hunt, (1976). *Aeronaut. Q.*, 27, 169.
- Lohner, R., Morgan K., Zienkiewicz, O. C. (1984) *Intern. J. Num. Meth. Fluids.* 4, 1043.
- Lohner, R., Morgan, K., Peraire, J., Vahdati, M. (1987) *Intern. J. Num. Meth. Fluids.* 7, 1093.
- Marple, V. A. and Chien, C. M. (1980) *Environ. Sci. and Tech.* 14, 976.
- Morgan K., Lohner, R., Jones, J. R., Peraire, J., Vahdati, M. (1986) *Proc. 6th Int. Symp. Finite Element Methods in Flow Problems*, INRIA.
- Powell, A. (1988) *J. Acoust. Soc. Am.* 83, 515.
- Rader, D. J. and Marple, V. A. (1985) *Aerosol Sci. and Tech.* 4, 141.

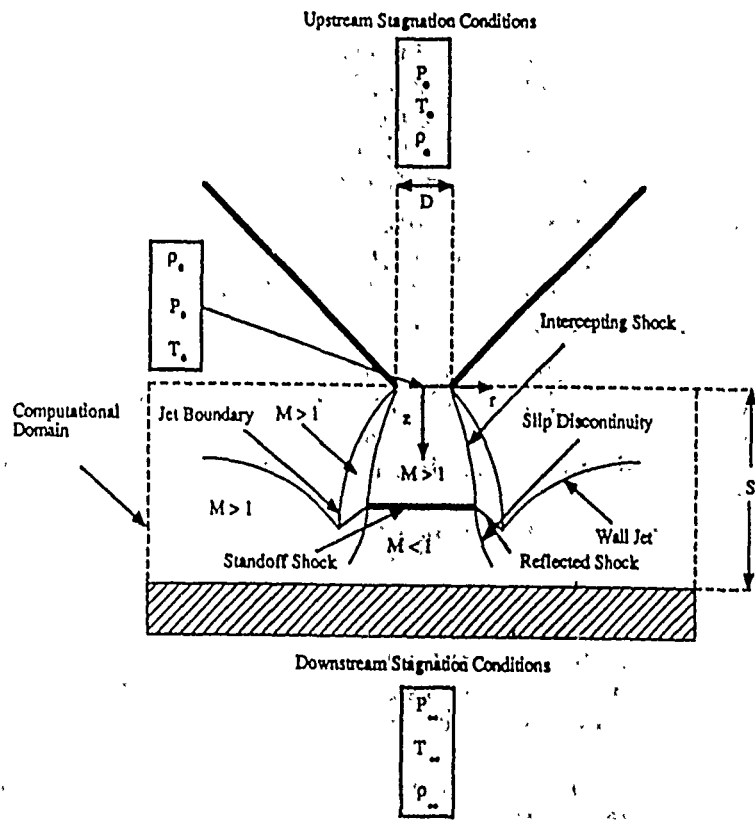


Figure 1

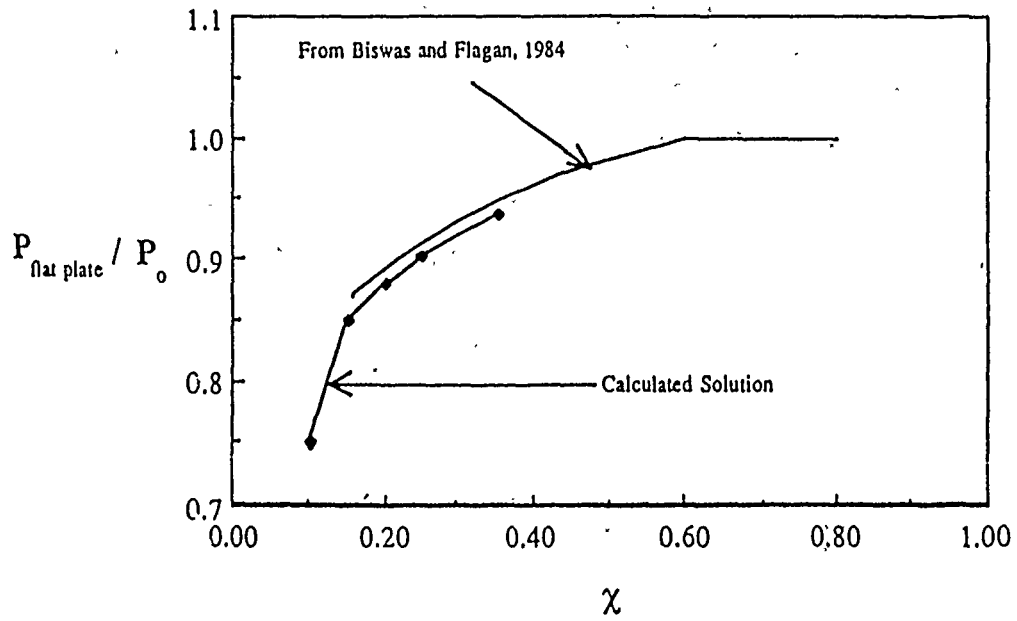


Figure 2

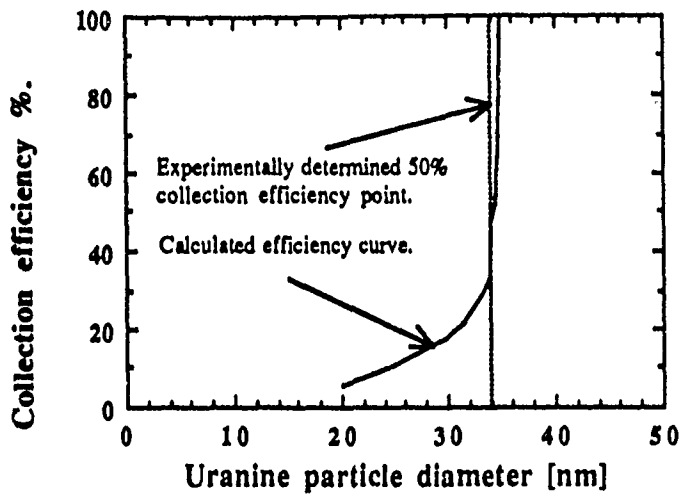


Figure 3.

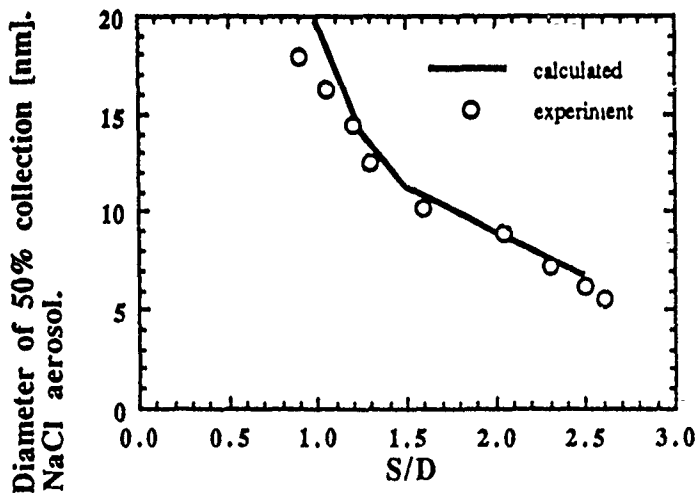


Figure 4.

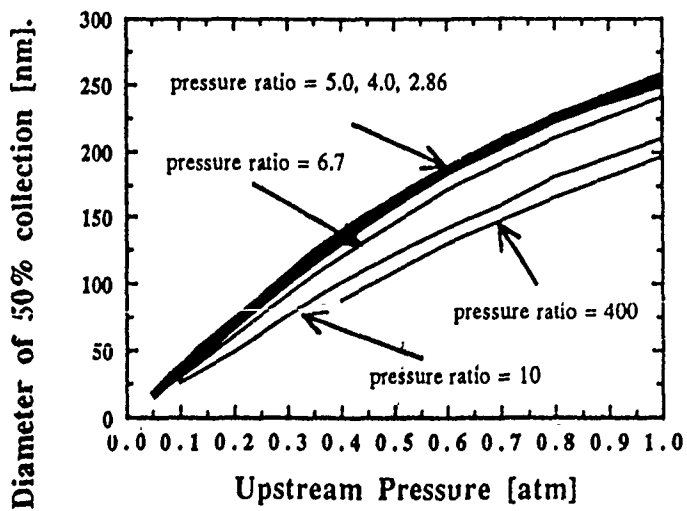


Figure 5.

PROBING THE STRUCTURE OF THE CORNEA OF THE EYE
WITH LIGHT SCATTERING*

R. A. Farrell, R. L. McCally, and D. E. Freund
The Milton S. Eisenhower Research Center
The Johns Hopkins University Applied Physics Laboratory
Laurel, MD 20707

RECENT PUBLICATIONS, SUBMITTALS FOR PUBLICATION AND PRESENTATIONS:

A) R. L. McCally and R. A. Farrell, "Light Scattering from Cornea and Corneal Transparency," to appear in New Developments in Noninvasive Studies to Evaluate Ocular Function, ed. by B. Masters (Springer-Verlag, New York, Heidelberg, Berlin).

B) R. L. McCally and R. A. Farrell, "Interaction of Light and the Cornea: Light Scattering versus Transparency," in The Cornea: Transactions of the World Congress on the Cornea III, ed. by H. Dwight Cavanagh (Raven Press Ltd., New York, 1988), pp. 165-171.

C) D. E. Freund, R. L. McCally and R. A. Farrell, "Effects of Fibril Orientations on Light Scattering in the Cornea," J. Opt. Soc. Am. 3, 1970-1982 (1986).

D) D. E. Freund, R. L. McCally and R. A. Farrell, "Direct Summation of Fields for Light Scattering by Fibrils with Applications to Normal Corneas," Appl. Opt. 25, 2739-2746 (1986).

E) R. H. Andreo and R. A. Farrell, "Corneal Small-Angle Light Scattering Patterns: Wavy Fibril Models," J. Opt. Soc. Am. 72, 1479-1492 (1982).

ABSTRACT

A strong interplay between theory and experiment has led to the development of light scattering as a tool to probe the microstructure of the eye's cornea. Models to explain corneal transparency and its loss upon swelling have been analyzed and tests devised to discern among them, especially on the basis of the wavelength dependence of scattering. Experiments support the theories based on the structures as revealed by electron microscopy. Analysis of the angular scattering led to a fundamental test of the underlying hypothesis of this research in terms of a predicted scaling relationship between scattering angle and wavelength.

*Work supported in part by NIH, the Navy and the Army.

Introduction

The cornea is the transparent portion in the front of the eye's outer coat (Fig. 1a) which, because of refraction at its curved interface with the air, provides about 75% of the focusing power needed for normal vision. Thus, normal vision requires that the cornea have the mechanical strength to maintain its curvature very accurately while withstanding the intraocular pressure, which is typically 14-18 mmHg in adult humans. Corneal structure is important therefore because it determines the cornea's mechanical properties and at the molecular level underlies the cornea's most essential characteristic--its transparency.

Understanding the structural basis of the cornea's transparency is a problem that has intrigued ophthalmological researchers and physicists alike. Indeed, we first became involved in transparency research over 20 years ago, and over the years our work has evolved toward developing light scattering as a tool to probe corneal structure. The purpose of this paper is to impart a bit of the flavor of this research to a new audience. Thus we will rely heavily on past reviews, particularly that in Ref. 1, and on other material that we have published over the years.²⁻⁸

A description of the cornea's basic anatomy is presented in order to provide a background for our discussion on the relationship between transparency, light scattering, and structure. Light microscopy shows that the cornea is a layered structure, as is illustrated in the schematic representation of Fig. 1b. At the front is a layer about six cells thick called the epithelium which lies on a thin structure called the basement membrane. At the very back of the cornea the endothelium is a single cell layer attached to a thin collagenous layer called Descemet's membrane. The stroma, which accounts for about 90% of the total corneal thickness, occupies the region between the basement membrane and

Descemet's membrane. For reference, human cornea averages about 520 microns in thickness, while in rabbits, a common experimental animal, it averages about 380 microns.⁹

Further inspection of light micrographs shows that the stroma itself is a layered structure. The layers (or lamellae) have relatively uniform thicknesses averaging 2 μm . A few flat cells known as keratocytes are interspersed between the lamellae and occupy approximately 3 to 5% of the cornea's volume.⁹ Each lamella is composed of relatively uniform diameter fibrils made of the protein collagen that are surrounded by an optically homogeneous macromolecular solution known as the ground substance (Fig. 2a). The average diameter of the fibrils is approximately 30 nm (Fig. 2b). Within a given lamella the fibrils, which extend entirely across the cornea, lie parallel to one another and also parallel to the surface of the cornea. Between adjacent lamellae the fibril axes tend to make large angles with one another.

Transparency of the cornea requires that there be little or no absorption and scattering of light. It has been observed that the cornea does not absorb in the visible portion of the spectrum and thus the slight decrease of the intensity of visible light as it passes through the cornea is caused by scattering.⁹ The transparency theories that we will discuss all assume that the collagen fibrils within the stroma are the primary source of scattering in the cornea. Because their diameter is small compared to the wavelengths of visible light and their refractive index is close to that of the ground substance, the fibrils are inefficient scatterers; however, they have the potential for making up for their inefficiency by their large numbers. Indeed, a simple calculation shows that cornea would not be transparent if the fibrils scattered independently of one another.^{2,9} This implies that the fibrils do not act as independ-

ent scatterers and that interference effects are important in explaining the cornea's transparency.^{2,7-9}

Maurice knew from crystallography that if the collagen fibrils were arranged so that they formed a perfect crystalline lattice, then only light passing through the lattice in the incident direction would add constructively. Light scattered in all other directions would interfere destructively since the average spacing between the fibrils is less than the wavelength of visible light. Thus he postulated that within a given lamella the fibrils were in fact arranged in a perfect two-dimensional hexagonal lattice since this would produce the observed transparency.⁹

However, electron micrographs (EM) such as the one in Fig. 2a never show the fibrils within a lamella as being arranged in the perfect manner suggested by Maurice. Of course, the fixation, dehydration and embedding procedures required for electron microscopy could disrupt the perfect order. Yet even a casual inspection of EM reveals that there is some order in the fibril positions--the arrangement of fibrils in micrographs is not random. We noticed this and posed the question whether there was sufficient ordering in the depicted fibril positions to render the cornea transparent.² That is, would the destructive interference produced by the ordering reduce the scattering to the observed level? In order to answer this question we developed a theory for corneal transparency based on the Zernike-Prins theory of x-ray scattering from liquids.¹⁰ The theory (to be discussed in more detail below) is applicable to a collection of parallel, infinitely long, weak dielectric cylinders of uniform diameter exhibiting short-range order such that it is possible to describe the arrangement of the cylinders with a radial distribution function. We modelled the stroma as a single lamella and showed that the fibril distribution could be characterized by

a radial distribution function. Application of the scattering theory to the radial distribution functions obtained from direct measurement of the fibril positions in EM of normal cornea (cf. Fig. 2c) showed that the depicted short-ranged ordering of fibril positions would reduce the scattering to a level consistent with that which is actually measured. This calculation, however, does not prove that the short-range order shown in EM is correct; but it does mean that the structure cannot be rejected as artifactual on the basis of a transparency argument.

Following Maurice's early lattice theory⁹ and our initial scattering calculations,² several other models were advanced to explain the cornea's transparency. They can be grouped as to whether they are based on long-range or short-range order. In addition to the lattice theory, the long-range order theories include a modification suggested by Feuk¹¹ in which the fibrils are said to be randomly distributed around perfect lattice positions, with the deviations from the ideal positions small compared to their spacing. Other short-range order theories include Benedek's correlation area model¹² and Twersky's model in which a modified hard-core produces correlation in fibril positions.¹³ Both of these analyses use a long wavelength approximation. Also included in the short-ranged theories is one based on the refractive index of fibrils being closely matched to that of the ground substance.¹⁴ In this equal refractive index theory, transparency would result from reduced scattering by the individual fibrils rather than from destructive interference.

The cornea is hydrophilic and corneas stored in solution will imbibe it and swell. Light scattering is increased and transparency is reduced in swollen corneas. One of the most notable features seen in electron micrographs of cold-swollen corneas is the voids or "lakes" that open up in the fibril distribution

(cf. Fig. 3). Of course, the voids may be artifacts, but Benedek¹² noted that if they were indeed real they would introduce large spatial fluctuations in the refractive index. He developed a theory which suggested that they could explain the increased scattering in swollen corneas. There are other theories as well, the principal one being due to Twersky.¹³ It associates the increased scattering with a reduction in the destructive interference that is brought about by a randomizing of the fibril positions due to an increased free volume per fibril in the hard-core model.

In the remainder of this paper, we will discuss in more detail the theories and experiments relevant to discerning corneal structure. The second section reviews the aforementioned transparency theories (in which the effects of lamellar orientations are ignored) in more detail and provides means for discriminating among them based on the predicted wavelength dependence of the scattering cross-section. We then describe experimental methods capable of measuring the wavelength dependence of scattering and show that the scattering is consistent with that expected from the observed EM structures. In the third section we discuss the effects of lamellar orientations on angular light scattering and devise a test for the hypothesis that the fibrils are the primary source of scattering in the cornea. Finally, section 4 briefly summarizes the results of this paper.

2) **Structural Implications of Unpolarized Light Scattering**

A. Transparency Theories

Although the details of the stromal ultrastructure depicted in EM may have been corrupted by the tissue preparation procedures, it is generally accepted that the stroma is composed of stacked sheets (lamellae), each of which contains long, thin, parallel collagen fibrils embedded in a ground substance. We note

that, for unpolarized light at normal incidence, the total scattering from a fibril is independent of its azimuthal orientation. Thus, the process of averaging over all lamellae orientations does not affect the value of the total scattering cross-section, a quantity needed for computing the fraction of light transmitted by the cornea. A calculation of the total scattering cross-section can be simplified, therefore, by assuming that the stroma is made up of a single thick lamella. Even with this simplification, predicting the light scattering to be expected from such an assembly would be a complicated multiple scattering problem. That is, the electric field experienced by any fibril would consist of the incident plane wave field from the light source and the scattered fields from the other fibrils. However, because the normal cornea is transparent, it is reasonable to simplify the calculations further by introducing the Born approximation in which the field experienced by a fibril is approximated by the incident plane wave field. At a distance from the cornea that is large compared to the linear dimensions of the illuminated region, the Born approximation to the scattered electric field, E_s , can be written as

$$E_s = \sum_{j=1}^N E_j e^{-i\mathbf{q}\cdot\mathbf{r}_j} . \quad (1)$$

In this equation, N is the total number of illuminated fibrils, $\mathbf{q} \equiv k(\hat{k}_s - \hat{k}_i)$, where $k = 2\pi/\lambda$ and \hat{k}_s and \hat{k}_i are unit vectors in the scattered and incident directions, respectively, and λ is the wavelength of the incident plane wave. The vector \mathbf{r}_j specifies the position of the j^{th} fibril relative to some fixed origin. The field that would be scattered by the j^{th} fibril if it were at the fixed origin is denoted by E_j , and the fibril's displacement from the origin is accounted for by the exponential phase factor.

The length of fibril that is illuminated is large compared to a light wavelength, so E_j is approximated by that from an infinitely long dielectric cylinder and the cross-section per unit length is calculated. In this approximation, \hat{k}_i and \hat{k}_s lie in a plane perpendicular to the fibril axis and the scattering angle, θ_s , is measured from the forward direction. The field E_j depends, in general, on the diameter and refractive index of the j^{th} fibril as well as the wavelength of incident radiation, the distance to the field point, and the scattering angle θ_s . Thus the field E_s depends on θ_s via both the phase factor and E_j . At this point we make the reasonable assumption that, for normal cornea, all the fibrils are identical and have radius a . In this case $E_j \equiv E_0$ is the same for all fibrils, and we can use Eq. (1) to write the scattered intensity as

$$I_s = |E_0|^2 N \left\{ 1 + \frac{1}{N} \sum_{j=1}^N \sum_{j'=1}^N e^{i\mathbf{q} \cdot (\mathbf{r}_j - \mathbf{r}_{j'})} \right\}, \quad (2)$$

where the prime on the second sum is to indicate that $j' \neq j$ and $|E_0|^2$ is the scattered intensity due to an infinitely long dielectric cylinder. For unpolarized light incident normal to the fibril axis, we can use the dielectric needle approximation to write the well-known result

$$|E_0|^2 = \frac{I_0 n^3 (\pi a)^4 (m^2 - 1)^2}{2r\lambda^3} \left\{ 1 + \left[\frac{2\cos\theta_s}{m^2 + 1} \right]^2 \right\} \quad (3a)$$

$$= \frac{I_0 \sigma_0(\theta_s)}{r} \quad (3b)$$

where I_0 is the intensity of the incident unpolarized plane wave, n is the refractive index of the ground substance, m is the relative refractive index of the fibrils, r is the distance from the cylinder axis to the observer, and $\sigma_0(\theta_S)$ is the differential cross-section (per unit length) of an isolated fibril. Thus the differential scattering cross-section per unit length can be written as

$$\sigma(\theta_S) = \sigma_0(\theta_S)N\left\{1 + \frac{1}{N} \sum_j \sum_{j'} e^{i\mathbf{q} \cdot (\mathbf{r}_j - \mathbf{r}_{j'})}\right\}. \quad (4)$$

The total cross-section per unit length is, of course, obtained by integrating $\sigma(\theta_S)$ over all values of θ_S from 0 to 2π .

The double sum in Eq. (4) accounts for interference among the fields scattered by different fibrils and its value depends critically on the nature of the fibril distributions. Each of the theories mentioned in the introduction can be distinguished by the approximation used to evaluate this double sum. For example, with a random assembly, the positions of the fibrils would be uncorrelated and the double sum would vanish because the independent phase factors average to zero. The total scattering is therefore simply N times the scattering from an isolated fibril. Using typical values for the refractive indices, Maurice was able to show that, under this assumption, the cornea would scatter more than 90% of the incident light at 500 nm and would therefore be opaque.⁹ The equal refractive index theory is based on other electron microscopic data which suggests that the collagen fibrils are so highly hydrated that their refractive index essentially matches that of the ground substance.¹⁴ Thus, the positive factor $(m^2-1)^2 \ll 1$ and the scattering by each of the (randomly arranged) fibrils would be so weak that even the factor of N would not be large enough to cause loss of transparency. For a perfect crystalline lat-

tice arrangement, correlation exists at all separation distances. Because the lattice spacing (fibril separation) is small compared to the light wavelengths, there would be no scattering. The interference term in Eq. (4) would equal $-N$ and the two terms in the braces would cancel.^{1,2,9}

On the other hand, we showed that in the dielectric needle approximation for fibrils having short-ranged order like that in typical micrographs (cf. Fig. 2a), the angular scattering cross-section could be expressed as²

$$\sigma(\theta_s) = \sigma_0(\theta_s) \left\{ 1 + 2\pi\rho \int_0^{R_C} r dr [g(r)-1] J_0(2kr \sin(\frac{\theta_s}{2})) \right\}, \quad (5)$$

where ρ is the bulk number density of fibrils per unit area in a cross-section cut, $g(r)$ is the radial distribution function (see Fig. 2c), R_C is the correlation length which is made sufficiently large that $g(r) = 1$ for $r > R_C$ and $J_0(x)$ is a Bessel function of the first kind of order zero. From this, we obtained the total scattering cross-section per fibril per unit length by integrating over scattering angles, with the result expressed as

$$\sigma_t = \frac{\sigma_1}{2} (1-f_1) + \frac{\sigma_2}{2} (1-f_2), \quad (6a)$$

where

$$f_1 = 2\pi\rho \int_0^{R_C} r dr [1-g(r)] J_0^2(kr) \quad (6b)$$

and

$$f_2 = 2\pi\rho \int_0^{R_C} r dr [1-g(r)] [J_0^2(kr) + J_2^2(kr)]. \quad (6c)$$

It turns out that, because most of the contributions to these integrals come from values of r for which $kr < 1$, the interference terms $1-f_1$ and $1-f_2$ are

essentially independent of wavelength over the visible spectrum;³ thus the wavelength dependence of σ_t would be that of the individual fibril (total) scattering cross-sections for parallel ($\sigma_1 = 2a\pi^2(m^2-1)^2(ka/2)^3$) and perpendicular polarization ($\sigma_2 = 2\sigma_1/(m^2+1)^2$), namely $\sigma_t \sim \lambda^{-3}$. In angular scattering, however, the effective wavelength is smaller at backscattering angles and it is possible to sense the higher order correction terms to the integral in Eq. (5), which vary as λ^{-2} . Thus, angular scattering measurements would have a lead term varying as λ^{-3} and a correction term varying as λ^{-4} . The other transparency models based on short-ranged order, namely those of Benedek¹² and Twersky,¹³ use a long wavelength approximation and therefore predict the same inverse-cubic dependence on wavelength, as does the equal refractive index model.

The other long-range order model, due to Feuk,¹¹ describes a quasi-crystalline arrangement that would result if the fibrils were displaced randomly from their (supposed) perfect lattice positions. Evaluation of the interference term in this case is facilitated by writing $r_j = r_{j0} + \delta_j$ in Eq. (4), where r_{j0} is the position of the j^{th} ideal lattice point and δ_j is the small random fluctuation of the j^{th} fibril about this lattice point. Expanding in a Taylor series about the ideal lattice positions, one finds that the lowest order contribution is just the ideal lattice contribution (equal to $-N$), which cancels the first term in the braces of Eq. (4) just as in the case of a perfect lattice. Because the displacements are assumed to be symmetrically distributed and independent of one another, terms that involve δ_j raised to an odd power average to zero. Thus, the first non-zero contribution is proportional to λ^{-2} which, when multiplied by the overall factor of λ^{-3} from $\sigma_0(\theta_S)$, gives a scattering cross-section proportional to λ^{-5} . Therefore, structure models having

short-range order can be distinguished from those with long-range order via light scattering experiments.^{3,4,15}

Models developed to explain the loss of transparency arising from the increased scattering that accompanies corneal swelling lend themselves to similar tests. Twersky¹³ explained this increased scattering on the basis of a hard-core model in which the collagen fibrils are coated by a material having the same refractive index as the ground substance. In this model, ordering is caused by the condition that two fibrils cannot approach each other closer than touching. Twersky fixed the effective hard-core diameter of the fibril so as to obtain sufficient short-range ordering in the fibril positions to allow agreement with the measured transmissivity of the normal cornea at 500 nm. He then showed that the increased volume per fibril in a cornea swollen to 1.5 times its normal thickness would induce a homogeneous disordering of the fibril arrangement sufficient to increase the scattering by an amount that would lead to reasonable agreement with the measured transmissivity of the swollen cornea at 500 nm. Because this homogeneous disordering only has the effect of making the fibril distribution more random, it would lead to a λ^{-3} wavelength dependence, as discussed above.

As noted in the Introduction, however, electron micrographs do not depict a homogeneous disordering of fibril positions; rather, they show that swelling is accompanied by the appearance of regions (called "lakes") completely void of fibrils, as shown in Fig. 3. Working on the hypothesis that lakes were not artifacts, Benedek and his co-workers^{12,16} devised a method for taking them into explicit account when calculating light scattering. The approach, shown schematically in Fig. 4, is based on recognizing that the actual fibril distribution is equivalent to one in which the lakes are populated by fibrils, minus a dis-

tribution consisting of the fibrils used to populate the lakes. One then calculates the fields resulting from these two distributions and keeps track of the terms resulting from the latter distribution in calculating the intensity. Quantitative calculations based on this method have not been carried out; but we were able to extend it and show that the presence of lakes would add a term to the total cross-section which varies as λ^{-2} and which would dominate in highly turbid corneas.³ Therefore, as with theories for transparency in normal corneas, measurements of the wavelength dependence of the total scattering cross-section can serve as a test to determine the appropriate structure model.

B. Experiments

Measurements of σ_t were carried out for normal and swollen corneas in order to test the theories discussed in the previous section. We note again that the process of averaging over the various lamella orientations that occurs during the measurement of σ_t would not alter its wavelength dependence. The total cross-section per fibril per unit length, σ_t , is determined from the fraction of light transmitted, F_T , which is the ratio of light transmitted through the cornea to the incident intensity. The two quantities are related by

$$F_T = \exp(-\rho\Delta\sigma_t) , \quad (7)$$

in which ρ is the average number density of fibrils (the number of fibrils per unit area in a cross-section cut through a lamella) and Δ is the stromal thickness.

The apparatus we used³ was a slight variant of apparatus depicted in Fig. 5. In it, the interference filters were removed, allowing the "white" light from a stabilized tungsten lamp to pass through the cornea. The light that was transmitted within an acceptance angle of $\pm 1.5^\circ$ was collected and fil-

tered through a monochromator, where it was detected by a photomultiplier. The cornea is surrounded by a nutritive, balanced saline solution that maintains its physiological condition (especially thickness) and also nearly matches its refractive index. The hydrostatic pressure maintains tension in the fibrils and produces a curved corneal surface.

Care must be exercised in analyzing the data to account properly for rabbit-to-rabbit variations in corneal thickness. For normal corneas, those variations alter F_T simply because of changes in Δ and do not reflect changes in the spatial distribution of collagen fibrils. In order to separate their effect, we average the quantity $(1/\Delta)\ln F_T$, which is equivalent to assuming that the variations in thickness result from variations in the amount of collagen laid down with an unvarying fibril distribution. In analyzing data from swollen corneas, we use the fact that the total number of fibrils remains constant; consequently,

$$\rho\Delta = \rho_0\Delta_0 , \quad (8)$$

where ρ_0 and Δ_0 are the initial (normal) fibril number density and thickness, respectively. Thus, the function that is averaged for the swollen corneas is

$$(\ln F_T / \Delta_0) = (\sigma_t \rho \Delta) / \Delta_0 = \sigma_t \rho_0 . \quad (9)$$

The experimental results are displayed in Fig. 6 for various degrees of swelling, R (swollen thickness/normal thickness). In the figure, we have actually plotted the quantity $\lambda^3 \langle \rho_0 \sigma_t \rangle$, where the brackets denote the average value. The fact that the data from normal corneas are well fit by a straight line of zero slope supports the short-range ordering models and dictates against the long-range ordering models, for which this quantity would have varied as $1/\lambda^2$.

These data do not invalidate the equal refractive index model of transparency; but this model can be eliminated on the basis of the observed birefringent properties of the cornea.^{5,9}

Our result for normal cornea, however, is in disagreement with measurements obtained by Feuk.¹⁵ He measured angular scattering at $\theta_S = 123^\circ$ and normalized the experimental results to the value at $\lambda = 390$ nm. We note that there is considerable scatter in his data for $\lambda < 450$ nm. In any event, he compared his results to analytical curves of the form $(390/\lambda)^n$, for $n = 3, 5$ and 7 , and concluded there was a λ^{-5} dependence, as predicted by his theory based on long-range order.¹¹ In view of this discrepancy, we devised an exquisitely sensitive test which was to measure the ratio of angular scattering from the cornea at a fixed scattering angle to the scattering from a Rayleigh scatterer.³ Since the wavelength dependence of the Rayleigh scatterer is λ^{-4} , the ratio would have a slope of $+1$ or -1 when plotted against wavelength (on a log-log scale) depending on whether the cornea has a wavelength dependence of λ^{-3} or λ^{-5} . The results shown in Fig. 7 for $\theta_S = 120^\circ$ have a slope of $+1$, clearly indicating that the corneal scattering varies as λ^{-3} .

In another test, we attempted to detect the correction terms in our angular scattering theory that were noted above. More specifically, the factor $J_0(2kr\sin(\frac{\theta_S}{2}))$ in the integral in Eq. (5) contributes second- and higher-order terms in the parameter $(2k\sin(\theta_S/2))$ which, when combined with the λ^{-3} factor from $\sigma_0(\theta_S)$, give a $\lambda^{-(2n+1)}$ contributions with $n = 2, 3, \dots$. Because of the factor $\sin(\theta_S/2)$, the higher-order terms will be more significant, for a given wavelength, as θ_S approaches 180° . Thus we checked to see if we could detect these terms by performing measurements at angles of 120° and 150° . The results are shown in Fig. 8. The quantities plotted are $c\lambda^3 [I_S(\theta_S, \lambda)/I_S(\theta_S, \lambda_0)] [I_0(\lambda_0)/I_0(\lambda)]$, where $\lambda_0 = 525$ nm and c is a constant.

The normalization by $I_S(\theta_S, \lambda_0)/I_0(\lambda_0)$ accounts for cornea-to-cornea variations in the scattering volume (or effective number of fibrils), and the pointed brackets indicate an average over several corneas. The value of $\lambda_0 = 525$ nm was selected because corneal scattering is significant at this wavelength, yet absorption is truly negligible. It might be noted that the data point at $\lambda_0 = 525$ nm is plotted at ~ 1.447 in each case because $\lambda_0^3 \approx 1.447 \times 10^8 \text{ nm}^3$. The data do not fall on a straight line of zero slope which shows the presence of higher order terms. The data for wavelengths greater than 550 nm are approximately constant, suggesting that the short-ranged structure is not sensed at these wavelengths. Unfortunately, the data are not accurate enough to warrant fitting them to a polynomial, especially in light of the cornea-to-cornea variations in $I_S(\theta_S, \lambda_0)$. However, the trends in the results of these experiments are again consistent with the short-ranged order theory based on the EM structures.

The data for the swollen corneas in Fig. 6 are fit by straight lines having positive slopes, as would be expected if σ_t contained an additional term that varies as $1/\lambda^2$. The data are therefore consistent with the lake model^{1,2} and dictate against the model relying on a homogeneous disruption of fibril positions. The value of the slope measures the lake contribution to the scattering, and, in agreement with electron micrographs, the data indicate that lakes are more important contributors at greater degrees of swelling. The data also suggest that lakes are present even at the lower degrees of swelling. Our EM show some evidence of lakes when the thickness ratio of the corneas is as small as 1.25 and definite evidence when the ratio is 1.5 or greater. In summary, the results of light scattering experiments are consistent with structural features shown in EM of normal and swollen corneas.

3)

Unpolarized Angular Light Scattering

A. Theory

The results of the previous section showed that our light scattering measurements were consistent with structure seen in EM when analyzed by the short-range order theory summarized in Eqs. (5-6) for normal corneas, and by Benedek's lake theory for swollen corneas.³⁻¹² However, it must be remembered that these comparisons assume that the collagen fibrils within the stroma are the primary source of scattering. Thus, it is prudent to find other ways of testing this hypothesis whenever possible. To this end, we undertook the study of unpolarized angular light scattering from the cornea.*

From Eq. (5) it is clear that the quantity

$$S(\lambda, \theta_s) \equiv \sigma(\theta_s) / \sigma_0(\theta_s) \quad (10)$$

should depend on wavelength and scattering angle only through an effective wave number given by

$$k_{eff} \equiv k \sin(\theta_s/2), \quad (11)$$

provided the corneal stroma can be treated as a single lamella composed of parallel infinitely long fibrils, as was done in the previously described transparency theories. The total depletion in beam intensity caused by traversing a single lamella can be obtained from Eq. (4) by integrating over all scattering angles θ_s , where θ_s is measured in a plane perpendicular to the fibril axis and scattering is restricted to that plane. The single lamella model is justified for transparency calculations since the calculated depletion does not depend on the particular azimuthal orientation of the fibril axes within the lamella. However, the fact that scattering is restricted to a plane that is perpendicular to the fibril axis means that fibril orientations in different lamellae must be

accounted for in calculating the scattered intensity at a particular detector location. The problem is illustrated in Figs. 9a and 9b. The geometry in Fig. 9a shows the finite acceptance band that is due to the finite acceptance angle of the detection optics. The fibril in this figure is oriented perpendicular to the x-y plane, so scattering is restricted to this plane. Thus, a detector rotating in the x-y plane would detect signal from such a fibril at all scattering angles θ_s .

However, the finite width of the acceptance band, δ , limits the angle ϕ_c that a fibril can be tilted and still have its scattered intensity detected in the x-y plane at some angle θ_s (except for $\theta_s = 0$ and 180°). If the spread of the scattered beam is small compared to δ , then the geometric construction of Fig. 9b can be used to show that scattered intensity will be detected only over scattering angles within the dark (solid and dashed) lines in the figure. The intersection of the dark solid line with the top of the acceptance band defines the maximum scattering angle $\theta_{s\max}(\phi_c)$ for which a fibril tilted at an angle ϕ_c will contribute to the signal measured by a detector in the x-y plane. This definition can be inverted to give the maximum tilt angle $\phi_{c\max}(\theta_s)$ that a fibril can have and still have its scattered beam contribute to the signal when the detector is in the x-y plane at a scattering angle θ_s . The angle $\phi_{c\max}(\theta_s)$ will be denoted by ϕ_{\max} to simplify notation. Simple geometric arguments can be used to express ϕ_{\max} in terms of θ_s and Ω (the angular acceptance of the detection optics shown in Fig. 9a.)* The result is

$$\tan[\phi_{\max}] = [\tan\Omega]/\sin\theta_s . \quad (11)$$

The angular acceptance must be small in order to achieve good angular resolution, and the scattering angles of interest are $30^\circ \leq \theta_s \leq 150^\circ$. Under

these conditions only the fibrils nearly perpendicular to the x-y plane, i.e., ϕ_c small, will contribute, so that $\phi_{\max} \approx \tan\phi_{\max}$.

The detected signal is equal to the intensity scattered by a single fibril, $I_f(\theta_s)$, times the number of fibrils that contribute to the scattering. If the distribution of fibril orientations is continuous near $\phi_c = 0$, then, for small ϕ_{\max} , the number of fibrils oriented to within $\pm\phi_{\max}$ of the z axis is equal to $N(2\phi_{\max})P(0)$, where N is the total number of illuminated fibrils, and P(0) is the probability density that a fibril will be oriented perpendicular to the xy plane. Thus, the scattered intensity at θ_s in the detector (xy) plane is

$$I(\theta_s, \phi_s) = 2NI_{\hat{f}}(\theta_s)P(0) \frac{\tan\Omega}{\sin\theta_s}, \quad (12)$$

where $\phi_s = \pi/2$ for positive y_s and $\phi_s = 3\pi/2$ for negative y_s , and where $I_f(\theta_s)$ can be approximated by the scattered-intensity per unit length of an infinitely long fibril given by Eq. (3). From this result, it is clear that

$$S'(\lambda, \theta_s) \equiv \sin\theta_s S(\lambda, \theta_s) = \sin\theta_s \sigma(\theta_s) / \sigma_0(\theta_s) \quad (13)$$

should depend on wavelength and scattering angle only through an effective wave number $k\sin(\theta_s/2)$. An alternative derivation of the result embodied in Eq. (13) can be found in Ref. 6, where a more rigorous treatment is given based on scattering from finite length cylinders.

B. Experiment

We measured angular scattering from several corneas in order to test the scaling relation given in Eq. (13). The measurements were made at scattering angles of 35°, 40°, 50°, 60°, 115°, 120°, 130°, 140° and 150° for the primary

wavelengths of the mercury source, viz., 404.7, 435.8, 546.1 and 577.7 nm.

The apparatus used for performing these measurements is shown in Fig. 5.

Complete details of this apparatus are given in Ref. 6. Figure 10 is a plot of $S(\lambda, \theta_s) \sin \theta_s$ as a function of k_{eff} , where the refractive index of the hydrated fibril was assumed to be 1.09 times that of the ground substance. The fact that all data lie on a single curve shows that the expected scaling is obeyed. The data in Fig. 10 represent the average from four corneas. We note that the individual data from each cornea exhibited the same scaling behavior as the averaged data. Measurements from a few corneas that had been stripped of their epithelial cell layer were also made and these also showed the same behavior.

The confirmation of the scaling relationship lends strong evidence to the assumption that the stromal collagen fibrils are the primary source of scattering. Thus the theories of corneal transparency, which are based on this assumption, remain on firm ground and the careful use of light scattering measurements to draw conclusions about corneal ultrastructure is warranted.

In this regard we note in passing that polarized light scattering measurements have been especially fruitful. They have been used to show that the distribution of fibril orientations in the central cornea is not random, but rather there are preferred orientation directions that appear to be fixed relative to the eye geometry in a given species.⁵ In addition, by varying the transcorneal pressure, we have shown that the four-lobed pattern seen at small angles when the cornea is placed between crossed-polarizer and analyzer is due to waviness or crimping of the fibrils within the lamellae caused by the release of tension.^{5,17} These investigations are not described here because of space (time) limitations, but the interested reader can find detailed descriptions in Refs. 5, 17 and 18.

4)

Summary

We introduced the problem of light scattering in the cornea and indicated the types of problems that are of interest in ophthalmic research. We have shown how an interplay between theory and experiment has made it possible to discern information about corneal structure for both normal and swollen corneas. Other problems of future interest are the understanding of the structure of scarred and dystrophied corneas.

References

1. R. A. Farrell, C. B. Barger, W. R. Green and R. L. McCally, "Collaborative Biomedical Research on Corneal Structure," Johns Hopkins APL Tech. Dig. 4, 65-79 (1983).
2. R. W. Hart and R. A. Farrell, "Light Scattering in the Cornea," J. Opt. Soc. Am 59, 766-774 (1969).
3. R. A. Farrell, R. L. McCally, and P.E.R. Tatham, "Wavelength Dependencies of Light Scattering in Normal and Cold Swollen Rabbit Corneas and their Structural Implications," J. Physiol. 233, 589-615 (1973).
4. R. A. Farrell and R. L. McCally, "On Corneal Transparency and its Loss with Swelling," J. Opt Soc. Am. 66, 342-345 (1977).
5. R. L. McCally and R. A. Farrell, "Structural Implications of Small-Angle Light Scattering from Corneas," Exp. Eye Res. 34, 99-113 (1982).
6. D. E. Freund, R. L. McCally, and R. A. Farrell, "Effects of Fibril Orientations on Light Scattering in the Cornea," J. Opt. Soc. Am. 3, 1970-1982 (1986).
7. R. L. McCally and R. A. Farrell, "Interaction of Light and the Cornea: Light scattering versus Transparency" in The Cornea, ed. by H. Dwight Cavanagh (Raven Press Ltd., New York, 1988), pp. 165-171.

8. R. L. McCally and R. A. Farrell, "Light Scattering from the Cornea and Corneal Transparency," to appear in New Developments in Noninvasive Studies to Evaluate Ocular Function, ed. by B. Masters (Springer-Verlag, New York, Heidelberg, Berlin).
9. D. M. Maurice, "The Structure and Transparency of the Cornea," *J. Physiol.* 136, 263-286 (1957).
10. F. Zernike, J. A. Prins, "Die Beugung von Röntgenstrahlen an Flüssigkeiten als Effekt der Molekülanordnung," *Z. Phys.* 41, 184 (1927).
11. T. Feuk, "On the Transparency of the Stroma in Mammalian Cornea," *IEEE Trans. Biomed. Eng.* BME-17, 186-190 (1970).
12. G. B. Benedek, "Theory of Transparency of the Eye," *Appl. Opt.* 10, 459-473 (1971).
13. V. Twersky, "Transparency of Pair-Correlated, Random Distributions of Small Scatterers with Applications to the Cornea," *J. Opt. Soc. Am.* 65, 524-530 (1975).
14. J. W. Smith and J. Frame, "Observations on the Collagen and Protein-Polysaccharide Complex of Rabbit Corneal Stroma," *J. Cell Sci.* 4, 421-436 (1968).
15. T. Feuk, "The Wavelength Dependence of Scattered Light Intensity in Rabbit Corneas," *IEEE Trans. Biomed. Eng.* BME-18, 92-96 (1971).
16. J. N. Goldman, G. B. Benedek, C. H. Dohlman and B. Kravitt, "Structural Alterations Affecting Transparency in Swollen Human Corneas," *Invest. Ophthalmol.* 7, 501-519 (1968).
17. R. L. McCally and R. A. Farrell, "Effect of transcorneal Pressure on Small-Angle Light scattering from Rabbit Cornea," *Polymer* 18, 444-448 (1977).
18. R. H. Andreo and R. A. Farrell, "Corneal Small-Angle Light scattering Patterns: Wavy Fibril Models," *J. Opt. Soc. Am.* 72, 1479-1492 (1982).

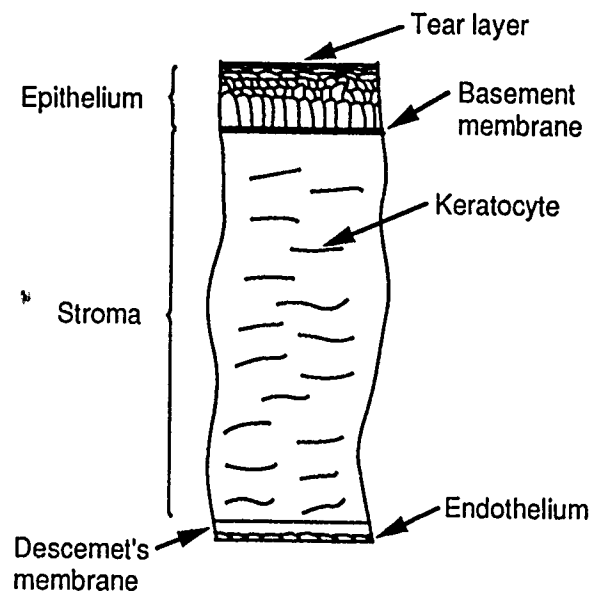
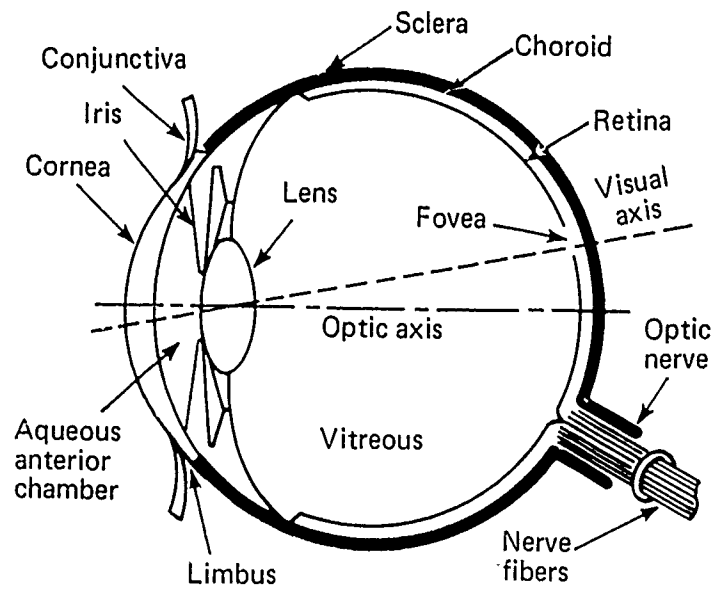


Figure 1 - Top, diagram showing the eye's important optical components; bottom, a diagram showing the layers of the cornea.



← 1 μm →

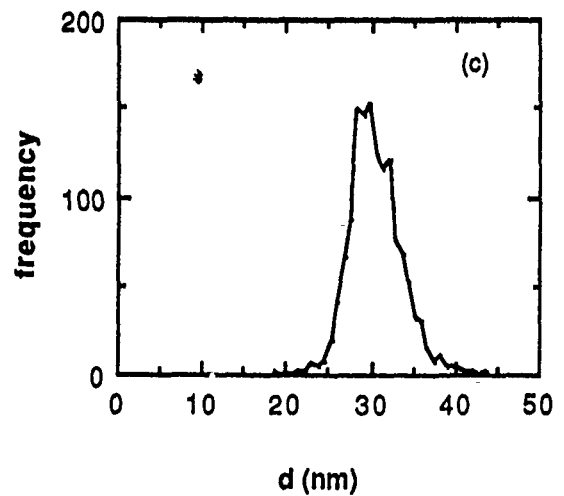
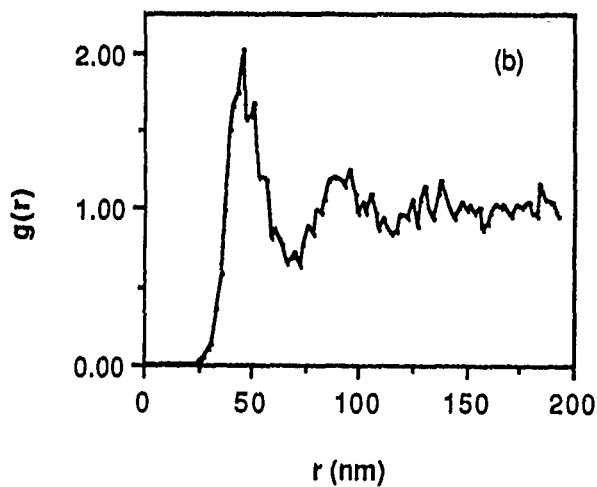


Figure 2 - (a) Electron micrograph (EM) of a region in the central rabbit cornea showing the dark-stained collagen fibrils in cross-section. (b) Radial distribution function of the fibril centers in the EM (a). The function $g(r)$ represents the relative probability of finding two centers separated by a distance r . (c) The distribution of fibril diameters in the EM (a).

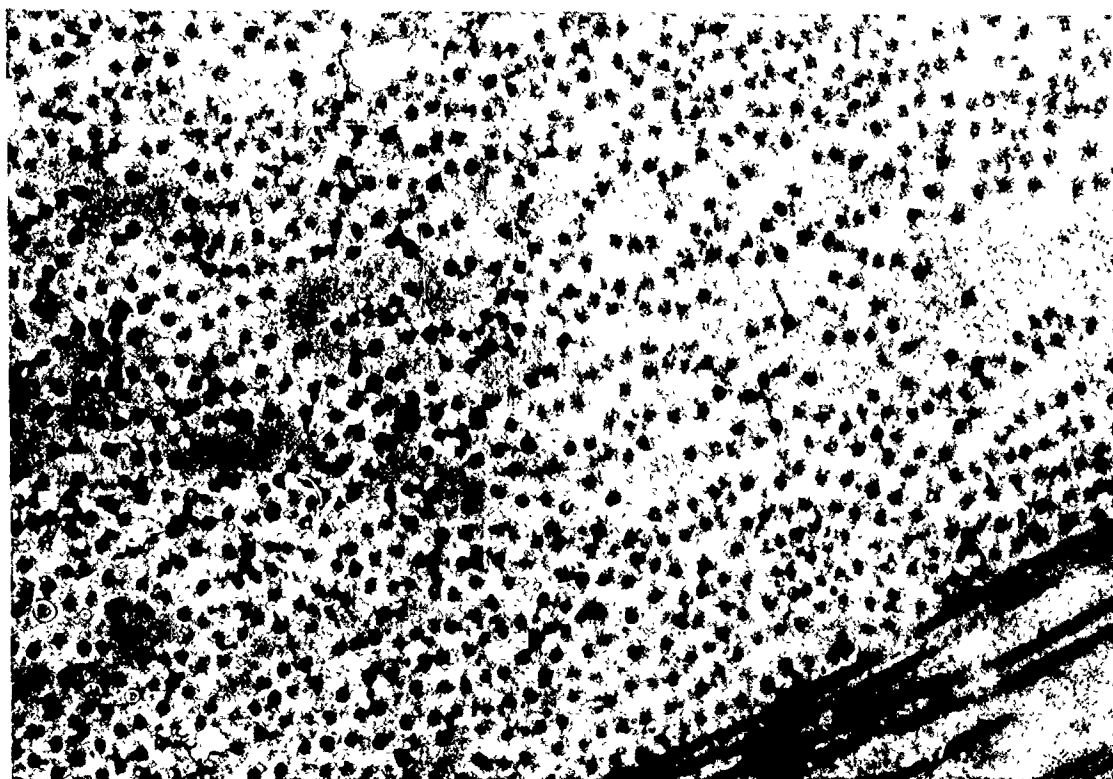


Figure 3 - Electron micrograph of a region in the stroma of a rabbit cornea swollen to twice its initial thickness. The EM shows the voids or "lakes" in the fibril distribution that have been implicated as the cause of increased scattering in edematous corneas.

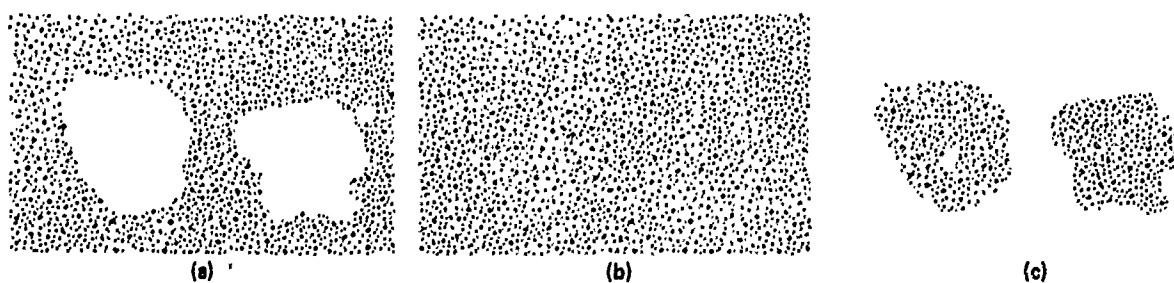


Figure 4 - Method of calculating the scattering from "lakes." (a) is a schematic representation of a fibril distribution that contains lakes. (b) shows the same distribution with the lakes filled in with fibrils having the same number density and relative spatial distribution as the other regions of (a). (c) shows only the fibrils used to fill the lakes. In the calculation these fibrils are given negative scattering amplitudes; thus, the field scattered by the sum of distributions (b) and (c) would be the same as that scattered by (a).

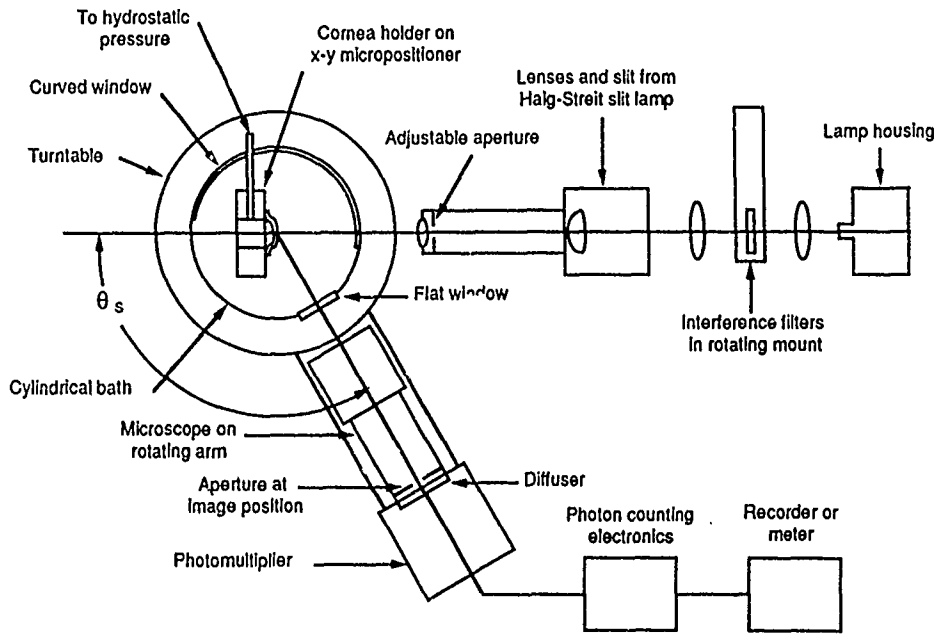


Figure 5 - Schematic diagram of the scattering apparatus configured for angular scattering measurements. (From Ref. 8)

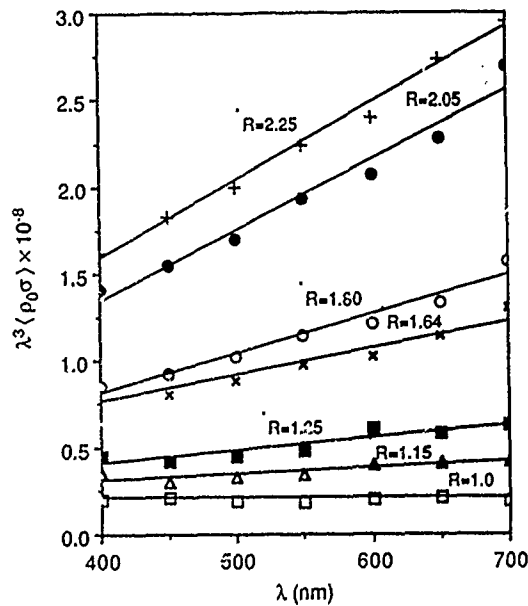


Figure 6 - Wavelength dependence of the total scattering cross-section for normal and cold-swollen corneas. As discussed in the text, premultiplication of $\langle \rho_0 \sigma \rangle$ by λ^3 removes the inverse cubic dependence on wavelength that is characteristic of the individual fibril cross-section. Zero slope for the normal cornea ($R=1$) implies the fibrils are distributed with short-ranged order. According to our extension of Benedek's lake theory,¹² scattering from lakes would result in straight lines with positive slopes. The slope would increase as the contribution from the lakes increases, as observed for $R \geq 1.15$. (Fig. based on Ref. 8).

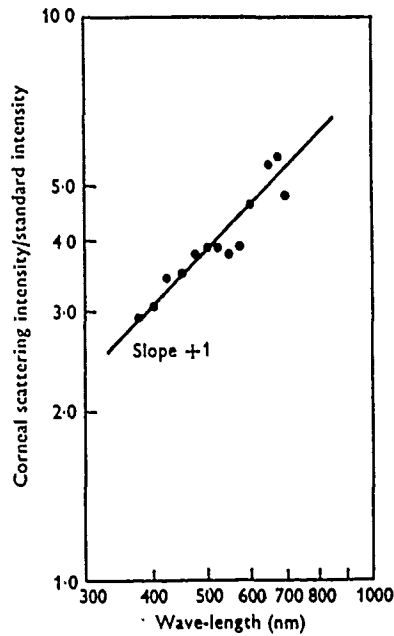


Figure 7 - Angular scattering at $\theta_s = 120^\circ$. Here the ratio of corneal scattering to the scattering from a Rayleigh scatterer is shown as a function of wavelength. As discussed in the text, the slope of +1 indicates the cornea scatters as $1/\lambda^3$, in agreement with short-ranged order structures as depicted in EM. (From Ref. 3).

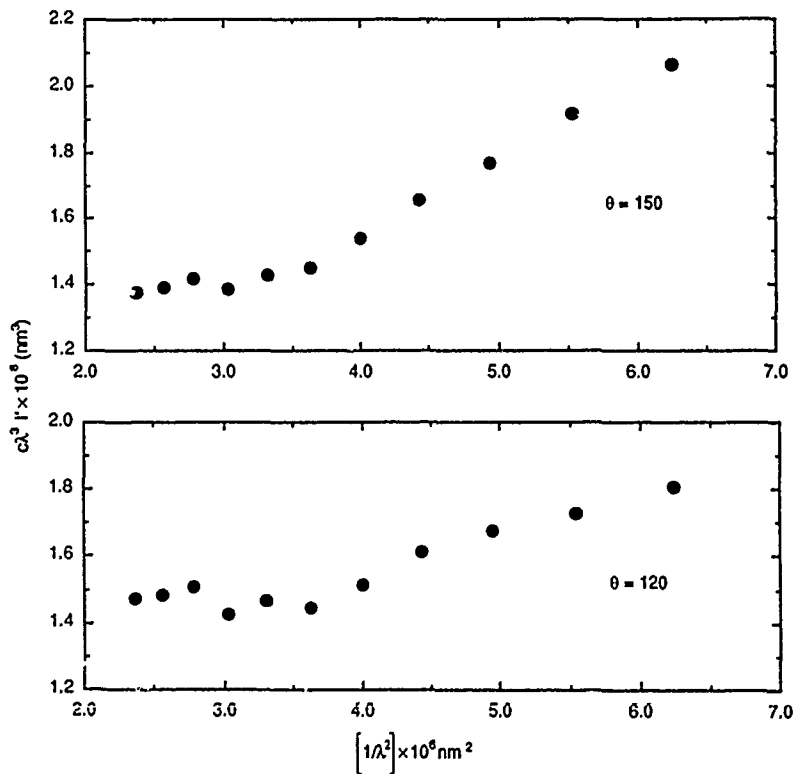


Figure 8 - Scattering measurements at 120° and 150° to demonstrate the existence of higher order terms in the angular scattering as discussed in the text. In the plot $I' = \langle [I(\theta_s, \lambda) / I(\theta_s, \lambda_0)] [(\lambda_0) / \lambda_0] \rangle$.

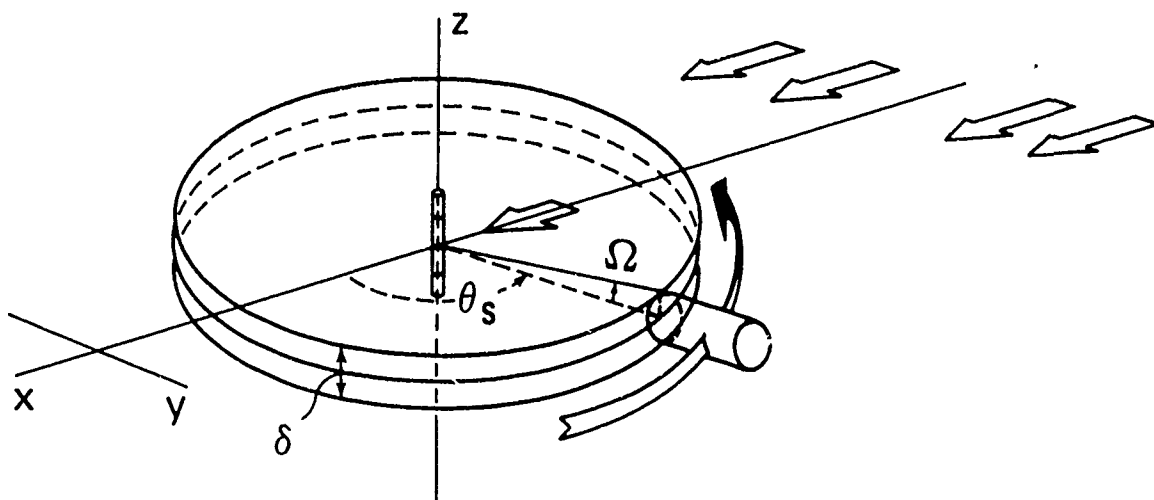
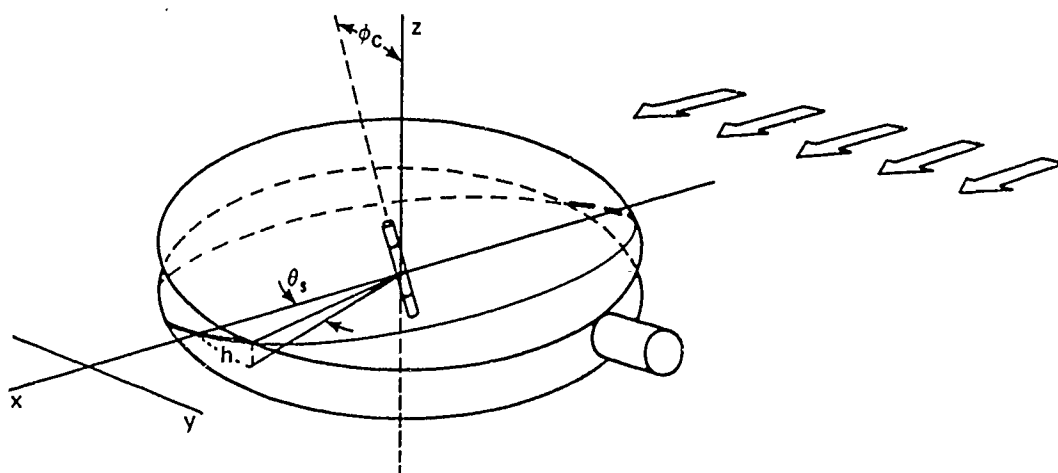


Figure 9 - (a) The geometry shows the finite acceptance band due to the angular acceptance optics. Scattering from a fibril oriented perpendicular to the x-y plane, as shown here, is confined to directions very near this plane (the angular spread out of the plane is much smaller than the acceptance angle Ω). Scattering from such a fibril would be detected at all scattering angles θ_s .



(b) This figure shows that the scattering from a fibril lying in the y-z plane, but tilted at an angle ϕ_c with respect to the z-axis, is essentially confined to the plane through its center that makes an angle ϕ_c with the x-y plane. Scattering from such a fibril would be detected only for $\theta_s \leq \theta_{s\max}(\phi_c)$ and for $\pi - \theta_{s\max}(\phi_c) < \theta_s < \pi$. (θ_s is measured between 0 and π .) The scattering would miss the detector acceptance band for other values of θ_s . (From Ref. 6).

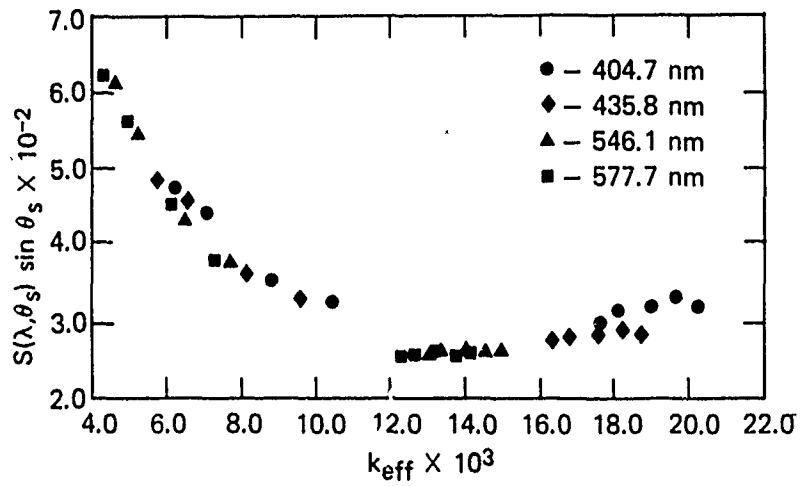


Figure 10 - Experimental measurements of the function $S(\lambda, \theta_s) \sin \theta_s$ as a function of k_{eff} . Scaling is observed, which provides strong evidence that the scattering is predominately from the matrix of fibrils. (From Ref. 6).

BLANK

RELATIONSHIP OF GROWTH CONDITIONS AND CONSEQUENT BACTERIAL SIZE
TO THE S_{34}/S_{11} ANGULAR SCATTERING PATTERN FOR BACTERIA

Burt V. Bronk, Willem P. Van de Merwe*, Donald R. Huffman⁺,
Mark Stanley*

Chemical Research Development and Engineering Center,
A.P.G. Md 21010-5423
Uniformed Services University of the Health Sciences*,
Bethesda, Md 20814-4799
University of Arizona⁺, Tucson, Az 85721

Recent Publications:

Reproducibility and Sensitivity of Polarized Light Scattering
for Identifying Bacterial Suspensions, W. Van de Merwe, D.
Huffman and B. Bronk, in press, Applied Optics (1989)

W. Van de Merwe, D. Huffman, and B. Bronk, "Establishing a
Standard for Polarized Light Scattering from Microbial Systems",
Proceedings of the International Conference on Lasers, 88,
R.C.Sze and F.J.Duarte, Editors, STS Press, Mclean Va. (1989).

Summary: Measurement of the angular dependence of the Mueller
matrix parameter, S_{34}/S_{11} , for the rod-like bacterium
Escherichia Coli was performed under several different
conditions of growth. Analysis of these patterns shows a
dependence on bacterial size which corresponds with a linear
dependence on wavelength. The wavelength dependence shows
interesting similarities with numerical results obtained from
Mie calculations for spheres with index of refraction close to
that of the suspending medium. The curves obtained from *E. Coli*
are different in appearance from those obtained from
Staphylococcus Epidermidis, a bacterium which is rather sphere-
like in shape. The general shift of the curves for a change
from log-phase to stationary phase growth is in the same
direction for both species of bacteria.

Introduction:

We have been interested for some time in evaluating
the potential of utilizing optical means for evaluating unknown
samples of micron-sized particles to determine whether a
particular microorganism is present. The application of
polarization modulation together with lock-in amplification has

made measurement of all 16 elements of the Mueller matrix, which describes polarized light scattering, a practical laboratory task(1,2). To date, only the elements S₁₁ and S₃₄ have been shown to produce reproducible angular scattering patterns with sufficiently characteristic features for bacteria in liquid suspension features to hold promise for aiding in the discrimination between different microorganisms. In this report as in our report to this conference in 1988, we discuss angular patterns for the combination of matrix elements:

$$(S_{11} + S_{34}) / (S_{11} + S_{31})$$

which in the cases discussed here is well approximated by

$$S_{34}/S_{11}.$$

While several laboratories had previously shown that the angular pattern for this signal showed interesting features for microorganisms, none had produced a unique signal which was reproducible in other laboratories. Since the measurement is very sensitive, there has been concern that small changes in the instrument or scattering cell could be the source of difficulty in reproducibility(4). While the possibility of such artifacts must be considered with care for each new apparatus, it turns out that much of the difficulty in reproducing this signal may be due to its sensitivity to very small changes in the organism being studied(3). We succeeded in choosing an organism and experimental conditions which gave an excellent match for the pattern produced for growths and measurements produced in separate laboratories (USUHS and University of Arizona(3).) This experimental system consisted of the *E. Coli* strain k12 containing the prophage for lambda virus. This bacterial strain was easily checked for changes in the original culture by heat-inducing the expression of the virus and lysis of the cells. Standard conditions were also defined as to growth medium, buffer for scanning, and stage of growth of the bacteria. We showed that the pattern obtained was quite sensitive to changes in growth conditions such as allowing the population of bacteria observed in "log-phase" to grow for a few more hours until the cells were in stationary phase. Because such small changes in growth conditions give rise to substantial changes in scattering pattern, we proposed that for the present, the observations from polarized light-scattering, were more of a "footprint" of a given suspended population of microorganisms rather than a "fingerprint" as it has been called elsewhere.

Experimental Methods:

The measuring apparatus is identical to that described in last years report and elsewhere (1-3). The microorganisms utilized were the *Escherichia Coli* strain k12/lambda used previously, as well as *E. Coli* B/r (ATCC 12407), which is another strain of the same bacteria. *E. Coli* k12 was grown in LB broth, while for growth of B/r, two different media were utilized, a minimal medium, M1, with glucose as the nutrient, and M5, an enriched medium(3). Some experiments were also performed with *Staphylococcus Epidermidis* (ATCC #146) grown in ATCC medium 265. This bacterium varies from sphere-like to spheroidal during its growth cycle, and so is substantially different in shape from *E. Coli* which is rod-like. Calculations were performed using a code for Mie scattering from spheres which is available in reference (2).

Since our current results suggest that the size and shape of the organisms are the predominant feature in determining the S_{34}/S_{11} scattering patterns, we have started to characterize the geometry of the populations with the use of scanning electron microscopy and computerized tabulation of various measurements. The preparation of the specimens for scanning electron microscopy was done as follows:

Preliminary Procedure:

1. Dry ~100 microliters of culture medium on glass slide.
2. Bathe dry slides in 1.25% glutaraldehyde solution for 2 hours.
3. Refrigerate in saline solution until further treatment.

Final Preparation:

1. Wash in buffer.
2. Fix in 2% osmium solution.
3. Wash in sodium cacodylate solution.
4. Dehydrate through graded alcohol solutions.
5. Run samples through critical point dryer.
6. Mount slides on stubs.
7. Coat slides with gold

Dimensions of the cells were obtained from photographs which were projected and measured using a Sigma-Scan apparatus and program from Jandel Scientific Co. Corte Madera, CA 94925.

Results:

In our report for last year's conference we observed that the angular pattern for S_{34}/S_{11} obtained with red HeNe laser light appears compressed in angle for the log-phase (growing) pattern for *E. Coli* k12/ λ compared to the pattern for the same cells grown in the same medium to stationary phase (starving). In Figure 1 we see that the same effect is observed for the B/r strain with blue HeCd laser light. There is an obvious difference in the size distribution of stationary phase cells compared to log-phase which can be seen by examination under the light microscope in that the stationary phase cells appear smaller. Another way to obtain size differences with bacteria is to vary the growth medium (5). We did this with *E. Coli* B/r and found that the population with larger bacteria resulting from growth in rich medium showed a compressed pattern (i.e. more structure) compared to the population with smaller cells (See Figure 4 in reference (3)).

As *E. Coli* cells progress, during the course of growth, from balanced log-phase to a more crowded condition, changes in the S_{34}/S_{11} scan can be observed over the course of one or two doublings. Since relatively small changes in shape or size evidently give rise to observable changes in the angular scans, we would like to have some additional measure of these changes. It is natural to consider microscopic photographs, and we have started to use the scanning electron microscope for this purpose. *E. Coli* bacteria have an approximately cylindrical shape with roughly spherical end-caps under the conditions in which we grow them. Thus two measurements, length and width of bacteria lying flat on a slide, give the major features. (Another feature which is not tabulated here is that an indentation gradually appears where two cells will pinch off at a later stage of the cell cycle.) We present histograms of the populations measured in Figure 2. Table I summarizes the averages obtained from these histograms. The large values obtained for the standard deviations in length are to be expected, since each individual cell on average doubles lengthwise during the cell cycle. The intrinsic variation in our measurement is better represented by the standard deviation given for the width than the much larger length variation. Since the length distribution is broad, one might be tempted to use a geometric average. We have used arithmetic averages, however, since for the present, we assume that all cells contribute approximately equally to the scans, and further, the dilution has been chosen so as to eliminate multiple scattering.

TABLE I

ELECTRON MICROSCOPE MEASUREMENTS* ON
E. COLI B/R

	Length	Width
<u>Log Phase</u>		
Medium M1 (Poor)	1.76 +/- 0.40	0.52 +/- 0.09
Medium M5 (Rich)	1.96 +/- 0.50	0.58 +/- 0.06
<u>Stationary Phase</u>		
Medium M1	1.16 +/- 0.23	0.51 +/- 0.05
Medium M5	1.28 +/- 0.32	0.54 +/- 0.05

*Above are arithmetic averages with sample size of ~300 for each group.
Histograms in Figure 2 show relative number of cells of length indicated.

It is interesting that the size changes are all in the "proper" direction relative to the scans. That is, larger cells always give rise to more structure than smaller cells (ie. the curves are compressed for larger cells). It is not resolved at this time whether it is changes in length or width which are predominant in changing the structure of the S_{34}/S_{11} curve. On the one hand, the widths are all about the same for a given population and further the aspect of the cells relative to the laser beam would have much less of an effect on the lights path relative to the cell's width than its length, since the cells are assumed to be randomly oriented. Thus many more widths than lengths would appear approximately the same to the light beam. On the other hand, there is very little change in width for a given medium in going from log to stationary phase whereas there is a substantial change in length which is reflected by a change in the curve for the scan of S_{34}/S_{11} (see Figure 1 and Table I).

In a separate histogram (not shown) of width vs length for a given growth we confirmed the well-known observation that the cells grow mainly in length, with the average width remaining the same in different parts of the cell cycle. There does however appear to be an increase in width as well as length when the cells are grown in richer medium. We must use these results with some caution since we have not evaluated the shrinkage in preparation of the cells for microscopy and there could be differential shrinkage, lengthwise vs widthwise, for example.

A further set of experiments which is comparable but not identical to changing the size of the cells is summarized in Figure 3 for *E. Coli* k12/ λ . Here scans were made at the several different laser wave-lengths indicated on the horizontal axis of the graphs. The angular positions of the maxima or minima were then plotted for each of the scans of S_{34}/S_{11} . It is seen that a good fit to the experimental data is obtained by assuming that the angle for a particular peak is proportional to wave-length.

For comparison, on the same graph we show the results of a calculation for spheres. The fitting of the calculation was done in the following manner. First, a sphere of roughly one micron diameter was chosen and the relative index of refraction was varied with values between 1.00 and 1.06 (real) with little effect on the curves. (It is clear that the index is close to 1.0 for most bacteria.) An index of 1.03 was chosen. Next it was observed that the height of the peaks approached 100% for a monodisperse distribution of spheres. The

height was lowered by selecting a Gaussian distribution of spheres with standard deviation of the diameters equal to about ten percent of its average value. Finally, the peak diameter was chosen to give the best fit to the data taken with red HeNe laser light. And nothing more!

We make some interesting observations. A very nice fit occurs for all wavelengths for at least two of the peaks and troughs at small angles. The overall appearance of the family of straight lines for the experiments with the rod-like bacteria differs, however, from that for the family of lines calculated for the spheres in several ways. The *E. Coli* lines, which are more numerous (due to more peaks) than those for the spheres, all appear to converge to a small region or point at short UV wavelength. In contrast, the line for the largest angle maxima for the sphere calculation does not slope down to small angle nearly as fast as do the other lines. Further, there is a pronounced gap between the largest angle peak line for the spheres and the other lines for the sphere which does not occur for the *E. Coli* lines. Finally, we point out, that while the signal is weakest, and hence most difficult to measure in the backward direction, extrapolation of our curves shows (paraphrasing Craig Bohren's remarks at this conference) that is wherethe action is.

Finally, in Figure 4, we present two scans for the bacteria *Staphylococcus Epidermidis* which is quite different in appearance from those for *E. Coli* at the same wavelength. We note that there is a large curve like an S tipped over on its side with smaller bumps superposed. The log-phase vs stationary phase curves show the same trend as the *E. Coli*, with respect to the S, whereas the smaller bumps may have more to do with the clustering of cells which is more pronounced in log-phase than stationary phase. While we haven't yet studied the *S. Epidermidis* scans in any detail, our results at this writing suggest that they are very different not only from the *E. Coli* curves, but they also appear to differ substantially from the curves calculated for spheres with index of refraction near one, which are discussed above.

REFERENCES

1. A.J.Hunt and D.R.Huffman, "A New Polarization-Modulation Light Scattering Instrument", Rev. Sci. Instrum. 44,1753-1762 (1973).
2. C.F.Bohren and D.R.Huffman, "Absorption and Scattering of Light by Small Particles"(Wiley, New York, 1983).
3. W.P.Van De Merwe, D.R.Huffman and B.V.Bronk, "Reproducibility and sensitivity of polarized light scattering for identifying bacterial suspensions", Applied Optics (1989, in press).
4. R.G.Johnston, S.B.Singham and G.C.Salzman, "Polarized Light Scattering", Comm. Molec. Cell. Biophys 5,171-192 (1988).
5. B.Bronk and D.Walbridge, "Sensitivity to UV Radiation as a Function of DNA Content in E.Coli B/r", Biophys. J. 31,381-392 (1980).

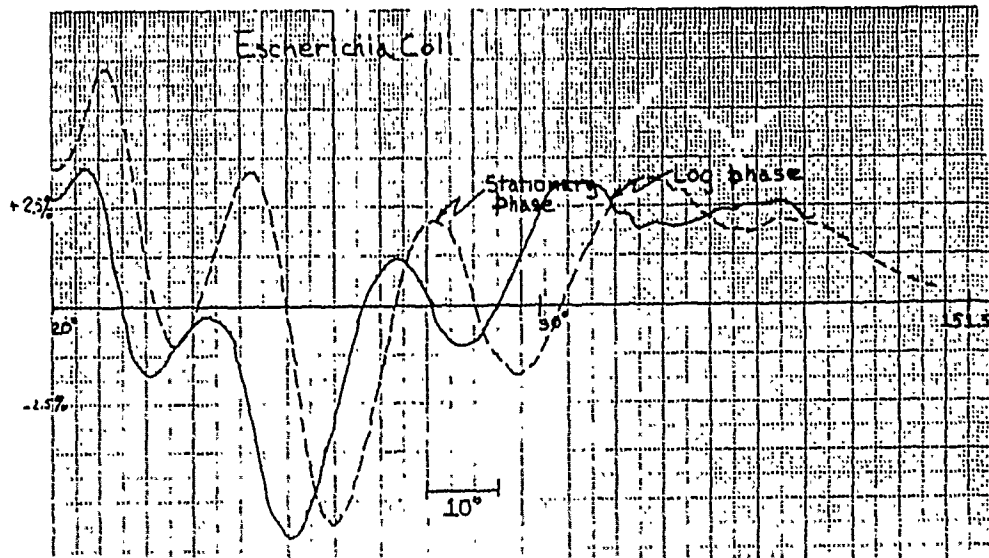


Figure 1. Graphs of S_{34}/S_{11} vs angle for *E. Coli* B/r grown in M5 medium. The log phase cells were grown through more than five doublings to an Optical Density at 600nm (O.D.) of 0.08. The stationary phase cells were grown overnight in the same medium. Cells were scanned at an O.D. of 0.05 in 9% NaCl solution. Laser light was at a wavelength of 442 nanometers. Scans were smoothed over about one angular degree.

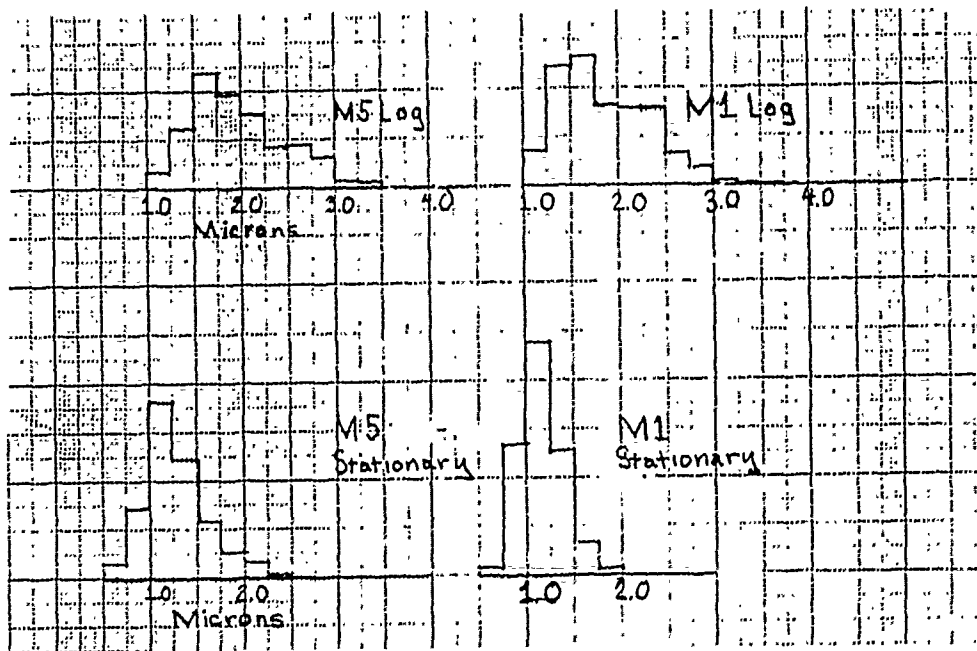


Figure 2. Histograms of lengths measured from scanning electron micrographs of *E. Coli* B/r grown in two different media and in either log phase or stationary phase. The widths obtained were between .51 and .58 microns and do not change during the cell division cycle (See Table I).

Figure 3. Experimental (E) and calculational (C) angular locations are shown for peaks (+) and troughs (o) in the S_{34}/S_{11} scans. The experiments were done with *E. Coli* k12/lambda bacteria grown overnight (stationary phase) in LB broth. The calculations used the Mie solutions for spheres with relative index of refraction, $n = 1.03$, and a Gaussian distribution of radii with a mean of 0.5 micron and standard deviation of 0.05 micron.

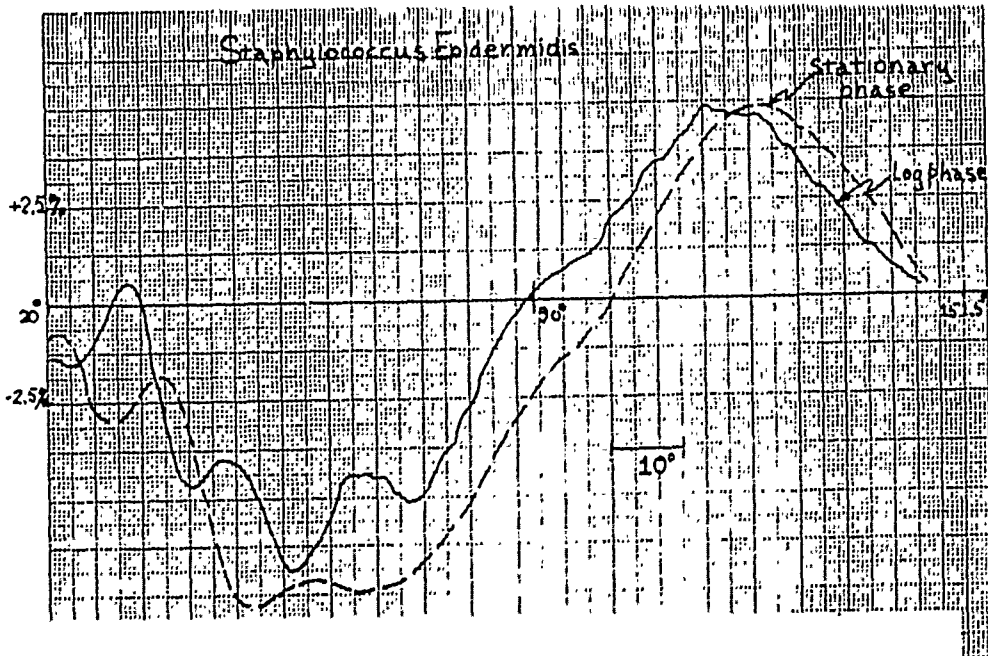
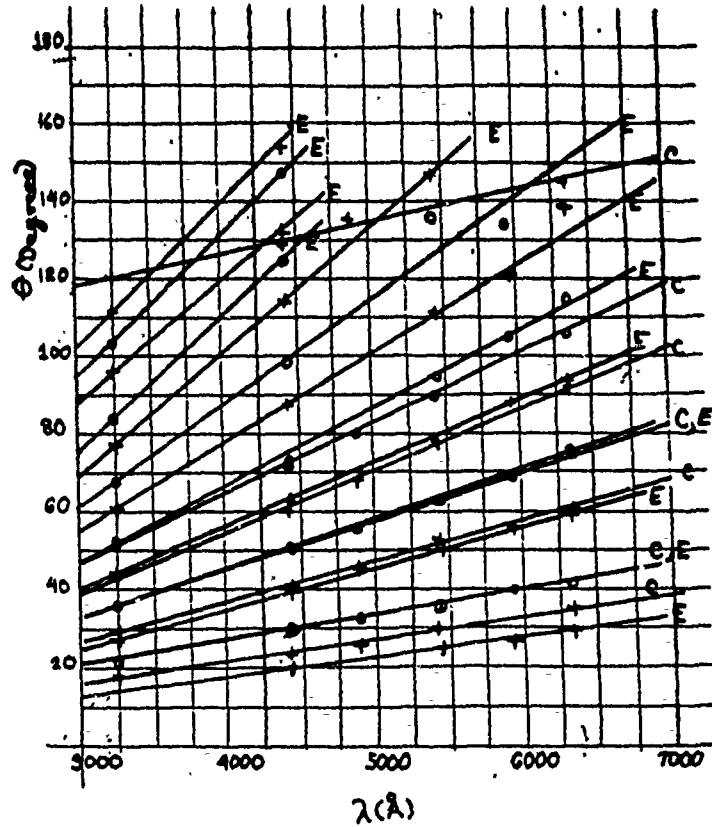


Figure 4. Graphs of S_{34}/S_{11} vs angle for *S. Epidermidis* cells. Log phase cells were grown to an O.D. of 0.05 before spinning down and resuspending in .9% NaCl solution. The stationary cells were grown for a total of seven hours to an O.D. of 2.2 starting from an O.D. of .004 before preparation for the scan. Laser light of 442 nm wavelength was used.

III. NONLINEAR EFFECTS AT HIGH ENERGY

COMPARISON BETWEEN THEORY AND EXPERIMENT FOR LASER-INDUCED PLASMA AND SHOCK WAVES IN DROPLETS

by
J. Carls and J. Brock
Chemical Engineering Department
University of Texas, Austin, Texas 78712

RECENT PUBLICATIONS, SUBMITTALS FOR PUBLICATION AND PRESENTATIONS

1. J. Carls and J. Brock, "Propagation of laser breakdown and detonation waves in transparent droplets", *Optics Letters* 13 273 (1988).
2. J. Brock, D. Zehavi, and P. Kuhn, "Binary aerosol formation in a laminar coaxial jet", *J. Aerosol Sci.* 4 462 (1988).
3. J. Carls and J. Brock, "Explosive vaporization of single droplets by lasers: comparison of models with experiments" *Optics Letters* 13 919 (1988)
4. J. Carls, G. Moncivais and J. Brock, "Time resolved Raman spectroscopy from optically levitated reacting droplets", *Proceedings of the 1988 CRDEC Scientific Conference on Obscuration and Aerosol Research*, CRDEC, U. S. Army, 1989
5. J. Carls, G. Moncivais and J. Brock, "Time resolved Raman spectroscopy from reacting, optically levitated microdroplets", Submitted for publication.
6. B. Jurcik and J. Brock, "Particle formation in shocked flows", *Proceedings of the 1988 CRDEC Scientific Conference on Obscuration and Aerosol Research*, CRDEC, U. S. Army, 1989
7. J. Carls and J. Brock, "High energy laser-particle interactions", *Proceedings of the 1988 CRDEC Scientific Conference on Obscuration and Aerosol Research*, CRDEC, U. S. Army, 1989
8. Y. Chen, J. Brock, and I. Trachtenberg, "Aerosol jet etching", *Aerosol Sci. Tech.*, In Press 1989
9. B. Jurcik and J. Brock, "A study of low pressure impaction processes", *J. Aerosol Science* 20, 560, 1989.
10. J. Carls, Y. Seo and J. Brock, "Laser-induced breakout and detonation waves in droplets: II. Model", Submitted for publication, 1989.
11. Y. Seo and J. Brock, "Distributions for moment simulation of aerosol evaporation", Submitted for publication, 1989.
12. B. Jurcik and J. Brock, "The theory of sonic impactors", Submitted for publication, 1989
13. J. Carls and J. Brock, "The effect of laser pulse frequency and amplitude modulation on energy absorption in ionized shocks", Submitted for publication, 1989.
14. J. Brock, "Aerosol dynamics", Chemical Engineering Seminar, Tokyo Institute of Technology, November 1988.
15. J. Brock, "Aerosol filtration", Chemical Engineering Seminar, Tokyo Institute of Technology, November, 1988.
16. J. Brock, "Advances in aerosol technology", Japan Chemical Engineering Society Lecture, Tokyo, December 1988.
17. J. Brock, "Laser-particle interactions", Invited Lecture, Institute of Chemistry and Physics (RIKEN), Wako, Japan, November 1988.
18. J. Brock, "Aerosol jet etching", Chemical Engineering Seminar, Kanazawa University, Kanazawa, Japan, November 1988.
19. J. Brock, "Aerosols and the environment", U.N.E.S.C.O. Lecture, Tokyo, Japan, December 1988.
20. L. Liebmann and J. Brock, "A finite element approach to laser-droplet interactions", 1989 CRDEC Scientific Conference on Obscuration and Aerosol Research, Aberdeen Proving Ground (Edgewood), Maryland, June 1989.
21. B. Jurcik and J. Brock, "Aerosol plumes: dispersion and characterization", 1989 CRDEC Scientific Conference on Obscuration and Aerosol Research, Aberdeen Proving Ground (Edgewood), Maryland, June 1989.
22. J. Carls and J. Brock, "Studies in nonlinear response of microparticles to laser radiation", 1989 CRDEC Scientific Conference on Obscuration and Aerosol Research, Aberdeen Proving Ground (Edgewood), Maryland, June 1989.
23. J. Carls and J. Brock (presented by M. Sitariski), "The response of single microparticles to high energy laser radiation", 20th Annual Meeting of the Fine Particle Society, Boston, Mass., August 1989.

ABSTRACT

A model for propagation of laser breakdown and detonation waves in droplets is described. The model explicitly accounts for the evolution of the plasma and its coupling to the laser radiation. Model predictions are found to agree well with experimental observations.

INTRODUCTION

The problem of laser-induced breakdown (LIB) of small droplets has been the subject of many recent studies^{e.g. 1-10}. Chang and coworkers have developed experimental techniques^{e.g. 1-6} permitting detailed study of laser-induced breakdown (LIB) of small droplets. Most recently, they have reported a new diagnostic technique⁶ which gives both temporal and spatial information on LIB-generated plasma at two selectable wavelengths. They have reported new results⁸ using this technique for LIB of a single water droplet containing Na salts exposed to single and multiple laser pulses. In this manner, they have been able to compare propagation speeds of H and Na in the exploding droplet and to obtain information on cooling rates of the plasma at various positions. Such information is essential in formulating models for the LIB processes in particles.

In a brief letter⁷, we have previously described theoretical results from a one dimensional model which accounts for evolution of the plasma and the resulting fluid flow, but does not include the plasma breakdown mechanism. The model was shown to give all the qualitative features of an experiment of Hsieh et al⁵, including laser-supported detonation waves. In addition, the model gave quantitative agreement with measured fluid velocities⁵ to within around 50%.

The apparent success of this one dimensional model has led us to extend our calculations to the analysis of the most recent experiments of Zheng et al⁸ on LIB of small droplets. We present here a presentation of model results and comparison with the experimental results of Zheng et al⁸.

PROCEDURE

All experiments on LIB of small droplets by visible lasers have been carried out in the geometrical optics regime. This implies that the heating is non-uniform and that the fluid flow is two dimensional. However, we have shown previously that a one dimensional model of the flow gives many of the features of the flow during LIB. This may be because the spectrograph in the experimental system used by Chang and coworkers^{e.g. 5,6} images only a region of narrow width along the axis of the droplet as defined by the direction of the laser beam. In this region, the laser forces a directional (planar) response of the fluid motion and the narrow shock widths minimize distortions of the planar shocks by the droplet geometry.

Fig. 1 shows schematically the experimental arrangement and the corresponding one dimensional model representation. The system we wish to simulate⁸ consists of a water droplet, surrounded by air and irradiated by a laser at 532 nm. The one dimensional Cartesian model represents the droplet as a region of high density (the liquid water) surrounded on either side by regions of low density (air). The model does not include prediction of the initiation of breakdown. Instead, a small region of plasma is initially assumed to have formed. In the model, this region is represented as a thin slab located close to the shadowed side of the "droplet." The model predicts the subsequent growth and evolution of the plasma during the laser pulse as well as the evolution of the nonionized regions. Even though the initiation of breakdown is not modeled, formation and coupling of the plasma to the laser radiation is included explicitly.

In the model, it is assumed that the laser beam propagates (largely unattenuated) into the droplet until reaching the plasma. There, part reflects from the plasma/liquid interface and the

rest is transmitted or absorbed. Fluid flow, described by the Euler equations, changes the plasma optical properties, and the plasma changes the fluid flow as it heats. Thus, absorption varies with time and position. This nonlinear "particle" - laser beam interaction is an essential feature of the LIB process for droplets.

The pressure gradient drives the fluid motion through the momentum equation in the Euler equations. The extent to which the pressure is reliably predicted for a substance determines, in part, how well the hydrodynamic simulation corresponds to observed behavior. For LIB, the fluid states must include the plasma state; our equation of state is accurate and complete in these respects. We assumed local thermodynamic equilibrium for the plasma and the other fluid states in the model, so that the pressure is obtained through an equation of state solely as a function of its mass density and internal energy.

The complete optical properties of a material are described by its dielectric function. The Drude model was used to determine the dielectric function of the plasma in this calculation. The reflectance at an interface is essential in the calculations and is given in terms of the complex index of refraction. For an equilibrium plasma, the electron number density is simply a function of the mass density and the internal energy. The electron density, necessary for calculation of the optical properties of the plasma state, can be found from the DC conductivity of the plasma.

MODEL RESULTS AND COMPARISON WITH EXPERIMENT

The experiments of Zheng et al⁸ modeled here involved LIB of 80 μm diameter water droplets containing 4 M Na ions exposed to 532 nm radiation from the second harmonic of a Q-switched Nd-YAG laser. The laser pulse had multiple peaks as indicated by Fig. 2. While the Na ions do influence the LIB threshold⁸, our model does not include the initial plasma formation mechanisms and so the effect of the ions is not predicted.

We assume that initially the mass density of the droplet region is 1000 kg/m^3 , the normal liquid density of water. The density of the surrounding gas is 1.2 kg/m^3 , normal air density. The droplet and the surrounding gas are at room temperature and one atmosphere. The plasma layer embedded in the droplet (see Fig. 1) is assumed to be at 30000 K and 500000 atmospheres. Initially the droplet is 80 μm in "diameter". The initial plasma layer occupies 2.5 μm of this, and is located about 7.5 μm from the shadowed face. The modulation in the experimental laser pulse of Zheng et al⁸ indicated in Fig. 2 was fit numerically.

In a previous study⁷ we simulated a single square wave laser pulse with a duration of 10 nsec. In this study, we fit the experimental laser pulses as measured by Zheng et al⁸ (see Fig.2). These laser pulses typically consisted of six to eight peaks; four of these were major peaks. The total duration of a pulse was around 40 nsec.

The modulation and increase of the interaction time of laser beam with the "particle" provide an improved test of the model assumptions. The modulation in the laser pulse gives additional spatial structure arising from the well defined peaks. Also, the longer interaction times are nearer the acoustic transit times for the "particle". Average pulse intensities were varied from 0.4 GW/cm^2 to 9.5 GW/cm^2 . In the experiments of Zheng et al⁸, these average values were obtained from measurement of total power over the known pulse duration.

Fig. 3 shows the results from the model for evolution of the density for the average laser intensity of 0.4 GW/cm^2 for the conditions specified above. The laser beam is in the direction of increasing values of "position" in the figures. The initial profile of the droplet and surrounding gas is shown as the rearmost profile at $t=0$. The plasma region is not visible because the density in the plasma region is the same as in the rest of the liquid; only

temperature, and therefore pressure, is higher. In the next curve, at $t = 2$ nsec, two compression (shock) waves have issued from the plasma region. These two waves form by compression and ionization of the adjacent liquid, causing two sharp peaks in the density. The flow out of the initial plasma region results in a drop in density in the region between the two density peaks.

The two density peaks shown in Fig. 3 for $t > 0$ are evidently different. The wave exiting the shadow face undergoes rapid decompression and a decrease in density. Its shock accelerates into a blast wave upon entering the ambient gas phase, compressing and heating the gas to ~ 6000 K. The second shock wave, moving through the droplet and toward the laser, also compresses, heats and ionizes the liquid it traverses. The shock strength determines the initial degree of ionization. As the liquid ionizes, it absorbs the laser radiation, leading to further ionization. With sufficient radiation energy, this feedback process can cause the liquid to become a strongly absorbing plasma. Therefore, the model includes two mechanisms for ionization: shock heating and laser heating. Since the nonplasma portions of the droplet are essentially transparent, strong laser heating occurs only after shock heating has ionized the liquid sufficiently.

In the experiment⁸, the leading edge of the first major peak in the laser pulse is responsible for creating the initial plasma region. The next major peak appears about 10 nsec later, although the laser energy between peaks is still about 20% of the peak values as indicated in Fig. 2. On the illuminated side, the density wave decays slowly until breakout occurs on the illuminated side (at around 14 nsec in Fig. 3) after which the amplitude of the density breakout wave decreases rapidly with a corresponding decrease in temperature, as shown in Fig. 4. At the same time, an expansion wave begins to propagate toward the shadow side. From Fig. 4, it can be seen that on the irradiated side the region of maximum temperature remains well within the space occupied by the original droplet; this observation is confirmed qualitatively by the experimental measurements⁸ at this intensity which show the regions of maximum H α and Na emissions on the illuminated side to be always within the space occupied by the original droplet[see Fig. 5(a) in Ref. 8]. However, at higher intensities (above around 1.8 GW/cm²) the experimental measurements⁸ show that the illuminated side maxima in intensities move outside the boundary of the original droplet on the illuminated side[see Figs. 3,4, and 5(b) in Ref. 8]; in this regime, a laser detonation wave develops with intense ionization, which effectively screens the shadow side wave from absorption of additional laser energy. This is seen clearly in the experimental results at high energies⁸ where no emission is recorded in the region behind the emission peaks propagating toward the laser. For the low intensity case (0.4 GW/cm²) shown in Figs. 3 and 4, the temperatures decrease monotonically with time which leads to smaller n_e and therefore greater transparency. As shown in Fig. 3, a weakly ionized blast wave begins to develop on the illuminated side at around 4 nsec which is subject to the subsequent peaks in the laser pulse. Subsequently, additional shocks develop since the fluid in the expanding wave is sufficiently transparent to permit absorption of a portion of the laser energy inside the space of the original droplet behind the leading shock. With reference to Fig. 4, this absorption occurs most strongly in the region of highest temperature and density. As indicated in Fig. 3, two shock structures develop behind the leading shock on the illuminated side as the additional peaks in the laser pulse arrive. Careful examination of Fig. 3 shows that these shocks develop from small shoulders in the density profiles on the illuminated side that occur on arrival of each major peak in laser intensity. In our previous simulations⁷, we used a single square wave pulse of duration around 10 nsec and observed only one shock; therefore,

the multiple shocks are due to the multiple peaks in the laser pulse over an approximately 40 nsec time period.

At 0.4 GW/cm^2 , the propagation velocity of the shock on breakout at the shadow face is 3.24 km/s from the model as compared with the measured value from $\text{H}\alpha$ emissions of 3.5 km/s ; similarly, at the illuminated face the velocity of the first shock is 4.9 km/s as compared with the experimental measurement of 5.3 km/s .

For the same conditions, the temperature versus time and position is shown in Fig. 4. The temperature drops rapidly in the wave propagating toward the shadow side until the blast wave develops in the ambient gas. In the region occupied by the original droplet, the temperature decreases monotonically with its maximum moving toward the shadow side; this behavior appears to be borne out by the experimental observations. The data of Fig. 4 were averaged spatially as shown in Fig. 5. The spatially averaged temperature profile resembles somewhat the measured spatially averaged $\text{H}\alpha$ intensity time profile [see Fig. 6 of Ref. 8]. In Fig. 5, the peak in the calculated spatially averaged temperature occurs at around 28 nsec after breakdown, near to the time of the maximum of the experimental emission peak. We point out that emission intensity is a function of both electron density and temperature and therefore an exact correspondence between temperature and emission intensity either in space or time cannot be made.

Fig. 6 shows density versus time and position for peak laser intensity of 9.5 GW/cm^2 . All other conditions are the same as for the lower intensity studied above. The air blast wave and plasma ejection are similar to Fig. 3. However, quite different behavior is found for the wave traveling toward the illuminated face. The high laser intensity causes the shocked, ionized liquid to absorb more energy than it uses compressing. Thus the pressure of the liquid rises, velocities increase, and the shock strengthens, as shown in Fig. 6. Fig. 6 indicates the creation of an optical detonation wave (ODW). However, the laser pulse modulation prevents development of a steady state ODW before breakout occurs on the illuminated side. As the wave reaches the illuminated side it breaks out of the droplet, accelerates to high velocities, and strongly compresses the ambient gas. The fluid behind the breakout wave is shielded by the relatively strongly ionized fluid in the breakout wave. Consequently, the multiple density peaks observed in Fig. 3 are not seen here. This qualitative picture is confirmed by the experimental observations [see Fig. 5(d) of Ref. 8], showing very little emission behind the large $\text{H}\alpha$ and Na intensity peaks which move outside the original illuminated side position toward the laser.

Fig. 7 shows the corresponding temperature versus time and position for peak laser intensity of 9.5 GW/cm^2 . As shown, the wave breaks out on the illuminated side and strongly compresses the ambient gas. At the relatively high temperatures in the breakout wave, there should be strong $\text{H}\alpha$ emissions. The general behavior shown in Figs. 6 and 7 appear to be confirmed by the experimental data⁸ showing that the region of $\text{H}\alpha$ emissions moves rapidly outside the illuminated face toward the laser with very little emission observed in the space originally occupied by the droplet [see Figs. 5(c) and 5(d) in Ref. 8]. Figs. 6 and 7 clearly show the shielding of the remaining fluid behind the breakout wave, as both density and temperature behind the original illuminated face decay monotonically at around 10 nsec following the initial breakdown at $t = 0$; the relatively strongly ionized fluids in the breakout wave on the illuminated side reflect and absorb most of the beam energy and very little reaches the fluid behind the breakout wave. The very high temperatures inside the drop are in the region of very low density between the waves that move toward and away from the illuminated

face. While the temperatures are high in this region, the electron density is relatively low and relatively low emission intensities should be expected from this region as confirmed by experiment. The persistence of the temperature peak in the low density region is attributed to the long relaxation times prevalent in this region.

An interesting result from this study is the effect of the laser pulse modulation on the total energy absorbed by the drop during the time duration of the pulse. In order to investigate this, we consider identical drops exposed to three laser pulses with intensity varying as shown in Fig. 8a; the total fluence of the three laser pulses for a time duration of 25 nsec is identical and equal to $237.5 \text{ joules/cm}^2$. The three curves shown in Fig. 8b show the dynamics of energy absorption by the drops in terms of normalized total energy content (the energy contained in the fluids in the computational domain divided by the initial energy content) as a function of time. It is interesting to note that at the end of 25 nsec when the three drops have been exposed to an identical laser power density, the drop exposed to the most strongly modulated pulse has gained almost 5% more energy than did the drop exposed to the constant laser pulse. We suggest that this is due to the relaxation in the reflectance of the shock moving toward the laser for the drop exposed to the strongly modulated pulse. This relaxation permits more energy to penetrate into the fluid to be absorbed than is the case for the drop exposed to the unmodulated pulse. In our model, this effect will depend on the hydrodynamic relaxation time as it affects the reflectance and it may be possible to optimize this absorption by adjusting the pulse modulation; we plan to investigate this in more detail elsewhere.

4. SUMMARY

The model presented here represents the first effort to describe the coupled electro/hydrodynamic interactions in laser induced droplet breakdown by direct numerical solution of the governing equations. Because of the extremely dynamic nature of the response and the nonlinear nature of the governing equations, a meaningful analytical solution cannot be obtained. The model was written to verify recent experiments. In our recent letter⁷ and in results discussed here, the observation of the same basic hydrodynamic features and relatively close quantitative agreement in shock velocities in both the model and the experiments^{e.g.6,8} are very encouraging, indicating that the model sufficiently reflects the actual physics of the process. The fact that carrier gas breakdown is observed on the irradiated side and not on the shadowed side in both the model and in experiments further shows that the model captures the essential details of both the hydrodynamics and the plasma absorption process. The use of a one dimensional model seems to be justified, at least in a first pass model, on the basis of the very directional response induced by the laser and the experimental measurement system^{5,6,8}. The most important addition to the model, and the reason for its success is the incorporation of the plasma, and modeling its salient features. The Drude model seems to account for the plasma optical behavior in a realistic and sufficient way, and the EOS allows the mechanical and flow properties of the plasma to be modeled appropriately. An additional test of our theory would be experimental confirmation of the effect of laser pulse modulation on energy absorption by the exploding drop. With our model, we found that pulse modulation slightly increased the total energy absorption. This finding may be of interest in the problem of efficient coupling of laser energy to materials in laser processing.

There are several ways in which the model can be improved in the future. First, the relatively good quantitative agreement found here and in reference 7 might be somewhat fortuitous because of the uncertainties in the plasma model and in the actual laser intensity used in the experiments. The experiments show a highly ionized, dense plasma developing, thus, using the Drude model seems appropriate. On the other hand, the electrical conductivity data used in this model are somewhat artificial, and data should be obtained for water. Also, some

aspects of the flow, such as the plasma ejection into the shadowed side, are fundamentally two dimensional. Extending the model to two dimensions would help to resolve these aspects much better. We believe that this extension to two dimensions is only justified because of the relatively good qualitative agreement between the experiments and this 1-d model. An additional improvement would be inclusion in the model of the actual breakdown mechanism. However, we point out again that even without any of these improvements, the model presented here agrees (as indicated here and in reference 7) remarkably well with experiments^{5,8}.

ACKNOWLEDGMENT

We gratefully acknowledge the support of this research by the U. S. Army Chemical Research and Development Engineering Center and the University of Texas Center for High Performance Computing. We particularly thank Dr. R. K. Chang, Yale University for supplying us with experimental data and for productive discussions. We thank Dr. M. Downer, University of Texas for his generous advice regarding the optics of plasmas.

REFERENCES

1. S.-X. Qian, J. B. Snow, H.-M. Tzeng, and R. K. Chang, *Science* 231 486 (1986).
2. W. F. Hsieh, J. H. Eickmans, and R. K. Chang, *J. Opt. Soc. Am.* B4 1816 (1987).
3. J. H. Eickmans, W. F. Hsieh, and R. K. Chang, *Appl. Opt.* 26 3721 (1987).
4. J.-Z. Zhang, J. K. Lam, C. F. Wood, B. T. Chu and R. K. Chang, *Appl. Opt.* 26 4731 (1987).
5. W. F. Hsieh, J.-B. Zheng, C. F. Wood, B. T. Chu and R. K. Chang, *Opt. Lett.* 12 576 (1987).
6. J. B. Zheng, W. F. Hsieh, S.-C. Chen and R. K. Chang, *Opt. Lett.* 13 559 (1988).
7. J. C. Carls and J. R. Brock, *Opt. Lett.* 13 273 (1988).
8. J.-B. Zheng, W. F. Hsieh, Shu-Chi Chen and R. K. Chang, Submitted for publication, 1989.
9. P. Chylek, M. Jarzembki, N. Chou, and R. Pinnick, *Appl. Phys. Lett.* 49, 1475 (1986).
10. R. Pinnick, P. Chylek, M. Jarzembki, E. Creegan, V. Srivastava, G. Fernandez, J. Pendleton and A. Biswas, *Appl. Opt.* 27, 987 (1988).

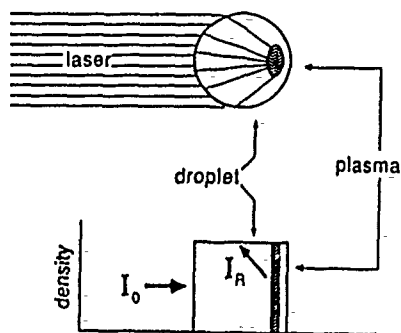


Fig. 1 Schematic of experimental system and the computational model. Plasma is shown by shaded areas. Plasma absorbs, reflects and transmits laser light.

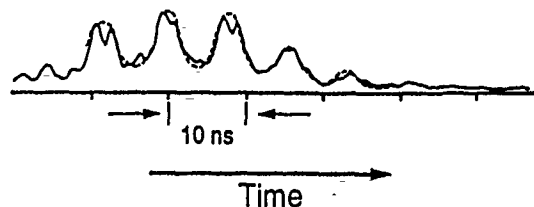


Fig.2 Structure of experimental⁸ laser pulse used in model simulations.

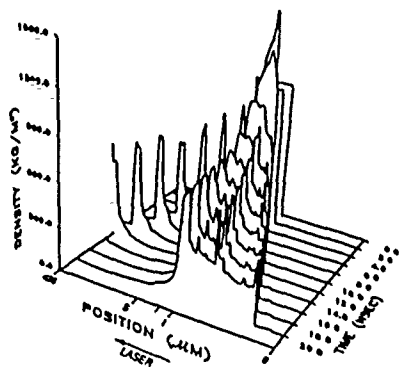


Fig. 3 Fluid densities as function of time and position. Max. laser intensity = 0.4 GW/cm^2 . I indicates illuminated side of drop, S the shadow side.

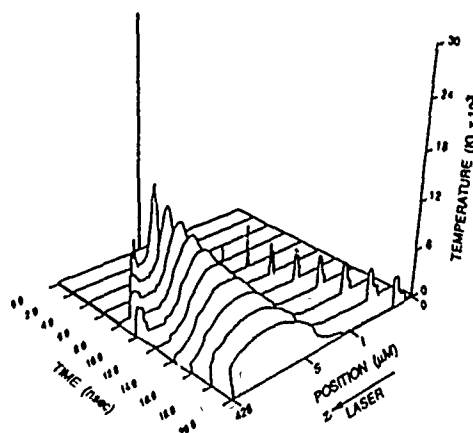


Fig. 4 Temperature as function of time and position. Max. laser intensity = 0.4 GW/cm^2 . I indicates illuminated side of drop, S the shadow side.

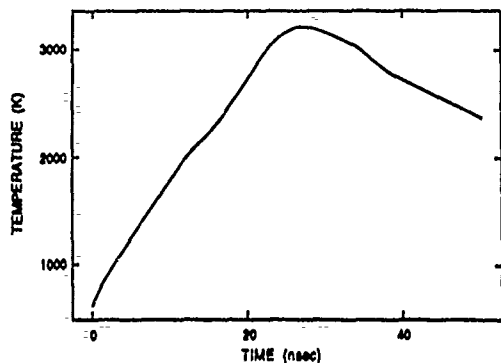


Fig. 5 Spatially averaged temperature as function of time. Max. laser intensity = 0.4 GW/cm^2

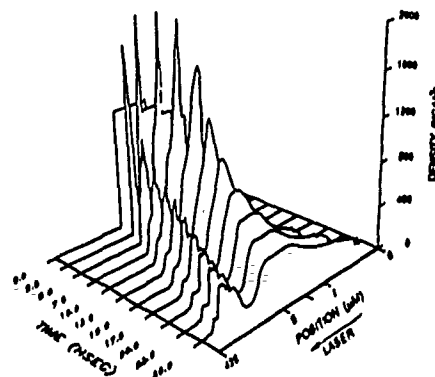


Fig. 6 Fluid densities as function of time and position. Maximum laser intensity = 9.5 GW/cm^2 . I indicates illuminated side, S the shadow side.

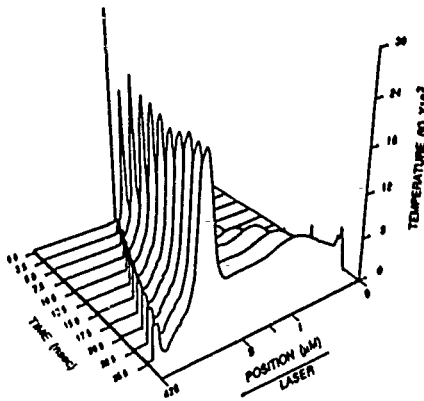


Fig. 7 Fluid temperatures as function of time and position. Maximum laser intensity = 9.5 GW/cm^2 I indicates illuminated side, S the shadow side.

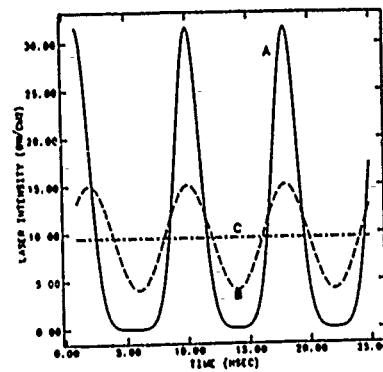


Fig. 8a Three theoretical laser pulse modulations used in study of effect of laser pulse modulation on energy absorption by droplets. The total laser power density is the same for the three pulses for the period of 25 nsec.

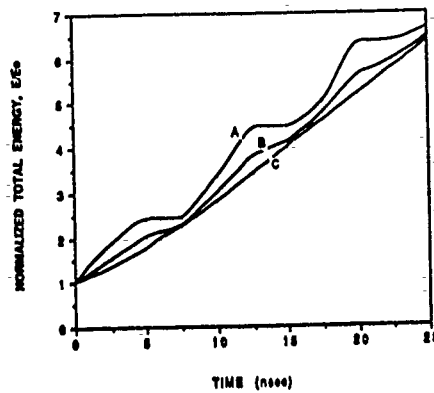


Fig. 8b Variation of total normalized energy content (total energy at time t divided by total energy at initial time) for droplets exposed to the three laser pulses shown in Fig. 8a. Note that the total energy absorbed is somewhat greater for drops exposed to modulated pulses at the end of the 25 nsec period.

BLANK

**Micron-Sized Droplets Irradiated With A Pulsed CO₂ Laser:
Measurements of Explosion and Breakdown Thresholds**

**A. Biswas, B. S. Park, R. L. Armstrong
Physics Department, New Mexico State University
Las Cruces NM 88003**

**R. G. Pinnick, J. D. Pendleton, S. G. Jennings, G. Fernandez
Atmospheric Sciences Laboratory, White Sands Missile Range
White Sands, NM 88002.**

1) R. G. Pinnick, A. Biswas, R. L. Armstrong, S. G. Jennings,
J. D. Pendleton, and G. Fernandez: "Micron-sized Droplets
Irradiated With A Pulsed CO₂ Laser: Measurements Of Explosion and
Breakdown Thresholds", Submitted to Applied Optics

2) B. S. Park, A. Biswas, R. L. Armstrong, R. G. Pinnick, :
"Delay Of Explosive Vaporization in Pulsed Laser Heated Droplets"
Submitted to Optics Letters.

ABSTRACT

When a pulsed CO₂ laser is incident upon partially absorbing liquid droplets energy is exchanged between the laser beam and the droplet to cause either droplet disintegration due to fast heating or at still higher laser fluences droplet induced breakdown with accompanying plasma formation. This report summarizes the minimum laser fluences (thresholds) for the above processes to occur. The time required for initiation of the droplet disintegration is also reported for different liquids and these findings together with the reported disintegration thresholds clearly indicate the prevalence of a superheating based mechanism operative for the case of water, for the other materials a satisfactory explanation is lacking due to both the uncertainty of the thermophysical constants at high temperatures and optical properties at 10.6 um. The latter will form the basis of future investigations.

1. INTRODUCTION

Measurements of the minimum laser fluence required to explode or disintegrate 10 - 60 μm radius droplets of water, ethanol, diesel, carbon-tetrachloride, bromoform and ethyl bromide are reported. Threshold fluences range from 0.4 J cm^{-2} for 10 μm radius ethanol drops to 20 J cm^{-2} for 30 μm bromoform drops. Threshold fluences for water drops are about 3 J cm^{-2} , independent of drop size. Comparison of the measurements to calculations of laser fluence required for considered absorbing droplets to reach superheat temperature are in good agreement¹ for cases where liquid material properties are known, suggesting that superheating of droplets is a dominant mechanism in causing explosion/disintegration. Measured droplet-induced laser breakdown thresholds are considerably higher than explosion thresholds and have less dependence on droplet size and composition. Highest breakdown threshold values are for water drops, which range from 150 to 280 J cm^{-2} (0.9 to $1.7 \times 10^9 \text{ W cm}^{-2}$), compared to 670 J cm^{-2} ($4.0 \times 10^9 \text{ W cm}^{-2}$) for clean air breakdown for the laser pulse length and spot size used.

The behavior of water is quite distinct from all the other materials studied in that measureable delays occur between the initiation of the CO_2 laser pulse and the droplet explosion, with these delays exceeding the laser temporal pulse length at fluence values close to the threshold. This delay can also be observed for some of the other materials but as shown in the next section it never exceeds the laser pulse length.

2. EXPERIMENTAL SETUP

The basic goal of our experiment was to investigate the interaction of micron-sized drops with an intense pulsed CO_2 laser beam. Because of the ($\sim 10\%$) shot-to-shot fluctuations in energy per pulse characteristic of our laser, we decided to utilize in our experiment a droplet generator capable of producing a stream of nearly uniform spherical droplets so that repetitive measurements could be made (Fig. 1a). To get sufficient laser fluence required for our experiment we operated the laser in a multiline mode (but with more than 90% energy output at 10.591 μm wavelength) and focused the beam to an approximate 325 μm x 220 μm spot. Typical temporal and spatial profiles of the CO_2 laser pulse are shown in Fig. 1b. A stream of drops was then directed through the focal volume where disintegration of drops, and at higher fluence levels, drop induced laser breakdown, occurred.

Time resolved photographs¹ of disintegrating drops were made through a microscope by back-illuminating the drops with an air plasma generated by a pulsed Nd:YAG laser synchronized with both the generator and the CO_2 laser. Thus the Nd:YAG produced plasma served as a fast ($\sim 100 \text{ ns}$ duration) strobe light allowing "snapshots" of exploding drops to be visually observed or recorded on film with a conventional 35 mm camera. Moreover the

observations could be made at a fixed time after initiation of the laser pulse at different fluence levels or at a fixed fluence at different times. A calorimeter permitted measurement of laser pulse energy; teflon and "Saran" wrap sheets provided for attenuation of laser energy.

3. RESULTS

Table I summarizes the values measured for explosion and breakdown thresholds for the different materials. Further details related to the observations made including photographs are presented elsewhere.¹

The earliest time for the disruption of the droplet at each energy is recorded while varying the CO₂ laser energy. A minimum laser energy value is reached below which no droplet disruption occurs; this defines the threshold fluence F_{th} . Figure 2 shows τ versus R for several materials² where τ is the delay in initiation of explosion and R is defined as $(F-F_{th})/F_{th}$, F being the measured fluence. It is noteworthy that the explosion of water droplets initiates long after the passage of the CO₂ laser pulse, while for all other materials studied disruption occurs during the CO₂ laser pulse. The data suggest that $\log \tau$ is linearly proportional to R . A simple theoretical model presented elsewhere² was used to explain this delay. The straight line fit to the experimental data (Fig. 2) yields a slope of 1.04 as compared to a slope of 1.02 predicted by the theoretical model, this agreement in the case of water data may be fortuitously good. Two facts should be emphasized in qualifying this agreement; firstly high temperature thermophysical properties used in estimating the slopes were determined by extrapolating the low temperature data and secondly the experimental errors do not permit a precise determination of the experimental slope. For the other materials studied a theoretically predicted slope could not be obtained due to a lack of knowledge of thermophysical constants at high temperatures.

4. CONCLUSION

The brief report above summarizes the threshold laser fluences for explosion and breakdown of micron-sized droplets irradiated by a CO₂ laser beam. Water seems to be distinct of all the materials studied in that superheating seems to be the sole mechanism for its explosion both in terms of the actual explosion thresholds agreeing with a calculation based on superheat, as well as the delay in the initiation in explosion. Future investigations directed at a better understanding of the underlying mechanism for explosion or disruption of the other material droplets require a better knowledge of their thermophysical and optical properties as well as further experimentation.

ACKNOWLEDGMENTS

This work was supported by Lawrence Livermore National Laboratory Contract 2025303 and Army Research Office Contract No. DAAL-03-87-K-0144.

REFERENCES

1. R. G. Pinnick, A. Biswas, R. L. Armstrong, S. G. Jennings, J. D. Pendleton, and G. Fernandez: "Micron-sized droplets irradiated with a pulsed CO₂ laser: measurement of explosion and breakdown thresholds", Submitted to Appl. Opt. and references therein.
2. B. S. Park, A. Biswas, R. L. Armstrong, R. G. Pinnick, : "Delay of Explosive Vaporization in Pulsed Laser Heated Droplets", submitted to Opt. Lett. and references therein.

Table I

Co₂ laser-induced droplet explosion and breakdown thresholds

Material	Drop Radius (μm)	Explosion Threshold		Breakdown Threshold	
		J cm^{-2}	MW cm^{-2}	J cm^{-2}	GW cm^{-2}
air	-			670	4.0
distilled water	12.2	2.42	14.5	284	1.70
	17.4	2.39	14.3	227	1.36
	17.4	2.47	14.8	240	1.44
	28.2	3.37	20.2	195	1.17
	29.1	2.70	16.2	156	0.94
	29.3	3.77	22.6	193	1.15
	29.4	3.90	23.4	148	0.88
	29.7	2.69	16.1	157	0.94
	37.7	3.00	18.0	209	1.25
	37.7	3.02	18.1	243	1.45
	40.4	3.11	18.6	164	0.99
	40.4	3.14	18.8	---	---
	51.6	2.56	15.3	156	0.93
	52.1	2.96	17.7	149	0.89
	boiled water	40.8	3.02	18.1	211
tap water	41.0	2.46	14.7	176	1.06
ethanol	10.4	0.42	2.51	281	1.68
	10.4	0.49	2.96	---	---
	16.6	0.49	2.94	153	0.92
	16.6	0.36	2.17	---	---
	30.1	0.73	4.3	214	1.28
	30.6	1.03	6.2	179	1.07
	30.7	1.01	6.0	190	1.14
	37.1	0.73	4.4	180	1.08
	43.3	0.88	5.2	180	1.08
	52.6	1.21	7.2	231	1.39
	54.2	1.40	8.4	169	1.01
	54.2	1.45	8.7	---	---
Diesel	9.33	1.21	7.2	108	0.65
	13.50	1.68	10.0	99	0.60
	17.60	1.55	9.30	102	0.61
	31.4	1.46	8.7	101	0.61
	32.4	2.40	14.4	91	0.54
	32.5	2.12	12.7	82	0.49
	40.8	1.78	10.7	99	0.59
	44.4	2.71	16.2	110	0.66
	55	2.42	14.5	121	0.72
	55	2.54	15.2	---	---

Material	Drop Radius (um)	Explosion Threshold		Breakdown Threshold	
		J cm ⁻²	MW cm ⁻²	J cm ⁻²	GW cm ⁻²
Diesel cylinder	31	7.6	45	147	0.88
Carbon	28.7	6.0	36	88	0.53
Tetra- Chloride	29.7	8.1	48	86	0.52
Bromoform	31.2	19.6	117	95	0.57
	31.2	17.8	107	70	0.42
	32	16.6	99	63	0.38
	32	24	146	72	0.43
	32	28	169	66	0.40
Ethyl Bromide	26.4	0.70	4.2	124	0.74

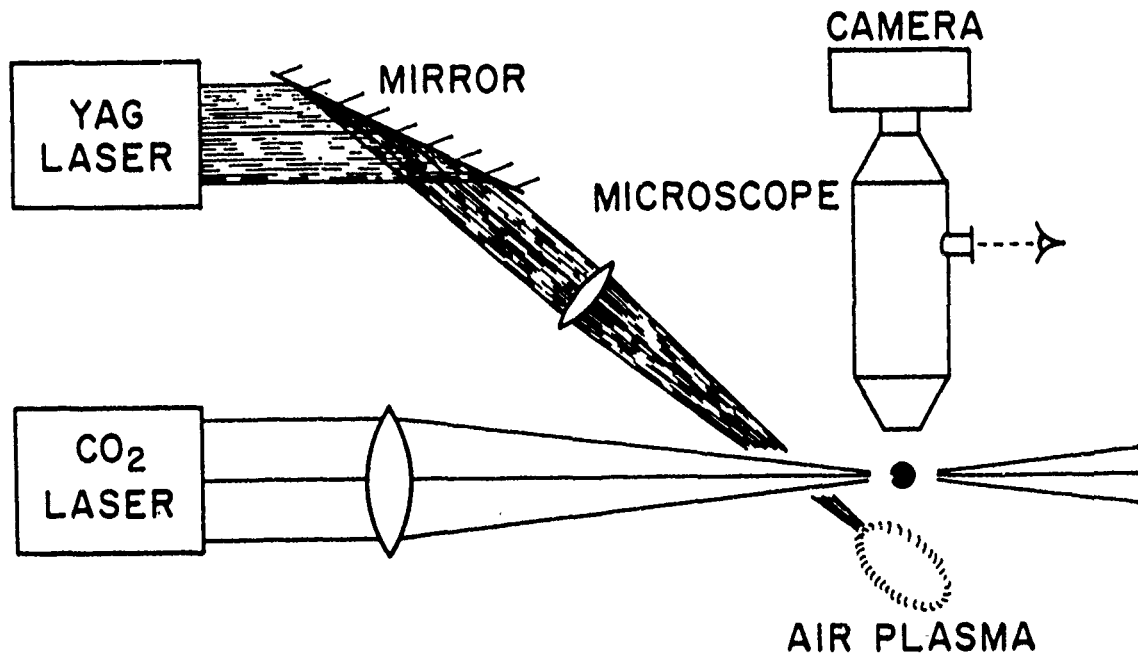


Figure 1a. Schematic of experimental setup for measurement of laser fluence required for droplet explosion and breakdown.

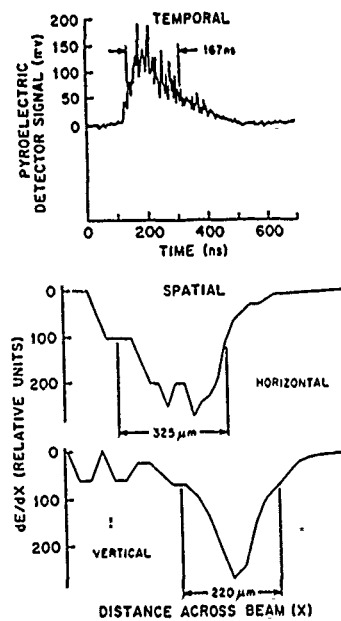


Figure 1b. Typical temporal and Spatial profile of the CO₂ laser beam at the focal volume.

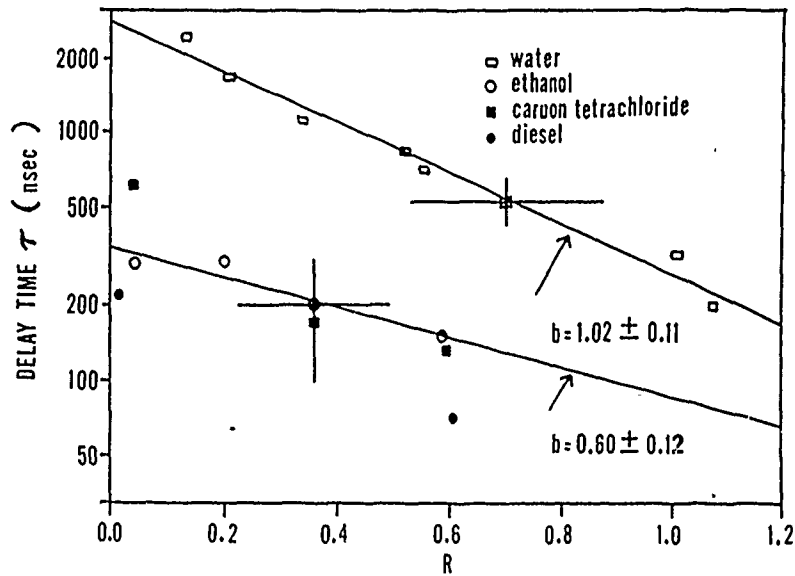


Fig. 2 Time delay for initiation of explosion, τ versus $R = (F - F_{th}) / F_{th}$ for several liquid droplets. The least squares fit lines for water and ethanol drops are shown

MOMENT SIMULATION OF AEROSOL EVAPORATION

Y. Seo and J. Brock
Chemical Engineering Department
University of Texas, Austin, Texas 78712

RECENT PUBLICATIONS, SUBMITTALS FOR PUBLICATION AND PRESENTATIONS

1. J. Carls and J. Brock, "Propagation of laser breakdown and detonation waves in transparent droplets", *Optics Letters* 13 273 (1988).
2. J. Brock, D. Zehavi, and P. Kuhn, "Binary aerosol formation in a laminar coaxial jet", *J. Aerosol Sci.* 4 462 (1988).
3. J. Carls and J. Brock, "Explosive vaporization of single droplets by lasers: comparison of models with experiments" *Optics Letters* 13 919 (1988)
4. J. Carls, G. Moncivais and J. Brock, "Time resolved Raman spectroscopy from optically levitated reacting droplets", *Proceedings of the 1988 CRDEC Scientific Conference on Obscuration and Aerosol Research*, CRDEC, U. S. Army, 1989
5. J. Carls, G. Moncivais and J. Brock, "Time resolved Raman spectroscopy from reacting, optically levitated microdroplets" , Submitted for publication.
6. B. Jurcik and J. Brock, "Particle formation in shocked flows", *Proceedings of the 1988 CRDEC Scientific Conference on Obscuration and Aerosol Research*, CRDEC, U. S. Army, 1989
7. J. Carls and J. Brock, "High energy laser-particle interactions", *Proceedings of the 1988 CRDEC Scientific Conference on Obscuration and Aerosol Research*, CRDEC, U. S. Army, 1989
8. Y. Chen, J. Brock, and I. Trachtenberg, "Aerosol jet etching", *Aerosol Sci. Tech.*, In Press 1989
9. B. Jurcik and J. Brock, "A study of low pressure impaction processes" , *J. Aerosol Science* 20, 560, 1989.
10. J. Carls, Y. Seo and J. Brock, "Laser-induced breakout and detonation waves in droplets: II. Model", Submitted for publication, 1989.
11. Y. Seo and J. Brock, "Distributions for moment simulation of aerosol evaporation", Submitted for publication, 1989.
12. B. Jurcik and J. Brock, "The theory of sonic impactors", Submitted for publication, 1989
13. J. Carls and J. Brock, "The effect of laser pulse frequency and amplitude modulation on energy absorption in ionized shocks", Submitted for publication, 1989.
14. J. Brock, "Aerosol dynamics", Chemical Engineering Seminar, Tokyo Institute of Technology, November 1988.
15. J. Brock, "Aerosol filtration", Chemical Engineering Seminar, Tokyo Institute of Technology, November, 1988.
16. J. Brock, "Advances in aerosol technology", Japan Chemical Engineering Society Lecture, Tokyo, December 1988.
17. J. Brock, "Laser-particle interactions", Invited Lecture, Institute of Chemistry and Physics (RIKEN), Wako, Japan, November 1988.
18. J. Brock, "Aerosol jet etching", Chemical Engineering Seminar, Kanazawa University, Kanazawa, Japan, November 1988.
19. J. Brock, "Aerosols and the environment", U.N.E.S.C.O. Lecture, Tokyo, Japan, December 1988.
20. L. Liebmann and J. Brock, "A finite element approach to laser-droplet interactions", 1989 CRDEC Scientific Conference on Obscuration and Aerosol Research, Aberdeen Proving Ground (Edgewood), Maryland, June 1989.
21. B. Jurcik and J. Brock, "Aerosol plumes: dispersion and characterization", 1989 CRDEC Scientific Conference on Obscuration and Aerosol Research, Aberdeen Proving Ground (Edgewood), Maryland, June 1989.
22. J. Carls and J. Brock, "Studies in nonlinear response of microparticles to laser radiation", 1989 CRDEC Scientific Conference on Obscuration and Aerosol Research, Aberdeen Proving Ground (Edgewood), Maryland, June 1989.
23. J. Carls and J. Brock (presented by M. Sitariski), "The response of single microparticles to high energy laser radiation", 20th Annual Meeting of the Fine Particle Society, Boston, Mass., August 1989.

ABSTRACT

A new class of particle size distributions is proposed having the necessary properties for simulation of aerosol evaporation by the moment method. A distribution from this class is used in moment simulation of free molecule aerosol evaporation. Moment results are compared with the exact analytical solution. It is demonstrated that it is possible to use the moment method, with its high computational efficiency, to simulate aerosol evaporation with reasonable accuracy.

INTRODUCTION

In a previous study (Brock and Oates, 1987), a moment method was developed for simulation of aerosol evaporation. In the application of this moment method, closure was obtained by use of the lognormal distribution. The lognormal distribution, however, is not well suited for this application. During aerosol evaporation, the particle size distribution, on a logarithmic scale of particle size, becomes skewed toward smaller particle sizes while the lognormal distribution, of course, remains symmetric. Therefore, we have investigated particle size distributions that would be more suitable for moment simulation of aerosol evaporation. This note is intended to illustrate the use of a new distribution for simulation of aerosol evaporation and to demonstrate that aerosol evaporation can be simulated with reasonable accuracy using the moment method.

NEW CLASS OF PARTICLE SIZE DISTRIBUTIONS

In order to simulate aerosol evaporation, a particle size distribution must become highly skewed toward smaller particle sizes on a logarithmic scale of particle size as evaporation proceeds. There are many possibilities for size distributions with this property. With appropriate choices for their parameters, the log gamma and log beta distributions, for example, have this property. However, these possibilities are constrained by some other desirable features. For example, distributions in this class should be capable of simulating evaporation, condensation and combinations of these processes such as occur during Ostwald ripening (Tsang and Brock, 1984). Also, the class should contain one or more standard distributions. For rapid estimates, it might also be desirable if moments of distributions in this class were related in simple closed form to their distribution parameters. This is not the case with the log gamma distribution, but for numerical applications it may not be a serious deficiency.

We suggest a class of particle size distributions with some of the properties noted above. Expressed in terms of the mass density function $n(x)$, it is:

$$n(x) = M_0 C_0 x^{-\alpha} \exp(-\beta (\text{ABS}(\ln(x/x_{av})))^{\nu}) \quad (1)$$

where M_0 is the total particle concentration and C_0 is a normalization constant. α is a positive or negative parameter. Also, $\beta > 0$ and $\nu > 1$ are positive parameters. x_{av} is an average particle mass. For $C_0 = (\beta/\pi)^{1/2}$, $\alpha = 1$ and $\nu = 2$, eq. (1) is the lognormal distribution. As an additional example, for $\nu = 1$ and $y = \ln(x/x_{av})$ with a restriction of y to positive values, eq. (1) is an exponential distribution. Fig. 1 shows plots of eq. (1) with a range of values of some of the parameters; the lognormal and what we term the double-sided exponential distribution ($\nu = 1$) are indicated as curves A and C respectively. Except in these special cases, the moments of eq. (1) cannot be expressed in closed form in terms of its parameters. However, this is also true such well known distributions as the log gamma and log beta.

However, for ease of exposition in the application of the moment method to the evaporation problem, we choose to present a study using the special case of eq. (1) where $\nu = 1$. We term this special case the double-sided exponential distribution :

$$n(x) = M_0 C_0 x^{-\alpha} \exp(-\beta \text{ABS}(\ln(x/x_{av}))) \quad (2).$$

The moments we use are defined by:

$$M_{n/3} = \int_{x^*}^{\infty} x^{n/3} n(x) dx \quad ; \quad n = 0, 1, 2, 3, \dots \quad (3)$$

where x^* is the smallest stable particle mass in the distribution.

The parameters of eq.(1) are easily found in terms of the moments, $M_{n/3}$:

$$M_{n/3} = 2M_0 C_0 (\beta/(\beta^2 - (\alpha - (n+3)/3))) (x_{av})^{((n+3)/3 - \alpha)} \quad (4)$$

subject to the constraints:

$$\begin{aligned} \beta &> 0 \\ \beta^2 - (\alpha - (n+3)/3)^2 &> 0 \end{aligned} \quad (5)$$

MOMENT SIMULATION OF EVAPORATION

As in the previous study (Brock and Oates (1987)), we examine the moment solution of the evaporation/condensation equation for the evolution of $n(x,t)$:

$$\partial n(x,t)/\partial t = - \partial(G(x,t) n(x,t))/\partial x \quad (6)$$

where G is the growth law. Here, for simplicity, we choose the free molecule evaporation expression where: $G \sim -x^{2/3}$. As we have shown previously, it is simple to include the case where vapor is conserved during evaporation.

With this growth law, the following moment equations are obtained from eq. (6) :

$$dM_{n/3}/dt = -x^{*(n+2)/3} n(x^*,t) - (n/3)M_{(n-1)/3} \quad (7)$$

where $n = 0, 1, 2, 3 \dots$ and x^* is the smallest stable particle mass in the distribution. We solve four of these moment equations to specify the distribution parameters in terms of the moments.

RESULTS AND DISCUSSION

In actual simulations, the value of x^* might be dictated by the physico-chemical properties of the aerosol - for example, x^* could be the minimum stable particle size. Here, the choice is arbitrary and we chose the value of x^* so as to minimize computational times. For various initial distributions we have compared exact analytical solutions of eq. (7) with moment solutions generated by the solution of eqs. (7) with eqs. (2) - (5). A representative result from these comparisons is shown in Fig. 2 for the following values at $t = 0$: $\alpha=2.$, $\beta=3.$, $x_{av}=7.E-15$. In comparison with our previous simulations using the lognormal distribution, it is apparent that the agreement between the analytical and moment solutions is good even for relatively long times. In this simulation, deviations begin to appear when $t \sim 5.E-5$; however, at this time the number concentration is already reduced by a factor of around 10^2 . In our previous study using the lognormal distribution, a

deviation in phase and amplitude appeared when the number concentration was only reduced by a few tens of percent. In this previous simulation using the lognormal distribution, we found that the phase led that of the analytical solution whereas with the distribution introduced here the phase lags (slightly) behind that of the analytical solution. This suggests that our distribution, eq. (1), with ν in the range $1 < \nu < 2$ -- that is, a distribution bounded by the double sided exponential, eq. (2), and the lognormal distribution (which is obtained for $\nu = 2, \alpha = 1$) -- might give an even better representation of the evaporation process. For the same conditions, the number concentrations from the moment and analytical solutions as a function of time are shown in Fig.3. The agreement is reasonably good over the lifetime of the aerosol, the two curves being almost indistinguishable except when the number decreases by more than a factor of around 10. The CPU time on the Dual Cyber 170/750 used for this evaporation calculation was less than 0.1 sec for a reduction in number concentration by a factor of around 10^2 .

In the calculations, the choice of the set of the four moment equations is arbitrary. From numerical experiments, we found that the set of moment equations for $M_0, M_{1/3}, M_1$ and $M_{4/3}$, appeared to give the best results. As the initial distribution was made broader, the phase lag noted in Fig. 2 became larger; it may be that alternative choices of the set of moment equations would improve this behavior. Also, it may be that the choice of the best set of moment equations will depend on the growth law. Therefore, we suggest that study be given to the optimal choice of the set of moment equations for a given simulation.

Additional work is recommended to examine the use of the more general distribution, eq. (1), or distributions such as the log gamma for moment simulation of aerosol evaporation. However, this limited study suggests that eq. (2) may provide a reasonable distribution for use in rapid estimation of aerosol evaporation, such as in aerosol dynamics simulations arising in computational fluid dynamics applications. More generally, it has been demonstrated that it is possible to use the moment method to simulate aerosol evaporation with reasonable accuracy.

ACKNOWLEDGMENTS

This work was supported by CRDEC, U. S. Army. One of us (JRB) thanks Tokyo Institute of Technology for a visiting professorship during a portion of the work.

REFERENCE

Brock, J.R. and Oates, J. (1987) *J. Aerosol Sci.* **18**, 59-64

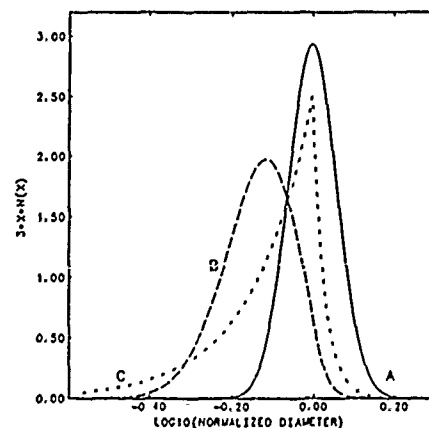


Fig. 1 Distributions generated from eq. (1) with various choices of parameters. For all three curves, $\beta = 3$. Curve A : $\alpha = 1, \nu = 2$; Curve B : $\alpha = 5, \nu = 1.5$; Curve C : $\alpha = 3, \nu = 1$.

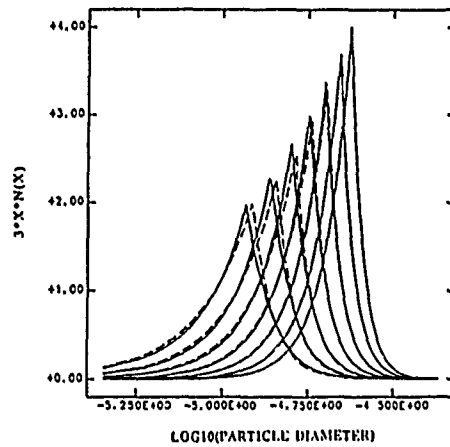


Fig. 2. Comparison of particle size distributions calculated from exact analytical solution of eq.(6) and moment solution for evaporation of aerosol with initial distribution, eq.(2), with parameters $\alpha = 2.$, $\beta = 3.$, $x_{av} = 7.E-15.$ ----- exact analytical solution - - - - moment solution. Time (in arbitrary units) is from 0.0 to 5.E-5 with a regular interval of 1.E-5 in direction of decreasing modal particle diameter.

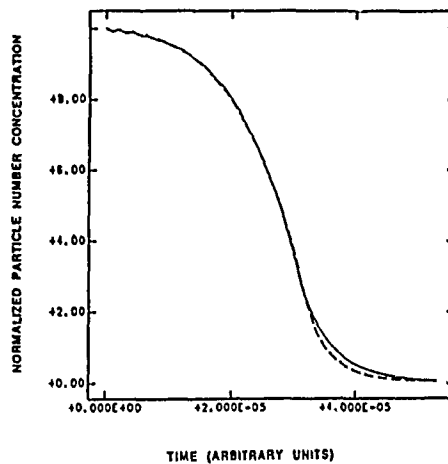


Fig. 3. Total normalized particle number concentration M_0 , as a function of time (in arbitrary units) for evaporating aerosol with initial distribution, eq.(2), with parameters $\alpha = 2.$, $\beta = 3.$, $x_{av} = 7.E-15.$ ——— M_0 from exact solution; - - - M_0 from moment solution.

BLANK

NONLINEAR EFFECTS OF EXCIMER LASER INTERACTION WITH WATER DROPLETS

D.R. Alexander, J.P. Barton, S.A. Schaub, and G. Holtmeier

Center for Electro-Optics
University of Nebraska-Lincoln
Lincoln, Nebraska 68588-0525

RECENT PUBLICATIONS, SUBMITTALS FOR PUBLICATION AND PRESENTATIONS

- A) D.R. Alexander, S.A. Schaub, J. Zhang, D.E. Poulain, and J.P. Barton, "Scattering of incident KrF laser radiation resulting from the laser-induced breakdown of H₂O droplets," *Opt. Lett.*, **14** (11), (1989).
- B) S.A. Schaub, D.R. Alexander, J.P. Barton, and M.A. Emanuel, "Focused laser beam interactions with methanol droplets: effects of relative beam diameter," *Appl. Opt.*, **28** (9), (1989).
- C) D.E. Poulain, "Interaction of solid aerosols with intense ultraviolet laser radiation," Masters Thesis, Mechanical Engineering Dept., Center for Electro-Optics, University of Nebraska-Lincoln, May 1989.
- D) D.E. Poulain, D. R. Alexander, J.P. Barton, S.A. Schaub, and J. Zhang, "Interaction of intense ultraviolet radiation with solid aerosols," submitted for publication to *J. Appl. Phys.*, August 1989.
- E) S.A. Schaub, D.R. Alexander, D.E. Poulain, and J.P. Barton, "Measurement of hypersonic velocities resulting from the laser-induced breakdown of aerosols using an excimer laser imaging system," to be published in *Rev. Sci. Instrum.*, December 1989.
- F) S.A. Schaub, D.R. Alexander, and J.P. Barton, "Theoretical model for the image formed by a spherical particle in a coherent imaging system: comparison to experiment," *Opt. Eng.*, **28** (5), (1989).
- G) J.P. Barton, D.R. Alexander, and S.A. Schaub, "Internal and near-surface electromagnetic fields for a spherical particle irradiated by a focused laser beam," *J. Appl. Phys.*, **64** (4), (1988).
- H) J.P. Barton, D.R. Alexander, and S.A. Schaub, "Internal fields of a spherical particle illuminated by a tightly-focused laser beam: focal point positioning effects at resonance," *J. Appl. Phys.*, **65** (8), (1989).
- I) J.P. Barton and D.R. Alexander, "Fifth-order corrected electromagnetic field components for a fundamental Gaussian beam," to be published in *J. Appl. Phys.*, October 1, 1989.
- J) J.P. Barton, D.R. Alexander, and S.A. Schaub, "Theoretical determination of net radiation force and torque for a spherical particle illuminated by a focused laser beam," to be published in *J. Appl. Phys.*, November 15, 1989.
- K) S.A. Schaub, J.P. Barton, and D.R. Alexander, "Simplified coefficient expressions for a spherical particle located on the propagation axis of a fifth-order Gaussian beam," submitted for publication to *Appl. Phys. Lett.*, July 1989.

- L) J.P. Barton, D.R. Alexander, and S.A. Schaub, "Theoretical determination of the radiation force distribution for a spherical particle illuminated by a focused laser beam," submitted for publication to J. Appl. Phys., September 1989.
- M) D.R. Alexander and J.P. Barton, "Interaction of high energy excimer laser radiation with small solid particles," Final Technical Report, CRDEC Contract No. DAAL03-87-K-0138, Dr. John White, Project Manager, October 1988.
- N) D.R. Alexander, D.E. Poulain, J.P. Barton, S.A. Schaub, and J. Zhang, "Interaction of excimer laser radiation with solid particles," proceedings of the 1988 CRDEC Conference on Obscuration and Aerosol Research, June 1988.
- O) J.P. Barton, D.R. Alexander, and S.A. Schaub, "Experimental and theoretical analysis of liquid droplets moving through a focused CO₂ laser beam," proceedings of the 1988 CRDEC Conference on Obscuration and Aerosol Research, June 1988.
- P) D.R. Alexander and J.P. Barton, "Gaussian laser beam illumination of a spherical particle at resonance conditions," presentation at 19th European Conference on Laser Interaction with Matter, Madrid, Spain, October, 1988.
- Q) D.R. Alexander, S.A. Schaub, J. Zhang, D.E. Poulain, and J.P. Barton, "Laser induced breakdown of H₂O droplets at 0.248 μm ," Workshop on the Physics of Directed Energy Propagation in the Atmosphere, Las Cruces, New Mexico, February 1989.
- R) J.P. Barton, D.R. Alexander, and S.A. Schaub, "Electromagnetic fields for a focused laser beam incident upon a spherical particle," Workshop on the Physics of Directed Energy Propagation in the Atmosphere, Las Cruces, New Mexico, February 1989.
- S) D.R. Alexander, D.E. Poulain, J.P. Barton, S.A. Schaub, and J. Zhang, "Nonlinear effects of excimer laser radiation with solid particles," presentation at the 1988 CRDEC Conference on Obscuration and Aerosol Research, Aberdeen Proving Ground, Maryland, June 1988.
- T) J.P. Barton, D.R. Alexander, and S.A. Schaub, "Internal and near-surface electromagnetic fields for a spherical particle in a focused laser beam," poster presentation at the 1988 CRDEC Conference on Obscuration and Aerosol Research, Aberdeen Proving Ground, Maryland, June, 1988.

Abstract

During this funding period results have been obtained for the interaction of KrF excimer laser radiation ($\lambda = 248 \text{ nm}$, $t_{pulse} = 17 \text{ ns}$) with $60 \mu\text{m}$ distilled water droplets for irradiance values ranging from 3 to 230 GW/cm^2 . Laser images of the droplet breakup during the time interval from 0 to 100 ns indicate the dynamic breakup processes to be highly nonlinear. At low irradiance (3 GW/cm^2) the material is ejected from both the illuminated and shadow hemispheres of the droplet, closely resembling internal electric field strengths obtained from plane wave Lorenz-Mie theory calculations. As the irradiance is increased to 6 GW/cm^2 the interaction on the shadow hemisphere becomes stronger while the interaction on the illuminated hemisphere decreases. At high irradiance (230 GW/cm^2) the droplets fragment in essentially a symmetric manner. Average material velocity from 0 to 50 ns after arrival of the high energy pulse ranged from 1000 m/s at 3 GW/cm^2 to 6000 m/s at 230 GW/cm^2 .

I. Introduction

The interaction of intense laser radiation with liquid droplets has been widely investigated during recent years in attempts to better understand the fundamental physics governing the interaction. Experimental investigations have been performed examining plasma formation,¹⁻⁵ shock propagation,⁶ and electrostrictive effects⁷ that occur during the laser/aerosol interaction. Theoretical models have also been developed to predict the behavior of droplets under high energy laser irradiation.^{8,9} Due to the complexity of the problem, most theories utilize plane wave theory in the analysis although recent work has generalized Lorenz-Mie theory for the case of a particle located at an arbitrary position illuminated by an arbitrarily defined incident beam.^{10,11} However, accounting for the influence of spatial varying droplet properties, initial plasma formation, and heat transfer make the laser/aerosol interaction problem nonlinear and extremely complex. In this paper we present further experimental evidence of the nonlinear interactions of high energy KrF laser pulses ($\lambda = 248$ nm) with $60 \mu\text{m}$ diameter distilled water droplets for irradiance values ranging from 3 GW/cm^2 to 230 GW/cm^2 .

II. Experimental Setup

A schematic of the experimental setup used in the research is shown in Fig. 1. The high energy laser beam is produced by a KrF excimer laser (Questek model 2860, $\lambda = 248$ nm) using unstable optics and is focused at the probe volume using a plano-convex lens ($d = 50$ mm, $f = 200$ mm). The FWHM cross section of the high energy beam at the focal point was determined by translating a knife-edge through the probe volume and was found to be approximately $95 \mu\text{m} \times 115 \mu\text{m}$ ($\approx 10^4 \mu\text{m}^2$). An imaging beam from a second excimer laser, identical to the first with the exception of using stable resonator optics and operating on ArF gas ($\lambda = 193$ nm), is incident in a direction orthogonal to both the high energy pulse and the motion of the water droplets. The use of 193 nm imaging laser was used to obtain higher resolution real-time images as well as to allow elimination of elastically scattering incident radiation by placing a 193 nm bandpass filter in line with the imaging optics. The FWHM pulse duration of the excimer laser pulses were measured using both a photodiode and streak camera and were found to be approximately 17 ns. The imaging pulses are synchronized with the high energy pulses by using an analog/digital delay unit (Questek 9200 laser sync/delay unit) while simultaneously monitoring the output pulse using a fast photodiode (Hamamatsu model C1083) and a digitizing oscilloscope (Hewlett Packard model 54200A). The delay between high energy pulses and imaging pulses could be varied from 0 to $100 \mu\text{s}$ in increments of 10 ns. The jitter for the entire system is approximately ± 7 ns. The monodisperse water droplets were generated using a vibrating orifice generator (TSI model 3450), and were allowed to fall in the direction of the gravitational field perpendicular to both the high energy beam and the imaging beam. The real time images were viewed using a UV sensitive vidicon (Cohu 2006 camera system) in conjunction with a digital image processing system¹². Use

of the image processing system allows accurate determination of the particle size prior to explosive breakup and the distance expelled material travels during the laser/aerosol interaction. The images were stored on an optical memory disk recorder (Panasonic model TQ-2023F) so that later analysis could be performed on the images.

III. Results

Figure 2 shows typical images of water droplets 0, 20, 40, and 100 ns after arrival of 3 GW/cm^2 KrF ($\lambda = 248 \text{ nm}$) laser pulses. In Figs. 2-5 the laser beam is propagating from right to left in the photographs. Although 0 ns delay was established prior to experiments by synchronizing the arrival of the high energy pulse with the imaging pulse as they reached the probe volume, it is clearly evident in the photographs that the interaction actually begins prior to what is considered as 0 ns delay. This is caused by the finite pulse widths (FWHM = 17 ns) of the high energy and imaging pulses. For increasing irradiance, the interaction process initiates nearer the initial rise of the high energy pulse. In contrast, the image that is obtained is integrated over the 17 ns duration of the imaging pulse. Thus, although the peaks of both pulses may arrive simultaneously at the probe volume, the image contains information from the first few nanoseconds after arrival of the high energy pulse. Also note that the images in Figs. 2-5 are not of a single droplet but of several different droplets imaged at fixed times after arrival of the high energy beam. Since the vibrating orifice generator and the laser pulse characteristics change little from pulse to pulse, the image variation from one pulse to the next is not significant. For the images shown in Fig. 2, note that the interaction is nearly symmetric with material being expelled from both the illuminated and shadow hemispheres of the droplet. Figure 3 shows for the same delay times a sequence of photographs for an incident irradiance of 6 GW/cm^2 . At this irradiance, the interaction off the illuminated hemisphere relative to the shadow hemisphere is much smaller. Even at 100 ns, little material is ejected from the illuminated surface. As the irradiance is further increased to 18 GW/cm^2 , the image shown in Fig. 4 at 0 ns shows no evidence of illuminated surface interaction. However, the interaction on the shadow surface is stronger than for lower laser irradiance. Only at later times is there any evidence of material leaving the illuminated hemisphere. Figure 5 shows the droplet images obtained under high irradiance (230 GW/cm^2). In this example, the nonlinear behavior is quite different. The material is ejected in a more symmetric manner than in previous cases and appears to form thin filaments of material at 0 ns delay time.

The behavior of the droplets shown in Figs. 2-5 can be compared to the square root of the internal and near-surface electric field distributions calculated using plane wave Lorenz-Mie theory which are shown in Fig. 6. The square root of the electric field is plotted in efforts to emphasize smaller electric field values (denoted by dark shades at the top of Fig. 6). From this figure, there appears to be four critical regions in which localized maxima appear. The absolute maximum of the electric field values occurs external to the shadow surface of the droplet and has the magnitude $|E/E_0| = 50$ where $|E_0|$ denotes the magnitude of the incident electric field. The high value results

of the focusing effect of the large droplet relative to the incident wavelength. Internal to the droplet surface but still within the shadow hemisphere is three localized peaks each of magnitude $|E/E_0| = 22$. Near the illuminated surface of the droplet lies the third critical region in which the magnitude is approximately $|E/E_0| = 16$. External to the illuminated hemisphere is also a smaller localized peak of magnitude $|E/E_0| = 8$. The local maxima inside the droplet result from constructive interference of laser light reflected from the inner droplet surface and the propagation of surface waves near the air/droplet interface. These four regions of high electric field values are characteristic of transparent droplets and have been discussed previously.¹³ We would expect that these four regions would identify the likely locations of initial laser breakdown. Comparing the calculations in Fig. 6 to the images shown in Fig. 2 we can see similarities in the sense that Fig. 6 shows a nearly equal (slightly higher within the shadow hemisphere) maximum electric field strength within the two hemispheres of the droplet. This would suggest that one would observe material interaction from both hemispheres of the droplet with the stronger interaction occurring from the shadow hemisphere of the droplet. The results in Fig. 2 confirm this prediction. In contrast however, the images in Fig. 3 show significantly less material leaving the illuminated surface of the particle. The dynamics of the breakup can be explained in a qualitative manner if we assume the breakdown intensity for the droplet is I_b (see Fig. 7) and that the initial breakdown occurs at the location of the maximum internal electric field, which is near the shadow surface of the droplet. If it is further assumed that the breakdown of the droplet will cause the once transparent region near the shadow surface to become an absorbing plasma, the initial breakdown region in the shadow hemisphere will act to shield the incident laser light from reflecting (or propagating around the sphere in the case of surface waves) to the illuminated hemisphere. Shown in Fig. 7 are P_h and P_l which represent the intensity profiles of a high energy and low energy pulse, respectively. If the droplet breakdown occurs at an intensity I_b , only the energy associated with the cross-hatched areas will be unaffected by the plasma. Thus a larger amount of energy can be redirected toward the front hemisphere for a low energy incident pulse. As the irradiance is increased we would expect proportionately less available energy for interaction within and near the illuminated hemisphere. This agrees with the observations in Figs. 2-4. For 230 GW/cm² interactions shown in Fig. 5, the 17 ns imaging pulse is not short enough to clearly resolve the early stages of the interaction process and future picosecond or femtosecond imaging work will be required to resolve the early stages of the interaction.

The imaging system can also be used to obtain approximate average velocity measurements for the material ejected at various stages during the laser/aerosol interaction. In order to evaluate the velocity of the ejected material it was necessary to make an assumption regarding the time at which material starts leaving the droplet surface ($\Delta t = 0$). As stated earlier in this paper and illustrated in the images, material ejection starts before what is considered 0 ns delay. For the results presented here, a time of 10 ns before the end of the imaging pulse was chosen as the time material begins leaving the droplet surface. Therefore, in calculating average velocities at 0 ns delay a $\Delta t = 10$ ns was used, at 20 ns delay a $\Delta t = 30$ ns was used, etc. Although this delay value will vary depending on the incident irradiance, we have used a constant value for all irradiances

since detailed resolution of these time are not presently possible in our laboratory. The average material velocity as a function of time and incident irradiance is shown in Fig. 8. The values range from approximately 1000 at 3 GW/cm² to 6000 m/s at 230 GW/cm² with an uncertainty of approximately ± 20 percent which is predominantly due to the difficulty in properly identifying the material boundary. Only limited data was available at high irradiances since the material quickly propagates out of the field of view of the imaging system.

IV. Plans for Future Work

Experimental work on the scattering of radiation in the retroreflective direction will be attempted and results compared with forward scattered radiation published in Ref. 2. Plans are to also study the $\lambda = 248$ nm interaction with nonspherical water droplets. Initial work in the area indicates aspect ratios of approximately 1.2 are required before significant effects can be observed. In order to resolve nonlinear effects at high irradiance values, we have initiated work in picosecond imaging. A femtosecond laser has been purchased and this system will be used for ultra fast diagnostics. Experimental and theoretical work will be performed on all of the above areas. Work on optical temperature measurements in aerosols continues to be pursued. Thin metal wires have been used to demonstrate that material is not spalled off the shadow surface of small solid aerosols. Additional theoretical modeling of $\lambda = 248$ nm interaction with solid matter will be undertaken.

V. Acknowledgments

We acknowledge support of this research by the U.S. Army Research Office under contract No. DAAL03-87-K-0138.

IV. References

1. R.K. Chang, J.H. Eickmans, W.-F. Hsieh, C.F. Wood, J.-Z. Zhang, and J.-b. Zheng, "Laser-induced breakdown in large transparent water droplets," *Appl. Opt.*, **27** (12), 2377 (1988).
2. D.R. Alexander, S.A. Schaub, J. Zhang, D.E. Poulain, and J.P. Barton, "Scattering of incident KrF laser radiation resulting from the laser-induced breakdown of H₂O droplets," *Opt. Lett.*, **14** (11), 548 (1989).
3. A. Biswas, H. Latifi, L.J. Radziemski, and R.L. Armstrong, "Irradiance and laser wavelength dependence of plasma spectra from single levitated aerosol droplets," *Appl. Opt.*, **27** (12), 2386 (1988).
4. W.-F. Hsieh, J.H. Eickmans, and R.K. Chang, "Internal and external laser-induced avalanche breakdown of single droplets in an argon atmosphere," *J. Opt. Soc. Am. B*, **4** (11), 1816 (1987).
5. A. Biswas, H. Latifi, P. Shah, L. J. Radziemski, and R.L. Armstrong, "Time-resolved spectroscopy of plasmas initiated on single, levitated aerosol droplets," *Opt. Lett.*, **12** (5), 313 (1987).
6. P. Kafalas and J. Herrmann, "Dynamics and energetics of the explosive vaporization of fog droplets by a 10.6 μm laser pulse," *Appl. Opt.*, **12** (4), 772 (1973).
7. J.-Z. Zhang and R.K. Chang, "Shape distortion of a single water droplet by laser-induced electrostriction," *Opt. Lett.*, **13** (10), 916 (1988).
8. J.C. Carls and J.R. Brock, "Explosive vaporization of single droplets by lasers: comparison of models with experiments," *Opt. Lett.*, **13** (10), 919 (1988).
9. S.M. Chitanvis, "Explosive vaporization of small droplets by a high-energy laser beam," *J. Appl. Phys.*, **62** (11), 4387 (1987).
10. B. Maheu, G. Gousbet, G. Grehan, "A concise presentation of the generalized Lorenz-Mie theory for arbitrary location of the scatterer in an arbitrary incident profile," *J. Optics (Paris)*, **19** (2), 59 (1988).
11. J.P. Barton, D.R. Alexander, and S.A. Schaub, "Internal and near-surface electromagnetic fields for a spherical particle irradiated by a focused laser beam," *J. Appl. Phys.*, **64** (4), 1632 (1988).
12. K.D. Ahlers and D.R. Alexander, "Microcomputer based digital image processing system developed to count and size laser-generated small particle images," *Opt. Eng.*, **24** (6), 1060 (1985).
13. W.-F. Hsieh, J.-B. Zheng, C.F. Wood, B.T. Chu, and R.K. Chang, "Propagation velocity of laser-induced plasma inside and outside a transparent droplet," *Opt. Lett.*, **12** (8), 576 (1987).

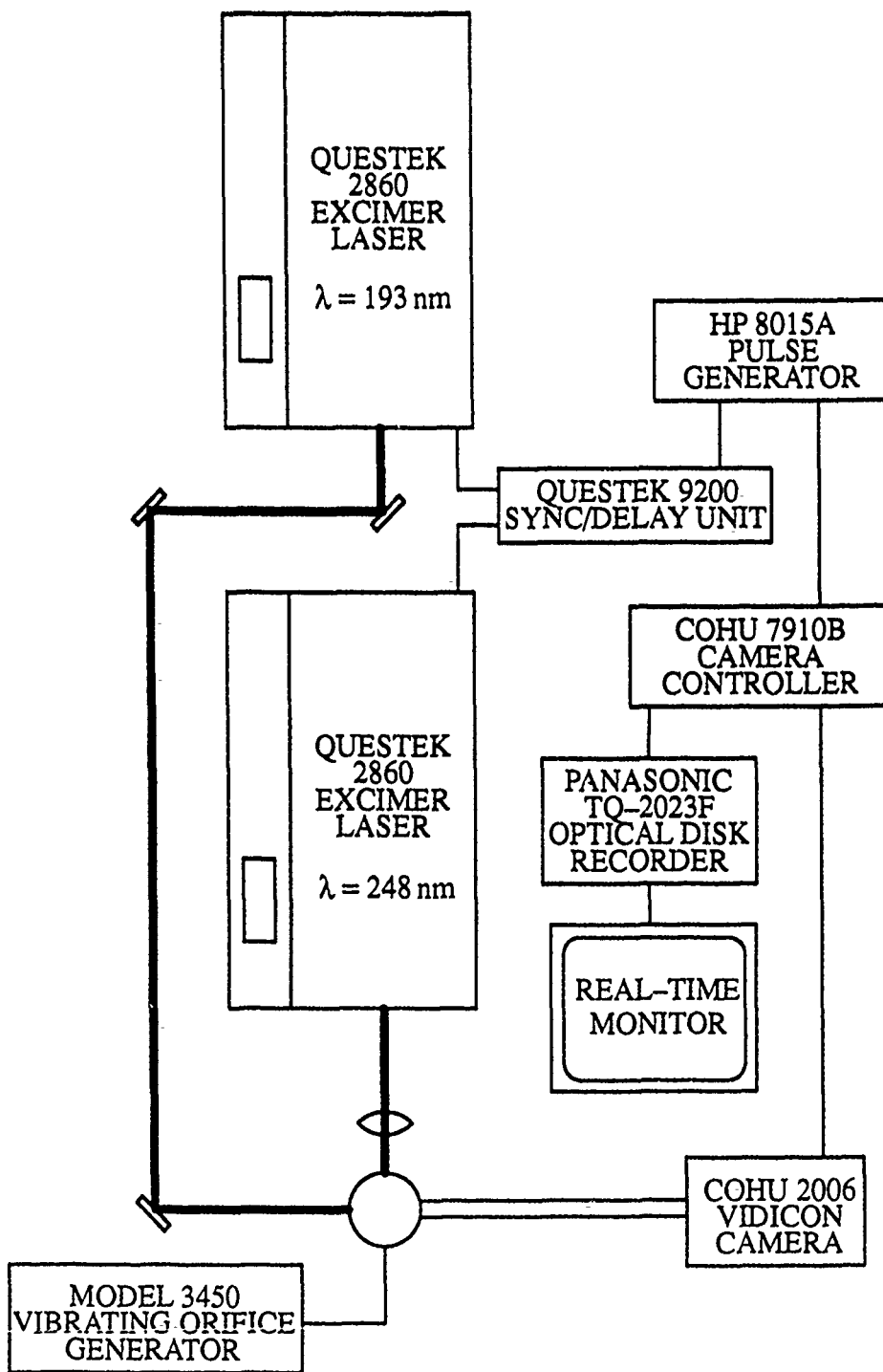


Fig. 1. Schematic of experimental setup.

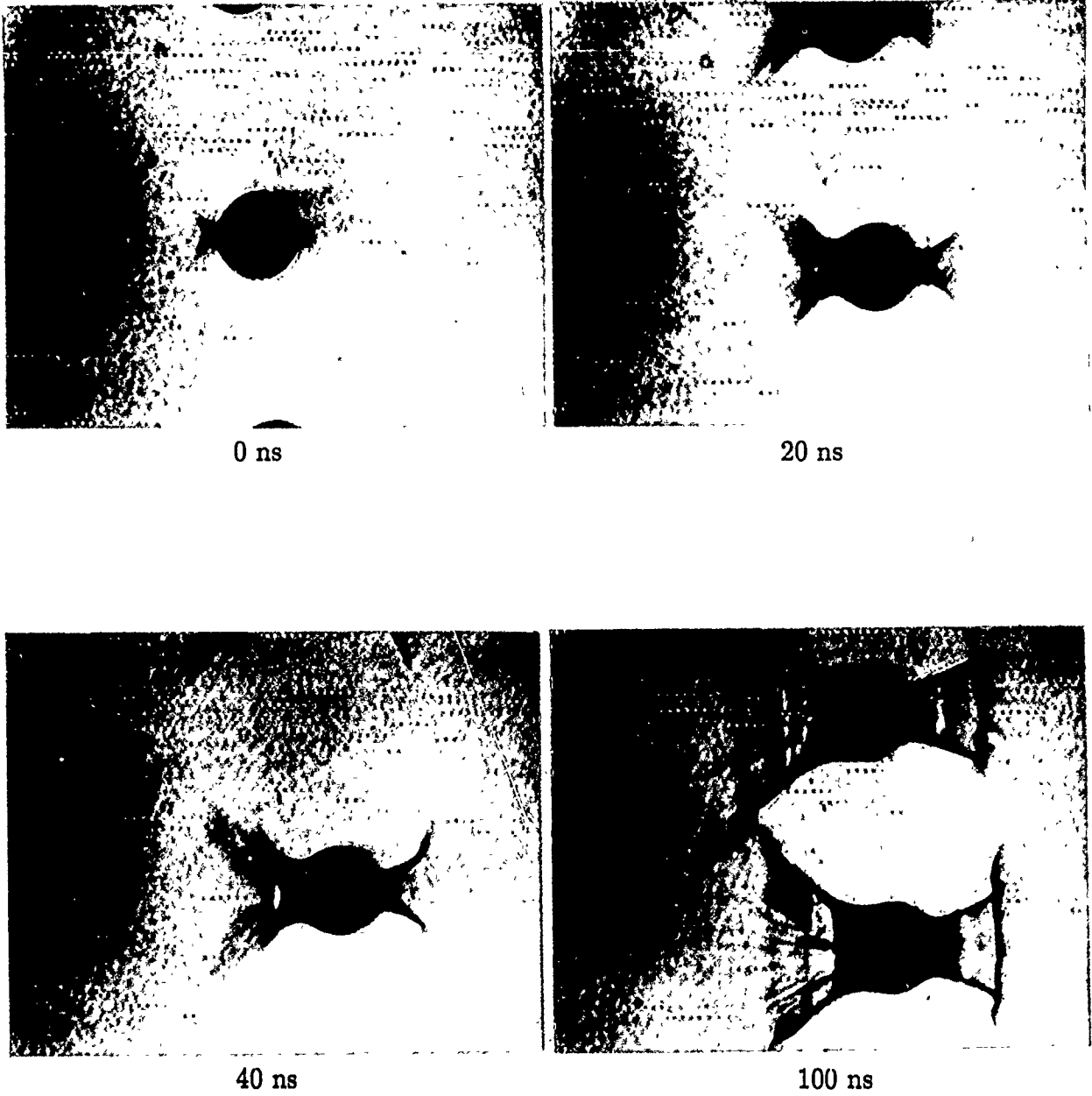


Fig. 2. Interaction of a 3 GW/cm^2 KrF ($\lambda = 248 \text{ nm}$) laser pulse with $60 \mu\text{m}$ water droplets seen 0, 20, 40, and 100 ns after arrival of the high energy pulse. The laser is propagating from right to left.

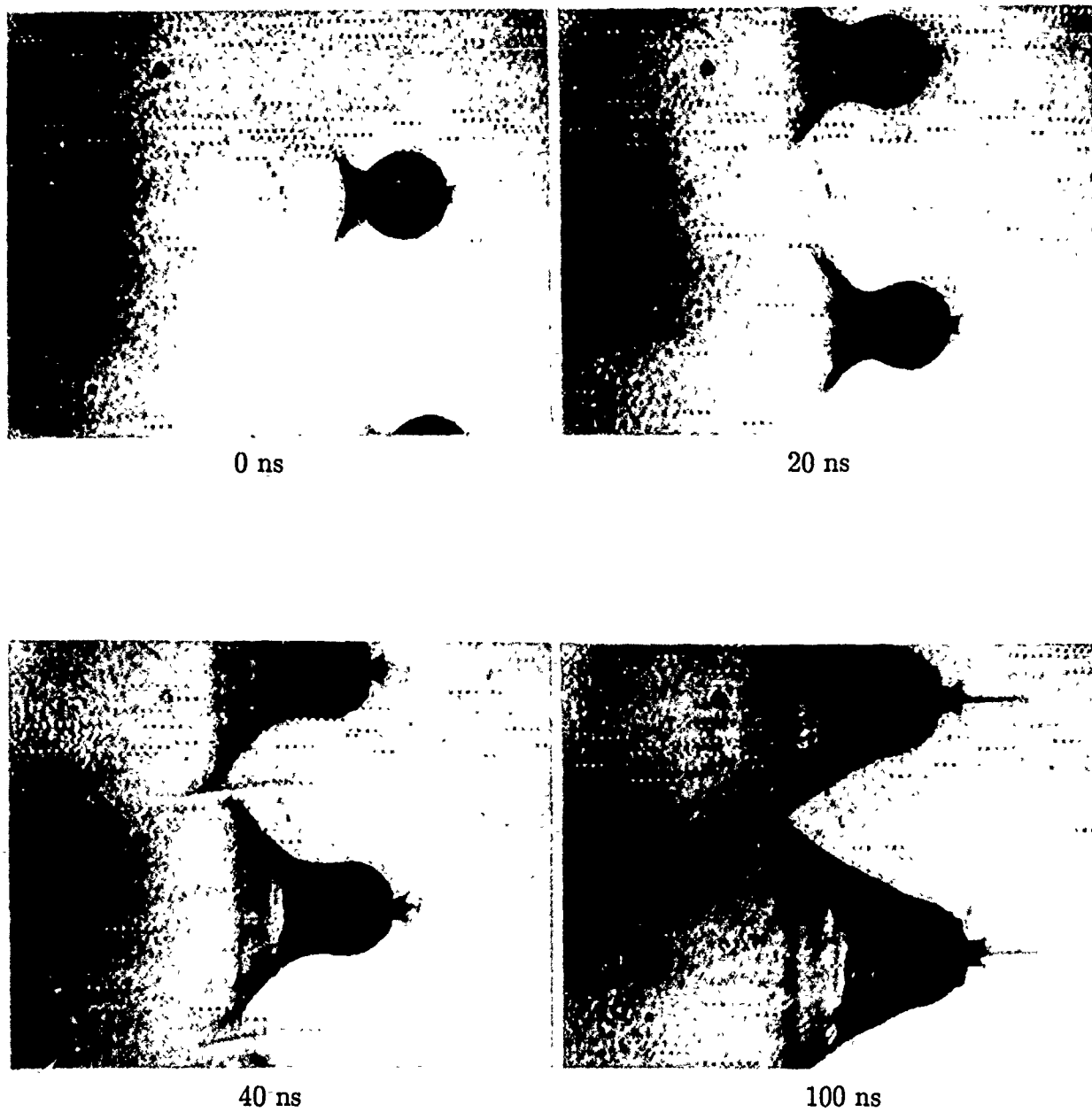


Fig. 3. Interaction of a 6 GW/cm^2 KrF ($\lambda = 248 \text{ nm}$) laser pulse with $60 \mu\text{m}$ water droplets seen 0, 20, 40, and 100 ns after arrival of the high energy pulse. The laser is propagating from right to left.

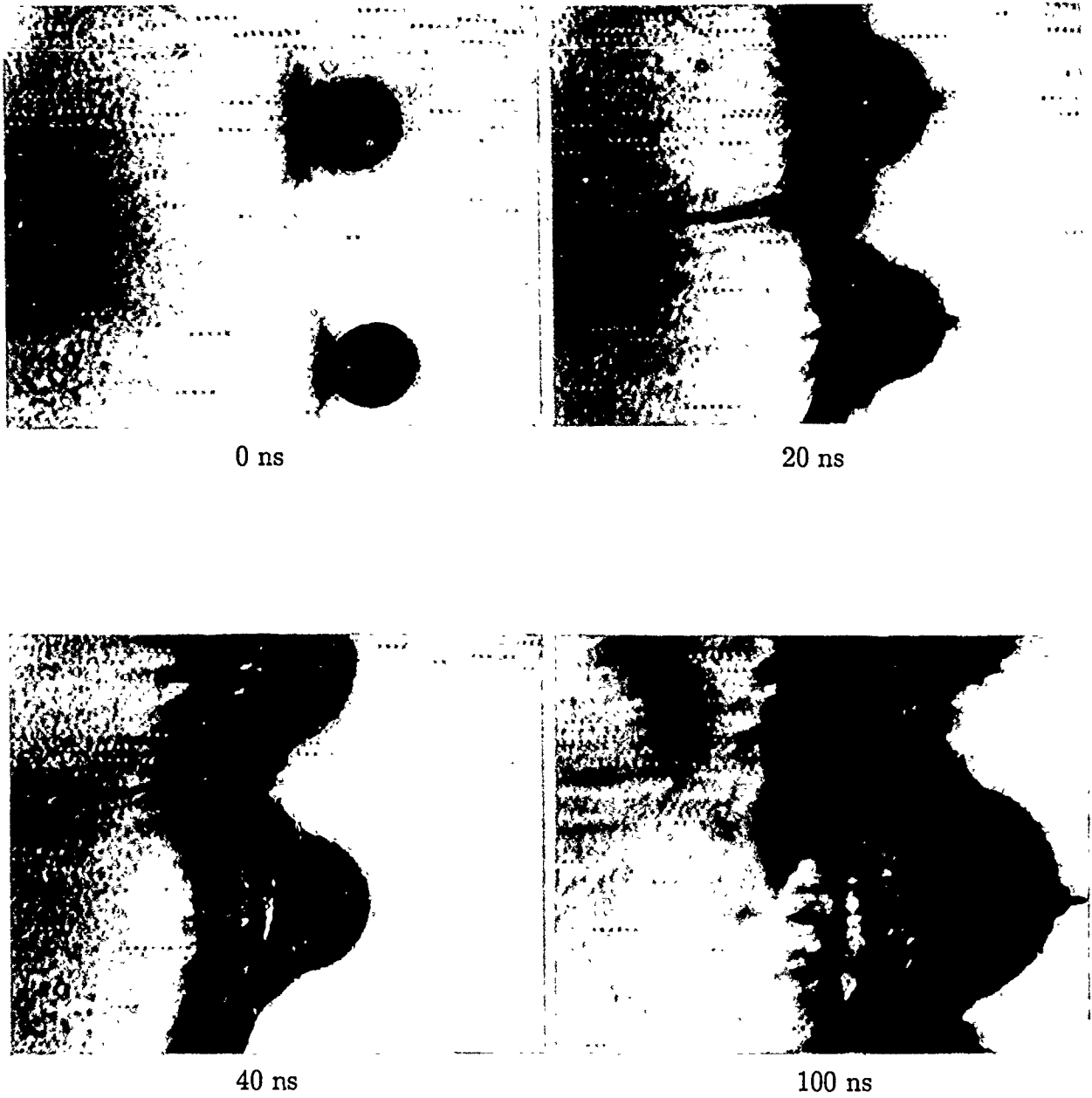


Fig. 4. Interaction of a 18 GW/cm^2 KrF ($\lambda = 248 \text{ nm}$) laser pulse with $60 \mu\text{m}$ water droplets seen 0, 20, 40, and 100 ns after arrival of the high energy pulse. The laser is propagating from right to left.

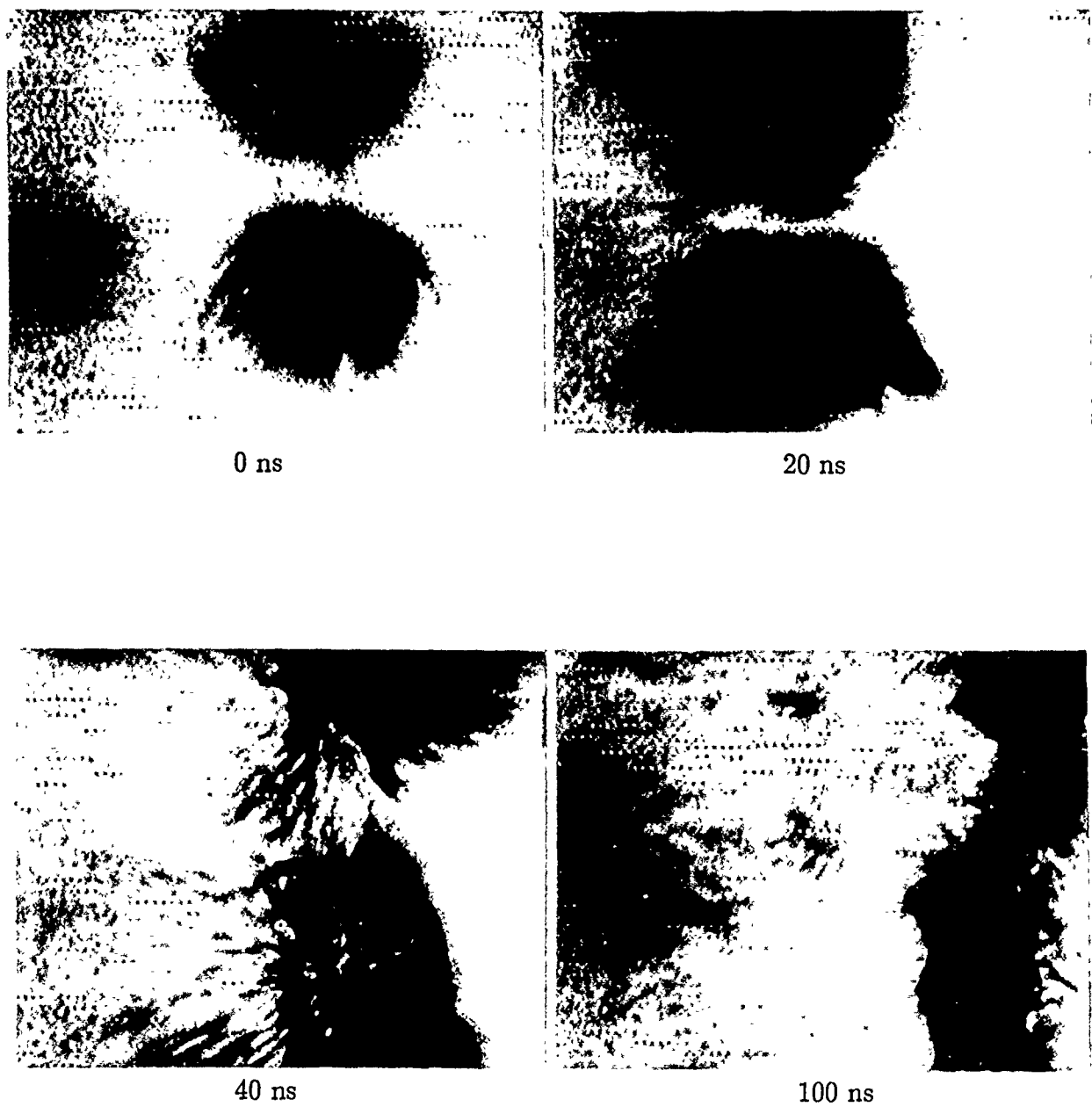


Fig. 5. Interaction of a 230 GW/cm^2 KrF ($\lambda = 248 \text{ nm}$) laser pulse with $60 \mu\text{m}$ water droplets seen 0, 20, 40, and 100 ns after arrival of the high energy pulse. The laser is propagating from right to left.

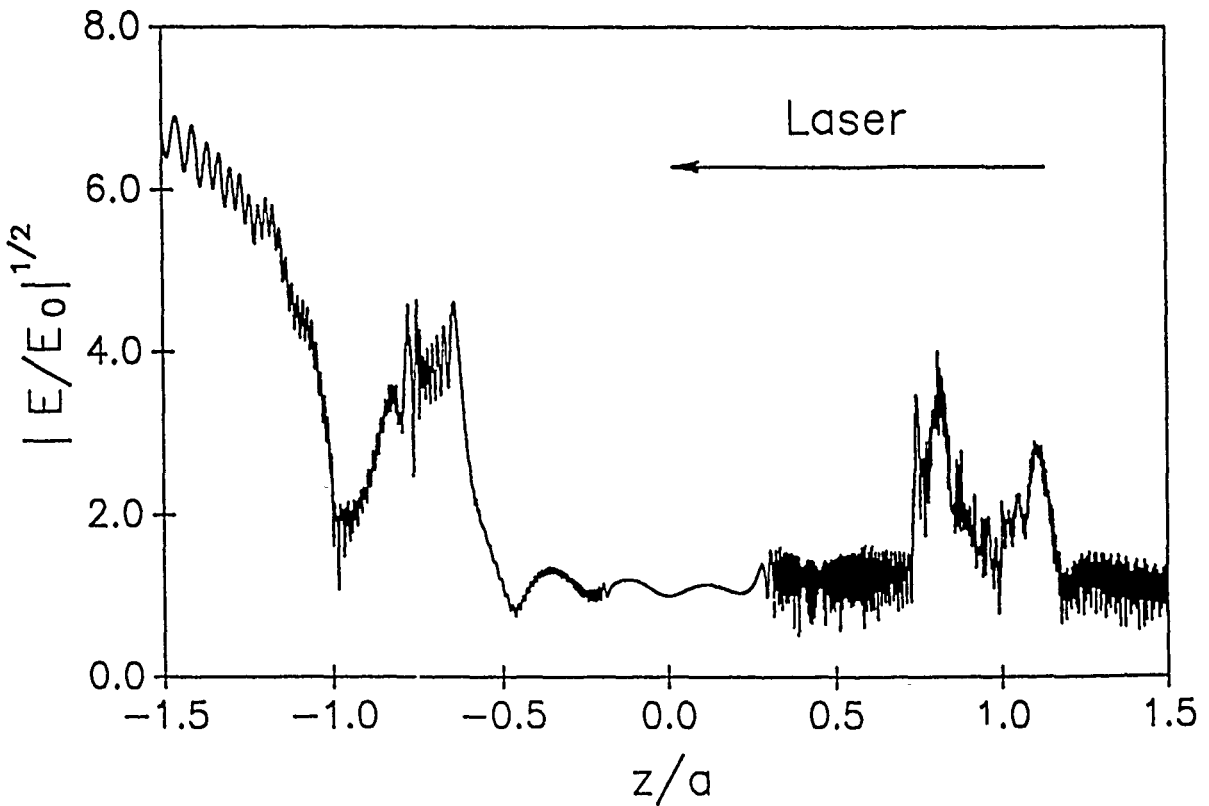
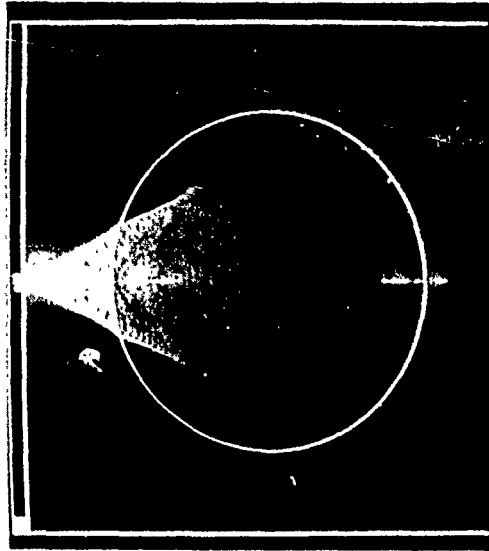


Fig. 6. Plane wave Lorenz-Mie theory calculations showing the square root of the internal and near-surface electric field distribution for a $60\ \mu\text{m}$ diameter water droplet ($\bar{n} = 1.36 + 3.5 \times 10^{-8}i$) irradiated by a KrF laser pulse ($\lambda = 248\ \text{nm}$). Laser is propagating from right to left. Top: Intensity (black = 0, white ≈ 7) plot for $-1.5 < y/a < 1.5$, $-1.5 < z/a < 1.5$ where a is the droplet radius (note the laser is propagating in the $+z$ direction with polarization in the x direction). Bottom: Centerline plot for the same parameters as given above.

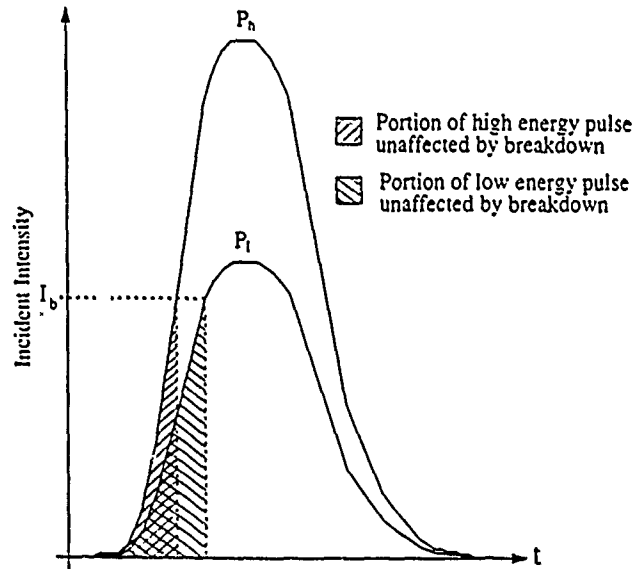


Fig. 7. Graphical representation of the relationship between the incident pulse energy and the portion unaffected by the laser-induced breakdown in the shadow hemisphere.

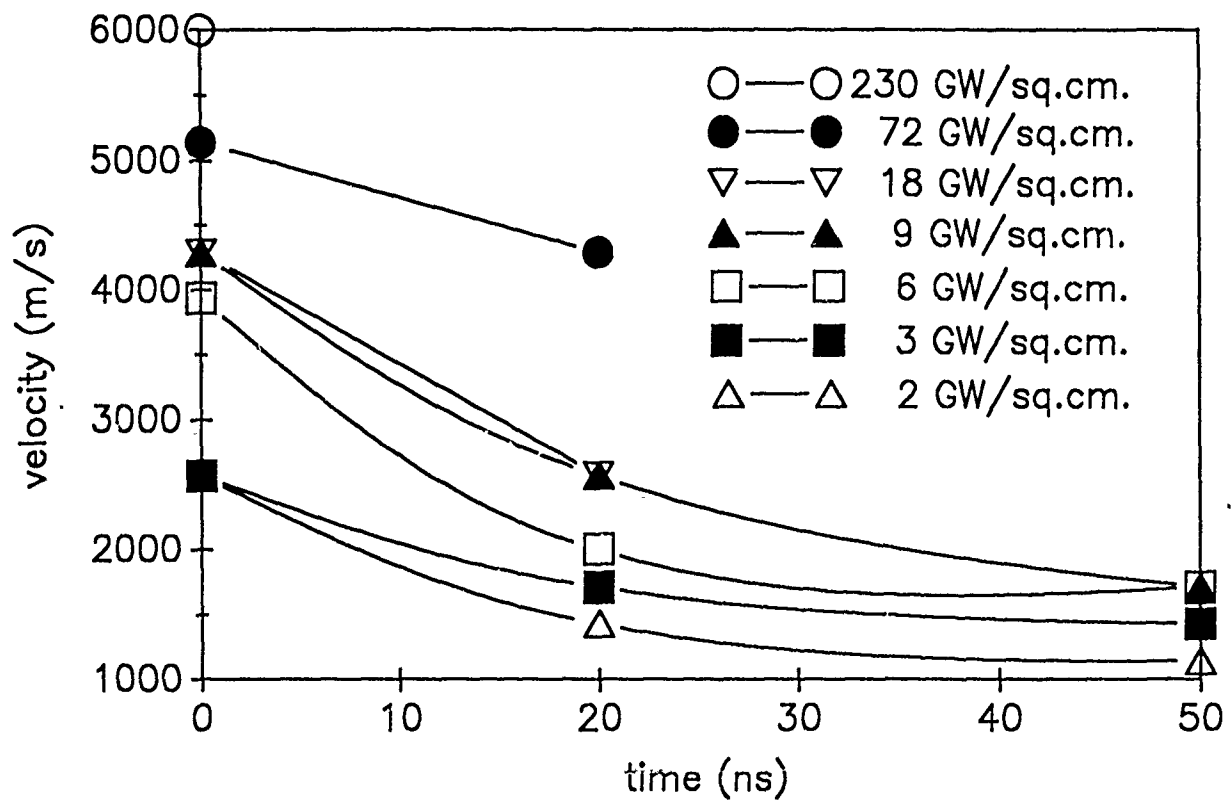


Fig. 8. Average material velocity as a function of image delay time for the interaction of KrF laser pulses ($\lambda = 248$ nm) with $60 \mu\text{m}$ diameter water droplets for laser irradiance varying from 3 to 230 GW/cm^2 .

Nonlinear Laser - Droplet Interactions: Stimulated Raman Scattering

A. Biswas, H. Latifi, R. L. Armstrong
Physics Department, New Mexico State University
Las Cruces, NM 88003

R. G. Pinnick
Atmospheric Sciences Laboratory, White Sands Missile Range,
White Sands, NM 88002

RECENT PUBLICATIONS:

1) A. Biswas, H. Latifi, R. L. Armstrong, and R. G. Pinnick, "Double Resonance Stimulated Raman Scattering from Optically Levitated Glycerol Droplets", Phys Rev. A (In Press).

ABSTRACT

Stimulated Raman scattering (SRS) from an optically levitated glycerol droplet supported simultaneously by resonances at the incident (input) laser wavelength and at the emitted (output) SRS wavelength is reported. The technique used enables identification of the structure resonance mode orders which contribute to the electromagnetic field enhancement of the incident laser energy which in turn causes the SRS threshold to be overcome. The output (SRS) resonance mode orders were also identified in several cases and these observations indicate a correspondence between input and output resonance mode order. Energy thresholds for obtaining SRS under the conditions stated above are reported and compared to other SRS measurements where the input resonance condition does not exist. Future investigations attempting to correlate the mode order of the contributing input/output resonance with observed SRS delays are envisaged.

1. INTRODUCTION

Previous measurements of SRS¹⁻⁸ have been made for droplets satisfying a resonance condition only at the emitted radiation (output) wavelength, since with the lasers and droplet generation methods used, there was no practical way to tune the incident laser wavelength or droplet size to an input resonance condition. In this paper we report conditions wherein the considered droplet is in resonance at both incident (input) and emitted (output) wavelengths - this is also referred to as the double resonance condition. Double resonance emissions have been postulated in fluorescence and Raman spectra,^{9,10} and have been observed in fluorescence emission spectra of fibers¹¹ and fluorescence excitation spectra of droplets.¹²

2. EXPERIMENTAL ARRANGEMENT

Figure 1 shows a schematic view of the experimental arrangement. Glycerol droplets trapped^{13,14} in a focused Argon ion laser beam (not shown) slowly evaporate at a rate of 0.4 nm/sec, allowing droplets to pass through resonance conditions with respect to the incident Nd:YAG laser wavelength. A position sensing, split photodiode feedback detector¹⁵ and a Pockel's cell (not shown in Fig. 1) coupled to the Argon laser output permit continuous recorded adjustment of laser power¹⁶ needed to keep the droplet stationary. In addition, scattered Argon laser light is recorded using a photodiode. Monitoring of levitating laser power^{16,17} and elastic scattering¹⁸ from the droplet permit determination of the droplet size to within an accuracy of 0.1% of its radius. The spectral content of the emitted SRS emission was measured by imaging the droplet onto a spectrometer equipped with a one-dimensional photo-diode array detector.

The levitated droplet is viewed through a microscope while irradiating it with Nd:YAG laser pulses. Quasi-periodic bursts of SRS which appear as bright full or partial red rings on the droplet rim occur only when the continuously evaporating droplet radius satisfies an input resonance condition.

3. RESULTS

Figures 2a and 2c show chart recorder traces¹⁹ for a typical evaporating droplet, Fig. 2a shows the monitored laser power and 2c the scattered Argon laser light from the droplet. Fig. 2b is the computed radiation pressure¹⁷ (Q_{pr}) where TE_n^l/TM_n^l designate a transverse electric/magnetic resonance with mode number n and mode order l . Figure 2d is the computed²⁰ scattered intensity appropriately averaged over angle and polarization to account for the finite acceptance angle of the detector and its orientation. Comparison of Figures 2a and 2c with 2b and 2d enable unique determination of droplet size shown on the abscissa. The vertical arrows along the abscissa correspond to radii at which bursts of SRS were observed to occur. Figure 2e shows the

computed Q_{pr} for the same drop sizes but at the incident Nd:YAG laser wavelength, and here it appears that the occurrence of SRS corresponds to fourth order input resonances.

Further details of analysis of several different size ranges of glycerol droplets are reported elsewhere.¹⁹ Table I shows a summary of some of the simultaneously identified input and output resonances. Here it is apparent that in most cases the mode order of the input and output resonances coincide. This observation suggests that the localized spatial region near the droplet rim where the input laser wavelength electromagnetic field undergoes enhancement is the same region from which the nonlinear inelastic scattering emission originates. In Table I the bare Q 's (zero imaginary refractive index) corresponding to the input and output resonances are also included.

Under the double resonance conditions reported here a lowering of SRS threshold from values observed in the absence of an input resonance is expected. However, checking the validity of this assertion poses an experimental problem since the size and material (5-7 μm radius glycerol droplets) investigated using optical levitation is not compatible with the droplet generator, where the condition of output resonance only can be attained. In spite of this incompatibility some comparisons were attempted using 12-16 μm radius glycerol/water mixture drops in the droplet generator (no input resonance, only output resonance) with 5-7 μm radius pure glycerol droplets optically levitated (input and output resonance). Table II summarizes the results from such comparisons, they suggest a definite lowering of the measured threshold energy required to obtain SRS but the difference in the droplet size and material poses uncertainties in the interpretations of these results.

4. CONCLUSIONS

In conclusion this report confirms experimentally the occurrence of double resonance assisted SRS and enables identification of the particular input resonances which contribute to the enhanced fields required to overcome SRS thresholds. As expected the energy thresholds appear to be lower, however, an exact comparison was not possible. Future work to investigate any correlation or the lack thereof between the identified contributing mode orders and the observed SRS delays will be attempted.

ACKNOWLEDGEMENTS

Biswas, Latifi and Armstrong were partially supported by U. S. Army Research Office Contract No. DAAL-03-87-K-0144.

REFERENCES

1. J. B. Snow, S. X. Qian and R. K. Chang, *Opt. Lett.* 10, 37, (1985).
2. S. X. Qian and R. K. Chang, *Phys. Rev. Lett.*, 56, 926, (1986).
3. R. G. Pinnick, A. Biswas, P. Chylek, R. L. Armstrong, H. Latifi, E. Creegan, V. Srivastava, M. Jarzembki, and G. Fernandez, *Opt. Lett.*, 13, 494, (1988).
4. J. Zhang, D. H. Leach and R. K. Chang, *Opt. Lett.* 13, 270, (1988).
5. W. F. Hsieh, J. Zheng, and R. K. Chang, *Opt. Lett.* 13, 497, (1988).
6. P. Chylek, A. Biswas, M. A. Jarzembki, V. Srivastava, and R. G. Pinnick, *Appl. Phys. Lett.*, 52, 1642, (1988).
7. R. G. Pinnick, P. Chylek, M. Jarzembki, E. Creegan, V. Srivastava, G. Fernandez, J. D. Pendleton and A. Biswas, *Applied Optics*, 27, 987, (1988).
8. R. G. Pinnick, A. Biswas, R. L. Armstrong, H. Latifi, E. Creegan, V. Srivastava, and G. Fernandez, *Opt. Lett.* 13, 1099, (1988).
9. R. K. Chang, S. X. Qian, and J. Eichmans, *Proceedings of the Methods of Laser Spectroscopy*, Edited by Y. Prior, A. Ben-Reuven, and M. Rosenbluh, p. 249, Plenum Press, NY, 1986.
10. H. Chew and D. S. Wang, *Phys. Rev. Lett.*, 49, 490, (1982).
11. J. F. Owen, P. W. Barber, P. B. Dorain and R. K. Chang, *Phys. Rev. Lett.* 47, 1075, (1981).
12. L. M. Folan, and S. Arnold, *Opt. Lett.* 13, 1, (1988).
13. A. Ashkin, and J. M. Dziedzic, *Phys. Rev. Lett.* 24, 156, (1970).
14. A. Ashkin and J. M. Dziedzic, *Science*, 187, 1073, (1975).
15. A. Ashkin and J. M. Dziedzic, *Appl. Phys. Lett.* 30, 202, (1977).
16. A. Ashkin and J. M. Dziedzic, *Phys. Rev. Lett.* 38, 1351, (1977).
17. P. Chylek, J. T. Kiehl and H. W. Ko. *Physical Review A*, 18, 2229, (1978).
19. A. Biswas, H. Latifi, R. L. Armstrong, R. G. Pinnick, *Phys Review A*, (In Press).

Table I

Identification of input and output resonances for double resonance SRS

Observed Radius (μm)	Input Resonance	% Error	Q_0	SRS Wavelength (μm)	Output Resonance	% Error	Q_0
5.5131	TE ₇₇ ³	0.1	3.3E06	0.6284	TM ₆₃ ³	0.08	4.6E04
5.6038	TM ₇₈ ³	0.03	2.5E06	0.6306	TM ₆₄ ³	0.09	6.0E04
5.9190	TM ₈₃ ³	0.07	1.1E07	0.6285	TE ₆₉ ³	0.02	3.7E05
	TE ₇₉ ⁴	0.09	1.3E05	0.6288	-	-	-
6.1067	TE ₈₂ ⁴	0.07	2.7E05	0.6302	TE ₆₇ ⁴	0.02	9.8E03
6.2335	TE ₈₄ ⁴	0.09	4.3E05	0.6282	TE ₆₉ ⁴	0.09	1.5E04
6.2532	TE ₈₉ ³	0.09	3.3E06	0.6284	TM ₇₃ ³	0.08	4.6E04
	TM ₈₄ ⁴	0.10	2.6E05	0.6303	TE ₆₉ ⁴	0.10	1.5E04
6.8281	TM ₉₃ ⁴	0.08	2.5E06	0.6319	TM ₇₆ ⁴	0.20	3.7E04
6.8890	TM ₉₄ ⁴	0.06	3.3E06	0.6285	TM ₇₇ ⁴	0.14	4.6E04
7.1957	TM ₉₉ ⁴	0.00	1.2E07	0.6309	TM ₈₁ ⁴	0.07	1.2E05
	TE ₉₅ ⁵	0.08	2.2E05	0.6294	TM ₇₇ ⁵	0.14	3.3E03
7.2771	TM ₉₆ ⁵	0.09	1.6E05	0.6340	TE ₇₈ ⁵	0.11	7.3E03
7.2917	TE ₁₀₁ ⁴	0.10	3.4E07	0.6312	TM ₈₂ ⁴	0.18	1.5E05

Table II

Measured Energy Thresholds for Optically Levitated Droplets under Double Resonance Conditions Compared With Droplet Generator Droplets Excited Under Output Resonance Condition Only.

	Drop Radius (um)	Material	Normalized* SRS Threshold	Normalized* Drop Break
LEVITATED DROP (DOUBLE RESONANCE)	5-7	Pure Glycerol	0.00042	0.0012
DROP GENERATOR (OUTPUT RESONANCE ONLY)	12-16	Glycerol/ Water mix (65:35)	0.0012	0.005

* Normalized means values are reported as a fraction of irradiance required for obtaining air breakdown in the laboratory which is nominally 300 GW/cm².

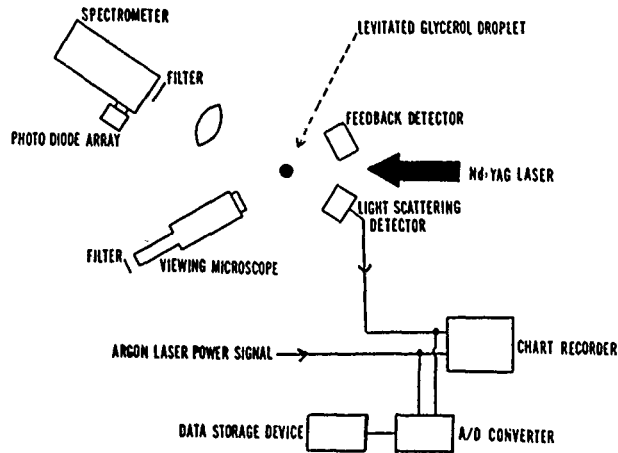


Figure 1. Schematic top view of experimental arrangement. The levitating Argon laser beam directed normally outward from the plane of the paper and the six sided glass cell enclosing the droplet are not shown.

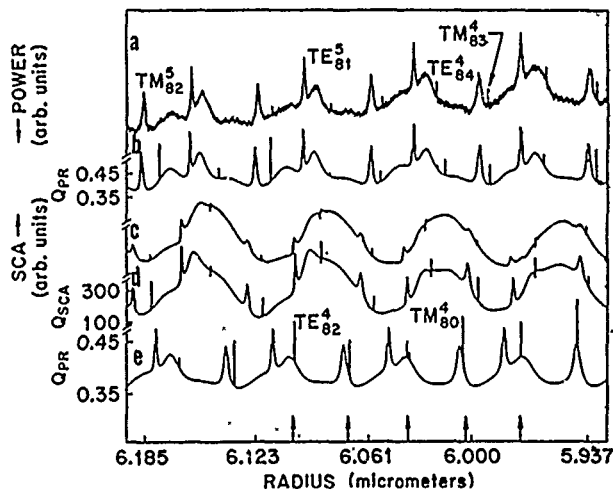


Figure 2 (a) Measured Argon laser power (radiation pressure) (c) measured scattered Argon laser light (SCA). (b) (d) calculated radiation pressure (Q_{pr}) and scattered intensities (Q_{sca}) at the Argon laser wavelength (514.5 nm). (e) calculated Q_{pr} for the Nd:YAG laser wavelength (532.0 nm). Vertical arrows show the radii at which double resonance SRS is observed.

BLANK

IV. OPTICAL PROPERTIES OF AEROSOLS

A FINITE ELEMENT APPROACH TO ABSORPTION AND SCATTERING OF ELECTROMAGNETIC RADIATION BY PARTICLES

L. Liebman and J. Brock
Chemical Engineering Department
University of Texas, Austin, Texas 78712

RECENT PUBLICATIONS, SUBMITTALS FOR PUBLICATION AND PRESENTATIONS

1. J. Carls and J. Brock, "Propagation of laser breakdown and detonation waves in transparent droplets", *Optics Letters* 13 273 (1988).
2. J. Brock, D. Zehavi, and P. Kuhn, "Binary aerosol formation in a laminar coaxial jet", *J. Aerosol Sci.* 4 462 (1988).
3. J. Carls and J. Brock, "Explosive vaporization of single droplets by lasers: comparison of models with experiments" *Optics Letters* 13 919 (1988)
4. J. Carls, G. Moncivais and J. Brock, "Time resolved Raman spectroscopy from optically levitated reacting droplets", *Proceedings of the 1988 CRDEC Scientific Conference on Obscuration and Aerosol Research*, CRDEC, U. S. Army, 1989
5. J. Carls, G. Moncivais and J. Brock, "Time resolved Raman spectroscopy from reacting, optically levitated microdroplets", Submitted for publication.
6. B. Jurcik and J. Brock, "Particle formation in shocked flows", *Proceedings of the 1988 CRDEC Scientific Conference on Obscuration and Aerosol Research*, CRDEC, U. S. Army, 1989
7. J. Carls and J. Brock, "High energy laser-particle interactions", *Proceedings of the 1988 CRDEC Scientific Conference on Obscuration and Aerosol Research*, CRDEC, U. S. Army, 1989
8. Y. Chen, J. Brock, and I. Trachtenberg, "Aerosol jet etching", *Aerosol Sci. Tech.*, In Press 1989
9. B. Jurcik and J. Brock, "A study of low pressure impaction processes", *J. Aerosol Science* 20, 560, 1989.
10. J. Carls, Y. Seo and J. Brock, "Laser-induced breakout and detonation waves in droplets: II. Model", Submitted for publication, 1989.
11. Y. Seo and J. Brock, "Distributions for moment simulation of aerosol evaporation", Submitted for publication, 1989.
12. B. Jurcik and J. Brock, "The theory of sonic impactors", Submitted for publication, 1989
13. J. Carls and J. Brock, "The effect of laser pulse frequency and amplitude modulation on energy absorption in ionized shocks", Submitted for publication, 1989.
14. J. Brock, "Aerosol dynamics", Chemical Engineering Seminar, Tokyo Institute of Technology, November 1988.
15. J. Brock, "Aerosol filtration", Chemical Engineering Seminar, Tokyo Institute of Technology, November, 1988.
16. J. Brock, "Advances in aerosol technology", Japan Chemical Engineering Society Lecture, Tokyo, December 1988.
17. J. Brock, "Laser-particle interactions", Invited Lecture, Institute of Chemistry and Physics (RIKEN), Wako, Japan, November 1988.
18. J. Brock, "Aerosol jet etching", Chemical Engineering Seminar, Kanazawa University, Kanazawa, Japan, November 1988.
19. J. Brock, "Aerosols and the environment", U.N.E.S.C.O. Lecture, Tokyo, Japan, December 1988.
20. L. Liebman and J. Brock, "A finite element approach to laser-droplet interactions", 1989 CRDEC Scientific Conference on Obscuration and Aerosol Research, Aberdeen Proving Ground (Edgewood), Maryland, June 1989.
21. B. Jurcik and J. Brock, "Aerosol plumes: dispersion and characterization", 1989 CRDEC Scientific Conference on Obscuration and Aerosol Research, Aberdeen Proving Ground (Edgewood), Maryland, June 1989.
22. J. Carls and J. Brock, "Studies in nonlinear response of microparticles to laser radiation", 1989 CRDEC Scientific Conference on Obscuration and Aerosol Research, Aberdeen Proving Ground (Edgewood), Maryland, June 1989.
23. J. Carls and J. Brock (presented by M. Sitarski), "The response of single microparticles to high energy laser radiation", 20th Annual Meeting of the Fine Particle Society, Boston, Mass., August 1989.

ABSTRACT

The problem of scattering and absorption of electromagnetic radiation by particles can be solved analytically for only the simplest cases, but numerical methods allow a straightforward extension to particles with arbitrary inhomogeneities and arbitrary shapes. In this paper a recently developed method involving CFD techniques is reviewed and applied to the problem of a dielectric sphere. Numerical results for the internal region are shown for the first time and a discussion on the effects of mesh refinement is presented. Qualitative arguments indicating the promise of finite element methods are given as well.

INTRODUCTION

Mie theory exactly describes the absorption and scattering of a plane electromagnetic wave by a dielectric sphere of arbitrary size and refractive index (van de Hulst, 1957; Kerker, 1969). This conceptually simple analytical solution is well known, but it involves cumbersome computations. Since the advent of high-speed computers, which utilize parallel and vector processing, much effort has been made to improve the analytical scattering algorithms (Wiscombe, 1979 and 1980). However, while it is relatively simple to generate data for the spherical problem, the analytical calculations can not be easily and straightforwardly extended to nonspherical particles. If a numerical rather than the analytical approach is taken, the extension to particles with arbitrary inhomogeneities and arbitrary shapes is more apparent since the general governing equations and the solution technique remain unchanged.

Previously a finite difference method was applied to the problem of a linearly polarized plane electromagnetic wave scattered by a perfectly conducting sphere (Ling, 1988). The results demonstrated the applicability of computational fluid dynamics (CFD) methods to the basic scattering problem. CFD methods offer geometrical flexibility, allowing generalization to more complex shapes and inhomogeneous particles. In this presentation, the investigation is broadened by using a finite element method to model scattering by a dielectric sphere. Preliminary results confirm that CFD methods are a promising technique.

THEORY

The problem to be solved consists of a plane polarized wave incident on a dielectric sphere; only linear scattering is considered. Assuming $\exp(i\omega t)$ dependence for all fields, the electric and magnetic fields must satisfy the vector wave equation both inside and outside the sphere:

$$\nabla^2 \mathbf{E} + k^2 \mathbf{E} = 0 \qquad \nabla^2 \mathbf{H} + k^2 \mathbf{H} = 0 \qquad (1,2)$$

where $k^2 = \omega^2 \epsilon \mu$. Additionally, the boundary conditions:

$$(\mathbf{E}_{\text{out}} - \mathbf{E}_{\text{in}}) \times \hat{\mathbf{r}} = 0 \qquad (\mathbf{H}_{\text{out}} - \mathbf{H}_{\text{in}}) \times \hat{\mathbf{r}} = 0 \qquad (3,4)$$

require that the tangential components of \mathbf{E} and \mathbf{H} must be continuous across the surface of the sphere (Bohren and Huffman, 1983) and the Sommerfeld radiation condition (Stratton, 1941) requires that the scattered fields represent divergent traveling waves as $r \rightarrow \infty$.

By introducing two auxiliary scalar functions, the electric and magnetic Debye potentials, ${}^e\Pi$ and ${}^m\Pi$ (Kerker, 1969; Born and Wolf, 1959), it is possible to reduce the vector equations (1) and (2) to a set of uncoupled scalar wave equations:

$$\nabla^2 {}^e\Pi + k^2 {}^e\Pi = 0 \qquad \nabla^2 {}^m\Pi + k^2 {}^m\Pi = 0. \qquad (5,6)$$

The field quantities then can be deduced from the potentials as follows:

$$\mathbf{E} = \nabla \times [\nabla (r {}^e\Pi) \times \hat{\mathbf{r}}] + i\omega\mu \nabla \times (r {}^m\Pi) \qquad (7)$$

$$\mathbf{H} = \nabla \times [\nabla (r {}^m\Pi) \times \hat{\mathbf{r}}] + i\omega\epsilon \nabla \times (r {}^e\Pi). \qquad (8)$$

Since the field variables are oscillatory in nature over the infinite domain it is advantageous to reformulate the problem once again, this time in terms of a generalized amplitude function which eliminates the oscillations due to the incident field (Ling, 1987). By making use of the superposition property of the fields, the Debye potentials outside the particle can be decomposed into incident and scattered components. The scattered components then are written as:

$${}^o\Pi_s = \frac{\cos \phi \sin \theta}{k^2} f_1(r, \theta) \frac{e^{ikr}}{r} \quad (9)$$

$${}^m\Pi_s = \sqrt{\frac{\epsilon}{\mu}} \frac{\sin \phi \sin \theta}{k^2} f_2(r, \theta) \frac{e^{ikr}}{r} \quad (10)$$

where $f(r, \theta)$ is a Debye amplitude function. Similar expressions can be written for the potentials inside the particle. By substituting equation (9) into (5) and equation (10) into (6) it can be shown that the problem to be solved becomes:

$$\frac{e^{ikr}}{k^2} \left[\frac{\partial^2 f_1}{\partial r^2} + 2ik \frac{\partial f_1}{\partial r} + \frac{3}{r^2} \cot \theta \frac{\partial f_1}{\partial \theta} + \frac{1}{r^2} \frac{\partial^2 f_1}{\partial \theta^2} - \frac{2}{r^2} f_1 \right] = 0 \quad (11)$$

$$\sqrt{\frac{\epsilon}{\mu}} \frac{e^{ikr}}{k^2} \left[\frac{\partial^2 f_2}{\partial r^2} + 2ik \frac{\partial f_2}{\partial r} + \frac{3}{r^2} \cot \theta \frac{\partial f_2}{\partial \theta} + \frac{1}{r^2} \frac{\partial^2 f_2}{\partial \theta^2} - \frac{2}{r^2} f_2 \right] = 0 \quad (12)$$

The boundary conditions (3) and (4) are, in terms of f_1 and f_2 :

$$\frac{\omega^{II} \epsilon^{II} e^{ik^{II}a}}{(k^{II})^2} f_1^{II}(a, \theta) - \frac{\omega^I \epsilon^I e^{ik^I a}}{(k^I)^2} f_1^I(a, \theta) = \frac{\omega^I \epsilon^I}{(k^I)^2 \sin \theta} W(a, \theta) \quad (13)$$

$$\frac{e^{ik^{II}a}}{k^{II}} f_2^{II}(a, \theta) - \frac{e^{ik^I a}}{k^I} f_2^I(a, \theta) = \frac{1}{k^I \sin \theta} W(a, \theta) \quad (14)$$

$$\frac{e^{ik^{II}a}}{(k^{II})^2} \left[ik^{II} f_1^{II} + \frac{\partial f_1^{II}}{\partial r} \right]_{r=a} - \frac{e^{ik^I a}}{(k^I)^2} \left[ik^I f_1^I + \frac{\partial f_1^I}{\partial r} \right]_{r=a} = \frac{1}{(k^I)^2 \sin \theta} \frac{\partial W}{\partial r} \Big|_{r=a} \quad (15)$$

$$\sqrt{\frac{\epsilon^{II}}{\mu^{II}}} \frac{e^{ik^{II}a}}{(k^{II})^2} \left[ik^{II} f_2^{II} + \frac{\partial f_2^{II}}{\partial r} \right]_{r=a} - \sqrt{\frac{\epsilon^I}{\mu^I}} \frac{e^{ik^I a}}{(k^I)^2} \left[ik^I f_2^I + \frac{\partial f_2^I}{\partial r} \right]_{r=a} = \sqrt{\frac{\epsilon^I}{\mu^I}} \frac{\partial W}{\partial r} \Big|_{r=a} \quad (16)$$

where:

$$W(r, \theta) = \frac{e^{ikr \cos \theta}}{\sin \theta} - \cot \left(\frac{\theta}{2} \right) \frac{e^{ikr}}{2} - \tan \left(\frac{\theta}{2} \right) \frac{e^{-ikr}}{2} \quad (17)$$

and the radiation condition can be expressed as:

$$\lim_{r \rightarrow \infty} \frac{\partial f_1}{\partial r} = 0 \qquad \lim_{r \rightarrow \infty} \frac{\partial f_2}{\partial r} = 0. \qquad (18)$$

In equations (13) through (16), "a" is the radius of the sphere, "I" denotes quantities outside the sphere, and "II" denotes quantities inside the sphere.

FINITE ELEMENT METHOD AND RESULTS

The system of equations is solved numerically on a Cray X-MP by a finite element method with 9-node Lagrange quadrilaterals (Becker, et al., 1981) that utilizes a frontal solver to invert the matrix (Irons and Ahmad, 1980). A multiplier method (Carey and Oden, 1984) is used to enforce the jump in solution across the particle boundary, which must coincide with element boundaries. The radiation boundary condition is imposed at a finite artificial surface, $r < \infty$, using an operator to annihilate the first two terms of the analytical solution (Bayliss, et al., 1982).

Results are presented for an example case in which a water droplet with a 20 μm radius is irradiated by a plane wave having $\lambda = 10.591 \mu\text{m}$. The refractive index of the particle is $1.179 + 0.071i$ and the size parameter is 11.9. In Fig. 1 node-to-node oscillations occur due to the absence of adequate elements near the sphere's surface, where large gradients exist in the amplitude function. Figs. 2 and 3 demonstrate the effects of decreasing ΔR , the internodal distance: the nodal oscillations disappear and the solution converges at a cost of increasing computation time. Adequate results occur with $\Delta R = 1.0 \mu\text{m}$, which requires less than two minutes of CPU time. Figs. 1-3 illustrate the convergence to the correct solution.

On a qualitative basis the findings compare favorably with those obtained by Ling (1988) for the perfect conductor. The amplitude functions exhibit a strong interaction region near the particle and are asymptotic in the far-field region, levelling off near 500 μm . Unlike the perfectly conducting sphere, however, the generalized Debye amplitude functions of a dielectric material are oscillatory. The numerical method appears to be capturing these oscillations successfully.

Further studies into the effects of mesh refinement in the theta direction and comparisons to analytical results are ongoing. Since current computation times are low and additional time saving techniques have not yet been implemented, additional refinements are not prohibited and extensions to particles with arbitrary inhomogeneities and arbitrary shapes are possible.

ACKNOWLEDGMENTS

This work was supported by CRDEC. U.S. Army. We wish to thank Drs. R. Ling, M. Lax, I Sindoni and E. Stuebing for helpful discussions on this problem.

REFERENCES

- Bayliss, A., M. Gunzburger, and E. Turkel, 1982. *SIAM J. Appl. Math.*, 42, 430.
- Becker, E. B., G. F. Carey, and J. T. Oden, 1981. *Finite Elements: An Introduction (Vol. I)*, Prentice-Hall, Englewood Cliffs, New Jersey.
- Bohren, C. F., and D. R. Huffman, 1983. *Absorption and Scattering of Light by Small Particles*, Wiley, New York.
- Born, M., and E. Wolf, 1959. *Principles of Optics*, Pergamon, London.
- Carey, G. F., and J. T. Oden, 1984. *Finite Elements: Computational Aspects (Vol. II)*, Prentice-Hall, Englewood Cliffs, New Jersey.
- Irons, B., and S. Ahmad, 1980. *Techniques of Finite Elements*, Ellis Horwood, Chichester.
- Kerker, M., 1969. *The Scattering of Light and Other Electromagnetic Radiation*, Academic, New York.
- Ling, R. T., 1987. *AIAA J.*, 25, 560.
- Ling, R. T., 1988. *J. Appl. Phys.*, 64, 3785.
- Stratton, J. A., 1941. *Electromagnetic Theory*, McGraw-Hill, New York.
- van de Hulst, H. C., 1957. *Light Scattering by Small Particles*, Wiley, New York.
- Wiscombe, W. J., 1979. National Center for Atmospheric Research Tech. Note, NCAR TN-140+STR.
- Wiscombe, W. J., 1980. *Appl. Opt.*, 19, 1505.

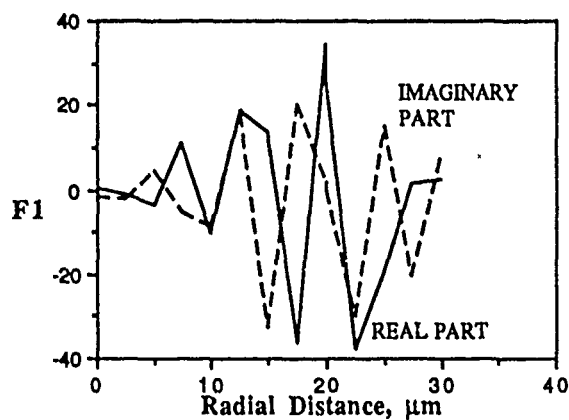


Figure 1. Debye amplitude function for the internal and near-external regions: f_1 at $\theta = \pi$. Particle radius = $20 \mu\text{m}$, $\Delta R = 2.5 \mu\text{m}$ and CPU = 15 sec.

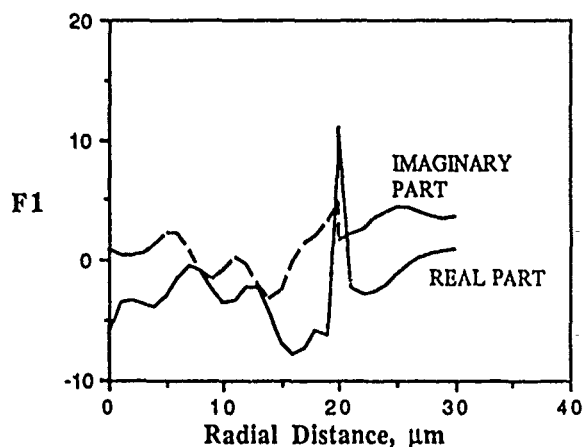


Figure 2. Debye amplitude function for the internal and near-external regions: f_1 at $\theta = \pi$. Particle radius = $20 \mu\text{m}$, $\Delta R = 1.0 \mu\text{m}$ and CPU = 100 sec.

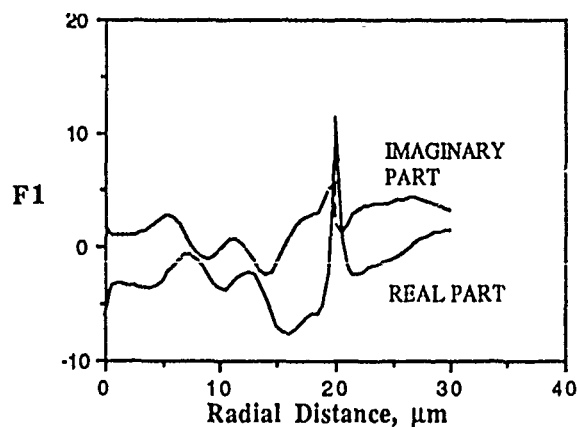


Figure 3. Debye amplitude function for the internal and near-external regions: f_1 at $\theta = \pi$. Particle radius = $20 \mu\text{m}$, $\Delta R = 0.5 \mu\text{m}$ and CPU = 360 sec.

BLANK

Absorption Measurements Using an Integrating Cavity

R. M. Pope, E. S. Fry, and R. L. Montgomery
Department of Physics, Texas A&M University
College Station, Texas 77843

Recent Publications and Submittals for Publication:

All publications are listed with the paper, "Scattering of Femtosecond Laser Pulses", by W. E. White, C. Wang, and E. S. Fry in these Proceedings.

ABSTRACT

The Integrating Cavity Absorption Meter (ICAM) provides an instrument capable of measuring optical absorption independent of scattering effects. The measurement of optical absorption has always been complicated by scattering effects. The most common and perhaps simplest method of measuring absorption is based on transmission of light through the sample. Scatterers produce systematic errors which prevent simple transmission type absorption measurements. The ICAM was developed as a method for measuring absorption independent of scattering effects. The ICAM is, in principal, rigorously independent of scattering effects. We develop the theory of the device, describe the instrumentation we are using and provide some initial results for measurement of absorption in the presence of varying concentrations of scatterers. This is the first report on the ICAM presented to this conference. Future research will involve extension of the capabilities of this device to the measurement of absorption spectra for aerosols and smokes.

CONCEPT

The ICAM uses a system of integrating cavities to produce isotropic illumination of the sample^{1,2}. To understand why the ICAM is independent of scattering, let us first consider the basic principle of a single integrating cavity.

The inside surface of a typical integrating cavity has a high diffuse reflectance (Lambertian). A beam of radiation introduced into the cavity and incident upon this Lambertian surface is diffusely reflected into all directions. After numerous reflections, the interior of the cavity is filled with a very uniform, isotropic radiance distribution. The radiance level is directly proportional to the total optical power introduced into the cavity. Any object placed inside the cavity will be uniformly illuminated from all directions. If nonabsorbing scatterers are placed in the cavity, the net irradiance incident on the wall of the cavity will remain unchanged. The cavity will contain the same amount of energy both before and after the addition of the scatterers; there is no loss of radiant energy due to scattering. Even if particles in the sample scatter radiation through some preferred angle, the Lambertian surface of the cavity will uniformly distribute the radiation so that the irradiance striking the wall of the cavity will be uniform. If the scatterers in the cavity have some characteristic absorption, the irradiance incident on the wall of the cavity will vary inversely with this absorption. By measuring this irradiance we can determine the absorption independent of scattering within the cavity.

In designing a system to produce isotropic illumination in an integrating cavity we want to avoid any bright spot at the point where light is introduced into the cavity and we want to avoid placing any object in the direct path of this input beam. We achieve this by using a system of integrating cavities and by careful selection of materials for construction of these cavities. Our system of integrating cavities consists of one cavity **A** completely contained within another **B** as shown in Figure 1.

The cells **A'** and **B'** which constitute the walls of these cavities are made of Spectralon™, a material with very high diffuse reflectivity throughout the visible and which is easily machineable. Cavity **B** is an air space. We place our sample in cavity **A**. When light enters cavity **B** it will bounce between the two cell walls filling cavity **B** with isotropic radiation. Irradiance incident on the wall of cell **B'** from within **B** is designated \bar{F}_2 .

The Spectralon wall, **A'**, allows some portion of the incident radiation to pass through it and into cavity **A**. The portion of incident radiation which passes through it is proportional to $(1-\rho)$, where ρ is the reflectivity of the wall. At each reflection, only a very small percentage of the incident

light enters cavity **A**, but the radiation bounces around many times in cavity **B** and effectively "tries" many times so that the radiance in **A** builds up to an appreciable value. Since the wall **A'** is surrounded by a uniform radiance, light enters cell **A** and the sample from every direction thus avoiding any bright spot from a beam entering the cavity.

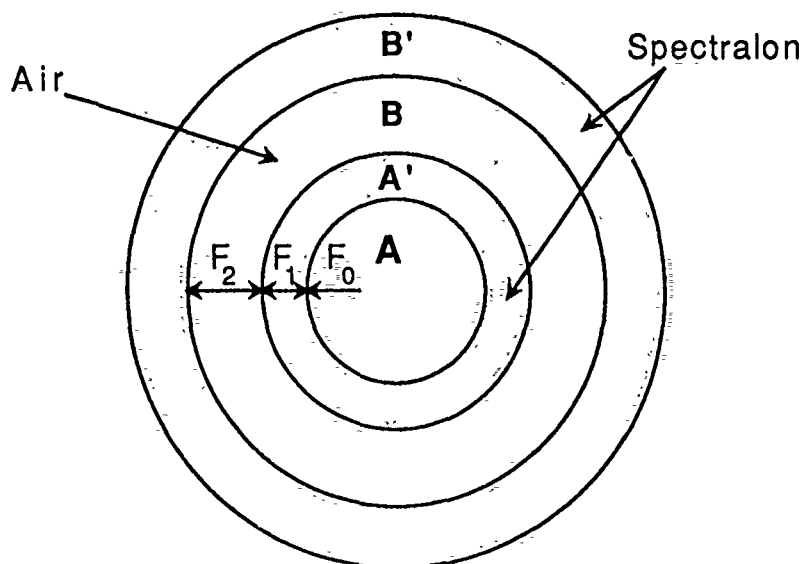


Figure 1. Cross-section of the Integrating Cavity System. Our device has cylindrical symmetry about an axis perpendicular to the figure.

We denote the irradiance on the inner wall of cell **A'** from within **A** as F_0 , and from within **A'** as F_1 . If the Spectralon and the sample are perfectly nonabsorbing the equilibrium condition is $F_2 = F_1 = F_0$. Using conservation of energy at the boundary between cell **A'** and the sample in cavity **A**, it is clear that the energy entering the sample equals the energy leaving the sample plus energy absorbed by the sample²,

	Energy Lost	Energy Lost	
Energy Supplied	Through Wall	Through Detector	Energy Absorbed
$F_1 A_0 (1 - \rho)$	$= F_0 A_0 (1 - \rho)$	$+ F_0 A_D$	$+ 4\alpha F_0 V_0$

(1)

where ρ denotes the reflectivity at the boundary (wavelength dependent), A_0 is the area of the boundary surface of cavity **A**, A_D is the area of the fiber

optic detector for measuring F_0 . V_0 denotes the volume of the sample, and α denotes the absorption coefficient of the sample. Solving this equation for the absorption coefficient gives,

$$\alpha = \frac{1}{4V_0} \left[\frac{F_1}{F_0} A_0 (1-\rho) - \{A_0(1-\rho) + A_D\} \right]. \quad (2)$$

Now the measured signals which are proportional to F_1 and F_0 are designated by S_1 and S_0 , respectively. The ratio F_1/F_0 can then be replaced by S_1/S_0 . If we now also note that for a fixed wavelength and volume, the parameters ρ , A_0 , A_D , and V_0 are all constants, then we can write,

$$\alpha = K_1 \frac{S_1}{S_0} - K_2, \quad (3)$$

or, explicitly showing the dependence on V_0 ,

$$\alpha V_0 = K_3 \frac{S_1}{S_0} - K_4, \quad (4)$$

where, K_1 , K_2 , K_3 , and K_4 are wavelength dependent calibration constants which must be experimentally determined.

One method of determining the K 's is to select a sample with a known absorption and vary the volume of the sample contained within cavity **A**. Using equation (4) the measured ratio's of S_1/S_0 corresponding to various sample volumes are then fitted to a straight line. The slope of the line determines K_3 and the intercept determines K_4 . K_1 and K_2 are then easily determined for any fixed volume. It is also possible to determine the constants K_1 and K_2 directly from equation (3) by using two or more samples of known absorption, and keeping the volume fixed.

APPARATUS

Figure 2 shows a schematic representation of the ICAM system. We use an Oriel model 66005 arc lamp system with a 150 watt Xenon lamp as our light source. A set of thirty-one 10nm bandwidth interference filters (1 filter every 10 nm from 400 to 700nm) determine the wavelength. Our light source is modulated at a reference frequency by an EG&G Princeton

Applied Research Model 197 light chopper. Six plastic optical fibers, 1.0 mm diameter, carry the light to the integrating cavities; three more fibers sample the irradiances F_0 , F_1 , and F_2 . These latter fibers are coupled to Burle 4840 photomultiplier tubes which send current signals to a lock in amplifier referenced to the light chopper frequency. A Keithley 199 digital volt meter converts the analog voltages (S_0 , S_1 , and S_2) from the amplifier into digital signals and sends them via a IEEE-488 bus to a Macintosh II minicomputer. Using LabView software a virtual instrument then displays the value of the absorption coefficient.

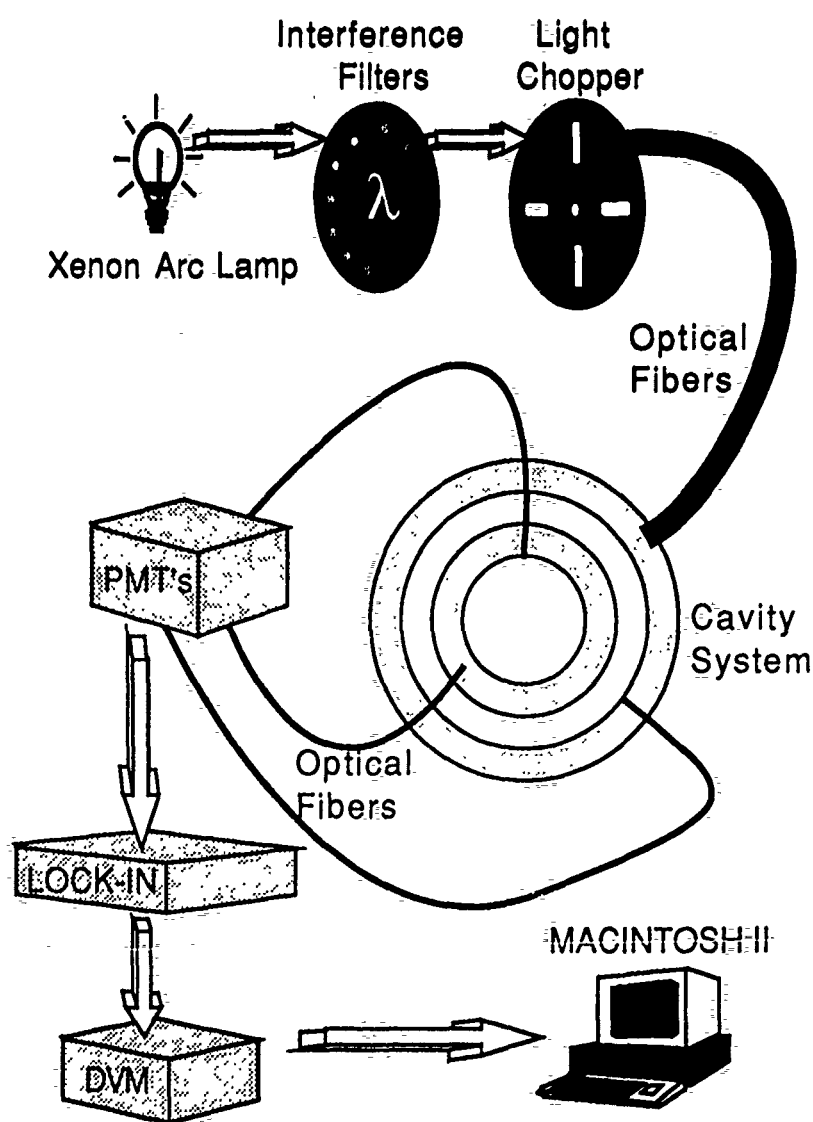


Figure 2. Schematic of the ICAM System

Figures 3 and 4 show cross sections of the ICAM integrating cavities, parallel and transverse to the Z-axis respectively. Both cavities are 15 cm long Spectralon cylinders. Spectralon end caps seal the 2 cavities and hold the inner cell coaxially with respect to the outer cell (figure 3). Six input fibers from the arc lamp pass through the end caps and terminate in the outer cavity. The three fibers entering each end cap are 120 degrees apart on a 6.4 cm diameter circle and those at one end are offset by 60 degrees with respect to those at the other. The inner cavity is lined with a quartz bulb which tapers into quartz capillary tubing at each end. This permits the exchange of samples without opening the cavities and avoids direct contact between the Spectralon and the sample.

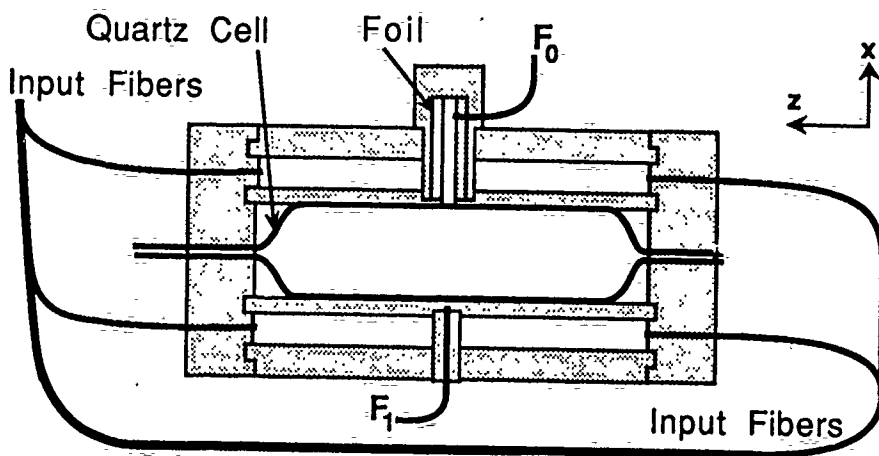


Figure 3. Cavity Cross Section Parallel to the Z-axis.

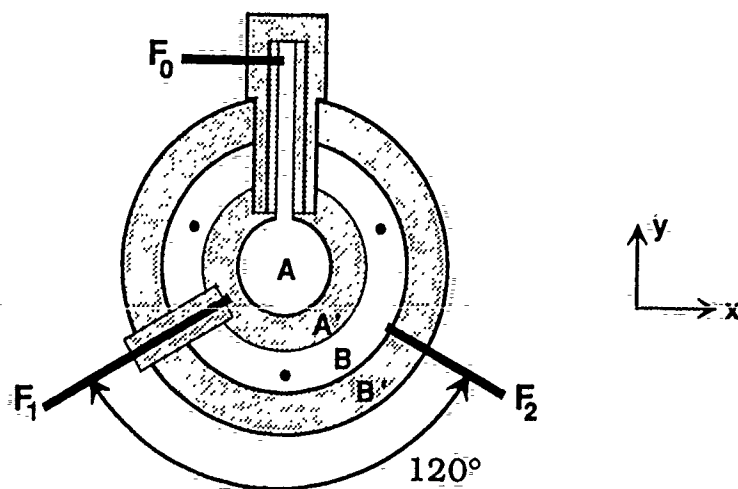


Figure 4. Cavity Cross Section Transverse to the Z-axis.

The optical fibers used to measure F_0 , F_1 , and F_2 are positioned at the midpoint of the cylinder axis and are symmetrically spaced every 120 degrees in the x-y plane (figure 4). The F_2 detector fiber terminates at the outer surface of cavity **B**. The F_1 detector fiber terminates at the midpoint of the inner wall, **A'**. This fiber is isolated from the radiances in cavity **B** and in the wall **B'**, by wrapping the fiber with aluminum foil and then inserting it into a 3/8" OD Spectralon tube. To measure the irradiance from within the sample cavity, **A**, a tube of Spectralon with 1/4" ID and 3/8" OD is inserted into the side of the cavity. A detector fiber at the end of this tube gives a signal proportional to the required irradiance. To prevent the radiances in **A'**, **B**, and **B'** from penetrating this tube we shield it with aluminum foil and then surround it with another Spectralon tube 3/8" ID by 3/4" OD. The outer Spectralon tube prevents the foil shielding from appreciably perturbing these radiances.

RESULTS

All initial work has been at 630 nm. Calibration was accomplished using a potassium permanganate solution whose absorption was accurately determined with a spectrophotometer. Figure 5 shows the measured ratio, S_1/S_0 , as a function of the volume of this solution in the sample cavity. A least squares procedure was used to fit this data to a straight line and the calibration constants were determined from the values of the slope and intercept using equations (3) and (4).

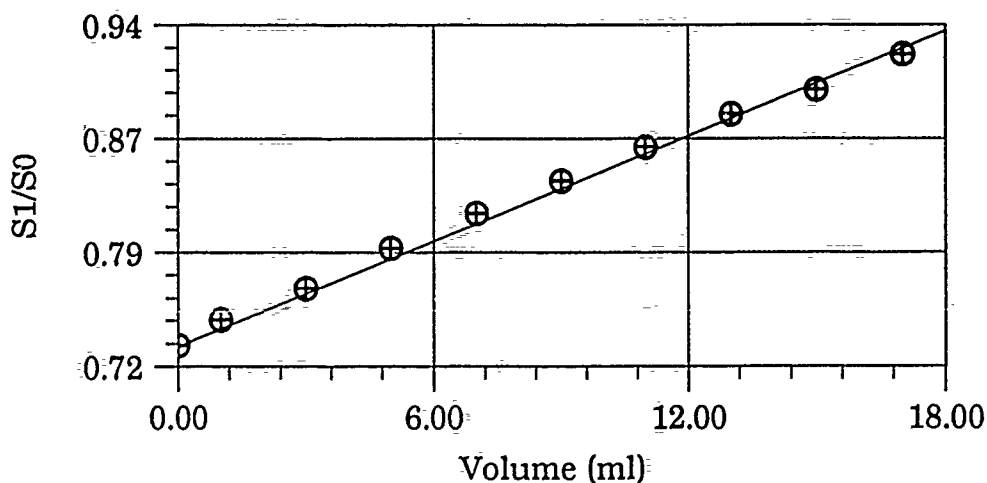


Figure 5. S_1/S_0 versus volume for fixed sample absorption.

Linearity of the ICAM was tested by measuring the absorption coefficient for a series of dye solutions containing incremental amounts of Irgalan Black (a commercial dye) dissolved in filtered/deionized water. As shown in figure 6, the data remained linear up to an absorption of 25 meter⁻¹.

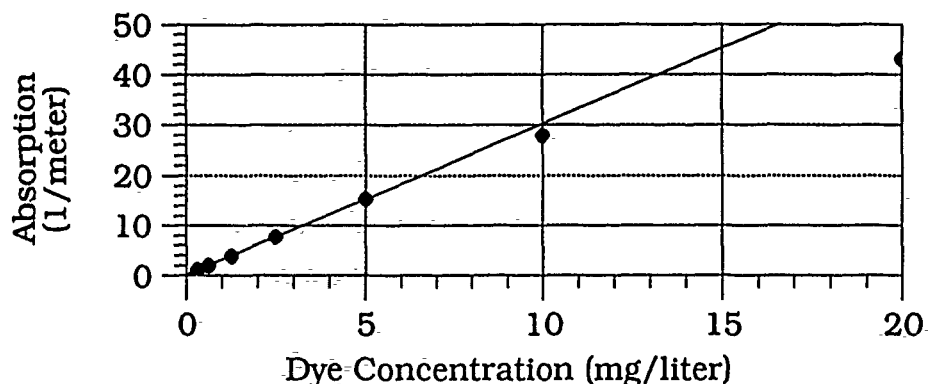


Figure 6. Linearity test; absorption versus dye concentration.

Of greatest importance is the effect on the observed absorption produced by the addition of nonabsorbing scattering particulates to the sample. Quartz powder was used for the scattering particles in this study. The particles are irregular and of the order of 0.5 to 10 microns in dimensions. They remain suspended in the water for the duration of the absorption measurements. The measured absorption of water at 630 nm as a function of increasing concentrations of scatterers is shown in figure 7.

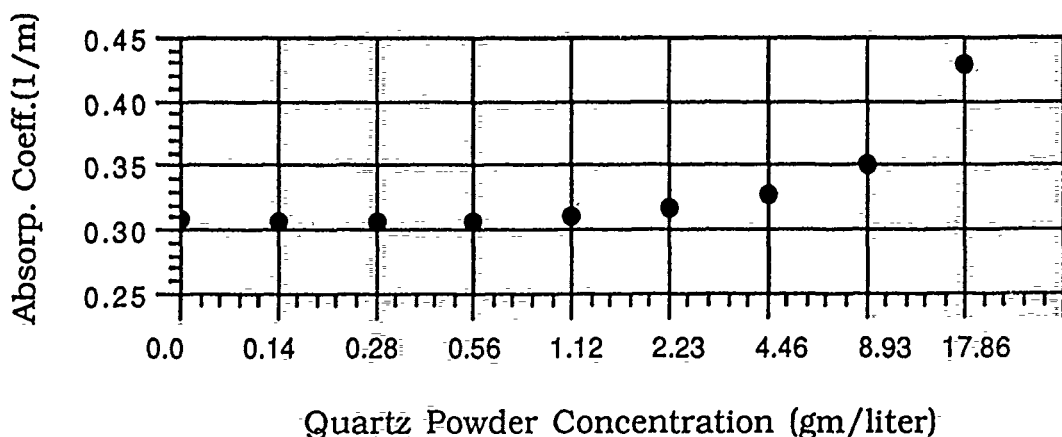


Figure 7. Observed absorption of water at 630 nm versus concentration of nonabsorbing scatterers.

For these measurements the calibration constants were $K_1=0.5197 \text{ cm}^{-1}$ and $K_2=0.8642 \text{ cm}^{-1}$. This measured absorption shows an anomalous increase with increasing concentration of scatterers beyond $\approx 1 \text{ gm/l}$. However, the effect is small; even at 9 gm/l the measured absorption is only in error by $\approx 15\%$. At 1 gm/l , where the scattering has negligible effect, the extinction length due to scattering is only about 7 cm . Since our cavity diameter is 3.7 cm , the corresponding scattering optical depth is 0.53 . At the same time, due to the high reflectivity of the walls and the corresponding large number of transits through the sample, the effective extinction length due to absorption by the water is $\approx 3.7 \text{ m}$.

In initial cavity designs, the observed increase in absorption at high concentrations of scatterers was attributed to creation of an anisotropy of the F_0 irradiance at the sample surface by the S_0 detector fiber. Specifically, the fiber is a radiation sink so the radiation density in its immediate vicinity is decreased. The cavity design shown in figure 3 was intended to decrease this effect; the F_0 irradiance is allowed to travel down a Spectralon tunnel where a fiber can sample the intensity without directly contacting the sample. The anisotropy caused by the detector will be averaged over the larger entrance area of this tunnel. The experimental results have shown that this was in fact not a major source of the problem.

Based on an analytic one-dimensional model, we now believe that the observed increase in absorption in the presence of a high concentration of particles is due to an anisotropy of the radiation density in the entire sample. Specifically, the scattering is so great that even with very weak absorption, the center of the sample is darker than the region close to the Spectralon wall. This effect will be dependent on the concentration of scatterers, the absorption of the sample, and on the path length through the sample. Future research efforts will involve experimental checks of the predictions of this one-dimensional model, development of a computer model for the true 3-dimensional system, and extension of the device to measurements of absorption in aerosols and smokes.

CONCLUSION

The ICAM is a unique instrument for measuring the total absorption of a sample in the presence of scatterers. For relatively high

concentrations of scatterers (up to a scattering optical depth less than ≈ 0.5), the absorption measurement is independent of the scattering effects. From a practical standpoint this is not a severe restriction and accurate absorption measurements are now feasible on samples that were previously not amenable to such studies.

BIBLIOGRAPHY

1. P. Elterman, "Integrating Cavity Spectroscopy", Appl. Opt. **9** , 2141-2142 (1970).
2. E.S. Fry, and G.W. Kattawar, "Measurement of the Absorption Coefficient of Ocean Water Using Isotropic Illumination" Proc. SPIE **925** , Ocean Optics IX, 142-148 (1988).

AN ASYMPTOTIC EXPANSION FOR
HANKEL FUNCTIONS WITH
COMPLEX INDEX
WITH APPLICATIONS

D. K. Cohoon

West Chester University
Department of Mathematics
and Computer Science
West Chester, PA 19383

December 22, 1989

Following the ideas of Carlini an asymptotic expansion for Hankel functions with large complex index is developed. We apply these formulas to exactly determine the electromagnetic fields induced within and scattered by a large N layer anisotropic sphere that has been subjected to an external source of electromagnetic radiation.

1 INTRODUCTION

The Hankel function $H_\nu^{(j)}(z)$ for $j \in \{1, 2\}$ and $\nu \in \mathbb{C}$ and $z \in \mathbb{C}$ is defined by the relations

$$H_\nu^{(1)}(z) = J_\nu(z) + iY_\nu(z) \quad (1.1)$$

and

$$H_\nu^{(2)}(z) = J_\nu(z) - iY_\nu(z) \quad (1.2)$$

where if $W = C_\nu$ represents any one of $H_\nu^{(j)}$ or any linear combination of $J_\nu(z)$ or $Y_\nu(z)$, then

$$z^2 \frac{d^2 W}{dz^2} + z \frac{dW}{dz} + (z^2 - \nu^2)W = 0 \quad (1.3)$$

and the solution with an integrable singularity at the origin is given by

$$J_\nu(z) = \left(\frac{z}{2}\right)^\nu \sum_{k=0}^{\infty} \left(\frac{(-z^2/4)^k}{k! \Gamma(\nu + k + 1)} \right) \quad (1.4)$$

and where for noninteger ν

$$Y_\nu = \frac{J_\nu(z) \cos(\nu\pi) - J_{-\nu}}{\sin(\nu\pi)} \quad (1.5)$$

with the latter expression being equal to its limiting value in case ν were an integer. Furthermore,

$$C_{\nu-1}(z) + C_{\nu+1}(z) = \frac{2\nu}{z} C_\nu(z) \quad (1.6)$$

2 ASYMPTOTIC EXPANSION

We begin by expressing the Hankel function in the form,

$$H_\nu^{(1)}(z) = H_\nu^{(1)}(z_0) \exp\left(\int_{z_0}^z u(\zeta) d\zeta\right) \quad (2.1)$$

Substituting into Bessel's equation (1.3), we find that

$$z^2 (u'(z) + u(z)^2) + zu(z) - \nu^2(1 - z^2) = 0 \quad (2.2)$$

and we seek a solution of the form

$$u(z) = \nu u_0 + u_1(z) + \frac{u_2}{\nu} + \frac{u_3}{\nu^2} + \dots \quad (2.3)$$

or equivalently,

$$\frac{u(z)}{\nu} = u_0 + \frac{u_1}{\nu} + \frac{u_2}{\nu^2} + \frac{u_3}{\nu^3} + \dots \quad (2.4)$$

The latter form makes it easy to represent $u(z)^2$ in the form

$$\left(\frac{u(z)}{\nu}\right)^2 = \sum_{j=0}^{\infty} \left(\sum_{k=0}^j (u_k(z)u_{j-k}(z)) \right) \frac{1}{\nu^j} \quad (2.5)$$

and since it is true that

$$\frac{u'(z)}{\nu^2} + \frac{u(z)^2}{\nu^2} + \frac{1}{\nu z} \left(\frac{u(z)}{\nu}\right) = \frac{1 - z^2}{z^2} \quad (2.6)$$

that we have the relationship

$$\begin{aligned} & \frac{u_0^{(1)}(z)}{\nu} + \frac{u_1^{(1)}(z)}{\nu^2} + \frac{u_2^{(1)}(z)}{\nu^3} + \frac{u_3^{(1)}(z)}{\nu^4} + \dots \\ & + \sum_{j=0}^{\infty} \left(\sum_{k=0}^j (u_k(z)u_{j-k}(z)) \right) \frac{1}{\nu^j} \\ & + \frac{1}{z} \left(\frac{u_0}{\nu} + \frac{u_1}{\nu^2} + \frac{u_2}{\nu^3} + \frac{u_3}{\nu^4} + \dots \right) = \frac{1 - z^2}{z^2} \end{aligned} \quad (2.7)$$

We can find all the values of the coefficients $u_k(z)$ simply by equating like powers of ν on both sides of this equation. We find, in particular, that

$$u_0 = \sqrt{\frac{1 - z^2}{z^2}} \quad (2.8)$$

The remaining coefficients may be evaluated without integration. For example, the next relationship tells us that

$$\frac{u_0^{(1)}(z)}{\nu} + \left(\frac{(u_0 u_1 + u_1 u_0)(z)}{\nu} \right) + \frac{u_0}{z\nu} = 0 \quad (2.9)$$

which tells us, after a little algebra, that

$$2u_1 = \frac{z}{1 - z^2} \quad (2.10)$$

The next step in the calculation is the evaluation of the integrals from z_0 to z of all the functions $u_k(z)$ which turn out to be completely elementary. Thus, one can develop a variety of asymptotic expansions of Hankel functions with controlled numerators by following a path through the complex z plane. One would start with a small value of z_0 and evaluate $H_\nu^{(1)}(z_0)$. We can make the integrals from z_0 to z as small as we please simply by making z close enough to z_0 . Thus, the numerators in the expansion could then be made arbitrarily small.

3 GENERALIZATIONS OF AIRY FUNCTIONS

There is another asymptotic expansion in terms of Airy functions. The Airy functions satisfy the differential equation,

$$v'' - xv = 0 \quad (3.1)$$

In this section we shall find explicit solutions of the ordinary differential equations of the form,

$$v'' - Cx^N v = 0 \quad (3.2)$$

and more generally of equations of the form

$$v'' - \frac{A}{x}v' + \left(\frac{B}{x^2} - Cx^N\right)v = 0 \quad (3.3)$$

which are, in turn, used in an asymptotic representation of Bessel and Hankel functions.

We remind ourselves that Bessel's differential equation,

$$z^2 W'' + zW' + (z^2 - \nu^2)W = 0 \quad (3.4)$$

has the solution $J_\nu(z)$. We are attempting here to find other differential equations, related to Bessel's equation, that include the Airy equations, as special cases. We consider functions of the form,

$$v(x) = x^q J_b(cx^p) \quad (3.5)$$

and observe that

$$v'(x) = qx^{q-1} J_b(cx^p) + pcx^{p+q-1} J_b^{(1)}(cx^p) \quad (3.6)$$

An additional differentiation reveals that

$$v''(x) = q(q-1)x^{q-2} J_b(cx^p) + pc(2q+p-1)x^{p+q-2} J_b^{(1)}(cx^p) + (pc)^2 x^{2p+q-2} J_b^{(2)}(cx^p) \quad (3.7)$$

Bessel's differential equation may be rewritten as

$$zW'' + W' + \left(z - \frac{\nu^2}{z}\right)W = 0 \quad (3.8)$$

so that

$$(cx^p)J_b^{(2)}(cx^p) + J_b^{(1)}(cx^p) + \left(cx^p - \frac{b^2}{cx^p}\right) J_b(cx^p) = 0 \quad (3.9)$$

Dividing all terms of equation (3.7) by p^2cx^{p+q-2} we see that

$$cx^p J_b^{(2)}(cx^p) + \frac{pc(2q+p-1)}{p^2c} J_b^{(1)}(cx^p) + \frac{q(q-1)}{p^2cx^p} J_b(cx^p) = \frac{v''(x)}{p^2cx^{p+q-2}} \quad (3.10)$$

Combining the last two equations we have two representations of

$$(cx^p)J_b^{(2)}(cx^p) = -J_b^{(1)}(cx^p) + \left(\frac{b^2}{cx^p} - cx^p\right) J_b(cx^p) = \frac{v''(x)}{p^2cx^{p+q-2}} - \frac{pc(2q+p-1)}{p^2c} J_b^{(1)}(cx^p) - \frac{q(q-1)}{p^2cx^p} J_b(cx^p) \quad (3.11)$$

Collecting terms in this equation, we find that

$$v''(x) = (p^2cx^{p+q-2}) \left\{ \frac{(2q+p-1)}{p} - 1 \right\} J_b^{(1)}(cx^p) + (p^2cx^{p+q-2}) \left\{ \left(\frac{b^2}{c} + \frac{q(q-1)}{p^2c}\right) \left(\frac{1}{x^p}\right) - cx^p \right\} J_b(cx^p) \quad (3.12)$$

If $b = \frac{1}{3}$, $p = \frac{3}{2}$, and $q = \frac{1}{2}$, then

$$\frac{2q+p-1}{p} - 1 = 0 \quad (3.13)$$

and

$$\frac{pb^2 + q(q-1)}{pc} = 0 \quad (3.14)$$

so that the last differential equation representation of $v''(x)$ specializes to

$$\frac{4v''(x)}{9c} = -cx\sqrt{x}J_b(cx^b) = -cxv(x) \quad (3.15)$$

or

$$v''(x) + \frac{9}{4}c^2v(x) = 0 \quad (3.16)$$

which if $3c = 2i$ reduces to the standard Airy equation, or equation (3.1).

Collecting terms in equation (3.11) we conclude that

$$v''(x) = p^2cx^{p+q-2} \left\{ \frac{2q+p-1}{p} - 1 \right\} J_b^{(1)}(cx^p) + \left(\frac{b^2}{c} + \frac{q(q-1)}{p^2c} \right) x^{q-2} J_b(cx^p) - p^2c^2x^{2p+q-2} J_b(cx^p) \quad (3.17)$$

Using equation (3.6) to express $v'(x)$ we have the relation

$$pcx^{p+q-2} J_b^{(1)}(cx^p) = \frac{v'(x)}{x} - qx^{q-2} J_b(cx^p) \quad (3.18)$$

Substituting this last expression for $v'(x)$ into the preceding representation of $v''(x)$ in terms of the Bessel function and its derivative, we conclude that

$$v''(x) = p \left\{ \frac{2q+p-1}{p} - 1 \right\} \left[\frac{v'(x)}{x} - qx^{q-2} J_b(cx^p) \right] + \left[\left(\frac{b^2}{c} + \frac{q(q-1)}{p^2c} \right) x^{q-2} \right] J_b(cx^p) - p^2c^2x^{2p+q-2} J_b(cx^p) \quad (3.19)$$

which in turn implies that

$$v''(x) = p^2c \left\{ \frac{2q+p-1}{p} - 1 \right\} \frac{v'(x)}{x} +$$

$$\left[\left(\frac{b^2}{c} + \frac{q(q-1)}{p^2c} \right) - pq \left\{ \frac{2q+p-1}{p} - 1 \right\} \right] x^{q-2} J_b(cx^b) - p^2c^2x^{2p+q-2} J_b(cx^p) \quad (3.20)$$

We now use equation (3.5) to make the replacement

$$J_b(cx^p) = \frac{v(x)}{x^q} \quad (3.21)$$

and conclude that

$$v''(x) = p^2c \left\{ \frac{(2q+p-1)}{p} - 1 \right\} \frac{v'(x)}{x} + \left[\left(\frac{b^2}{c} + \frac{q(q-1)}{p^2c} \right) - pq \left\{ \frac{2q+p-1}{p} - 1 \right\} \right] x^{-2}v(x) - p^2c^2x^{2p-2}v(x) \quad (3.22)$$

If

$$q = 1/2 \quad (3.23)$$

then there is no $v'(x)$ term in the equation, and if in addition,

$$b = 1/(2p) \quad (3.24)$$

we see that there is no $x^{-2}v(x)$ term, and if

$$2p - 2 = N, \quad (3.25)$$

then the differential equation takes the form

$$v''(x) + \left(\frac{N+2}{2} \right)^2 c^2 x^N v(x) = 0 \quad (3.26)$$

If we choose

$$c = \frac{2i\sqrt{C}}{N+2} \quad (3.27)$$

then

$$v''(x) - Cx^N v(x) = 0 \quad (3.28)$$

and if

$$c = \frac{2\sqrt{C}}{N+2} \quad (3.29)$$

we have

$$v''(x) + Cx^N v(x) = 0 \quad (3.30)$$

4 APPLICATIONS

We have implemented algorithms to exactly describe the interaction of electromagnetic radiation with an N layer structure whose regions of continuity of tensorial electromagnetic properties are delimited by concentric spheres which may themselves be covered by impedance sheets. The core of the spherical structure may be penetrable or perfectly conducting. The code was validated by making sure that

- the stimulating external source of radiation was accurately represented by the number of vector wave functions, spherical harmonics, used to represent the electric and magnetic fields in each of the layers,
- the boundary conditions are satisfied at each of the layer interfaces, and
- the total radiation entering the spherical structure, minus the total radiation scattered away as calculated using the Poynting vector on

the outer surface of the structure exactly balanced with the

ML the magnetic losses within the layers,

DL the dielectric losses within the layers,

CL the conductive losses within the layers, and

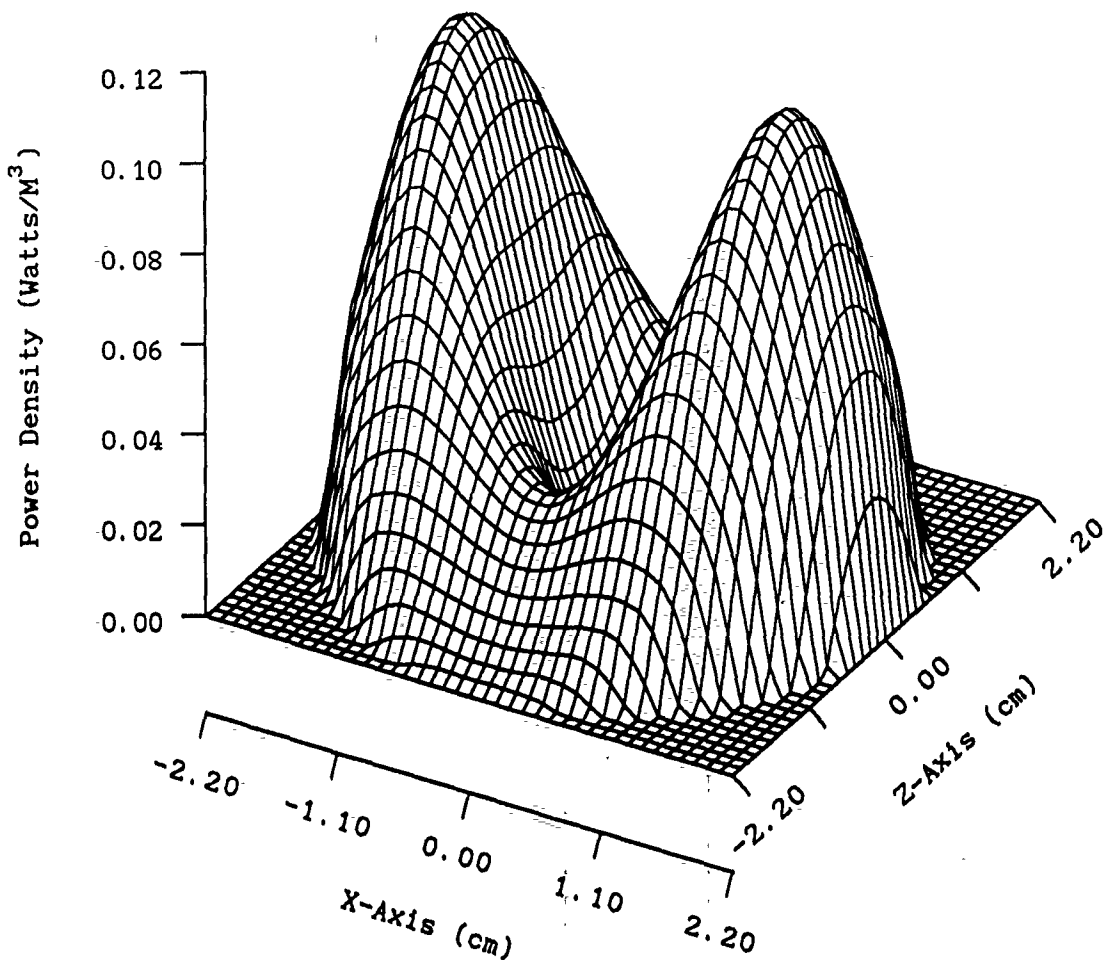
ISL the impedance sheet losses on the impedance sheets separating the surfaces.

The following calculations show the capability of the Hankel function routines in treating the interaction of electromagnetic radiation with large conductors coated with a thin layer of anisotropic material with a high permittivity.

Absorbed Power in the X-Z Plane $ka = 2.0$

$$\sigma = 0.0 + 0.0i \quad \mu = 1.0 + 0.0i$$

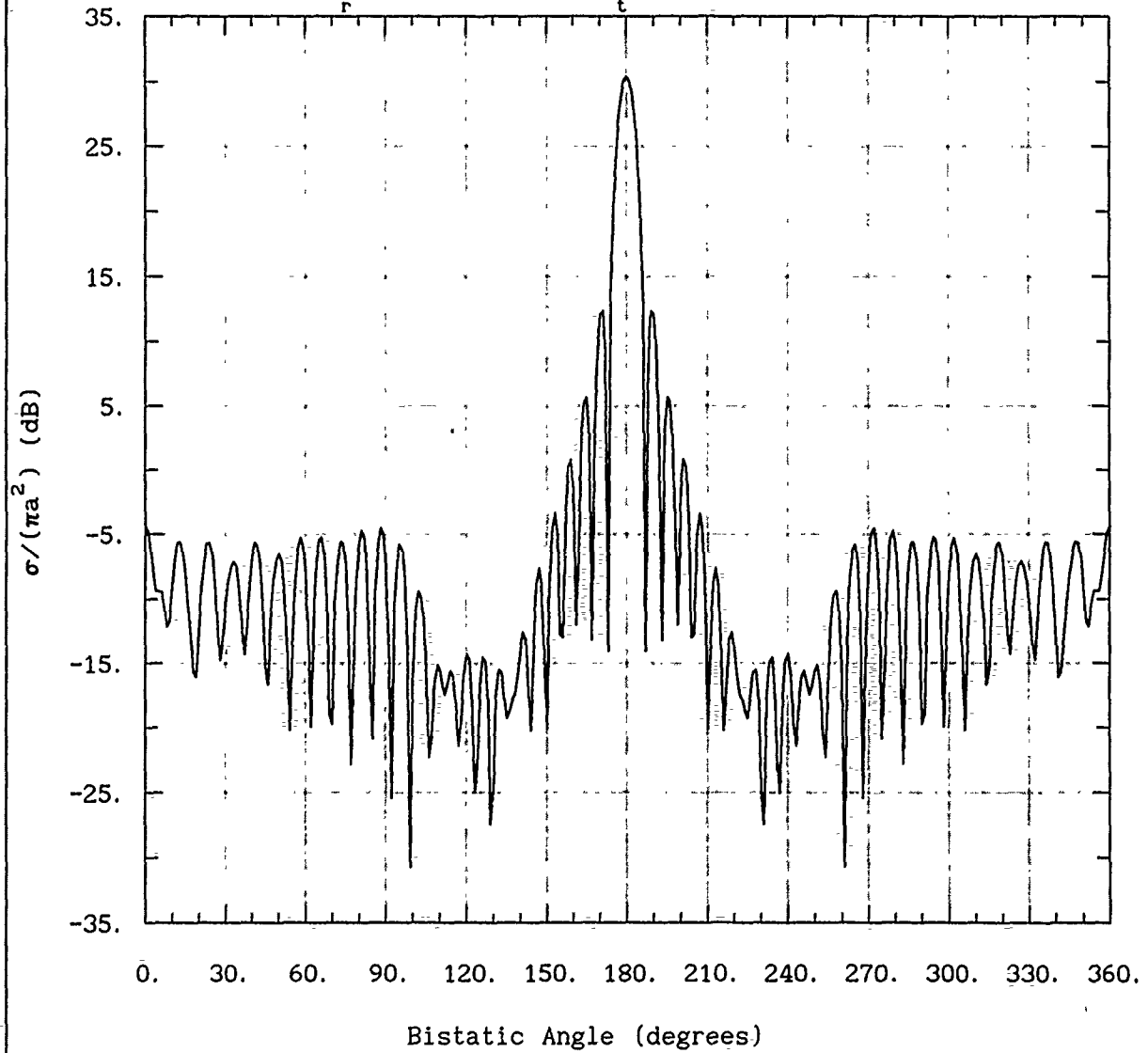
$$\epsilon_r = 2.0 + 0.0i \quad \epsilon_t = 4.0 + 0.5i$$



Bistatic Cross Section for Sphere $k_0 a = 30.0$

H-Polarization $\mu = 1.0 + 0.0i$ $\sigma = 0.0 + 0.0i$

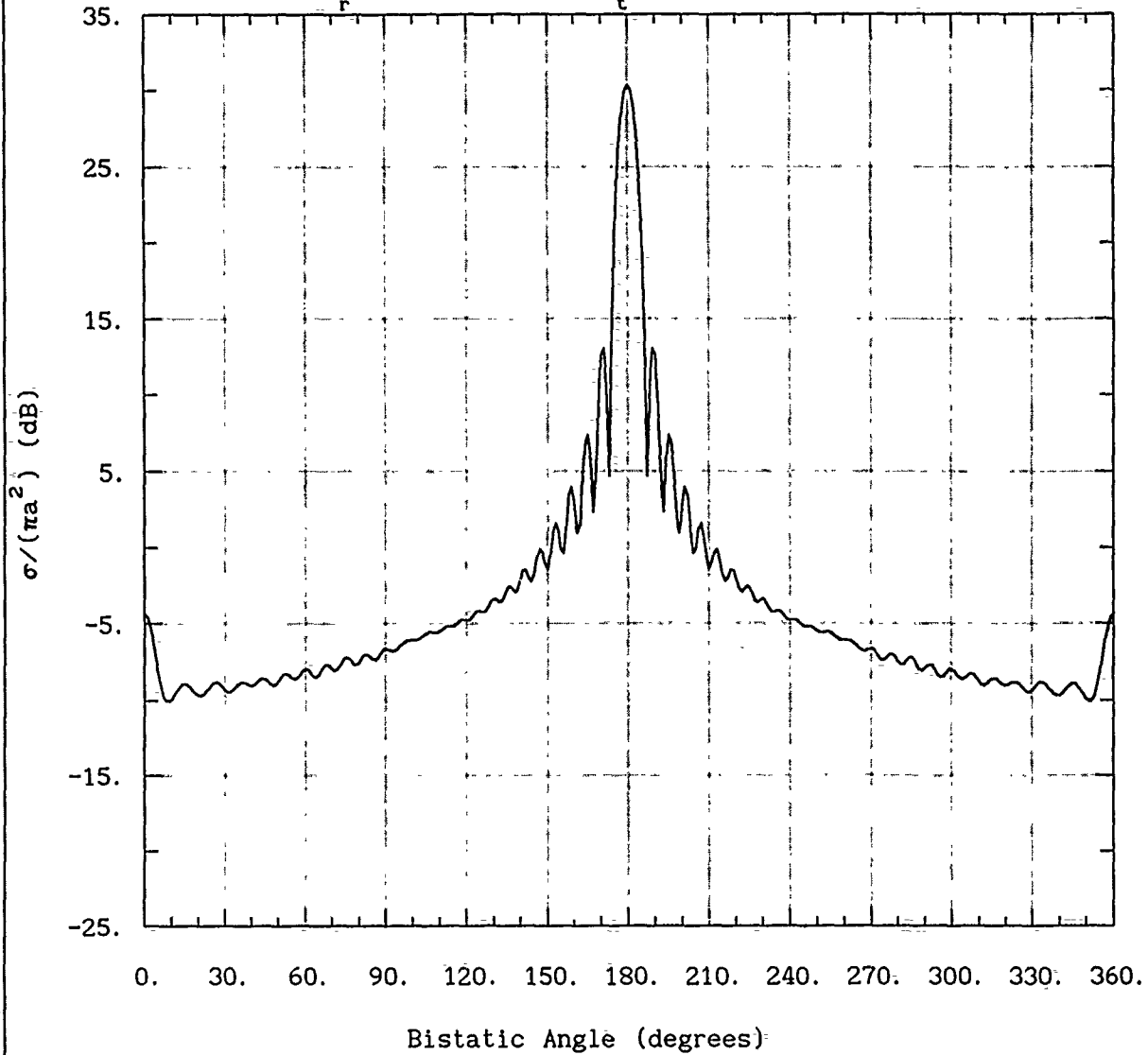
$\epsilon_r = 2.0 + 0.0i$ $\epsilon_t = 4.0 + 0.5i$



Bistatic Cross Section for Sphere $k_0 a = 30.0$

E-Polarization $\mu = 1.0 + 0.0i$ $\sigma = 0.0 + 0.0i$

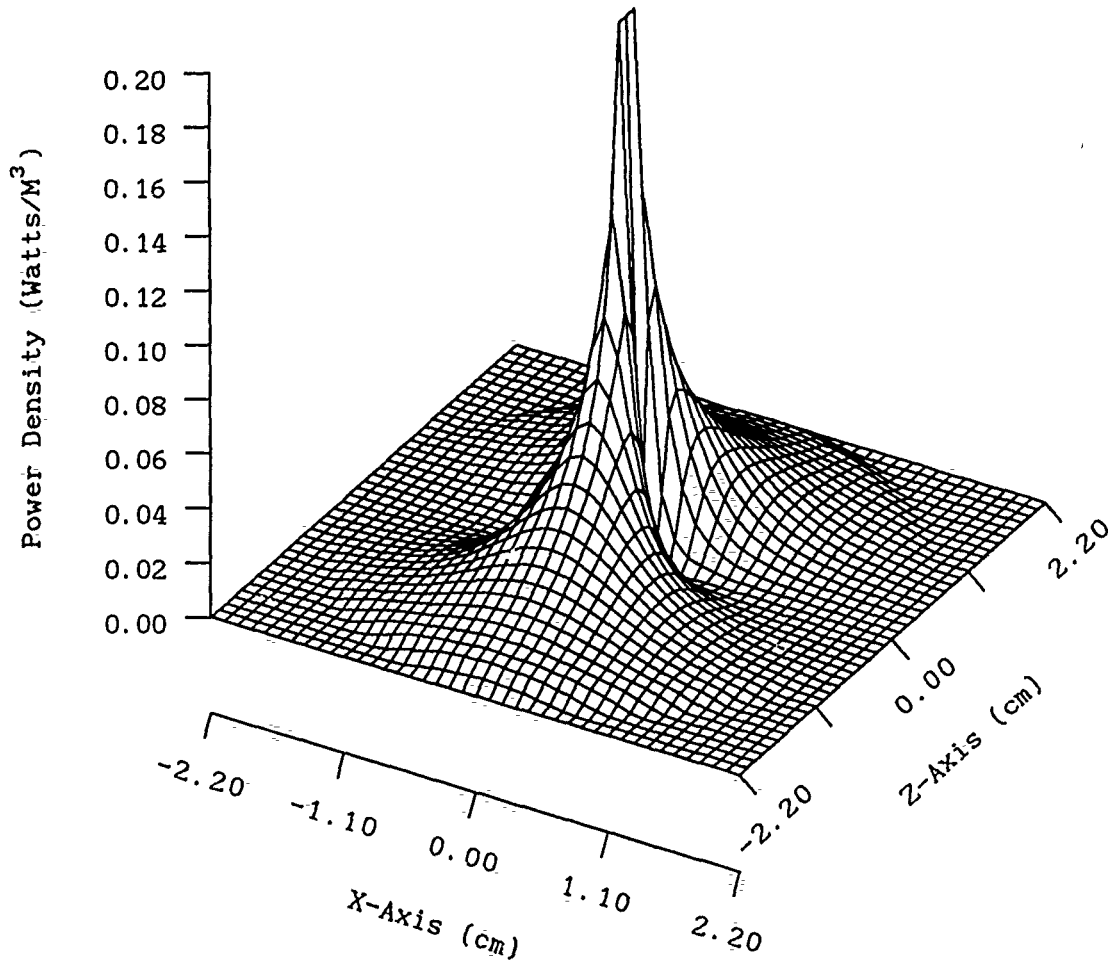
$\epsilon_r = 2.0 + 0.0i$ $\epsilon_t = 4.0 + 0.5i$



Absorbed Power in the X-Z Plane $ka = 2.0$

$$\sigma = 0.0 + 0.0i \quad \mu = 1.0 + 0.0i$$

$$\epsilon_r = 4.0 + 0.5i \quad \epsilon_t = 2.0 + 0.0i$$



References

- [1] Abramowitz, Milton and Irene Stegun. *Handbook of Mathematical Functions* New York: Dover(1972)
- [2] Bell, Earl L., David K. Cohoon, and John W. Penn. *Mie: A FORTRAN program for computing power deposition in spherical dielectrics through application of Mie theory. SAM-TR-77-11* Brooks AFB, Tx 78235: USAF School of Aerospace Medicine (RZ) Aerospace Medical Division (AFSC) (August, 1977)
- [3] Bell, Earl L., David K. Cohoon, and John W. Penn. *Electromagnetic Energy Deposition in a Concentric Spherical Model of the Human or Animal Head SAM-TR-79-6* Brooks AFB, Tx 78235: USAF School of Aerospace Medicine (RZ) Aerospace Medical Division (AFSC) (December, 1982).
- [4] Burr, John G., David K. Cohoon, Earl L. Bell, and John W. Penn. Thermal response model of a Simulated Cranial Structure Exposed to Radiofrequency Radiation. *IEEE Transactions on Biomedical Engineering. Volume BME-27, No. 8* (August, 1980) pp 452-460.
- [5] Cohoon, D. K., J. W. Penn, E. L. Bell, D. R. Lyons, and A. G. Cryer. *A Computer Model Predicting the Thermal Response to Microwave Radiation SAM-TR-82-22* Brooks AFB, Tx 78235: USAF School of Aerospace Medicine. (RZ) Aerospace Medical Division (AFSC) (December, 1982).

- [6] Garcia, C. B. and W. I. Zangwill. *Pathways to Solutions, Fixed Points, and Equilibria*. Englewood Cliffs, NJ: Prentice Hall(1981)
- [7] Hochstadt, Harry. *The Functions of Mathematical Physics*. New York: Dover(1986).
- [8] Hormander, Lars. *Linear Partial Differential Operators* New York: Academic Press (1963)
- [9] Watson, G. N. *A Treatise on the Theory of Bessel Functions* Cambridge, England: Cambridge University Press (1958)
- [10] Whittaker, E. T. and G. N. Watson. *A Course of Modern Analysis* London: Cambridge University Press (1986).

ELECTROMAGNETIC FIELD CALCULATIONS FOR A TIGHTLY-FOCUSED LASER BEAM INCIDENT UPON A SPHERICAL PARTICLE

J.P. Barton, D.R. Alexander, and S.A. Schaub
Center for Electro-Optics
College of Engineering
University of Nebraska
Lincoln, Nebraska 68588

RECENT PUBLICATIONS, SUBMITTALS FOR PUBLICATION, AND PRESENTATIONS:

- A). J.P. Barton, D.R. Alexander, and S.A. Schaub, "Experimental and theoretical analysis of liquid droplets moving through a focused CO₂ laser beam," Proceedings of the 1988 CRDEC Scientific Conference on Obscuration and Aerosol Research.
- B). J.P. Barton, D.R. Alexander, and S.A. Schaub, "Experimental and theoretical analysis of liquid droplets moving through a focused CO₂ laser beam," presentation at the 1988 CRDEC Scientific Conference on Obscuration and Aerosol Research, June, 1988.
- C). J.P. Barton, D.R. Alexander, and S.A. Schaub, "Internal and near-surface electromagnetic fields for a spherical particle in a focused laser beam," poster presentation at the 1988 CRDEC Scientific Conference on Obscuration and Aerosol Research, June, 1988.
- D). D.R. Alexander, D.E. Poulain, J.P. Barton, S.A. Schaub, and J. Zhang, "Nonlinear effects of excimer laser radiation with solid particles in a vacuum," presentation at the 1988 CRDEC Scientific Conference on Obscuration and Aerosol Research, June, 1988.
- E). D.R. Alexander, D.E. Poulain, J.P. Barton, S.A. Schaub, and J. Zhang, "Nonlinear effects of excimer laser radiation with solid particles in a vacuum," Proceedings of the 1988 CRDEC Scientific Conference on Obscuration and Aerosol Research.
- F). J.P. Barton, D.R. Alexander, and S.A. Schaub, "Internal and near-surface electromagnetic fields for a spherical particle irradiated by a focused laser beam," *J. Appl. Phys.* **64**, 1632 (1988).
- G). S.A. Schaub, D.R. Alexander, J.P. Barton, and M.A. Emanuel, "Focused laser beam interactions with methanol droplets: effects of relative beam diameter," *Appl. Opt.* **28**, 1666 (1989).
- H). S.A. Schaub, D.R. Alexander, and J.P. Barton, "Theoretical model for the image formed by a spherical particle in a coherent imaging system: comparison to experiment," *Opt. Engr.* **28**, 565 (1989).
- I). J.P. Barton, D.R. Alexander, and S.A. Schaub, "Internal fields of a spherical particle illuminated by a tightly-focused laser beam: focal point positioning effects at resonance," *J. Appl. Phys.* **65**, 2900 (1989).
- J). D.R. Alexander, S.A. Schaub, J. Zhang, D.E. Poulain, and J.P. Barton, "Scattering of incident KrF laser radiation resulting from the laser induced breakdown of H₂O droplets," *Opt. Lett.* **14**, (1989).
- K). S.A. Schaub, D.R. Alexander, D.E. Poulain, and J.P. Barton, "Measurement of hypersonic velocities resulting from the laser-induced breakdown of aerosols using an excimer laser imaging system," *Rev. Sci. Instru.*, to be published (Dec., 1989).
- L). J.P. Barton and D.R. Alexander, "Fifth-order corrected electromagnetic field components for a fundamental Gaussian beam," *J. Appl. Phys.*, to be published (Oct. 1, 1989).
- M). J.P. Barton, D.R. Alexander, and S.A. Schaub, "Theoretical determination of net radiation force and torque for a spherical particle illuminated by a focused laser beam," *J. Appl. Phys.*, to be published (Nov. 15, 1989).
- N). S.A. Schaub, J.P. Barton, and D.R. Alexander, "Simplified coefficient expression for a spherical particle located on the propagation axis of a fifth-order Gaussian beam," submitted to *Appl. Phys. Lett.* (1989).
- O). D.E. Poulain, D.R. Alexander, J.P. Barton, and J. Zhang, "Interaction of intense ultraviolet radiation with solid aerosols," submitted to *J. Appl. Phys.* (1989).
- P). J.P. Barton, D.R. Alexander, and S.A. Schaub, "Theoretical determination of the radiation force distribution for a spherical droplet illuminated by a focused laser beam," submitted to *J.*

Appl. Phys. (1989).

Q). J.P. Barton, D.R. Alexander, and S.A. Schaub, "Electromagnetic fields for a focused laser beam incident upon a spherical particle," presentation at the Workshop on the Physics of Directed Energy Propagation through the Atmosphere, Center for Atmospheric Sciences, New Mexico State University, Las Cruces, New Mexico, Feb. 28 - Mar. 1, 1989.

R). D.R. Alexander, S.A. Schaub, J. Zhang, D.E. Poulain, and J.P. Barton, "Laser induced breakdown of H₂O droplets at 0.248 μm ," presentation at the Workshop on the Physics of Directed Energy Propagation through the Atmosphere, Center for Atmospheric Sciences, New Mexico State University, Las Cruces, New Mexico, Feb. 28 - Mar. 1, 1989.

S). J.P. Barton, D.R. Alexander, and S.A. Schaub, "Electromagnetic field calculations for a tightly-focused laser beam incident upon a spherical particle," presentation at the 1989 CRDEC Scientific Conference on Obscuration and Aerosol Research, June, 1989.

T). D.R. Alexander, J.P. Barton, and S.A. Schaub, "Laser induced breakdown of H₂O droplets and solid wires at 0.248 μm ," presentation at the 1989 CRDEC Scientific Conference on Obscuration and Aerosol Research, June, 1989.

ABSTRACT

New applications and extensions of our spherical particle/arbitrary beam electromagnetic interaction theory are presented. The topics include a further analysis of focal point positioning effects at resonance, the determination of the net radiation force and torque on the particle, the determination of the spatial distribution of radiation forces within and upon the surface of the particle, and the determination of the interactive internal and external electromagnetic fields for a beam incident upon two adjacent particles of differing size and material and of arbitrary spatial positioning. Future work will involve further refinement of these developments and an effort to obtain direct comparisons between theoretical calculations and corresponding experimental measurements.

I. INTRODUCTION

The theoretical determination of the electromagnetic fields (and resultant electromagnetic phenomena) associated with the interaction of a tightly-focused monochromatic beam (laser beam) with a spherical particle is considered. The electromagnetic fields are calculated using our spherical particle/arbitrary beam interaction theory.¹ The spherical particle/arbitrary beam interaction theory has been previously used to investigate the heating of droplets within² and moving through³ a focused laser beam, and to investigate the effects of focal point positioning on the excitation of structural resonances within a spherical particle.⁴ In this paper, after giving a brief review of the spherical particle/arbitrary beam interaction theory (including the development an improved Gaussian beam description) in Sec. II., the following recent applications and extensions of the theory are presented: in Sec. III., further analysis of focal point positioning effects at resonance; in Sec. IV., net radiation force and torque on a particle; in Sec. V., radiation force distributions within and upon the surface of a particle; and in Sec. VI., beam incident upon two adjacent particles of differing size and material and of arbitrary spatial positioning.

II. REVIEW OF SPHERICAL PARTICLE/ARBITRARY BEAM THEORY

A continuous, monochromatic beam propagating within a homogeneous, isotropic, nonmagnetic, nonabsorbing dielectric media incident upon a homogeneous, isotropic, nonmagnetic spherical particle is assumed. For a beam of arbitrary, but known, mathematical description, the electromagnetic fields internal to and external to the spherical particle can be determined using an extension of plane wave Lorenz-Mie theory which we refer to as the spherical particle/arbitrary beam interaction theory. A complete derivation of the procedure is presented in Ref. 1. The field component equations, in nondimensionalized form, are given in App. A. A spherical coordinate system with the origin at the sphere center is utilized. For the calculations of this paper, the beam is assumed to be a fundamental (TEM₀₀ mode) Gaussian-profiled, linearly-polarized beam propagating in the +z axis direction with predominate electric field polarization in the x axis direction.

In order to calculate the electromagnetic field components internal to and external to the spherical particle, it is necessary that the electromagnetic field components of the incident beam

be known. A fifth-order corrected Gaussian beam description was derived⁵ which provides an improved solution to Maxwell's equations in comparison with the previously used first-order Gaussian beam description.¹ The use of the fifth-order corrected Gaussian beam description is particularly important for calculations involving tightly-focused beams, where the beam waist diameter may be of the same order as the wavelength. The equations for the electromagnetic field components for a fifth-order corrected Gaussian beam are presented in App. B. The derivation of these equations is given in Ref. 5.

The fundamental parameters for the analysis of a focused Gaussian beam incident upon a spherical particle are as follows: the dielectric constant of the medium, ϵ_{ext} ; the particle size parameter, $\alpha = 2\pi a/\lambda_{ext}$, where a is the particle radius and λ_{ext} is the wavelength of the incident beam in the external media; the complex relative refractive index of the particle, $\tilde{n} = (\tilde{\epsilon}_{int}/\epsilon_{ext})^{1/2}$; the beam waist diameter, w_0 ; and the coordinate location of the center of the spherical particle relative to the focal point of the incident beam, (x_0, y_0, z_0) . Electromagnetic field components are nondimensionalized relative to the incident beam focal point electric field, E_0 , which can be related to the beam power by⁶

$$|E_0|^2 = \frac{16P}{\sqrt{\epsilon c w_0^2 (1 + s^2 + 1.5s^4)}} \quad (1)$$

where $s = (1/\alpha \tilde{w}_0)$. A tilde ($\tilde{\quad}$) above a spatial quantity indicates that the quantity has been nondimensionalized relative to the particle radius, a .

III. FURTHER ANALYSIS OF FOCAL POINT POSITIONING EFFECTS AT RESONANCE

In a recently published paper,⁴ our spherical particle/arbitrary beam interaction theory was used to investigate the effect of beam focal point positioning on the excitation of structural resonances within a spherical particle. In this work, calculations were performed using parameters corresponding to having a $1.06 \mu m$ wavelength, $4 \mu m$ waist diameter, linearly-polarized Gaussian beam incident upon a $10 \mu m$ diameter water droplet ($\tilde{n} = 1.33 + 5.0 \times 10^{-6}i$). The effect of focal point positioning on the excitation of resonances was evaluated for both a droplet at a magnetic wave resonance (34^{th} mode, 1^{st} order, $a = 4.954 \mu m$, $\alpha = 29.365$, $\tilde{w}_0 = 0.404$) and a droplet at an electric wave resonance (34^{th} mode, 1^{st} order, $a = 5.019 \mu m$, $\alpha = 29.753$, $\tilde{w}_0 = 0.399$). For such a tightly-focused beam (beam waist diameter less than the droplet diameter) it was found that structural resonances are not excited for on-sphere-center focal-point positioning. Resonance excitation requires edge illumination. For the magnetic wave resonance droplet, the resonance was excited when the beam focal point was moved from the sphere center towards the surface of the sphere along the y axis (perpendicular to the direction of incident electric field polarization) and, for the electric wave resonance droplet, the resonance was excited when the beam focal point was moved from the sphere center towards the surface of the sphere along the x axis (parallel to the direction of incident electric field polarization). Maximum resonance excitation occurs when the beam focal point is located just beyond the surface of the droplet (at $\tilde{y}_0 \approx \pm 1.175$ for the magnetic wave resonance droplet and at $\tilde{x}_0 \approx \pm 1.160$ for the electric wave resonance droplet).

The excitation of resonance for edge illumination is exhibited by the development of a solid ring of increased normalized source function ($S = |\vec{E}|^2/|E_0|^2$) just inside the sphere surface. Fig. 1 shows the normalized source function distribution in the y - z plane for the magnetic wave resonance droplet with on-edge illumination ($\tilde{x}_0 = 0, \tilde{y}_0 = -1.175, \tilde{z}_0 = 0$). Further details may be found in Ref. 4.

It was suggested,⁶ that the ring of increased normalized source function just within the surface of an edge illuminated, excited resonance, droplet may be the result of the droplet acting as an optical cavity with light circling near the surface of the droplet. To test this hypothesis, the calculation of Fig. 1 was repeated with two beams incident upon the droplet: the original beam at the right-hand side of the droplet ($\tilde{y}_0 = -1.175$) and a second identical beam at the left-hand-side of the droplet ($\tilde{y}_0 = +1.175$). If the droplet is acting as an optical cavity, the two beams should produce circles of light propagating in opposite directions which will result in a pattern of constructive and destructive interference. As shown in Fig. 2, this was the obtained result. The

interference pattern for a resonance droplet with on-edge, two beam illumination is quite similar to that observed for the same resonance droplet with plane wave illumination as is given in Ref. 4.

As a further test of the optical cavity nature of a droplet at resonance, the spatial distribution of the time-averaged Poynting vector was calculated for the magnetic wave resonance droplet with single beam incident illumination corresponding to Fig. 1. A plot of the Poynting vector distribution in the y-z plane is given in Fig. 3. Since the region near the surface of the droplet is of primary interest, the plot emphasizes the near-surface and extends from $\bar{r} = 0.8$ (at the center of the plot) to $\bar{r} = 1.0$ (at the outer radius of the plot). As seen in Fig. 3, the Poynting vectors indicate a circular flow of energy just within the surface of the droplet.

Further calculations investigating the optical cavity nature of a droplet at resonance is in progress and will be submitted in the form of a journal paper in the near future.

IV. NET RADIATION FORCE AND TORQUE

Series form expressions for the net radiation force and torque induced on a spherical particle illuminated by an arbitrarily-defined monochromatic beam were derived. As an example, the net force and torque for a $5 \mu m$ diameter water droplet optically levitated by a vertically-oriented, tightly-focused ($2w_0 = 2 \mu m$), TEM₀₀ mode argon-ion laser beam were determined and examined for on and off propagation axis and on and off structural resonance conditions. This work is presented in a paper in press (Ref. 7) and the reader is referred to this paper for details. Only a partial summary will be provided here.

For a steady-state condition, the net radiation force, \bar{F} , on the particle can be determined by integrating the dot product of the outwardly-directed normal unit vector, \hat{n} , and the electromagnetic stress tensor, \bar{T} , over a surface enclosing the particle,⁸

$$\langle \bar{F} \rangle = \langle \oint_S \hat{n} \cdot \bar{T} dS \rangle \quad (2)$$

where $\langle \rangle$ represents a time average. The appropriate form of the electromagnetic stress tensor to use in Eq. (1) is the topic of recent reviews by Robinson⁹ and Brevik.¹⁰ Apparently, for steady-state optical conditions, the traditional Minkowski form of the electromagnetic stress tensor,

$$\bar{T} = \frac{1}{4\pi} [\bar{E}\bar{D} + \bar{H}\bar{H} - \frac{1}{2}(\bar{E} \cdot \bar{D} + \bar{H} \cdot \bar{H})\bar{I}] \quad (3)$$

will give correct results. Similarly, the net radiation torque, \bar{N} , on the particle can be determined by performing a surface integral of the dot product of the outwardly-directed normal unit vector, \hat{n} , and the pseudo-tensor, $\bar{T} \times \bar{r}$, over a surface enclosing the particle,⁸

$$\langle \bar{N} \rangle = - \langle \oint_S \hat{n} \cdot (\bar{T} \times \bar{r}) dS \rangle. \quad (4)$$

Series form expressions for the net radiation force and torque on a spherical particle can be derived by 1.) using Eq. (3) to substitute for \bar{T} in Eqs. (2) and (4); 2.) choosing the integration surface as a spherical surface in the far field ($\bar{r} \Rightarrow \infty$), 3.) substituting for the electromagnetic field components using the series expressions of App. A, and 4.) integrating directly by applying recursion, product, and orthogonality relationships among the spherical harmonic functions. After a great deal of effort, series expressions for the components of net radiation force and torque in terms of the incident field coefficients (A_{lm}, B_{lm}) and the scattered field coefficients (a_{lm}, b_{lm}) were derived and subsequently verified. These equations are given in App. C.

The theoretical expressions of App. C were used to determine the radiation force and torque as a function of droplet position relative to the incident beam focal point for a $5 \mu m$ diameter water droplet in air optically levitated by a single, vertically-oriented, focused TEM₀₀ mode (Gaussian-profiled) argon-ion laser beam ($\lambda = 0.5145 \mu m$, $\bar{n} = 1.334 + 1.2 \times 10^{-9}i$). The laser beam is tightly-focused to a beam waist diameter ($2w_0$) of $2 \mu m$ (less than the droplet diameter).

Figure 4 shows the calculated power for levitation as a function of droplet diameter for droplets located on the incident beam propagation axis ($x_0 = y_0 = 0$) for an elevation just below the focal point at $z_0 = -5 \mu\text{m}$ and an elevation well above the focal point at $z_0 = +50 \mu\text{m}$. (These are positions of stable levitation, as will be shown later, in Fig. 5.) At $z_0 = -5 \mu\text{m}$, the beam diameter is about $2.6 \mu\text{m}$ (less than the droplet diameter) while at $z_0 = +50 \mu\text{m}$ the beam diameter has spread to about $16.5 \mu\text{m}$ (greater than the droplet diameter).

Although there is no directly comparable experimental data, the requirement of a few milliwatts of laser power to levitate a $5 \mu\text{m}$ diameter water droplet in air (as shown in Fig. 4) is consistent with the measurements of Ashkin and Dziedzic¹¹ in which a $4 \mu\text{m}$ diameter latex sphere was levitated using $\approx 1 \text{ mW}$ of laser power and the levitation of a glycerol droplet evaporating from a diameter of $12 \mu\text{m}$ to $1 \mu\text{m}$ required a range of laser powers from 40 mW to 0.2 mW .

At an elevation of $z_0 = 50 \mu\text{m}$, Fig. 4 indicates that at certain droplet diameters there is a decrease in the necessary power to levitate. This phenomena is a result of structural resonances within transparent water droplets at this wavelength. These structural resonances can each be associated with the excitation of particular radial modes of the general electromagnetic wave solution. The presence of structural resonances in the power to levitate at a given elevation has been experimentally observed by Ashkin and Dziedzic^{12,13}. Ashkin and Dziedzic¹² also observed that if the droplet is levitated near the focal point where the beam diameter is less than the diameter of the sphere, then structural resonances are not present. Figure 4 indicates a lack of structural resonances for $z_0 = -5 \mu\text{m}$ where the beam diameter ($2.6 \mu\text{m}$) is less than the droplet diameter ($5 \mu\text{m}$) consistent with Ashkin and Dziedzic's observation. As discussed in Sec. III., structural resonances in spherical particles require edge illumination for excitation and thus would not be excited for the tightly-focused conditions at $z_0 = -5 \mu\text{m}$.

The nature (electric or magnetic), mode, and order of the structural resonances of Fig. 4 were identified, and detailed calculations were performed for the three basic types of droplets: a droplet at a magnetic wave resonance (35^{th} mode, 1^{st} order, $d = 4.9266 \mu\text{m}$), a droplet at an electric wave resonance (35^{th} mode, 1^{st} order, $d = 4.9912 \mu\text{m}$), and an intermediate nonresonance droplet ($d = 4.96 \mu\text{m}$).

Figure 5 shows the power to levitate a droplet located on the propagation axis as a function of elevation for each of the three types of droplets. There is an increase in required laser power for droplets located near the focal point because of decreased diffraction due to the strong focusing through the center of the spherical droplet. For a given type of droplet there are then three local extrema in levitation power. A first minimum, P_{min}^1 , that occurs below the focal point, a maximum, P_{max} , that occurs near the focal point, and a second minimum, P_{min}^2 , that occurs above the focal point. (For the cases considered here, $P_{\text{min}}^1 < P_{\text{min}}^2$.) Stable levitation occurs in regions of positive slope of P versus z_0 . From Fig. 5 it is then apparent that there are three general regimes of stable levitation. 1.) If $P_{\text{max}} < P$, then the droplet will stably levitate at a single elevation above the focal point. 2.) If $P_{\text{min}}^2 < P < P_{\text{max}}$ then the droplet levitation is bistable, and the droplet can be stably levitated either above the focal point or below the focal point. 3.) If $P_{\text{min}}^1 < P < P_{\text{min}}^2$ then the droplet will stably levitate at a single elevation below the focal point. If $P < P_{\text{min}}^1$ then the droplet cannot be stably levitated at any position. Bistable levitation for a spherical particle levitated using a tightly-focused laser beam has been experimentally observed by Ashkin and Dziedzic¹⁴, who also observed that the particle could be easily transferred from one stable position to the other and back. If the particle begins at the above focal point position, a decrease in laser power will allow the particle to drop towards the focal point until $P = P_{\text{min}}^2$. If the laser power is further decreased slightly, the particle will drop through the focal point to the below focal point position since $P_{\text{min}}^1 < P_{\text{min}}^2$. Increasing the laser power would raise the particle towards the focal point until $P = P_{\text{max}}$. If the laser power is further increased slightly above P_{max} , the particle will rise through the focal point back to the above focal point position.

For the droplet located on the laser beam propagation axis (z -axis), the horizontal force components and all components of torque are zero, as is obvious from symmetry and as was verified by the equations in App. C. If the droplet is displaced in the horizontal direction, stabilizing forces act so as to push the droplet back towards the beam propagation axis. (This is true for $\text{Re}(\bar{n}) > 1$, as considered here. If $\text{Re}(\bar{n}) < 1$, then the horizontal forces push the droplet away from the

propagation axis and there is no stable levitation.) Also, if the droplet is displaced in the horizontal direction, a torque is induced on the droplet since the beam intensity profile now presents an asymmetrical incident light distribution across the droplet. Calculations of horizontal acceleration ($a = \langle F \rangle / m$) and induced angular acceleration ($\dot{\omega} = N/I$, where $I = 2ma^2/5$) were performed for droplet displacement along both the x-axis and y-axis for elevations of $z_o = + 50 \mu m$ and $z_o = - 5 \mu m$. Accelerations were calculated assuming a laser power necessary to levitate the droplet at the particular elevation as if the droplet were located on the propagation axis as is given in Fig. 5.

Figures 6 and 7 are for droplets at an elevation of $5 \mu m$ below the focal point where the beam diameter ($2w_o = 2.6 \mu m$) is less than the droplet diameter. Figure 6 shows the restoring acceleration for a droplet displacement along the x-axis. The restoring accelerations are similar for all three types of droplets and are a maximum at about $2 \mu m$ away from the propagation axis. (Note in Figs. 4 and 5, the levitation powers for all three types of droplets are approximately equal at $z_o = - 5 \mu m$.)

Figure 7 shows the y-component angular acceleration ($N_x = N_z = 0$) induced when the droplet is displaced along the x-axis at the $z_o = - 5 \mu m$ elevation. The induced angular acceleration increases from zero as the droplet is moved away from the propagation axis and reaches a maximum before diminishing to zero as the droplet is moved on out of the beam. The induced torque is greatest for the electric wave resonance droplet for x-axis displacements. The x-component angular acceleration ($N_y = N_z = 0$) induced when the droplet is displaced along the y-axis (not shown) has features similar to those for the x-axis displacement except that it is the magnetic wave resonance droplet that has the greatest induced torque. The increase in induced torque for the resonance droplets as the droplet is moved to the edge of the beam is consistent with the developments of Ref. 4 where it was found that structural resonances are excited by on-edge illumination with electric wave resonances more strongly excited for beams moved along the x-axis (in the direction of the incident beam electric field polarization) and magnetic wave resonances more strongly excited for beams moved along the y-axis (perpendicular to the incident beam electric field polarization). Additional results and observations are presented in Ref. 7.

V. RADIATION FORCE DISTRIBUTION

For a small particle illuminated by intense laser light, the internal absorption of the light and the reflection and refraction of the light at the surface result in changes of electromagnetic momentum which produce local forces. The theoretical determination of the net radiation force and torque induced on a spherical particle illuminated by a focused laser beam was considered in Sec. IV. Of additional interest is the determination of the spatial distribution of the radiation forces within and upon the surface of the particle. An understanding of the distribution of the radiation forces would be particularly useful for applications involving the laser diagnostics of liquid droplets. For liquid droplets, an asymmetrical radiation force distribution may appreciably distort the shape of the droplet, which, in turn, may affect expected light scattering patterns, structural resonance excitation, etc. Also, as suggested by Zhang and Chang,¹⁵ radiation forces could be used to control the shape of droplets (droplets either optically levitated or within a monodispersed stream) for subsequent experimental study.

Theoretical expressions have been derived for the body forces and surface stresses that occur when a homogeneous liquid droplet is illuminated by a continuous laser beam. Using our spherical particle/arbitrary beam interaction theory to provide the required electromagnetic field components, spatial distributions of radiation forces for a spherical water droplet in air levitated by a focused laser beam (corresponding with the arrangement analyzed in Sec. IV.) have been calculated. This work has been submitted for publication.¹⁶ A partial summary is given here.

Applying the divergence theorem to Eq. (2), the time averaged electromagnetically induced force per unit volume (body force) at any point within the liquid droplet is thus equal to the local divergence of the electromagnetic stress tensor,

$$\langle \vec{F}''' \rangle = \langle \vec{\nabla} \cdot \vec{T} \rangle \quad (5)$$

For calculation purposes, Eq. (5) can be simplified by substituting for the stress tensor (from Eq. (3)), applying Maxwell's equations, and taking the time average. (Note for a homogeneous particle the dielectric constant is uniform and the local charge density is zero so $\vec{\nabla} \cdot \vec{E} = 0$.) Eq. (5) then becomes

$$\langle \vec{F}''' \rangle = \frac{1}{8\pi} \text{Re} \{ -i\epsilon_I (\vec{E} \cdot \vec{\nabla}) \vec{E}^* - i\frac{\omega}{c} (\bar{\epsilon} - \epsilon_R) (\vec{E} \times \vec{H}^*) \} \quad (6)$$

where $\bar{\epsilon} = \epsilon + i4\pi\sigma/\omega$ and both the dielectric constant, $\epsilon = \epsilon_R + i\epsilon_I$, and the electrical conductivity, $\sigma = \sigma_R + i\sigma_I$, may be complex.

In addition to the electromagnetically induced body force, there is also an electromagnetically induced stress at the surface of the droplet. Returning to Eq. (2) and considering a cylindrical control volume of incremental cross sectional area, ΔS , and incremental length, ΔL , centered about a general position on the surface of the sphere, it follows in the limit that

$$\langle \vec{P} \rangle = \lim_{\Delta S \rightarrow 0} \lim_{\Delta L \rightarrow 0} \frac{\vec{F}}{\Delta S} = \langle \hat{r} \cdot \vec{T}_{ext} - \hat{r} \cdot \vec{T}_{int} \rangle \Big|_{r=a} \quad (7)$$

where \vec{P} is the electromagnetically induced surface stress. Substituting into Eq. (7) expressions for the internal (inside the sphere) and external (outside the sphere) stress tensors, utilizing the boundary conditions,

$$\begin{aligned} \epsilon_{ext} E_r^{ext} &= \bar{\epsilon}_{int} E_r^{int}, \\ E_\theta^{ext} &= E_\theta^{int}, \\ E_\phi^{ext} &= E_\phi^{int}, \\ \vec{H}_{ext} &= \vec{H}_{int}, \end{aligned}$$

and taking the time average provides an expression for the surface stress in terms of the electromagnetic field components,

$$\langle \vec{P} \rangle = \frac{1}{8\pi} \text{Re} \left\{ \frac{1}{2} [(\bar{\epsilon}_{int}^* - \epsilon_{int}) |E_r^{int}|^2 + (\epsilon_{int} - \epsilon_{ext}) (E_\theta^2 + E_\phi^2)] \hat{r} + (\bar{\epsilon}_{int}^* - \epsilon_{int}) E_r^{int*} (E_\theta \hat{\theta} + E_\phi \hat{\phi}) \right\}. \quad (8)$$

The theoretical expressions for the body force, Eq. (6), and the surface stress, Eq. (8), were found to be consistent with the net radiation force expressions in App. C. The net radiation force on a droplet should be equal to the sum of a volume integral of the body forces and a surface integral of the surface stresses,

$$\langle \vec{F} \rangle = \int_0^a \int_0^\pi \int_0^{2\pi} \langle \vec{F}''' \rangle r^2 \sin\theta d\phi d\theta dr + \int_0^\pi \int_0^{2\pi} \langle \vec{P} \rangle a^2 \sin\theta d\phi d\theta. \quad (9)$$

Using our spherical particle/arbitrary beam interaction theory to provide the required electromagnetic field components, the integrals of Eq. (9) were numerically evaluated for several different particle size parameter, complex relative refractive index, and incident beam-orientation arrangements. For each case, the net radiative force components from Eq. (9) were identical to those determined using the coefficient-series expressions of App. C.

Equations (6) and (8) were used to determine the radiation force distributions for a 5- μm water droplet optically levitated using a vertically-oriented, argon-ion laser beam corresponding with the arrangement analyzed for net force and torque in Sec. IV. The assumed continuous TEM₀₀ mode (Gaussian-profiled), linearly polarized laser beam is focused with a beam waist diameter of 2 μm ($2w_0 = 2\mu\text{m}$) and propagates in the +z axis direction with the electric field polarization in the x axis direction. Force distributions were calculated for the droplet both on and off the laser beam propagation axis and for the droplet 50 μm above the beam focal point (where the beam diameter of 16.5 μm is greater than the droplet diameter) and for the droplet 5 μm below the beam focal

point (where the beam diameter of $2.6 \mu m$ is less than the droplet diameter). As in Sec. IV., calculations were performed for the three basic types of droplets: a droplet at a magnetic wave resonance (35th mode, 1st order, $d = 4.9266 \mu m$), a droplet at an electric wave resonance (35th mode, 1st order, $d = 4.9912 \mu m$), and an intermediate nonresonance droplet ($d = 4.96 \mu m$).

At the $0.5145 \mu m$ wavelength, water is a weakly absorbing dielectric with $\bar{n} = 1.334 + 1.2 \times 10^{-9}i$ and thus $\epsilon_R = n_R^2 - n_I^2 = 1.780$, $\epsilon_I = 2n_R n_I = 3.20 \times 10^{-9}$, $\sigma_R = 0$, and $\sigma_I = 0$. From Eqs. (6) and (8) it follows that $\langle F''' \rangle \approx 0$, $P_\theta \approx 0$, and $P_\phi \approx 0$, so, for these conditions, the radiative forces are predominately outwardly-directed radial surface stresses.

The surface stress distributions shown in Figs. 8-12 provide the surface stress vector at 5° intervals around the circumference of the droplet in the x-z plane (in Figs. 8-13 the z axis is upwards, the x axis to the right) linearly scaled relative to the maximum surface stress magnitude, P_{max} . The assumed laser power is that necessary to levitate the droplet at the given elevation *as if the droplet was located on the propagation axis*.

Figure 8 shows the surface stress distribution for the nonresonance droplet levitated on the beam propagation axis at an elevation of $50 \mu m$ above the focal point. At this elevation the beam diameter is about three times the diameter of the droplet. As seen in Fig. 8, the largest forces are concentrated across the top of the droplet (in the direction of the beam propagation) with a secondary concentration of smaller forces across the bottom of the droplet. These surface forces are approximately azimuthally symmetric so that the surface force distribution in the y-z plane (plane perpendicular to the incident electric field polarization) is similar to that in the x-z plane for the nonresonance droplet.

Figure 9 shows the surface stress distribution for the electric wave resonance droplet levitated on the beam propagation axis at an elevation of $50 \mu m$ above the focal point. As for the nonresonance droplet, the largest surface stresses are concentrated across the top of the droplet with a secondary concentration of smaller forces across the bottom of the droplet. Unlike the nonresonance droplet, however, the electric wave resonance droplet exhibits a significant surface stress over the entire circumference, not just near the top and bottom of the droplet. The maximum surface stress for the electric wave resonance droplet is also about three times larger than the maximum surface stress for the nonresonance droplet at this elevation. The excitation of the electric wave resonance, as discussed in Ref. 4, occurs predominately in the x-z plane (the plane of incident electric field polarization). The surface stress distribution for the electric wave resonance droplet is not azimuthally symmetric and is similar to that of the nonresonance droplet in the y-z plane. For the magnetic wave resonance droplet (not shown) the situation is the opposite of that of the electric wave resonance droplet: the surface stress is "excited" in the y-z plane and is not "excited" in the x-z plane.

Figure 10 presents the surface stress distribution for the nonresonance droplet levitated on the beam propagation axis at an elevation of $5 \mu m$ below the focal point. At this elevation the beam diameter is about half the diameter of the droplet. As seen in Fig. 10, the largest surface stresses are concentrated near the top of the droplet with a secondary concentration of much smaller surface stresses near the bottom of the droplet. The maximum surface stress is about ten times greater than for the nonresonance droplet levitated at the $+ 50 \mu m$ elevation and the surface stress is confined to a smaller area. The surface stresses are approximately azimuthally symmetric.

Resonance excitation requires droplet edge illumination, and the electric and magnetic wave resonances are not excited for the on propagation axis location at $z_0 = - 5 \mu m$ where the incident beam passes through the middle of the droplet. The surface stress distributions for the electric and magnetic wave resonance droplets for the on propagation axis location at $z = - 5 \mu m$ (not shown) are similar to that of the nonresonance droplet.

If the droplet is horizontally displaced, there is a net restoring force that accelerates the droplet back towards the beam propagation axis (see Sec. IV.). Figure 11 presents the surface stress distribution for the nonresonance droplet levitated $5 \mu m$ below the focal point and displaced $3 \mu m$ along the x-axis. As shown in Fig. 11, for the displaced droplet the surface stresses are skewed towards the left which produces the net restoring force. Fig. 12 shows the same situation, but for the electric wave resonance droplet. The edge illumination caused by the horizontal displacement of the droplet excites the resonance which produces large surface stresses over the entire circumference

of the droplet in the x-z plane. For the magnetic wave resonance droplet (not shown) the resonance is excited in the y-z plane when the droplet is displaced along the y-axis.

As previously mentioned, at the $0.5145 \mu\text{m}$ wavelength, water is weakly absorbing and body forces are small. The body forces do, however, significantly contribute for the case of the x-axis displaced electric wave resonance droplet (and the y-axis displaced magnetic wave resonance droplet) at the $z_0 = -5 \mu\text{m}$ elevation. As shown in Sec. IV., the x-axis displaced electric wave resonance droplet at the $z_0 = -5 \mu\text{m}$ elevation incurs a net torque about the negative y-axis. Since the surface stresses are essentially radial, the surface stresses do not contribute to this torque. In Sec. III. it was shown that edge illuminated droplets at resonance have an increase in electric field magnitude that forms a ring just inside the surface of the droplet. At resonance the droplet acts as an optical cavity with light circling just inside the surface. Absorption of this light results in a loss of momentum which produces a net torque about the center of the droplet.

Figure 13 shows the calculated body force distribution in the x-z plane for the electric wave resonance droplet at the $-5 \mu\text{m}$ elevation and displaced $3 \mu\text{m}$ along the x-axis. Since the body forces are concentrated near the surface of the droplet, the distribution is plotted extending from $\bar{r} = 0.8$ (at the center of the plot) to $\bar{r} = 1.0$ (at the outer circumference of the plot). The body force vectors form a circling pattern which produces a net torque on the droplet. For the magnetic resonance droplet displaced along the y-axis (not shown) the body forces circle in the y-z plane.

VI. BEAM INCIDENT UPON TWO ADJACENT SPHERES OF ARBITRARY ARRANGEMENT

Utilizing our spherical particle/arbitrary beam interaction theory, we have developed a procedure for determining the electromagnetic fields for an arbitrary beam incident upon two adjacent particles of differing size and material and of arbitrary spatial positioning. (The generalization to three or more adjacent particles would be straightforward). The two particles may be of different size, may have different composition (differing complex relative index of refractions), and may have any spatial orientation relative to each other and relative to the incident beam. It is not necessary that there be a single incident beam; having multiple beams coming from different directions would require minimal additional computation.

The theoretical approach, in the most general sense, is similar to that introduced by Fuller and Kattawar.^{17,18} Since our spherical particle/arbitrary beam interaction theory permits the determination of the electromagnetic fields of a particle for *any* known incident field, the procedure is as follows. The spherical particle/arbitrary beam interaction theory is used to calculate the external electromagnetic field for the beam incident upon particle 1. The external electromagnetic field of particle 1 is used as the incident field upon particle 2 and the scattered field of particle 2 is determined. The scattered field of particle 2 is added to the incident beam to form an updated field incident upon particle 1 and the external field of particle 1 is recalculated. The newly calculated external field of particle 1 is then used as the incident field upon particle 2 and the scattered field of particle 2 is recalculated. The process is continued until there is no longer a significant change in the electromagnetic fields. For particles spaced one radius or more apart surface-to-surface, convergence typically occurs within two or three of these multiple "reflections."

The parameters of the laser beam incident upon two adjacent particles problem are then the dielectric constant of the medium (ϵ_{ext}), the waist diameter of the laser beam (w_0), the size parameters of the two particles (α_1 and α_2), the complex relative index of refractions of the two particles (\bar{n}_1 and \bar{n}_2), the location of particle 1 relative to the focal point of the laser beam (x_0, y_0, z_0), the location of particle 2 relative to particle 1 (x_{12}, y_{12}, z_{12}), and the location of the plot reference relative to particle 1 ($x_{ref}, y_{ref}, z_{ref}$). Spatial quantities are normalized using the radius of particle 1 (a_1).

Figure 14 presents the internal and near-surface normalized source function distribution in the y-z plane for a linearly-polarized (electric field polarization in the x axis direction), $100 \mu\text{m}$ waist diameter CO_2 laser beam ($\lambda = 10.6 \mu\text{m}$) incident upon two $45 \mu\text{m}$ diameter water droplets separated by $35 \mu\text{m}$ surface-to-surface along the propagation axis. These conditions correspond to an experiment performed within our Laboratory in which a CO_2 laser beam was directed upon two parallel streams of water droplets so that the illuminated droplet would act as a lens to focus the

laser light upon the shadow side droplet.¹⁹ This focusing effect is apparent in Fig. 14. Figure 15 presents the same situation as Fig. 14 but with the internal field suppressed to zero. As can be seen, the maximum droplet heating rate (proportional to S) occurs at the front surface of the shadow side droplet, for this arrangement, which is in agreement with our experimental observations.¹⁹

Figure 16 provides a normalized source function distribution for a more general case. A 40 μm waist diameter CO_2 laser beam is incident upon a 50 μm diameter methanol droplet ($\bar{n}_1 = 1.395 + 0.0163i$) and a 30 μm water droplet ($\bar{n}_2 = 1.179 + 0.072i$). The droplets are offset from each other and offset from the propagation axis of the beam in the y - z plane. The effect is an interesting splitting of the beam.

Further investigation of electromagnetic phenomena associated with a beam incident upon adjacent spherical particles, including particles at resonance, is in progress.

VII. FUTURE WORK

Besides continuing the developments discussed here, future topics that will be considered include obtaining direct comparisons between spherical particle/arbitrary beam interaction theory calculations and corresponding experimental measurements, developing an infinite cylinder/arbitrary beam interaction theory, developing an arbitrary shaped particle/arbitrary beam interaction theory, and developing a nonhomogeneous spherical particle/arbitrary beam interaction theory.

ACKNOWLEDGEMENT

This work was supported in part by the Army Research Office under contract No. DAAL03-87-K-0138.

REFERENCES

1. J.P. Barton, D.R. Alexander, and S.A. Schaub, "Internal and near-surface electromagnetic fields for a spherical particle irradiated by a focused laser beam," *J. Appl. Phys.* **64**, 1632 (1988).
2. S.A. Schaub, D.R. Alexander, J.P. Barton, and M.A. Emanuel, "Focused laser beam interactions with methanol droplets: effects of relative beam diameter," *Appl. Opt.* **28**, 1666 (1989).
3. J.P. Barton, D.R. Alexander, and S.A. Schaub, "Experimental and theoretical analysis of liquid droplets moving through a focused CO_2 laser beam," Proceedings of the 1988 CRDEC Scientific Conference on Obscuration and Aerosol Research.
4. J.P. Barton, D.R. Alexander, and S.A. Schaub, "Internal fields of a spherical particle illuminated by a tightly-focused laser beam: focal point positioning effects at resonance," *J. Appl. Phys.* **65**, 2900 (1989).
5. J.P. Barton and D.R. Alexander, "Fifth-order corrected electromagnetic field components for a fundamental Gaussian beam," *J. Appl. Phys.*, to be published (Oct. 1, 1989).
6. R.K. Chang, personal communication (1989).
7. J.P. Barton, D.R. Alexander, and S.A. Schaub, "Theoretical determination of net radiation force and torque for a spherical particle illuminated by a focused laser beam," *J. Appl. Phys.*, to be published (Nov. 15, 1989).
8. J.D. Jackson, *Classical Electrodynamics*, 2nd ed. (John Wiley & Sons, New York, 1975).
9. F.N.H. Robinson, "Electromagnetic stress and momentum in matter," *Phys. Rep.* **16**, 315 (1975).
10. I. Brevik, "Experiments in phenomenological electrodynamics and the electromagnetic energy-momentum tensor," *Phys. Rep.* **52**, 133 (1979).
11. A. Ashkin and J.M. Dziedzic, "Optical levitation of liquid drops by radiation pressure," *Science* **187**, 1073 (1975).
12. A. Ashkin and J.M. Dziedzic, "Observation of resonances in the radiation pressure on dielectric spheres," *Phys. Rev. Lett.* **38**, 1351 (1977).
13. A. Ashkin and J.M. Dziedzic, "Observation of optical resonances of dielectric spheres by light scattering," *Appl. Opt.* **20**, 1803 (1981).

14. A. Ashkin and J.M. Dziedzic, "Stability of optical levitation by radiation pressure," *Appl. Phys. Lett.* **24**, 586 (1974).
15. J.Z. Zhang and R.K. Chang, "Shape distortion of a single water droplet by laser-induced electrostriction," *Opt. Lett.* **13**, 916 (1988).
16. J.P. Barton, D.R. Alexander, and S.A. Schaub, "Theoretical determination of the radiation force distribution for a spherical droplet illuminated by a focused laser beam," submitted to *J. Appl. Phys.* (1989).
17. K.A. Fuller and G.W. Kattawar, "Consummate solution to the problem of classical electromagnetic scattering by an ensemble of spheres. I: Linear chains," *Opt. Lett.* **13**, 90 (1988).
18. K.A. Fuller and G.W. Kattawar, "Consummate solution to the problem of classical electromagnetic scattering by an ensemble of spheres. II: Clusters of arbitrary configuration," *Opt. Lett.* **13**, 1063 (1988).
19. D.R. Alexander, J.P. Barton, S.A. Schaub, M.A. Emanuel, and J. Zhang, "Experimental and theoretical analysis of the interaction of laser radiation with fluid cylinders and spheres," *Proceedings of the 1987 CRDEC Scientific Conference on Obscuration and Aerosol Research.*

APPENDIX A: ELECTROMAGNETIC FIELD EQUATIONS

INCIDENT FIELD

$$E_r^{(i)} = \frac{1}{\bar{r}^2} \sum_{l=1}^{\infty} \sum_{m=-l}^l [l(l+1) A_{lm} \psi_l(\alpha\bar{r}) Y_{lm}(\theta, \phi)] \quad (\text{A1})$$

$$E_{\theta}^{(i)} = \frac{\alpha}{\bar{r}} \sum_{l=1}^{\infty} \sum_{m=-l}^l \left[A_{lm} \psi_l'(\alpha\bar{r}) \frac{\partial Y_{lm}(\theta, \phi)}{\partial \theta} - \frac{m}{\sqrt{\epsilon_{ext}}} B_{lm} \psi_l(\alpha\bar{r}) \frac{Y_{lm}(\theta, \phi)}{\sin \theta} \right] \quad (\text{A2})$$

$$E_{\phi}^{(i)} = \frac{\alpha}{\bar{r}} \sum_{l=1}^{\infty} \sum_{m=-l}^l \left[i m A_{lm} \psi_l'(\alpha\bar{r}) \frac{Y_{lm}(\theta, \phi)}{\sin \theta} - \frac{i}{\sqrt{\epsilon_{ext}}} B_{lm} \psi_l(\alpha\bar{r}) \frac{\partial Y_{lm}(\theta, \phi)}{\partial \theta} \right] \quad (\text{A3})$$

$$H_r^{(i)} = \frac{1}{\bar{r}^2} \sum_{l=1}^{\infty} \sum_{m=-l}^l [l(l+1) B_{lm} \psi_l(\alpha\bar{r}) Y_{lm}(\theta, \phi)] \quad (\text{A4})$$

$$H_{\theta}^{(i)} = \frac{\alpha}{\bar{r}} \sum_{l=1}^{\infty} \sum_{m=-l}^l \left[B_{lm} \psi_l'(\alpha\bar{r}) \frac{\partial Y_{lm}(\theta, \phi)}{\partial \theta} + m \sqrt{\epsilon_{ext}} A_{lm} \psi_l(\alpha\bar{r}) \frac{Y_{lm}(\theta, \phi)}{\sin \theta} \right] \quad (\text{A5})$$

$$H_{\phi}^{(i)} = \frac{\alpha}{\bar{r}} \sum_{l=1}^{\infty} \sum_{m=-l}^l \left[i m B_{lm} \psi_l'(\alpha\bar{r}) \frac{Y_{lm}(\theta, \phi)}{\sin \theta} + i \sqrt{\epsilon_{ext}} A_{lm} \psi_l(\alpha\bar{r}) \frac{\partial Y_{lm}(\theta, \phi)}{\partial \theta} \right] \quad (\text{A6})$$

SCATTERED FIELD

$$E_r^{(s)} = \frac{1}{\bar{r}^2} \sum_{l=1}^{\infty} \sum_{m=-l}^l [l(l+1) a_{lm} \xi_l^{(1)}(\alpha\bar{r}) Y_{lm}(\theta, \phi)] \quad (\text{A7})$$

$$E_{\theta}^{(s)} = \frac{\alpha}{\bar{r}} \sum_{l=1}^{\infty} \sum_{m=-l}^l \left[a_{lm} \xi_l^{(1)'}(\alpha\bar{r}) \frac{\partial Y_{lm}(\theta, \phi)}{\partial \theta} - \frac{m}{\sqrt{\epsilon_{ext}}} b_{lm} \xi_l^{(1)}(\alpha\bar{r}) \frac{Y_{lm}(\theta, \phi)}{\sin \theta} \right] \quad (\text{A8})$$

$$E_{\phi}^{(s)} = \frac{\alpha}{\bar{r}} \sum_{l=1}^{\infty} \sum_{m=-l}^l \left[i m a_{lm} \xi_l^{(1)'}(\alpha\bar{r}) \frac{Y_{lm}(\theta, \phi)}{\sin \theta} - \frac{i}{\sqrt{\epsilon_{ext}}} b_{lm} \xi_l^{(1)}(\alpha\bar{r}) \frac{\partial Y_{lm}(\theta, \phi)}{\partial \theta} \right] \quad (\text{A9})$$

$$H_r^{(s)} = \frac{1}{\bar{r}^2} \sum_{l=1}^{\infty} \sum_{m=-l}^l [l(l+1) b_{lm} \xi_l^{(1)}(\alpha\bar{r}) Y_{lm}(\theta, \phi)] \quad (\text{A10})$$

$$H_{\theta}^{(s)} = \frac{\alpha}{\bar{r}} \sum_{l=1}^{\infty} \sum_{m=-l}^l \left[b_{lm} \xi_l^{(1)'}(\alpha\bar{r}) \frac{\partial Y_{lm}(\theta, \phi)}{\partial \theta} + m \sqrt{\epsilon_{ext}} a_{lm} \xi_l^{(1)}(\alpha\bar{r}) \frac{Y_{lm}(\theta, \phi)}{\sin \theta} \right] \quad (\text{A11})$$

$$H_{\phi}^{(s)} = \frac{\alpha}{\bar{r}} \sum_{l=1}^{\infty} \sum_{m=-l}^l \left[i m b_{lm} \xi_l^{(1)'}(\alpha \bar{r}) \frac{Y_{lm}(\theta, \phi)}{\sin \theta} + i \sqrt{\epsilon_{ext}} a_{lm} \xi_l^{(1)}(\alpha \bar{r}) \frac{\partial Y_{lm}(\theta, \phi)}{\partial \theta} \right] \quad (\text{A12})$$

INTERNAL FIELD

$$E_r^{(w)} = \frac{1}{\bar{r}^2} \sum_{l=1}^{\infty} \sum_{m=-l}^l [l(l+1) c_{lm} \psi_l(\bar{n} \alpha \bar{r}) Y_{lm}(\theta, \phi)] \quad (\text{A13})$$

$$E_{\theta}^{(w)} = \frac{\alpha}{\bar{r}} \sum_{l=1}^{\infty} \sum_{m=-l}^l \left[\bar{n} c_{lm} \psi_l'(\bar{n} \alpha \bar{r}) \frac{\partial Y_{lm}(\theta, \phi)}{\partial \theta} - \frac{m}{\sqrt{\epsilon_{ext}}} d_{lm} \psi_l(\bar{n} \alpha \bar{r}) \frac{Y_{lm}(\theta, \phi)}{\sin \theta} \right] \quad (\text{A14})$$

$$E_{\phi}^{(w)} = \frac{\alpha}{\bar{r}} \sum_{l=1}^{\infty} \sum_{m=-l}^l \left[i m \bar{n} c_{lm} \psi_l'(\bar{n} \alpha \bar{r}) \frac{Y_{lm}(\theta, \phi)}{\sin \theta} - \frac{i}{\sqrt{\epsilon_{ext}}} d_{lm} \psi_l(\bar{n} \alpha \bar{r}) \frac{\partial Y_{lm}(\theta, \phi)}{\partial \theta} \right] \quad (\text{A15})$$

$$H_r^{(w)} = \frac{1}{\bar{r}^2} \sum_{l=1}^{\infty} \sum_{m=-l}^l [l(l+1) d_{lm} \psi_l(\bar{n} \alpha \bar{r}) Y_{lm}(\theta, \phi)] \quad (\text{A16})$$

$$H_{\theta}^{(w)} = \frac{\alpha}{\bar{r}} \sum_{l=1}^{\infty} \sum_{m=-l}^l \left[\bar{n} d_{lm} \psi_l'(\bar{n} \alpha \bar{r}) \frac{\partial Y_{lm}(\theta, \phi)}{\partial \theta} + m \sqrt{\epsilon_{ext}} \bar{n}^2 c_{lm} \psi_l(\bar{n} \alpha \bar{r}) \frac{Y_{lm}(\theta, \phi)}{\sin \theta} \right] \quad (\text{A17})$$

$$H_{\phi}^{(w)} = \frac{\alpha}{\bar{r}} \sum_{l=1}^{\infty} \sum_{m=-l}^l \left[i m \bar{n} d_{lm} \psi_l'(\bar{n} \alpha \bar{r}) \frac{Y_{lm}(\theta, \phi)}{\sin \theta} + i \sqrt{\epsilon_{ext}} \bar{n}^2 c_{lm} \psi_l(\bar{n} \alpha \bar{r}) \frac{\partial Y_{lm}(\theta, \phi)}{\partial \theta} \right] \quad (\text{A18})$$

$$a_{lm} = \frac{\psi_l'(\bar{n} \alpha) \psi_l(\alpha) - \bar{n} \psi_l(\bar{n} \alpha) \psi_l'(\alpha)}{\bar{n} \psi_l(\bar{n} \alpha) \xi_l^{(1)'}(\alpha) - \psi_l'(\bar{n} \alpha) \xi_l^{(1)}(\alpha)} A_{lm} \quad (\text{A19})$$

$$b_{lm} = \frac{\bar{n} \psi_l'(\bar{n} \alpha) \psi_l(\alpha) - \psi_l(\bar{n} \alpha) \psi_l'(\alpha)}{\psi_l(\bar{n} \alpha) \xi_l^{(1)'}(\alpha) - \bar{n} \psi_l'(\bar{n} \alpha) \xi_l^{(1)}(\alpha)} B_{lm} \quad (\text{A20})$$

$$c_{lm} = \frac{\xi_l^{(1)'}(\alpha) \psi_l(\alpha) - \xi_l^{(1)}(\alpha) \psi_l'(\alpha)}{\bar{n}^2 \psi_l(\bar{n} \alpha) \xi_l^{(1)'}(\alpha) - \bar{n} \psi_l'(\bar{n} \alpha) \xi_l^{(1)}(\alpha)} A_{lm} \quad (\text{A21})$$

$$d_{lm} = \frac{\xi_l^{(1)'}(\alpha) \psi_l(\alpha) - \xi_l^{(1)}(\alpha) \psi_l'(\alpha)}{\psi_l(\bar{n} \alpha) \xi_l^{(1)'}(\alpha) - \bar{n} \psi_l'(\bar{n} \alpha) \xi_l^{(1)}(\alpha)} B_{lm} \quad (\text{A22})$$

$$A_{lm} = \frac{1}{l(l+1) \psi_l(\alpha)} \int_0^{2\pi} \int_0^{\pi} \sin \theta E_r^{(i)}(a, \theta, \phi) Y_{lm}^*(\theta, \phi) d\theta d\phi \quad (\text{A23})$$

$$B_{lm} = \frac{1}{l(l+1) \psi_l(\alpha)} \int_0^{2\pi} \int_0^{\pi} \sin \theta H_r^{(i)}(a, \theta, \phi) Y_{lm}^*(\theta, \phi) d\theta d\phi \quad (\text{A24})$$

$\xi_l^{(1)} = \psi_l - i\chi_l$ where ψ_l, χ_l are the Riccati-Bessel functions. Y_{lm} is the spherical harmonic function. $\bar{r} = r/a$ where a is the sphere radius.

APPENDIX B: FIFTH-ORDER CORRECTED GAUSSIAN BEAM EQUATIONS

$$E_x = E_o \{ 1 + s^2 [-\rho^2 Q^2 + i\rho^4 Q^3 - 2Q^2 \xi^2] + s^4 [+2\rho^4 Q^4 - 3i\rho^6 Q^5 - 0.5\rho^8 Q^6 + (8\rho^2 Q^4 - i2\rho^4 Q^5) \xi^2] \} \psi_0 e^{-i\zeta/s^2}, \quad (B1)$$

$$E_y = E_o \{ s^2 [-2Q^2 \xi \eta] + s^4 [(8\rho^2 Q^4 - 2i\rho^4 Q^5) \xi \eta] \} \psi_0 e^{-i\zeta/s^2}, \quad (B2)$$

$$E_z = E_o \{ s[-2Q\xi] + s^3 [(+6\rho^2 Q^3 - 2i\rho^4 Q^4) \xi + s^5 [(-20\rho^4 Q^5 + 10i\rho^6 Q^6 + \rho^8 Q^7) \xi]] \} \psi_0 e^{-i\zeta/s^2}, \quad (B3)$$

$$H_x = \sqrt{\epsilon} E_o \{ s^2 [-2Q^2 \xi \eta] + s^4 [(8\rho^2 Q^4 - 2i\rho^4 Q^5) \xi \eta] \} \psi_0 e^{-i\zeta/s^2}, \quad (B4)$$

$$H_y = \sqrt{\epsilon} E_o \{ 1 + s^2 [-\rho^2 Q^2 + i\rho^4 Q^3 - 2Q^2 \eta^2] + s^4 [+2\rho^4 Q^4 - 3i\rho^6 Q^5 - 0.5\rho^8 Q^6 + (8\rho^2 Q^4 - i2\rho^4 Q^5) \eta^2] \} \psi_0 e^{-i\zeta/s^2}, \quad (B5)$$

and

$$H_z = \sqrt{\epsilon} E_o \{ s[-2Q\eta] + s^3 [(+6\rho^2 Q^3 - 2i\rho^4 Q^4) \eta + s^5 [(-20\rho^4 Q^5 + 10i\rho^6 Q^6 + \rho^8 Q^7) \eta]] \} \psi_0 e^{-i\zeta/s^2} \quad (B6)$$

where $\psi_0 = iQ \exp(-i\rho^2 Q)$, $Q = 1/(i + 2\zeta)$, $\rho^2 = \eta^2 + \xi^2$, $s = 1/kw_0$, $\xi = x/w_0$, $\eta = y/w_0$, and $\zeta = z/kw_0^2$. Note: these equations are for an assumed time dependence of $e^{+i\omega t}$. If a time dependence of $e^{-i\omega t}$ is assumed, then the complex conjugate of the equations can be used.

APPENDIX C: NET RADIATION FORCE AND TORQUE EQUATIONS

$$\begin{aligned}
 \frac{\langle F_x \rangle + i \langle F_y \rangle}{a^2 E_0^2} = & + \frac{\alpha^2}{16\pi} i \sum_{l=1}^{\infty} \sum_{m=-l}^l \left\{ \sqrt{\frac{(l+m+2)(l+m+1)}{(2l+1)(2l+3)}} l(l+2) \times \right. \\
 & [2\epsilon_{ext} a_{lm} a_{l+1,m+1}^* + \epsilon_{ext} a_{lm} A_{l+1,m+1}^* + \epsilon_{ext} A_{lm} a_{l+1,m+1}^* + 2b_{lm} b_{l+1,m+1}^* \\
 & + b_{lm} B_{l+1,m+1}^* + B_{lm} b_{l+1,m+1}^*] \\
 & + \sqrt{\frac{(l-m+1)(l-m+2)}{(2l+1)(2l+3)}} l(l+2) \times \\
 & [2\epsilon_{ext} a_{l+1,m-1} a_{l,m}^* + \epsilon_{ext} a_{l+1,m-1} A_{l,m}^* + \epsilon_{ext} A_{l+1,m-1} a_{l,m}^* + 2b_{l+1,m-1} b_{l,m}^* \\
 & + b_{l+1,m-1} B_{l,m}^* + B_{l+1,m-1} b_{l,m}^*] \\
 & \left. - \sqrt{(l+m+1)(l-m)} \sqrt{\epsilon_{ext}} [-2a_{lm} b_{l,m+1}^* + 2b_{lm} a_{l,m+1}^* - a_{lm} B_{l,m+1}^* \right. \\
 & \left. + b_{lm} A_{l,m+1}^* + B_{lm} a_{l,m+1}^* - A_{lm} b_{l,m+1}^*] \right\} \quad (C1)
 \end{aligned}$$

$$\begin{aligned}
 \frac{\langle F_z \rangle}{a^2 E_0^2} = & - \frac{\alpha^2}{8\pi} \sum_{l=1}^{\infty} \sum_{m=-l}^l \text{Im} \left\{ l(l+2) \sqrt{\frac{(l-m+1)(l+m+1)}{(2l+3)(2l+1)}} \times \right. \\
 & [2\epsilon_{ext} a_{l+1,m} a_{l,m}^* + \epsilon_{ext} a_{l+1,m} A_{l,m}^* + \epsilon_{ext} A_{l+1,m} a_{l,m}^* + 2b_{l+1,m} b_{l,m}^* + b_{l+1,m} B_{l,m}^* + \\
 & \left. B_{l+1,m} b_{l,m}^*] + \sqrt{\epsilon_{ext}} m [2a_{lm} b_{l,m}^* + a_{lm} B_{l,m}^* + A_{lm} b_{l,m}^*] \right\} \quad (C2)
 \end{aligned}$$

$$\begin{aligned}
 \frac{\langle N_x \rangle}{a^3 E_0^2} = & - \frac{\alpha}{8\pi} \sum_{l=1}^{\infty} \sum_{m=-l}^l \text{Re} \left\{ l(l+1) \sqrt{(l-m)(l+m+1)} \times \right. \\
 & [\epsilon_{ext} a_{lm} a_{l,m+1}^* + b_{lm} b_{l,m+1}^* + \\
 & \left. \frac{1}{2} (\epsilon_{ext} a_{lm} A_{l,m+1}^* + \epsilon_{ext} a_{l,m+1} A_{lm}^* + b_{lm} B_{l,m+1}^* + b_{l,m+1} B_{lm}^*)] \right\} \quad (C3)
 \end{aligned}$$

$$\begin{aligned}
 \frac{\langle N_y \rangle}{a^3 E_0^2} = & - \frac{\alpha}{8\pi} \sum_{l=1}^{\infty} \sum_{m=-l}^l \text{Im} \left\{ l(l+1) \sqrt{(l-m)(l+m+1)} \times \right. \\
 & [\epsilon_{ext} a_{lm} a_{l,m+1}^* + b_{lm} b_{l,m+1}^* + \\
 & \left. \frac{1}{2} (\epsilon_{ext} a_{lm} A_{l,m+1}^* - \epsilon_{ext} a_{l,m+1} A_{lm}^* + b_{lm} B_{l,m+1}^* - b_{l,m+1} B_{lm}^*)] \right\} \quad (C4)
 \end{aligned}$$

$$\frac{\langle N_z \rangle}{a^3 E_0^2} = - \frac{\alpha}{8\pi} \sum_{l=1}^{\infty} \sum_{m=-l}^l (l+1)m [\epsilon_{ext} |a_{lm}|^2 + |b_{lm}|^2 + \text{Re}(\epsilon_{ext} a_{lm} A_{lm}^* + b_{lm} B_{lm}^*)] \quad (C5)$$

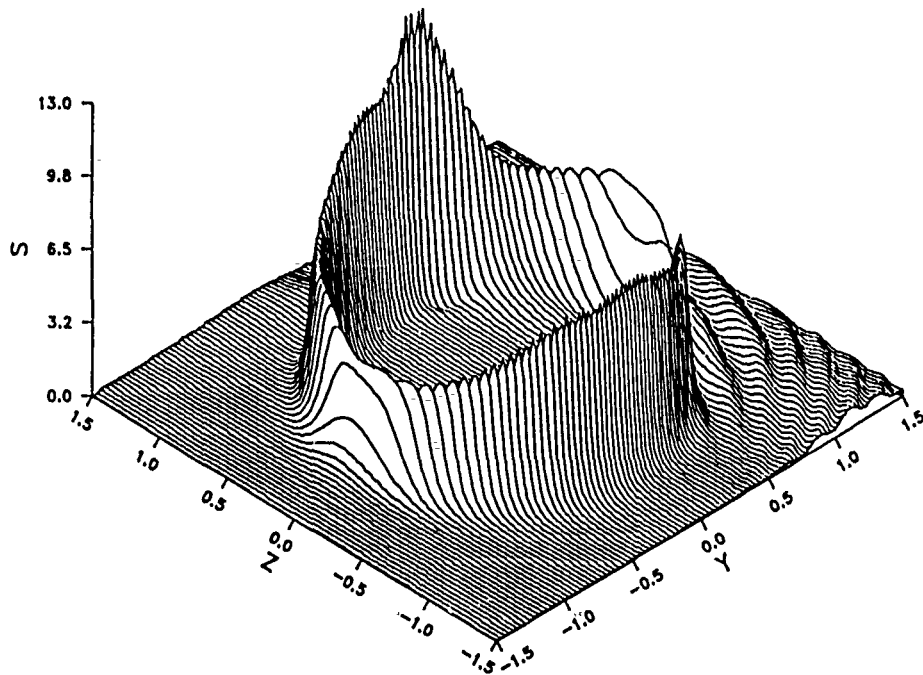


FIG 1. Normalized source function in the equatorial (y - z) plane for a transverse (x direction) polarized Gaussian beam incident upon a sphere at magnetic wave resonance. $\bar{n} = 1.33 + 5.0 \times 10^{-6}i$, $\bar{w}_o = 0.404$, $\bar{x}_o = 0.0$, $\bar{y}_o = -1.175$, $\bar{z}_o = 0.0$, and $\alpha = 29.365$. [$1.06 \mu\text{m}$ wavelength, $4 \mu\text{m}$ waist diameter beam incident upon a $9.908 \mu\text{m}$ diameter (34^{th} mode, 1^{st} order mag. wave res.) water droplet with on edge y -axis illumination]

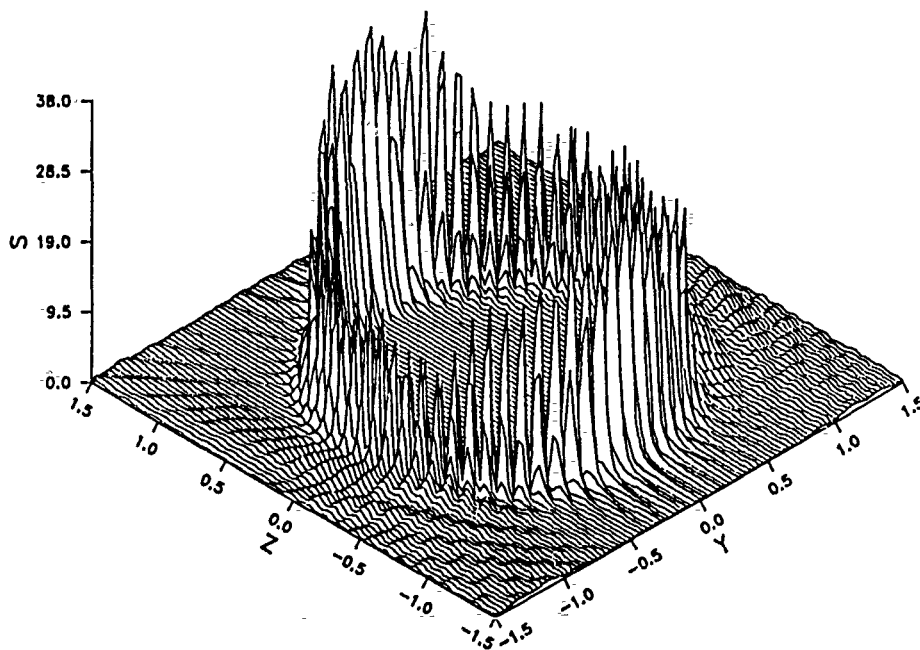


FIG 2. Normalized source function in the equatorial (y - z) plane for two transverse (x direction) polarized Gaussian beams incident upon a sphere at magnetic wave resonance. $\bar{n} = 1.33 + 5.0 \times 10^{-6}i$, $\bar{w}_o = 0.404$, $\bar{x}_o = 0.0$, $\bar{y}_o = +1.175$ and -1.175 , $\bar{z}_o = 0.0$, and $\alpha = 29.365$. [$1.06 \mu\text{m}$ wavelength, $4 \mu\text{m}$ waist diameter beams incident upon a $9.908 \mu\text{m}$ diameter (34^{th} mode, 1^{st} order mag. wave res.) water droplet with on edge y -axis illumination]

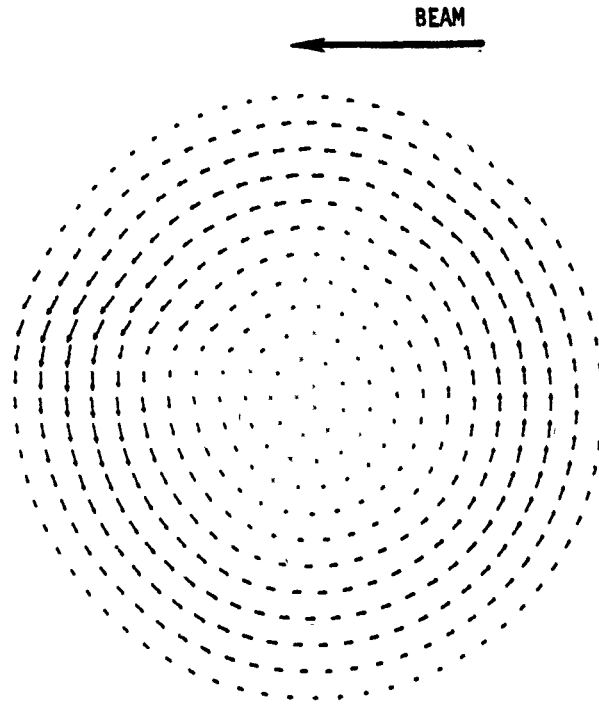


FIG 3. Poynting vector in the equatorial ($y-z$) plane for a transverse (x direction) polarized Gaussian beam incident upon a sphere at magnetic wave resonance. $1.0 > \bar{r} > 0.8$, $\bar{n} = 1.33 + 5.0 \times 10^{-6}i$, $\bar{w}_o = 0.404$, $\bar{x}_o = 0.0$, $\bar{y}_o = -1.175$, $\bar{z}_o = 0.0$, and $\alpha = 29.365$. [$1.06 \mu\text{m}$ wavelength, $4 \mu\text{m}$ waist diameter beam incident upon a $9.908 \mu\text{m}$ diameter (34^{th} mode, 1^{st} order mag. wave res.) water droplet with on edge y -axis illumination]

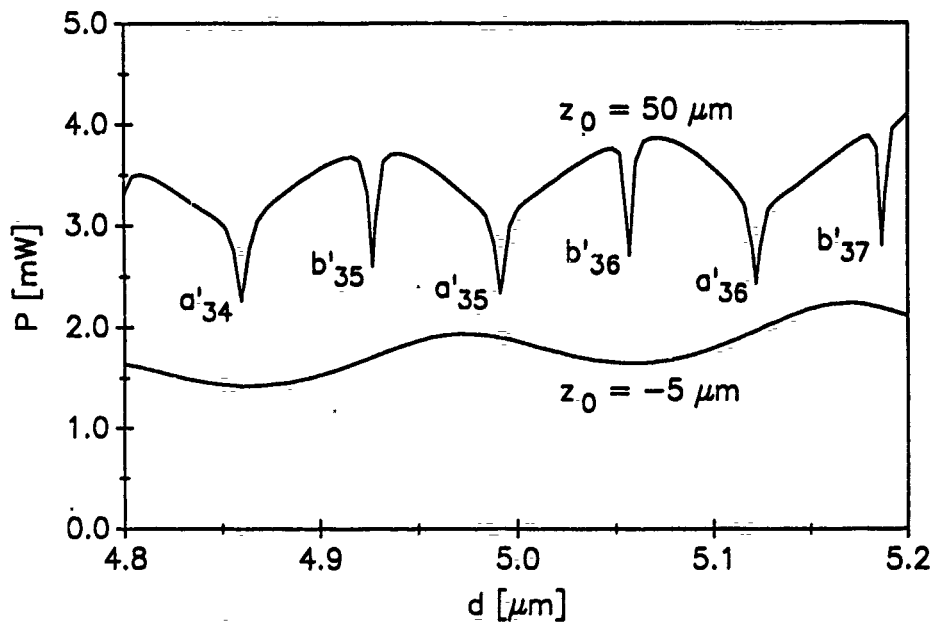


FIG. 4. Power versus droplet diameter for the optical levitation of a water droplet in air using a focused, TEM_{00} mode, linearly polarized laser beam for droplet propagation axis positions of $z_o = -5 \mu\text{m}$ and $+50 \mu\text{m}$. ($x_o = y_o = 0$, $\bar{n} = 1.334 + 1.2 \times 10^{-9}i$, $\lambda = 0.5145 \mu\text{m}$, and $w_o = 1 \mu\text{m}$.)

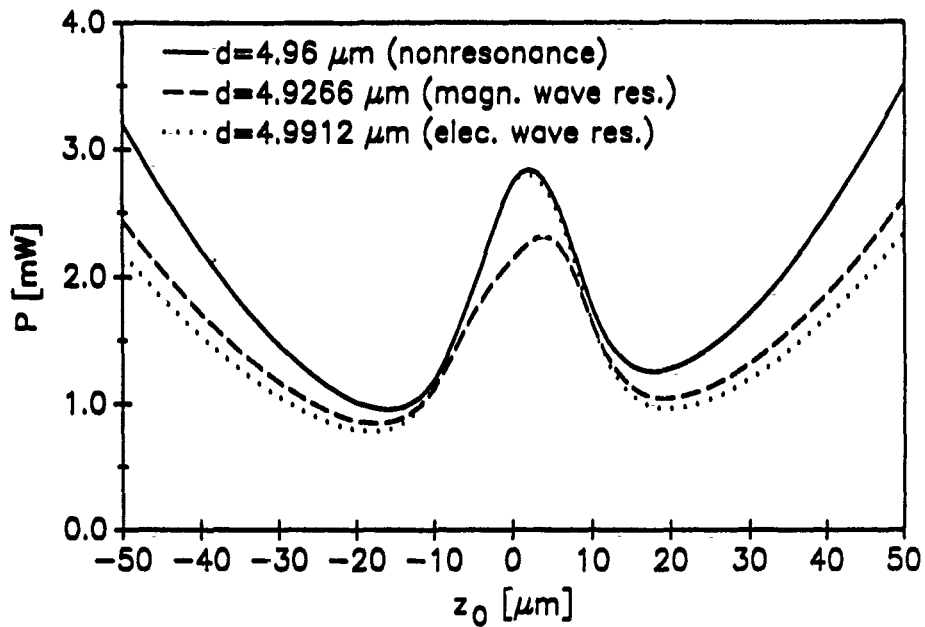


FIG. 5. Power versus propagation axis position for the optical levitation of a water droplet in air using a focused, TEM_{00} mode, linearly polarized laser beam for nonresonance ($d = 4.96 \mu m$), magnetic wave resonance ($d = 4.9266 \mu m$), and electric wave resonance ($d = 4.9912 \mu m$). ($x_0 = y_0 = 0$, $\bar{n} = 1.334 + 1.2 \times 10^{-9}i$, $\lambda = 0.5145 \mu m$, and $w_0 = 1 \mu m$.)

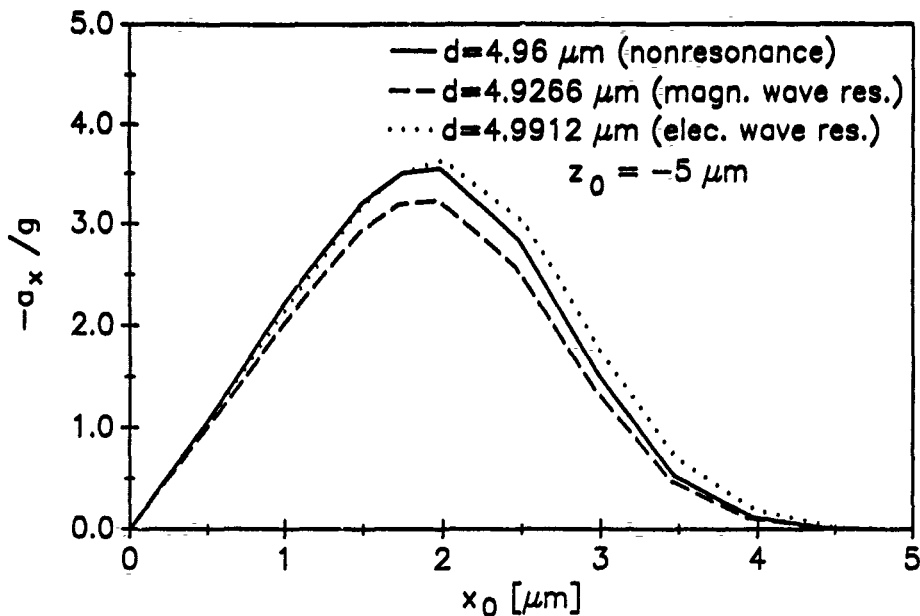


FIG. 6. x-axis acceleration versus x-axis displacement for optical levitation of a water droplet in air using a focused, TEM_{00} mode, linearly polarized (x-axis direction) laser beam at a droplet propagation axis position of $z_0 = -5 \mu m$ for nonresonance ($d = 4.96 \mu m$), magnetic wave resonance ($d = 4.9266 \mu m$), and electric wave resonance ($d = 4.9912 \mu m$). ($y_0 = 0$, $\bar{n} = 1.334 + 1.2 \times 10^{-9}i$, $\lambda = 0.5145 \mu m$, and $w_0 = 1 \mu m$.)

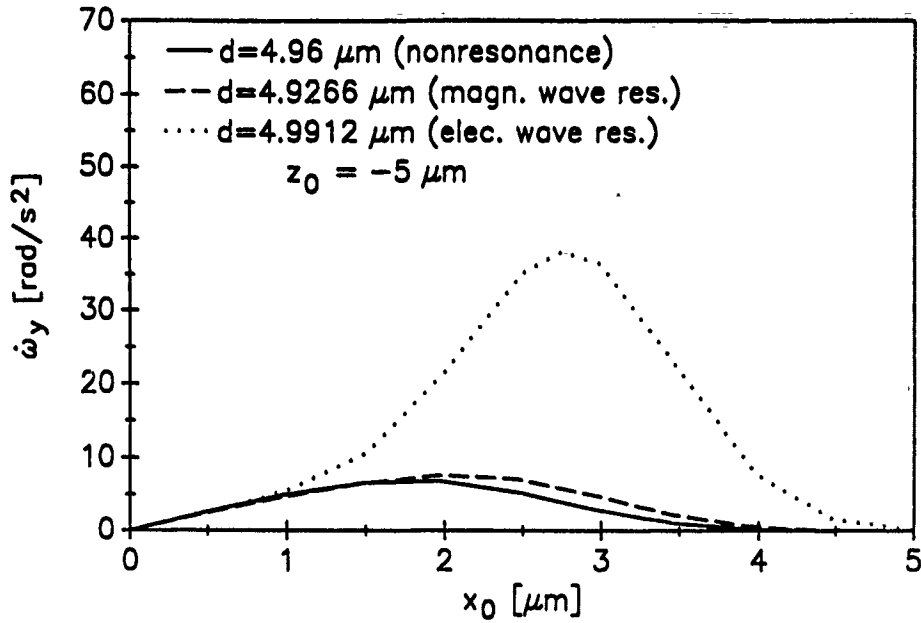


FIG. 7. y -axis angular acceleration versus x -axis displacement for optical levitation of a water droplet in air using a focused, TEM_{00} mode, linearly polarized (x -axis direction) laser beam at a droplet propagation axis position of $z_0 = -5 \mu\text{m}$ for nonresonance ($d = 4.96 \mu\text{m}$), magnetic wave resonance ($d = 4.9266 \mu\text{m}$), and electric wave resonance ($d = 4.9912 \mu\text{m}$). ($y_0 = 0$, $\bar{n} = 1.334 + 1.2 \times 10^{-9}i$, $\lambda = 0.5145 \mu\text{m}$, and $w_0 = 1 \mu\text{m}$.)

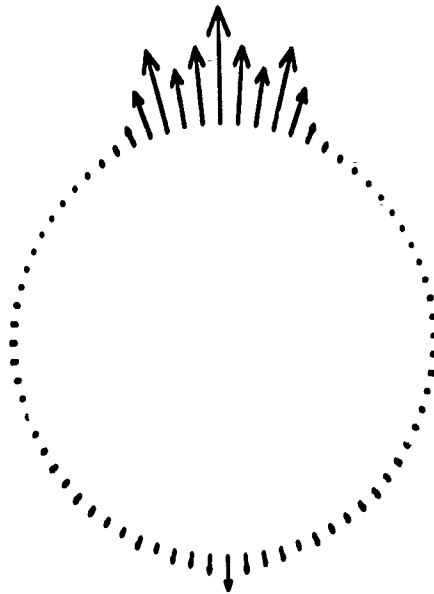


FIG. 8. Surface stress distribution in the x - z plane for a nonresonance water droplet ($d = 4.96 \mu\text{m}$) optically levitated $50 \mu\text{m}$ above the focal point of a $2 \mu\text{m}$ waist diameter, 3.52 mW , argon-ion ($\lambda = 0.5145 \mu\text{m}$) laser beam. Droplet positioned on the propagation axis. $P_{\text{max}} = 0.624 \text{ Pa}$.

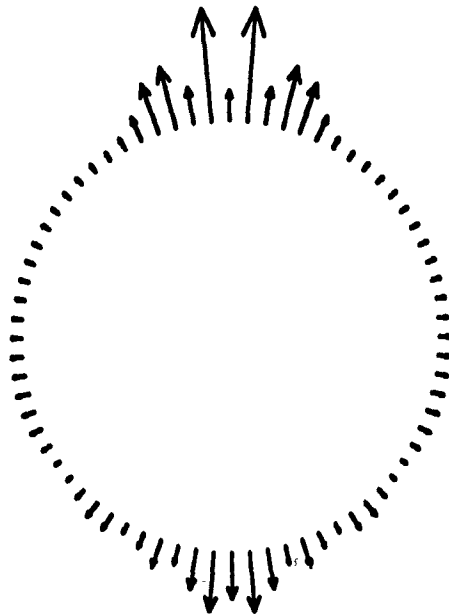


FIG. 9. Surface stress distribution in the x - z plane for an electric wave resonance water droplet ($d = 4.9912 \mu m$) optically levitated $50 \mu m$ above the focal point of a $2 \mu m$ waist diameter, $2.35 mW$, argon-ion ($\lambda = 0.5145 \mu m$) laser beam. Droplet positioned on the propagation axis. $P_{max} = 1.94 Pa$.

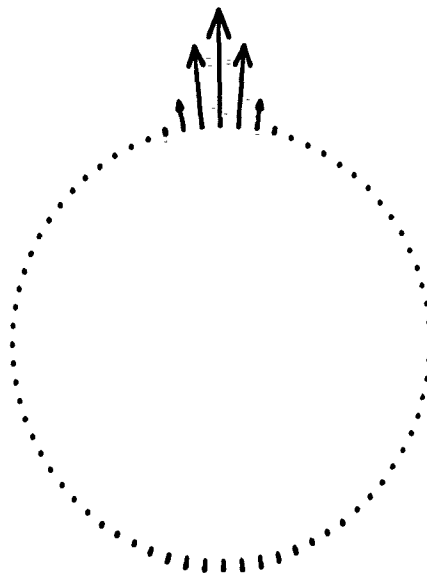


FIG. 10. Surface stress distribution in the x - z plane for a nonresonance water droplet ($d = 4.96 \mu m$) optically levitated $5 \mu m$ below the focal point of a $2 \mu m$ waist diameter, $1.91 mW$, argon-ion ($\lambda = 0.5145 \mu m$) laser beam. Droplet positioned on the propagation axis. $P_{max} = 6.46 Pa$.

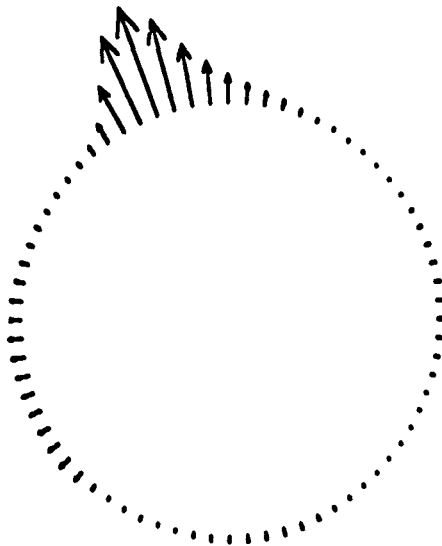


FIG. 11. Surface stress distribution in the x-z plane for a nonresonance water droplet ($d = 4.96 \mu m$) optically levitated $5 \mu m$ below the focal point of a $2 \mu m$ waist diameter, 1.91 mW , argon-ion ($\lambda = 0.5145 \mu m$) laser beam. Droplet displaced $3 \mu m$ along the x-axis. $P_{max} = 2.12 \text{ Pa}$.

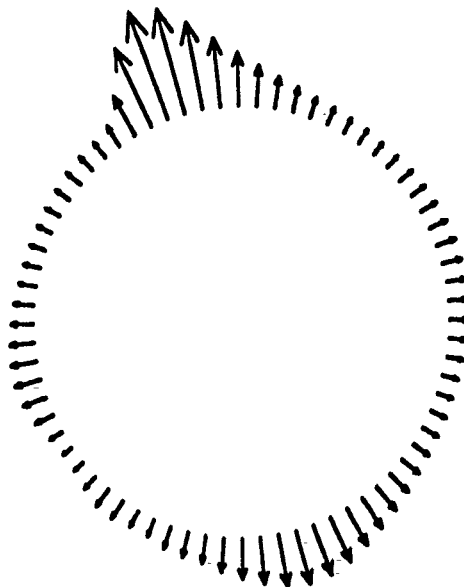


FIG. 12. Surface stress distribution in the x-z plane for an electric wave resonance water droplet ($d = 4.9912 \mu m$) optically levitated $5 \mu m$ below the focal point of a $2 \mu m$ waist diameter, 1.89 mW , argon-ion ($\lambda = 0.5145 \mu m$) laser beam. Droplet displaced $3 \mu m$ along the x-axis. $P_{max} = 13.90 \text{ Pa}$.

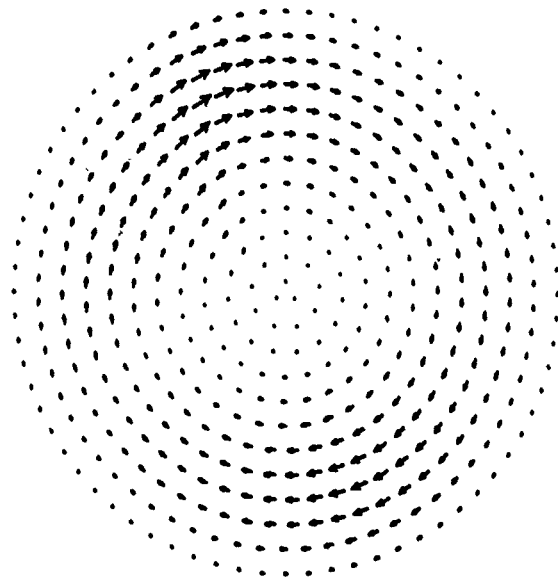


FIG. 13. Body force distribution in the x - z plane ($1.0 > r/a > 0.8$) for an electric wave resonance water droplet ($d = 4.9912 \mu\text{m}$) optically levitated $5 \mu\text{m}$ below the focal point of a $2 \mu\text{m}$ waist diameter, 1.89 mW , argon-ion ($0.5145 \mu\text{m}$) laser beam. Droplet displaced $3 \mu\text{m}$ along the x -axis. $F_{max}''' = 0.40 \text{ N/m}^3$.

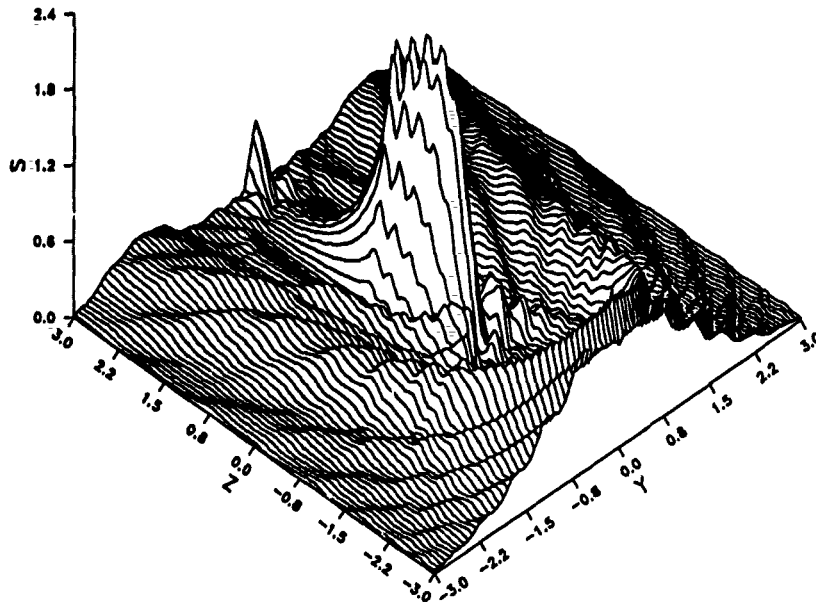


FIG 14. Normalized source function in the equatorial (y - z) plane for a transverse (x direction) electric field polarized Gaussian beam, propagating in the $+z$ axis direction (right-to-left), incident upon two adjacent spheres. $\bar{n}_1 = \bar{n}_2 = 1.179 + 0.072i$, $\alpha_1 = \alpha_2 = 13.337$, $\bar{w}_o = 2.222$, $\bar{x}_o = \bar{y}_o = 0.0$, $\bar{z}_o = -1.778$, $\bar{x}_{12} = \bar{y}_{12} = 0.0$, $\bar{z}_{12} = 3.556$, $\bar{x}_{ref} = \bar{y}_{ref} = 0.0$, $\bar{z}_{ref} = 1.778$ [$10.6 \mu\text{m}$ wavelength (CO_2 laser), $100 \mu\text{m}$ waist diameter beam incident upon two $45 \mu\text{m}$ diameter water droplets separated along the propagation axis by $35 \mu\text{m}$ surface-to-surface]

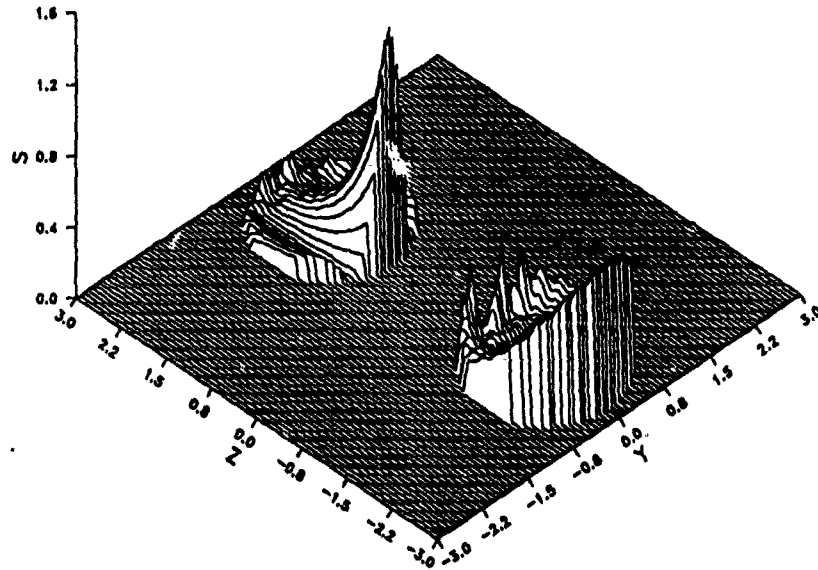


FIG 15. Normalized source function in the equatorial (y - z) plane for a transverse (x direction) electric field polarized Gaussian beam, propagating in the $+z$ axis direction (right-to-left), incident upon two adjacent spheres. (External field suppressed.) $\bar{n}_1 = \bar{n}_2 = i 1.79 + 0.072i$, $\alpha_1 = \alpha_2 = 13.337$, $\bar{w}_o = 2.222$, $\bar{x}_o = \bar{y}_o = 0.0$, $\bar{z}_o = -1.778$, $\bar{x}_{12} = \bar{y}_{12} = 0.0$, $\bar{z}_{12} = 3.556$, $\bar{x}_{ref} = \bar{y}_{ref} = 0.0$, $\bar{z}_{ref} = 1.778$ [10.6- μm wavelength (CO_2 laser), 100 μm waist diameter beam incident upon two 45 μm diameter water droplets separated along the propagation axis by 35 μm surface-to-surface.]

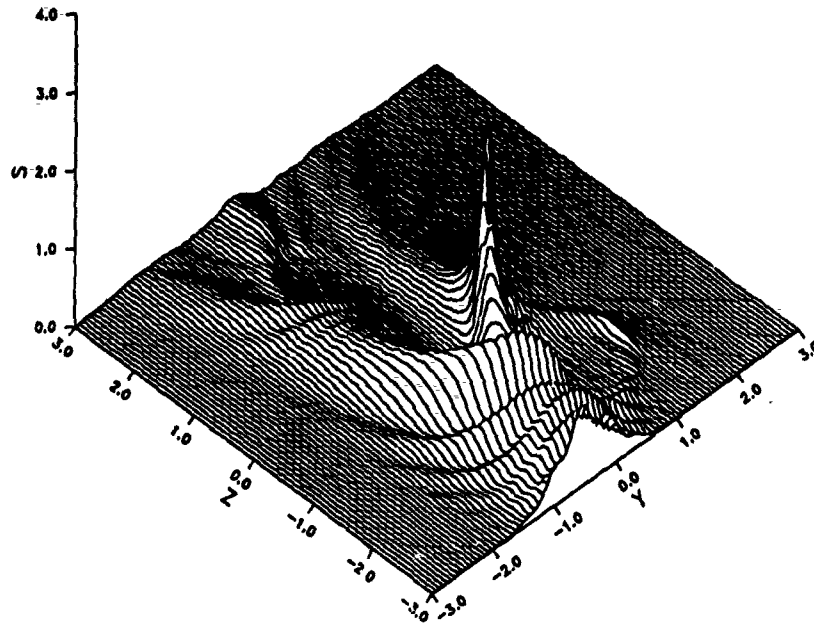


FIG 16. Normalized source function in the equatorial (y - z) plane for a transverse (x direction) electric field polarized Gaussian beam, propagating in the $+z$ axis direction (right-to-left), incident upon two adjacent spheres. $\bar{n}_1 = 1.395 + 0.0163i$, $\alpha_1 = 14.82$, $\bar{n}_2 = 1.179 + 0.072i$, $\alpha_2 = 8.89$, $\bar{w}_o = 0.8$, $\bar{x}_o = 0.0$, $\bar{y}_o = 1.0$, $\bar{z}_o = 0.0$, $\bar{x}_{12} = 0.0$, $\bar{y}_{12} = -1.0$, $\bar{z}_{12} = 3.0$, $\bar{x}_{ref} = 0.0$, $\bar{y}_{ref} = -0.5$, $\bar{z}_{ref} = 1.5$ [10.6 μm wavelength (CO_2 laser), 40 μm waist diameter beam incident upon adjacent 50 μm diameter methanol and 30 μm diameter water droplets offset in the y - z plane.]

BLANK

**ELECTROMAGNETIC SCATTERING AND DEPOLARIZATION ACROSS
ROUGH SURFACE – FULL WAVE SOLUTIONS**

Ezekiel Bahar and Guorong Huang

Department of Electrical Engineering
University of Nebraska-Lincoln
Lincoln, Nebraska 68588-0511

RECENT PUBLICATIONS, SUBMITTALS FOR PUBLICATION AND PRESENTATIONS:

A) E. Bahar, "Non Specular Scattering by Irregular Layered Media", Proceedings of the 1988 Scientific Conference on Obscuration and Aerosol Research, in press.

B) E. Bahar, International Working Group Meeting on "Wave Propagation in Random Media", Tallin, U.S.S.R. , Sept. 19-23, 1988, invited paper, "Stokes Parameters for Propagation Media with Random Distributions of Irregular Shaped Particles".

C) E. Bahar, International Working Group Meeting on "Wave Propagation in Random Media", Tallin, U.S.S.R. , Sept. 19-23, 1988, invited paper, "Scattering Depolarization and Enhanced Backscatter from Random Rough Surfaces".

D) E. Bahar, International Geoscience and Remote Sensing Symposium, Edinburgh University, Edinburgh, United Kingdom, Sept. 13-16, 1988, "The Incoherent Like and Cross Polarized Backscatter Cross Sections of an Anisotropic Rough Sea Surface with Swell," (FRA-211), 1988.

E) E. Bahar and M. Fitzwater, International Union of Radio Science (URSI) Meeting, University of Colorado, Boulder, Colorado, Jan. 4-6, 1989, "Full-Wave Copolarized Nonspecular Transmission and Reflection Scattering Matrix Elements for Rough Surfaces".

F) E. Bahar, IEEE AP-S International Symposium and URSI Radio Science Meeting, June 26-30, 1989, San Jose, California, "Physical Interpretation of the Full Wave Solutions for the Electromagnetic Fields Scattered from Irregular Stratified Media".

G) E. Bahar and R. Kubik, International Geoscience and Remote Sensing Symposium, Vancouver, Canada, July 10-14, 1989, "Scattering Cross Section Modulation for Arbitrarily Oriented Composite Rough Surfaces Unified Full Wave Approach".

H) E. Bahar and M. Haugland, International Geoscience and Remote Sensing Symposium, Vancouver, Canada, July 10-14, 1989, "Interpretation of the Appollo Lunar Surface Data Using the Unified Full Wave and the Two Scale Full Wave Approach".

I) E. Bahar, Progress in Electromagnetic Research Symposium, MIT, Cambridge,

Massachusetts, July 25-26, 1989, "Diffuse Specific Intensities and Backscatter Enhancement for Random Distribution of Finitely Conducting Particles with Rough Surfaces".

J) E. Bahar, Progress in Electromagnetic Research Symposium, MIT, Cambridge, Massachusetts, July 25-26, 1989, "Scattering Cross Sections and Backscatter Enhancement for Two Dimensional Rough Surfaces with Different Correlation Lengths".

K) E. Bahar, URSI International Symposium on Electromagnetic Theory at the Royal Institute of Technology, Stockholm, Sweden, August 14-17, 1989, "Physical Models of Nonspecular Scattering in Irregular Stratified Media".

L) E. Bahar and R. Kubik, International Union of Radio Science Commission F Symposium on Radio and Nonionized Media at La Londe-les-Maures, France, Sept. 11-15, 1989, "Synthetic Aperture Radar Polarimetric Images for Swell and Ship Wakes - Full Wave Approach".

M) E. Bahar and G. Huang, 1989 CRDEC Scientific Conference on Obscuration and Aerosol Research, Aberdeen, MD, June 26-30, 1989, "Transmission Scattering and Depolarization Across Rough Surfaces - Full Wave Solutions".

N) E. Bahar, National Science Foundation Workshop on Future Directions in Electromagnetic Research, Panel member on Scattering and Inverse Scattering Techniques, July 27, 1989, Boston, Massachusetts, Invited paper on Electromagnetic Scattering by Randomly Rough Boundaries.

O) E. Bahar, "Generalized Fourier Transforms for the Acoustic Pressure and Velocity in Compressible Viscous Stratified Media", Wave-Motion, in press.

P) E. Bahar, "Scattering of Acoustic Waves in Irregular Layered Media Full Wave Solutions", Wave Motion, in press.

Q) E. Bahar, "Full Wave Solutions for the Scattering of Acoustic Waves Excited by Arbitrary Source Distributions in Irregular Layered Media", Wave Motion, in press.

R) E. Bahar, "Physical Interpretation of the Full Wave Solutions for Electromagnetic Fields Scattered from Irregular Stratified Media", Radio Science, Vol. 23, No. 5, pp. 749-759, Sept.-Oct. 1988.

S) E. Bahar and M. A. Fitzwater, "Full Wave - Co-Polarized Non Specular Transmission and Reflection Scattering Matrix Elements for Rough Surfaces", Journal of the Optical Society of America, A, Vol. 5, pp. 1873-1882, Nov. 1988.

T) E. Bahar and M. A. Fitzwater, "Full Wave Physical Models of Nonspecular Scattering in Irregular Stratified Media", IEEE Transactions on Antennas and Propagation, in press.

U) E. Bahar and M. A. Fitzwater, "Depolarization and Backscatter Enhancement in Light Scattering from Random Rough Surfaces - Theory and Experiment", Journal of the Optical Society of America, A, Vol. 6, pp. 33-43, January 1989.

V) E. Bahar, C. M. Hertzinger and M. A. Fitzwater, "The Incoherent Like and Cross Polarized

Backscatter Cross Sections of an Anisotropic Rough Sea Surface with Swell, *Journal of Geophysical Research - Oceans*, Vol. 94, No. C2, pp. 2159-2169, February 1989.

W) E. Bahar, "Acoustic Scattering by Two-Dimensionally Rough Interfaces Between Dissipative Acoustic Media - Full Wave, Physical Acoustics and Perturbation Solutions", Submitted for review.

X) E. Bahar and M. A. Fitzwater, "Scattering Cross Sections for Two-Dimensional Rough Surfaces with Different Correlation Lengths", *Journal of Wave-Material Interaction*, Vol. 3, No. 3, pp. 199-218, July 1988.

Y) E. Bahar and R. Kubik, "Scattering Cross Section Modulation for Arbitrarily Oriented Composite Rough Surfaces: Unified Full Wave Approach", *Proceedings of the IGARSS '89 Conference on Remote Sensing*, Vol. 3, pp. 1292-1295, July 10-14, 1989, Vancouver, Canada.

Z) E. Bahar and M. Haugland, "Interpretation of the Apollo Lunar Surface Data Using the Unified and the Two Scale Full Wave Approach", *Proceedings of the IGARSS '89 Conference on Remote Sensing*, Vol. 3, pp. 1296-1299, July 10-14, 1989, Vancouver, Canada.

AA) E. Bahar, "Physical Models of Nonspecular Scattering in Irregular Stratified Media", *Proceeding of the 1989 Union of the International Radio Science Symposium on Electromagnetic Theory*, pp. 503-505 August 1989, Stockholm, Sweden.

BB) E. Bahar, **Scattering Cross Sections and Backscatter Enhancement for Two Dimensional Rough Surfaces with Different Correlation Lengths**, *Proceedings of Progress in Electromagnetic Research Symposium*, Boston, Massachusetts, pp. 146-147, July, 1989.

CC) E. Bahar, **Diffuse Specific Intensities and Backscatter Enhancement from Random Distributions of Finitely Conducting Particles with Rough Surfaces**, *Proceedings of Progress in Electromagnetic Research Symposium*, Boston, Massachusetts, pp. 398-399, July, 1989.

DD) E. Bahar, **Electromagnetic Wave Scattering by Randomly Rough Boundaries**, Invited paper on review on **Progress and Emerging Future Directions - Scattering and Inverse Scattering Techniques Panel**, *Proceedings of the National Science Foundation Workshop on Future Direction in Electromagnetic Research*, Boston, Massachusetts, July, 1989, in press.

EE) E. Bahar and R. Kubik, "Synthetic Aperture Radar Polarimetric Images for Swell and Ship Wakes - Full Wave Approach", *Proceedings of the International Union of Radio Science Symposium on Radio Wave Propagation and Remote Sensing*, September, 1989, pp. 7.1.1-7.1.4, La Londe-les-Maures France.

ABSTRACT

Full wave solutions are derived for the vertically and horizontally polarized waves scattered across a two dimensionally rough interface separating two different propagating media. Since the normal to the rough surface is not restricted to the reference plane of incidence, the waves are depolarized upon scattering and the single scattered radiation fields are expressed as integrals of a surface element transmission scattering matrix that also account for coupling between the vertically and horizontally polarized waves. The integrations are over the rough surface area as well as the complete two dimensional wave spectrum of the radiation fields. The full wave solutions satisfy the duality and reciprocity relationships in electromagnetic theory and they are invariant to coordinate transformations. It is shown that in the high frequency limit the full wave solutions reduce to the physical optics solutions, while in the low frequency limit (for very small mean square height and negligible slopes) the full wave solutions reduce to Rice's small perturbation solutions. Thus the full wave solution accounts for specular point scattering as well as diffuse, Bragg-type scattering in a unified self consistent manner. It is therefore not necessary to use hybrid perturbed - physical optics solutions based on two scale models of composite surfaces with large and small roughness scales.

1. INTRODUCTION

Radio waves incident upon a rough surface separating two propagating media characterized by different electric permittivities and magnetic permeabilities, scatter diffusely as they are reflected off or transmitted across the rough surface. When the normal to the rough surface is not restricted to the reference plane of incidence, the reflected and transmitted scattered waves are also depolarized. In this work full wave solutions are derived for the single scattered waves that are transmitted across a two dimensionally rough interface. It is an extension to the two dimensional scalar scattering problem in which the normal to the rough surface was restricted to the reference plane of incidence (Bahar and Fitzwater 1988). Thus in this work it is necessary to solve the vector scattering problem in which the vertically and horizontally polarized waves are coupled and the scattering is characterized by a 2×2 surface element transmission scattering matrix.

The vertically and horizontally polarized fields that are scattered and depolarized across the rough surface are expressed as integrals of the slope dependent scattering matrices and a height dependent phase term. The integration is over the rough surface and the complete radiation wave spectrum. For observation points at large distances from the rough surface, the integrals over the wave spectrum can be performed analytically using the steepest descent method.

It is shown that in the high frequency limit, when the major contributions to the surface integral come from the neighborhood of the stationary phase (specular) points of the rough surface (where the normal to the rough surface and the incident and scatter wave vectors satisfy Snell's law), the full wave solutions reduce to the physical optics solutions based on the Kirchhoff approximations of the surface fields (Beckmann and Spizzichino 1963). On the other hand, in the low frequency limit, when the mean square height is very small compared to the electromagnetic wavelength and when the surface slopes are negligibly small, the full wave solutions reduce to Rice's (1951) small perturbation solutions. Thus on applying the unified full wave approach to rough surface scattering problems, it is not necessary to artificially decompose the composite rough surface into surfaces with large and small scales of roughness. The hybrid perturbed - physical optics solutions based on the two scale models of the rough surfaces depend on the wave number where the rough surface spectral splitting is assumed to occur (Brown 1978) and they fail to account for backscatter depolarization by the large scale surface.

In Section 2 the rough surface scattering problem is formulated for a surface whose normal is restricted to the x, y plane. The full wave approach is outlined and the explicit expressions for the vertically and horizontally polarized scattered fields are presented in matrix form. The principal properties of these full wave solutions (reciprocity, duality etc.) are discussed and their relationships to other solutions are considered. In Section 3 the restrictions on the surface normal are removed and the full wave single scatter solutions are presented for general two dimensionally rough surfaces. These solutions are invariant to coordinate transformations.

2. FORMULATION OF THE PROBLEM

Full wave expressions are derived for the electromagnetic fields scattered across a rough surface

$$\begin{aligned} y &= h(x) & \text{for } |x| < L \\ y &= 0 & \text{for } |x| > L \end{aligned} \quad (2.1)$$

separating two semi-infinite media characterized by the complex permittivity ϵ and permeability μ

$$\begin{aligned} \epsilon &= \epsilon_0 & \mu &= \mu_0 & \text{for } y > h \\ \epsilon &= \epsilon_1 = \epsilon_r \epsilon_0 & \mu &= \mu_1 = \mu_0 \mu_r & \text{for } y < h \end{aligned} \quad (2.2)$$

in which the dimensionless quantities ϵ_r and μ_r are the relative permittivity and permeability, respectively. Thus the normal to the rough surface is in the x, y plane,

$$\vec{n} = \frac{-h_x \vec{a}_x + \vec{a}_y}{(h_x^2 + 1)^{1/2}}, \quad h_x = \frac{\partial h}{\partial x} \quad (2.3)$$

The excitation is assumed to be a uniform plane wave incident on the rough interface from medium

$y > h$ in the direction

$$\vec{n}_0^i = \sin\theta_0^i \cos\phi^i \vec{a}_x - \cos\theta_0^i \vec{a}_y + \sin\theta_0^i \sin\phi^i \vec{a}_z \quad (2.4)$$

Thus scattering is not restricted to the incident plane (normal to $\vec{n}_0^i \times \vec{a}_y$) and the incident wave is depolarized by the rough interface. To obtain the full wave solution to the three dimensional rough surface scattering problem (see Fig. 1), the transverse (y, z) components of the electric and magnetic fields are expressed completely in terms of generalized field transforms (Bahar 1973a). The complete field transforms are substituted into Maxwell's equations. On imposing the exact boundary conditions at the rough interface and using the biorthogonal properties of the basis functions, Maxwell's equations are converted into rigorous sets of generalized telegraphists' equations for the forward and backward propagating wave amplitudes (Bahar 1973b). A second order iterative solution to the generalized telegraphists' equations accounts for first order (single) scattering by the rough surface. In earlier work the explicit expressions were derived for the scattering fields reflected back into the medium $y > h(x)$. In this work the explicit full wave expressions are derived for the like and cross polarized fields scattered across the rough interface into medium $y < h(x)$. Thus these single scattered fields are expressed as an integral involving the rough surface element transmission scattering matrix.

$$F_{10} = \begin{bmatrix} F_{10}^{VV} & F_{10}^{VH} \\ F_{10}^{HV} & F_{10}^{HH} \end{bmatrix} \quad (2.5a)$$

The first and second subscripts 1, 0 denote the medium of the scattered ($y < h$) and incident ($y > h$) waves and the first and second superscripts V, H denote the polarization of the incident and scattered waves, respectively. Thus F^{PQ} are the like and cross polarized scattering coefficients for $P = Q$ and $P \neq Q$, respectively. The two element column matrices G_1^f and G_0^i denote the scattered and incident vertically and horizontally polarized radiation fields,

$$G_1^f = \begin{bmatrix} E_1^{Vf} \\ E_1^{Hf} \end{bmatrix} = \eta_1 \begin{bmatrix} H_1^{Vf} \\ -H_1^{Hf} \end{bmatrix}, \quad G_0^i = \begin{bmatrix} E_0^{Vi} \\ E_0^{Hi} \end{bmatrix} = \eta_0 \begin{bmatrix} H_0^{Vi} \\ -H_0^{Hi} \end{bmatrix} \quad (2.5b)$$

in which $\eta_j = \sqrt{\mu_j/\epsilon_j}$ is the intrinsic wave impedance for $j = 0, 1$. The full wave single scattered fields radiated across the rough interface can be expressed in matrix form as follows,

$$G_1^f = \frac{1}{(2\pi i)^2} \iiint_{-\infty}^{\infty} C_1 F_{10} G_0^i e^{-i\vec{k}_1 \cdot \vec{r}} \{ e^{i(\vec{k}_1 - \vec{k}_0) \cdot \vec{r}_s} - e^{i(\vec{k}_1 - \vec{k}_0) \cdot \vec{r}_t} \} \left(\frac{k_z}{i} \right) dx, dz, dv_1, dw = G_{11}^f - G_{12}^f \quad (2.6)$$

in which the scattered and incident wave vectors in medium 1 and 0 are

$$\vec{k}_1 = u \vec{a}_x - v_1 \vec{a}_y + w \vec{a}_z, \quad v_1 = k_1 \cos \theta_1 = k_1 C_1 \quad (2.7a)$$

$$\vec{k}_0^i = k_0 \vec{n}_0^i \quad (2.7b)$$

and the corresponding wave numbers are $k_j = \omega \sqrt{\mu_j \epsilon_j}$. The position vector to a point on the rough surface is

$$\vec{r}_s = x_s \vec{a}_x + h(x_s) \vec{a}_y + z_s \vec{a}_z \equiv \vec{r}_t + h(x_s) \vec{a}_y \quad (2.8)$$

and \vec{r}_t is its component in the x, z (reference) plane. The position vector to the observation point (x, y, z) is \vec{r} . The integration is over the rough surface (dx, dz_s) and the radiation field spectrum (dv, dw). In (2.6) the second term G_{12}^j can be shown to be the primary field transmitted across an unperturbed planar surface $y = 0$ and the first term G_{11}^j is the total (specularly and diffusely) scattered field (Bahar and Fitzwater 1988). For $|k_{1z}| \gg 1$, the far field approximation for the scattered field can be obtained on integrating with respect to dv, dw using the steepest descent method.

Thus the like and cross polarized scattered fields transmitted across the rough interface in the direction

$$\vec{n}_1^j = \vec{k}_1^j / k_1^j = \sin \theta_1^j \cos \phi^j \vec{a}_x - \cos \theta_1^j \vec{a}_y + \sin \theta_1^j \sin \phi^j \vec{a}_z \quad (2.9)$$

is given by

$$G_1^j = G_1 \int_{-L}^L \int_{-L}^L C_1^j F_{10}(\theta^j, \theta^i) G_0^i \exp\{i(\vec{k}_1^j - \vec{k}_0^i) \cdot \vec{r}_s\} dx, dz_s \quad (2.10)$$

where

$$G_1 = -\frac{ik_1}{2\pi r^j} e^{-ik_1 r^j} \quad (2.10a)$$

The explicit expressions for the elements of the transmission scattering matrix F_{10} are

$$C_1^j F_{10}^{VV} = \frac{2\eta_r C_1^j C_0^i}{(C_0^j + \eta_r C_1^j)(C_0^i + \eta_r C_1^i)(C_0^i - n_r C_1^i)} \{(1 - \mu_r) \cos(\phi^j - \phi^i) + (\frac{1}{\epsilon_r} - 1)[S_0^j S_0^i + n_r C_0^j C_1^i \cos(\phi^j - \phi^i)]\} \quad (2.11a)$$

$$C_1^j F_{10}^{HH} = \frac{2C_1^j C_0^i}{(C_0^j + C_1^j/\eta_r)(C_0^i + C_1^i/\eta_r)(C_0^i - n_r C_1^i)} \{(1 - \epsilon_r) \cos(\phi^j - \phi^i) + (\frac{1}{\mu_r} - 1)[S_0^j S_0^i + n_r C_0^j C_1^i \cos(\phi^j - \phi^i)]\} \quad (2.11b)$$

$$C_1^j F_{10}^{VH} = \frac{2\eta_r C_1^j C_0^i \sin(\phi^j - \phi^i)}{(C_0^j + \eta_r C_1^j)(C_0^i + C_1^i/\eta_r)(C_0^i - n_r C_1^i)} \{n_r C_1^i (\frac{1}{\mu_r} - 1) + C_0^i (1 - \epsilon_r)\} \quad (2.11c)$$

$$C_1^j F_{10}^{HV} = - \frac{2C_1^j C_0^i \sin(\phi^j - \phi^i)}{(C_0^j + C_1^j/\eta_r)(C_0^i + \eta_r C_1^i)(C_0^i - n_r C_1^j)} \{n_r C_1^i (\frac{1}{\epsilon_r} - 1) + C_0^j (1 - \mu_r)\} \quad (2.11d)$$

in which $\eta_r = \sqrt{\mu_r/\epsilon_r}$ and $n_r = \sqrt{\mu_r \epsilon_r}$ are the relative intrinsic impedance and the refractive index.

The sines and cosines of the angles of incidence and scatter in medium $j = 0, 1$ are S_j^i, S_j^j, C_j^i and C_j^j , respectively. In view of Snell's law

$$k_0 S_0^i = k_1 S_1^i \quad \text{and} \quad k_0 S_0^j = k_1 S_1^j \quad (2.12)$$

The expressions for the transmission scattering matrix are in agreement with the reciprocity relationships in electromagnetic theory thus for $P = Q$ and $P \neq Q$

$$\eta_0 C_0^j F_{01}^{PQ}(\vec{k}_1^j, \vec{k}_0^i) = \eta_1 C_1^j F_{10}^{QP}(-\vec{k}_0^i, -\vec{k}_1^j) \quad (2.13)$$

in which F_{01} denotes the transmission scattering coefficients for waves incident in medium 1 ($y < h$). The scattering matrix elements also satisfy the duality relationships in electromagnetic theory. For scattering in the specular direction (the incident and scattered waves are related by Snell's law) the like-polarized scattering coefficients are related to the Fresnel transmission coefficients for the vertically and horizontally polarized waves.

$$F_{10}^{VV}(\theta_1^j = \theta_1^i) = \eta_r T_{10}^{VV}(\theta_1), \quad F_{10}^{HH}(\theta_1^j = \theta_1^i) = T_{10}^{HH}(\theta_1) \quad (2.14)$$

It is interesting to note that for $\theta_1^j = 0$, the like and cross polarized coefficient are related as follows

$$- F_{10}^{HV}(\phi^j = \phi + \frac{\pi}{2}) = F_{10}^{VV}(\phi^j = \phi), \quad F_{01}^{HV}(\phi^j = \phi + \frac{\pi}{2}) = F_{01}^{VV}(\phi^j = \phi) \quad (2.15a)$$

$$F_{10}^{VH}(\phi^j = \phi + \frac{\pi}{2}) = F_{10}^{HH}(\phi^j = \phi), \quad - F_{01}^{VH}(\phi^j = \phi + \frac{\pi}{2}) = F_{01}^{HH}(\phi^j = \phi) \quad (2.15b)$$

3. FULL-WAVE SCATTERING ACROSS TWO-DIMENSIONALLY ROUGH SURFACES WITH ARBITRARY SLOPES

In order to apply the single scatter solutions in Section 2 to rough surfaces with arbitrary slope angles γ and δ , \vec{n} in (2.3) is replaced by

$$\begin{aligned} \vec{n} &= \sin\gamma \cos\delta \vec{a}_x + \cos\gamma \vec{a}_y + \sin\gamma \sin\delta \vec{a}_z \\ &= (-h_x \vec{a}_x + \vec{a} - h_z \vec{a}_z) / (h_x^2 + h_z^2 + 1)^{1/2}, \end{aligned} \quad (3.1)$$

and it is necessary to perform the following transformations. The scattering matrix in (2.5) is transformed as follows

$$F_{10} \rightarrow T_1^j F_{10}^n T_0^i \quad (3.2)$$

where the 2×2 matrix T_0^i transforms the incident vertically and horizontally polarized waves in the reference plane of incidence ($\vec{n}_0^i \times \vec{a}_y$) to incident vertically and horizontally polarized waves in the local plane of the incidence ($\vec{n}_0^i \times \vec{n}$). Similarly, the 2×2 matrix T_1^j transforms the scattered vertically and horizontally polarized waves in the local scatter plane ($\vec{n}_1^j \times \vec{n}$) back to the scattered vertically

and horizontally polarized waves in the reference scatter plane ($\vec{n}_1^f \times \vec{a}_y$) (Bahar 1981). Furthermore, the incidence and scatter angles appearing in the expressions for the scattering coefficients F_{10}^n are the local angles of incidence and scatter. Thus for instance (Bahar 1981),

$$C_1^f \rightarrow C_1^{fn} = -\vec{n}_1^f \cdot \vec{n} \quad (3.3a)$$

$$C_0^i \rightarrow C_0^{in} = -\vec{n}_0^i \cdot \vec{n} \quad (3.3b)$$

Furthermore the rough surface element in (2.6) is transformed as follows

$$dx_s dz_s \rightarrow dA = dx_s dz_s / (\vec{n} \cdot \vec{a}_y) \quad (3.4)$$

Thus for rough surfaces with large slopes (2.10) is rewritten as follows

$$G_1^f = G_1 \iint_{A_i} C_1^{fn} T_1^f F_{10}^n T_0^i G_0^i \exp\{i(\vec{k}_1^f - \vec{k}_0^i) \cdot \vec{r}_s\} dA \quad (3.5)$$

in which G_1 is given by (2.10a) and A_i is the illuminated area on the rough surface. At the specular points of the rough surface where the expression for the phase in (3.5), $(\vec{k}_1^f - \vec{k}_0^i) \cdot \vec{r}_s$ is stationary, the normal to the rough surface \vec{n} satisfies the relationship

$$\vec{n} \times (n_r \vec{n}_1^f - \vec{n}_0^i) = 0 \quad (3.6)$$

Thus the incident and scattered waves vectors satisfy Snell's law at the stationary phase points where $\vec{n} \rightarrow \vec{n}_s$ is parallel to the vector $n_r \vec{n}_1^f - \vec{n}_0^i$. At these stationary phase points, the like polarized scattering coefficients are related to the Fresnel transmission coefficients

$$F_{10}^{VV}(\vec{n} \rightarrow \vec{n}_s) = \eta_r T_{10}^{VV}(\theta_s) \quad (3.7a)$$

$$F_{10}^{HH}(\vec{n} \rightarrow \vec{n}_s) = T_{10}^{HH}(\theta_s) \quad (3.7b)$$

where

$$\cos \theta_{1s} = -\vec{n}_1^f \cdot \vec{n}_s \quad \text{and} \quad \cos \theta_{0s} = -\vec{n}_0^i \cdot \vec{n}_s. \quad (3.7c)$$

Thus it can readily be shown that in the high frequency limit when the major contributions to the scattered fields come from the neighborhood of the specular points, the full wave solution reduces to the physical optics solution based on the Kirchhoff approximations of the surface fields (Beckmann and Spizzichino). On the other hand, in the low frequency limit when the slopes of the rough surfaces are negligibly small ($\vec{n} \rightarrow \vec{a}_y$) and the mean square height $\langle h^2 \rangle$ of the rough surface is very small compared to the wavelength ($k_0^2 \langle h^2 \rangle \ll 1$), the full wave solution (2.5) reduces precisely to the small perturbation solution of Rice (Rice 1951, Tsang et al 1985). Thus on applying the full wave approach to composite surfaces with different roughness scales it is not necessary to artificially decompose the rough surface into a small scale surface and a large scale surface that are assumed to be statistically independent (Wright 1868; Valenzuela 1968; Barrick 1970; Brown 1978).

6. CONCLUDING REMARKS

The full wave solutions, for the electromagnetic waves scattered across a two dimensionally rough interface between two different propagating media, are expressed in matrix form as integrals of the rough surface element scattering matrix. The integrations are over the rough surface area and the two dimensional radiation field wave number spectra. These solutions satisfy the reciprocity and duality relationships in electromagnetic theory and they are invariant to coordinate transformations. In the high frequency limit they reduce to the physical optics solutions and in the low frequency limit they reduce to Rice's small perturbation solution. Thus the full wave solution accounts for specular point scattering as well as diffuse, Bragg-type scattering in a unified self consistent manner and there is no need to adopt a two scale model of composite rough surfaces.

ACKNOWLEDGMENTS

The work reported in this paper is sponsored by the U.S Army AMCCOM contract number DAAA15-86-K-0023/P00004. The authors wish to thank A. Carrieri for his encouragement and suggestions.

REFERENCES

- [1] E. Bahar, "Depolarization of Electromagnetic Waves Excited by Distributions of Electric and Magnetic Sources in Inhomogenous Multilayered Structures of Arbitrary Thickness - Generalized Field Transforms", J. Math. Phys. Vol 14 no 11, 1502-1509 (1973a)
- [2] E. Bahar, "Depolarization of Electromagnetic Waves Excited by Distributions of Electric and Magnetic Sources in Inhomogenous Multilayered Structures of Arbitrary Thickness - Full Wave Solutions", J. Math. Phys. Vol 14 no 11, 1510-1515 (1973b)
- [3] E. Bahar, "Full-Wave Solutions for the Depolarization of the Scattered Radiation Fields by Rough Surface with Arbitrary Slope", IEEE Trans. Antennas Propag. AP-29, no. 3 (1981)
- [4] E. Bahar and M. A. Fitzwater, "Full Wave Copolarized Nonspecular Transmission and Reflection Scattering Matrix Elements for Rough Surfaces", J. Opt. Soc. Am. A5, 1873-1882 (1988)
- [5] D. E. Barrick, "Rough Surfaces", in Radar Cross Section Handbook, G. T. Rudd, ed. (Plenum, New York, 1970) chap. 9
- [6] P. Beckmann and A. Spizzichino, "The Scattering of Electromagnetic Waves from Rough Surfaces", (MacMillan, New York, 1963)
- [7] G. S. Brown, "Backscattering from a Gaussian-distributed perfectly conducting rough surface", IEEE Trans. Antennas Propag., AP-26(3), 472-482, 1978.
- [8] S. O. Rice, "Reflection of Electromagnetic Waves from A Slightly Rough Surface", Commun. Pure

- Appl. Math. 4, 351-378 (1951)
- [9] L. Tsang, J. A. Kong and R. T. Shin, "Theory of Microwave Remote Sensing", (Wiley, New York, 1985)
- [10] G. R. Valenzuela, "Scattering of Electromagnetic Waves from A Tilted Slightly Rough Surface", Radio Sci. 3, 1057-1066 (1968)
- [11] J. W. Wright, "A New Model for Sea Clutter", IEEE Trans. Antennas Propag. AP-16, 217-223 (1968)

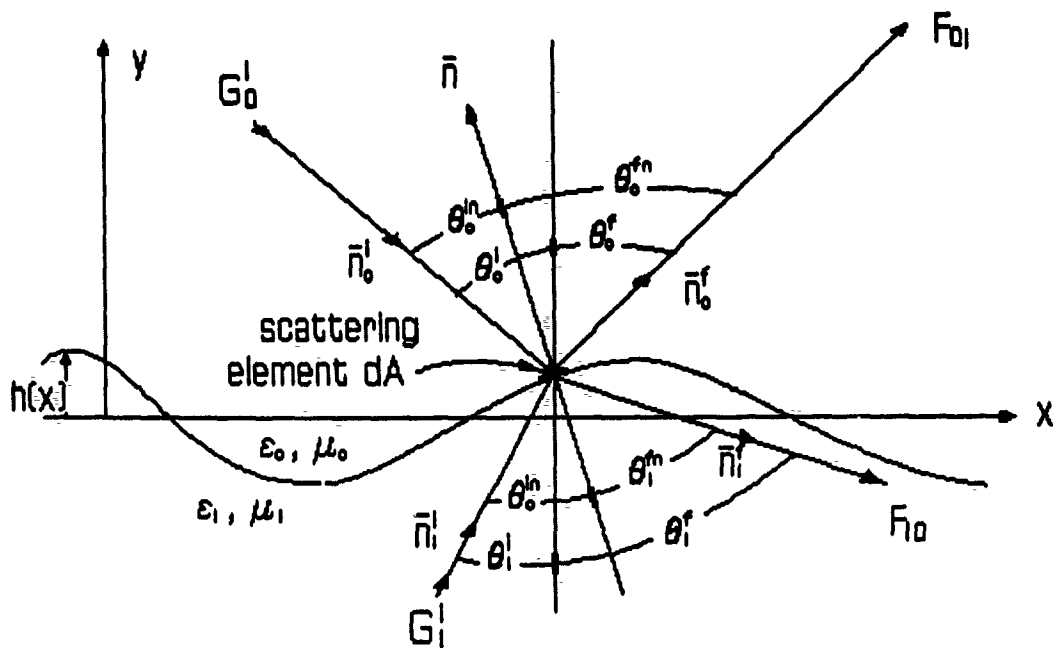


Fig. 1 Electromagnetic Scattering across rough surface

BLANK

HOMOTOPY
AS AN ELECTROMAGNETIC DESIGN
METHOD
APPLIED TO A PERFECT
CONDUCTOR COVERED WITH
BIANISOTROPIC COATINGS
HAVING NONTRIVIALY DISPERSIVE
MAGNETIC PROPERTIES

D.K. Cohoon
West Chester University
Department of Mathematics
and Computer Science
West Chester, PA 19383

R. M. Purcell
340 Media Station Road
Media, PA 19063

October 25, 1989

The homotopy method is proposed as a method of going from the solution of a simple problem to the solution of a complex problem along a homotopy path. In this paper we reduce the problem of keeping track of modes of propagation of radiation in multilayer structures comprised of electromagnetically anisotropic or possibly bianisotropic materials to that of solving, in open subsets Ω of \mathbb{C}^N , systems of nonlinear equations.

Extensions of parameters to abstract algebras in which the system of equations have trivial solutions is used to develop starting values for a system of differential equations whose solution at the end point represents the solution of the electromagnetic problem of interest.

We apply the method to the problem of determining modes of propagation of electromagnetic energy in an anisotropic coating on a perfect conductor. The problem is to track the modes of propagation as the frequency of the radiation and the thickness of the coating change in a smooth manner. Magnetically the coating passes through a region of anomalous dispersion as the frequency changes.

1 INTRODUCTION

We suppose that $f(z)$, $g(z)$, and $h(z)$ are functions from an open subset Ω of \mathbb{C}^N into a topological vector space \mathcal{V} . We suppose that their zero sets are respectively Z_f , Z_g , and Z_h . Suppose that \mathcal{A} is a mapping from $h(\Omega)$ into Ω and we seek a solution of the equation

$$f(\mathcal{A}h(z)) = g(z) \tag{1.1}$$

under the assumption that

$$Z_g \cap Z_h = \emptyset$$

We create a starting solution by introducing a one parameter family of mappings $\mathcal{A}(s)$ and solutions $z(s)$ satisfying equation (1.1) and having the initial conditions

$$\mathcal{A}(0)h(z_{(j,g)}) = z_{(i,f)} \quad (1.2)$$

and

$$z(0) = z_{(j,g)} \quad (1.3)$$

which is the j th zero of $g(z)$ in the set Z_g of zeros. Then we may develop a system of differential equations in the parameter s of the form

$$z'(s) = C(s, z(s)) \quad (1.4)$$

in the real parameter s whose solution $z(1)$ at $s = 1$ gives a solution of equation (1.1). This is a variant of the globally convergent homotopy method of Chow and Yorke or the general path following methods of Garcia ([1]). The solution is started off by simply observing that

$$z(0) = z_{(i,f)} \quad (1.5)$$

Then collecting terms in the equation

$$\frac{d}{ds} f(C(s)h(z(s))) = \frac{d}{ds} g(z(s)) \quad (1.6)$$

yields an ordinary differential equation in $z(s)$.

2 A TRANSCENDENTAL EQUATION

Suppose we wished to solve the equation

$$f(Az) = \sin(Az) = Bz + C = g(z) \quad (2.1)$$

where A , B , and C are complex. Then we would have

$$Z_f = \{n\pi : n \in \mathbf{Z}\} \quad (2.2)$$

and

$$Z_g = \{-C/B\} \quad (2.3)$$

Then

$$z(0) = -C/B \quad (2.4)$$

and

$$\mathcal{A}(s) = \left(\frac{n\pi}{Az(0)} \right) (1-s) + sA \quad (2.5)$$

If we assume that

$$\sin(\mathcal{A}(s)z(s)) = Bz(s) + C, \quad (2.6)$$

then taking the derivative of both sides of this equation with respect to s we see that

$$\cos(\mathcal{A}(s)z(s))(\mathcal{A}'(s)z(s) + \mathcal{A}(s)z'(s)) = Bz'(s) \quad (2.7)$$

Collecting coefficients of $z'(s)$ we find that

$$z'(s)(\cos(\mathcal{A}(s)z(s))\mathcal{A}(s) - B) = -\mathcal{A}'(s)z(s)\cos(\mathcal{A}(s)z(s)) \quad (2.8)$$

and

$$z'(s) = \frac{\mathcal{A}'(s)z(s)\cos(\mathcal{A}(s)z(s))}{B - \mathcal{A}(s)\cos(\mathcal{A}(s)z(s))} \quad (2.9)$$

If we can solve this ordinary differential equation, then the solution $z(1)$ will represent a solution of equation (1)

3 BIANISOTROPIC COATINGS

Here we consider the problem of finding solutions of the Maxwell equations

$$\text{curl}(\vec{E}) = -i\omega\bar{\mu}\vec{H} - \bar{\alpha}\vec{E} \quad (3.1)$$

and

$$\text{curl}(\vec{H}) = i\omega\bar{\epsilon}\vec{E} + \bar{\beta}\vec{H} + \bar{\sigma}\vec{E} \quad (3.2)$$

where $\bar{\mu}$ denotes the tensor magnetic permeability, $\bar{\sigma}$ denotes the tensor conductivity, and $\bar{\epsilon}$ denotes the tensor electric field-permittivity in a coating on a perfect conductor. We assume further that $\bar{\alpha}$ and $\bar{\beta}$ are coupling tensors and that the material is dispersive. We are particularly interested in seeing what happens to modes of propagation in complex coatings as the thickness of the coating changes and the frequency of the propagating radiation changes and the materials become anomalously dispersive. We assume that the tangential component of the electric field vector \vec{E} vanishes on the perfect conductor, and that the electric vector is decaying as you travel in the free space above the coating farther and farther away from the coating. The field regularity conditions on \vec{E} and \vec{H} are that their

tangential components are continuous as you pass from the coating into free space.

Theorem 3.1 *The most general solution of Maxwell's equations in free space which do not depend on y and have an x dependence of the form $\exp(-ikx)$ have x , y , and z components which satisfy the ordinary differential equation,*

$$\frac{\partial^2 W}{\partial z^2} + (-k^2 + k_0^2)W = 0 \quad (3.3)$$

There are at most two unknown parameters needed to represent the solution if it decays as z approaches infinity. In general one only needs four parameters.

Proof. This follows because the free space Maxwell's equations, with

$$k_0^2 = \omega^2 \mu_0 \epsilon_0 \quad (3.4)$$

imply that

$$E_x = \frac{i}{\omega \epsilon_0} \frac{\partial H_y}{\partial z}, \quad (3.5)$$

$$E_z = \frac{-k}{\omega \epsilon_0} H_y, \quad (3.6)$$

$$E_y = \frac{-i}{\omega \epsilon_0} \left(\frac{\partial H_x}{\partial z} + ikH_z \right), \quad (3.7)$$

$$\frac{\partial H_x}{\partial z} + i \left(\frac{k^2 - k_0^2}{k} \right) H_x \quad (3.8)$$

and, an equation that arises from saying that

$$\text{curl}(\vec{E}) = -i\omega\mu_0\vec{H} \quad (3.9)$$

which is

$$\frac{i}{\omega\epsilon_0} \frac{\partial^2 H_z}{\partial z^2} - \frac{k}{\omega\epsilon_0} \frac{\partial H_z}{\partial z} = -i\omega\mu_0 H_z \quad (3.10)$$

The reasoning is that there are only two parameters needed to represent H_y , which then implies that these same parameters represent E_x and E_z . Finally there are two parameters which are needed to represent H_x , which means that these same two parameters represent H_z , and consequently, since E_y is represented in terms of H_x and H_z , these two parameters also represent E_y . If we insist that the field vectors decay as you go farther and farther away from the coating, then we would pick the coefficient of the decaying parameter to represent H_y and H_x , which means that then only two parameters are needed to represent any such solution of Maxwell's equations outside the waveguide.

Theorem 3.2 *In a bianisotropic coating on a perfect conductor, where delimited by the plane $z = 0$ and the plane $z = L$, and between 0 and L the tensors $\bar{\alpha}$, $\bar{\epsilon}$, $\bar{\beta}$, and $\bar{\mu}$ are smooth functions of z if we assume a modal dependence on x of the form $\exp(-ikx)$, where k is a complex parameter, then only two parameters are needed to represent the field vectors, and requiring continuity of tangential components of \vec{E} and \vec{H} across the boundary of the coating give a single dispersion relation involving the complex parameter k .*

4 A SIMPLE ANISOTROPIC COATING

We further specialize the problem to one of practical interest. We suppose that the coating has permittivity ϵ_x and ϵ_z in the x and z directions respectively and a magnetic permeability μ_y along the y axis. We assume that there is an electromagnetic field with a magnetic vector parallel to the y -axis which satisfies the above regularity and boundary conditions, and has the form

$$\vec{H} = H_y \vec{e}_y = g(z) \exp(-ikx + i\omega t) \quad (4.1)$$

By substituting into the Maxwell equations (3.1) and (3.2) and enforcing the regularity conditions and decay conditions, we obtain an ordinary differential equation that must be satisfied by the function $g(z)$ and we find a single transcendental equation,

$$\tan(\kappa_1(z - z_0)) = \epsilon_x \left(\frac{\sqrt{(k^2 - \omega^2 \mu_0 \epsilon_0)}}{\epsilon_0 \kappa_1} \right) \quad (4.2)$$

where

$$\kappa_1^2 = \omega^2 \mu_y \epsilon_x - k^2 \frac{\epsilon_x}{\epsilon_z} \quad (4.3)$$

To see this we observe that Maxwell's equations have the form,

$$\begin{aligned} \text{curl}(\vec{H}) &= -\frac{\partial H_y}{\partial z} \vec{e}_x + \frac{\partial H_y}{\partial x} \vec{e}_z = \\ &= (i\omega \vec{\epsilon} + \vec{\sigma}) \vec{E} \end{aligned} \quad (4.4)$$

so that if the tensors are simply diagonal, then

$$\vec{E} = \left[\frac{-1}{i\omega \epsilon_x + \sigma_x} g'(z) \vec{e}_x + \left(\frac{-ik}{i\omega \epsilon_z + \sigma_z} \right) g(z) \vec{e}_z \right] \exp(-ikx + i\omega t) \quad (4.5)$$

Combining equations (4.4) and (4.5) we see that

$$\text{curl}(\vec{E}) = -i\omega \mu_y H_y \vec{e}_y =$$

$$-\bar{e}_y \left\{ \frac{1}{i\omega\epsilon_x + \sigma_x} \frac{\partial^2 H_y}{\partial z^2} + \frac{1}{i\omega\epsilon_x + \sigma_x} \frac{\partial^2 H_y}{\partial x^2} \right\} \quad (4.6)$$

Substituting equation (4.1) into equation (4.6) we find that

$$g_1''(z) + \left\{ \omega^2 \mu_y \epsilon_x - k^2 \left(\frac{\epsilon_x}{\epsilon_z} \right) \right\} g_1(z) = 0 \quad (4.7)$$

In the free space above the anisotropic, dispersive coating, this equation specializes to,

$$g_1''(z) + \left\{ \omega^2 \mu_0 \epsilon_0 - k^2 \right\} g_1(z) = 0 \quad (4.8)$$

If we define

$$\tilde{\lambda}_1^2 = \omega^2 \mu_y \epsilon_x - k^2 \frac{\epsilon_x}{\epsilon_z} \quad (4.9)$$

and assume that the electric vector is zero at $z = z_0$, which is the plane bounding the perfect conductor, then we may suppose that there is a constant C_1 such that

$$g_1(z) = C_1 \cos(\tilde{\lambda}_1(z - z_0)) \quad (4.10)$$

and assuming that the radiation decays as z becomes more and more positive, then we may assume that there is a constant D_2 such that

$$g_2(z) = D_2 \exp(-\lambda_2(z - z_1)) \quad (4.11)$$

where

$$\lambda_2^2 = k^2 - \omega^2 \mu_0 \epsilon_0 \quad (4.12)$$

At the boundary $z = z_1$ we require the continuity of tangential components of \vec{E} and \vec{H} which implies that since in free space

$$H_y = D_2 \exp(-\lambda_2(z - z_1)) \quad (4.13)$$

we have from just continuity of tangential \vec{H} at $z = z_1$ that

$$D_2 = -C_1 \cos(\tilde{\lambda}_1(z_1 - z_0)) \quad (4.14)$$

and from the continuity of tangential components of \vec{E} across the boundary we have since in the coating material

$$E_x = \frac{-1}{i\omega\epsilon_x} g'_1(z) \exp(-ikx + i\omega t) \quad (4.15)$$

we conclude that equating tangential \vec{E} on either side of $z = z_1$ we have

$$-\lambda_2 D_2 = -\tilde{\lambda}_1 C_1 \frac{\epsilon_0}{\epsilon_x} \sin(\tilde{\lambda}_1(z_1 - z_0)) \quad (4.16)$$

Thus, having assumed that $z = z_1$ is the plane bounding the coating on the perfect conductor, which is itself delimited by the plane $z = z_0$. The regularity conditions and the requirement that the electric vector \vec{E} decay as z becomes larger and larger, tells us that the propagation constant k , which is also given by

$$k = \alpha - i\beta \quad (4.17)$$

must satisfy the relationship,

$$\tan^2(\kappa_1(z_1 - z_0)) = \left(\frac{\epsilon_x}{\epsilon_0} \right)^2 \left[-\frac{\epsilon_x}{\epsilon_x} + \frac{\omega^2(\mu_y \epsilon_x - \mu_0 \epsilon_0)}{-k^2 \epsilon_x / \epsilon_x + \omega^2 \mu_y \epsilon_x} \right] \quad (4.18)$$

We extend parameters appearing in the space to an algebra which contains the ordinary parameters in a way that in the extended algebra, the equations under consideration have a simple solution. For the example we

are considering, it turns out that we only need the ordinary algebra of complex numbers. The thickness of the coating is $z_1 - z_0$ and this is the value at $s = 1$ of the parameterized generalized thickness,

$$t(s) = \left(\frac{(1-s)n\pi}{\kappa_1(s)} \right) + s(z_1 - z_0) \quad (4.19)$$

so that the derivative of the thickness, which now belongs to an algebra containing the real numbers, with respect to the homotopy parameter s is given by

$$t'(s) = -\frac{n\pi}{\kappa_1(s)} + \kappa_1'(s)(1-s) \left(\frac{n\pi}{\kappa_1(s)^2} \right) + (z_1 - z_0) \quad (4.20)$$

Replacing the term $(z_1 - z_0)$ in equation (4.18) by the $t(s)$ given by equation (4.19) we obtain the relation,

$$\tan^2(\kappa_1(s)t(s)) = \frac{\epsilon_x}{\epsilon_0} \left[-\frac{\epsilon_x}{\epsilon_x} + \frac{\omega^2(\mu_y \epsilon_x - \mu_0 \epsilon_0)}{-k^2(s)\epsilon_x/\epsilon_x + \omega^2 \mu_y \epsilon_x} \right] \quad (4.21)$$

We have an obvious solution of equation (4.21) when $s = 0$. Also, the derivative of the propagation constant $\kappa_1(s)$ with respect to the parameter s is given by

$$\frac{d\kappa_1}{ds} = - \left(\frac{\epsilon_x}{\epsilon_x} \left\{ \frac{k(s)}{\kappa_1(s)} \right\} \right) \frac{dk}{ds} \quad (4.22)$$

Then use equation (4.22) to define terms arising in the representation of the derivative of the left side of equation (4.21). It is clear that

$$\begin{aligned}
\frac{d}{ds} \{ \tan^2(\kappa_1(s)t(s)) \} = & \\
& t(s) \tan(\kappa_1(s)t(s)) \sec^2(\kappa_1(s)t(s)) \frac{d\kappa_1}{ds} \\
& + \left[\kappa_1(s) \tan(\kappa_1(s)t(s)) \sec^2(\kappa_1(s)t(s)) \right] \left\{ z_1 - z_0 - \frac{n\pi}{\kappa_1(s)} + \right. \\
& \left. + \left[\frac{(1-s)n\pi}{\kappa_1(s)^2} \right] \frac{d\kappa_1}{ds} \right\} \quad (4.23)
\end{aligned}$$

Using equation (4.22) we deduce from equation (4.23) that

$$\begin{aligned}
\frac{d}{ds} \{ \tan^2(\kappa_1(s)t(s)) \} = & \\
& t(s) \tan(\kappa_1(s)t(s)) \sec^2(\kappa_1(s)t(s)) \left[-\frac{\epsilon_x k(s)}{\epsilon_x \kappa_1(s)} \right] \frac{dk}{ds} \\
& + \left[\kappa_1(s) \tan(\kappa_1(s)t(s)) \sec^2(\kappa_1(s)t(s)) \right] \left\{ z_1 - z_0 - \frac{n\pi}{\kappa_1(s)} + \right. \\
& \left. - \left[\frac{(1-s)n\pi \epsilon_x k(s)}{\kappa_1(s)^2 \epsilon_x \kappa_1(s)} \right] \frac{dk}{ds} \right\} \quad (4.24)
\end{aligned}$$

To simplify the representation of this derivative we introduce the functions,

$$C(s) = \kappa_1(s) \tan(\kappa_1(s)t(s)) \sec^2(\kappa_1(s)t(s)) \quad (4.25)$$

and where

$$B(s) = t(s) \tan(\kappa_1(s)t(s)) \sec^2(\kappa_1(s)t(s)) \left(-\frac{\epsilon_x k(s)}{\epsilon_x \kappa_1(s)} \right) \quad (4.26)$$

Using the above definitions we find that

$$\frac{d}{ds} \left\{ \tan^2(\kappa_1(s)t(s)) \right\} = B(s) \frac{dk}{ds} + C(s) \left\{ z_1 - z_0 - \frac{n\pi}{\kappa_1(s)} \right\} - C(s) \left[\frac{(1-s)n\pi}{\kappa_1(s)^2} \frac{\epsilon_x}{\epsilon_x} \frac{k(s)}{\kappa_1(s)} \right] \frac{dk}{ds} \quad (4.27)$$

We also define,

$$\mathcal{E}(s) = C(s) \left(z_1 - z_0 - \frac{n\pi}{\kappa_1(s)} \right) \quad (4.28)$$

and we define

$$\mathcal{F}(s) = -C(s) \left[\frac{(1-s)n\pi}{\kappa_1(s)^2} \frac{\epsilon_x}{\epsilon_x} \frac{k(s)}{\kappa_1(s)} \right] \quad (4.29)$$

Thus, the derivative of the left side of equation (4.21) is, therefore, given by

$$\frac{d}{ds} \left\{ \tan^2(\kappa_1(s)t(s)) \right\} = B(s) \frac{dk}{ds} + \mathcal{E}(s) + \mathcal{F}(s) \frac{dk}{ds}, \quad (4.30)$$

where the functions $B(s)$, $\mathcal{E}(s)$, and $\mathcal{F}(s)$ are given by equations (4.26), (4.28), and (4.29).

We now need to define the derivative with respect to the homotopy parameter s of the right side of equation (4.21). Applying the differentiation operation to both sides of (4.21) we find that

$$\frac{d}{ds} \left\{ \tan^2(\kappa_1(s)t(s)) \right\} = \left(\frac{\epsilon_x}{\epsilon_0} \right)^2 \left\{ 0 - \frac{\omega^2(\mu_y \epsilon_x - \mu_0 \epsilon_0)}{(-k(s)^2 \epsilon_x / \epsilon_x + \omega^2 \mu_y \epsilon_x)^2} \left[-2 \frac{\epsilon_x}{\epsilon_x} k(s) \frac{dk}{ds} \right] \right\} \quad (4.31)$$

To simplify representation of the derivative of the right side of equation (4.21). We introduce the function,

$$A(s) = k(s) \frac{\epsilon_x}{\epsilon_x} \left(\frac{\epsilon_x}{\epsilon_0} \right)^2 \frac{\omega^2(\mu_y \epsilon_x - \mu_0 \epsilon_0)}{(-k(s)^2 \epsilon_x / \epsilon_x + \omega^2 \mu_y \epsilon_x)^2} \quad (4.32)$$

From equations (4.31) and (4.32) we see that

$$\frac{d}{ds} \{ \tan^2(\kappa_1(s)t(s)) \} = 2\mathcal{A}(s) \frac{dk}{ds} \quad (4.33)$$

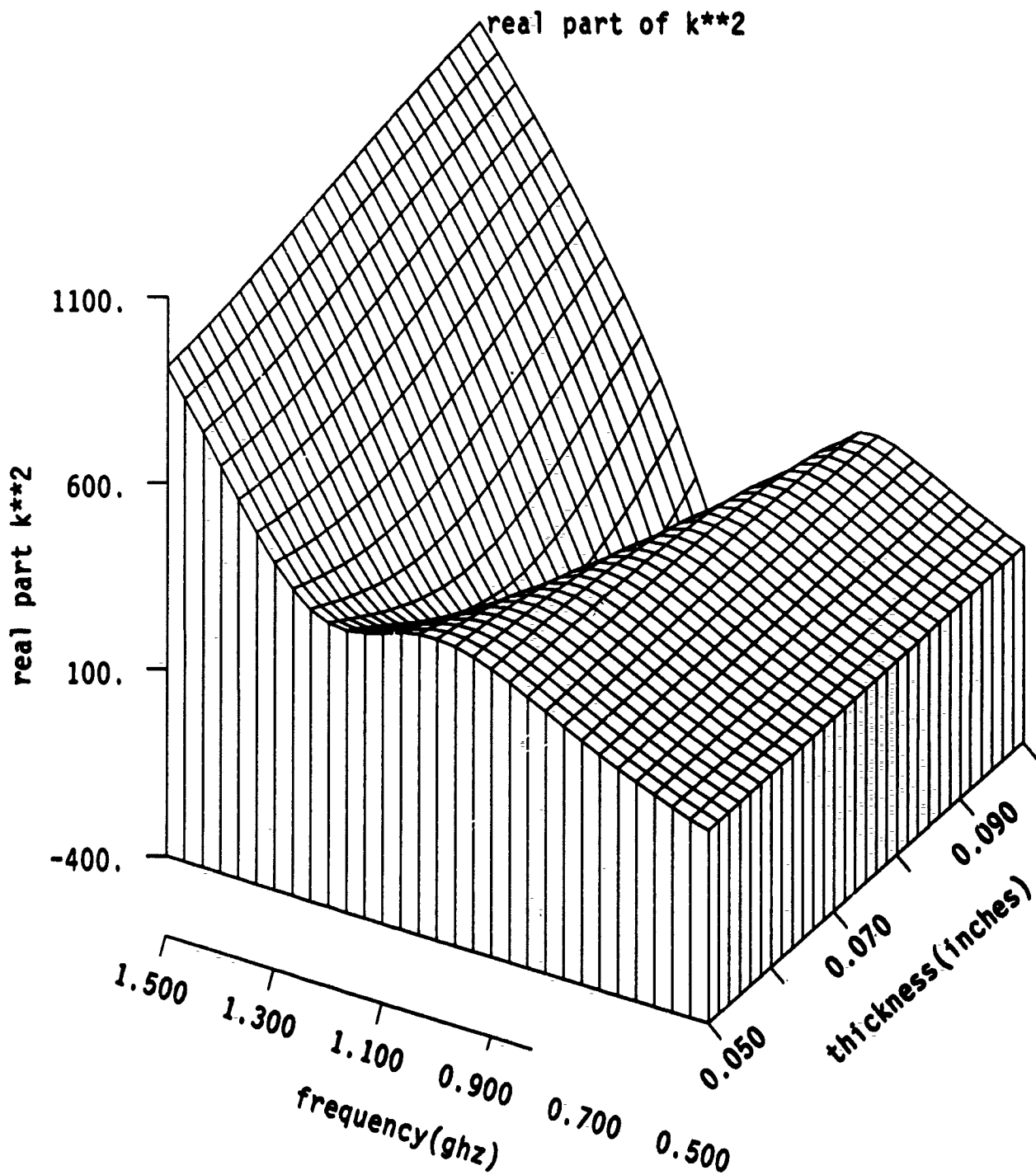
Combining equations (4.30) and (4.33) we find that

$$\{ 2\mathcal{A}(s) - \mathcal{B}(s) - \mathcal{F}(s) \} \frac{dk}{ds} = \mathcal{E}(s) \quad (4.34)$$

From equation (4.34) we obtain the ordinary differential equation for the propagation modes given by

$$\frac{dk}{ds} = \left(\frac{\mathcal{E}(s)}{2\mathcal{A}(s) - \mathcal{B}(s) - \mathcal{F}(s)} \right) \quad (4.35)$$

This system of differential equations was solved for a range of frequencies and thicknesses when the permeability of the magnetic material passed through a region of anomalous dispersion. The square of the propagation constant as a function of layer thickness and frequency is shown on the following page



5 A LINEAR FRACTIONAL TRANSFORMATION

In this section we show that the dispersion relation has a representation as an equation involving a linear fractional transformation. The solution of the dispersion relation is equivalent to the determination of zeros of an equation of the form,

$$\cosh(\sqrt{w}) = \frac{Aw + B}{Cw + D} \quad (5.1)$$

To see this we assume that in the free space above the coating that

$$H_y = g_2(z) \exp(-ikx + i\omega t) \quad (5.2)$$

where

$$g_2''(z) + (\omega^2 \mu_0 \epsilon_0 - k^2)g_2(z) = 0 \quad (5.3)$$

If we assume that

$$\lambda^2 = k^2 - \omega^2 \mu_0 \epsilon_0 \quad (5.4)$$

then the most general form of the magnetic field is

$$H_y = (D_1 \exp(\lambda(z - z_1)) + D_2 \exp(-\lambda(z - z_1))) \exp(-ikx + i\omega t) \quad (5.5)$$

The electric field in this region has an x component and a z component. Since in free space, the relation

$$\text{curl}(\vec{H}) = i\omega \epsilon_0 \vec{E} \quad (5.6)$$

If we define

$$\kappa_1^2 = \omega^2 \mu_y \epsilon_x - k^2 \left(\frac{i\omega \epsilon_x + \sigma_x}{i\omega \epsilon_x + \sigma_x} \right) \quad (5.7)$$

and use Maxwell's equations we find that

$$g''(z) + \kappa_1^2 g(z) = 0 \quad (5.8)$$

so that in general if we realize that the x component of the electric field vanishes at $z = z_0$ that

$$g(z) = C(\exp(i\kappa_1(z - z_0)) + \exp(-i\kappa_1(z - z_0))) \quad (5.9)$$

so that within the material coating the x component of the electric vector is given by

$$E_x = \frac{-1}{i\omega \epsilon_x + \sigma_x} C \{i\kappa_1 \exp(i\kappa_1(z - z_0)) - i\kappa_1 \exp(-i\kappa_1(z - z_0))\} \quad (5.10)$$

and in the free space above the coating we find that

$$E_x = \frac{-1}{i\omega \epsilon_0} \{D_1 \lambda_2 \exp(\lambda_2(z - z_1)) - \lambda_2 \exp(-\lambda_2(z - z_1))\} \exp(-ikx + i\omega t) \quad (5.11)$$

If we let \mathcal{D} be defined by

$$\mathcal{D} = \frac{\lambda_1}{\lambda_2} \left(\frac{i\omega \epsilon_0}{i\omega \epsilon_x + \sigma_x} \right) \quad (5.12)$$

we find that setting D_1 equal to zero so that the fields decay at infinity or setting D_2 equal to zero so that the fields would grow as you get further and further from the coating both yield exactly the same equation,

$$\cosh(2\lambda_2(z_1 - z_0)) = \left(\frac{\mathcal{D}^2 + 1}{\mathcal{D}^2 - 1} \right) \quad (5.13)$$

which has the form of equation (5.1). If we subtract the right side of equation (5.13) from the left side of the same equation and obtain the function

$$\Psi(k) = \cosh(2\lambda_2(z_1 - z_0)) - \left(\frac{\mathcal{D}^2 + 1}{\mathcal{D}^2 - 1} \right) \quad (5.14)$$

then solution can be understood as the crossing points of the contours given by

$$\operatorname{Re}(\Psi(k)) = 0 \quad (5.15)$$

and

$$\operatorname{Im}(\Psi(k)) = 0 \quad (5.16)$$

These contours are shown on the following page. The function Ψ is considered to be a function of α and β , where the propagation constant k is given by

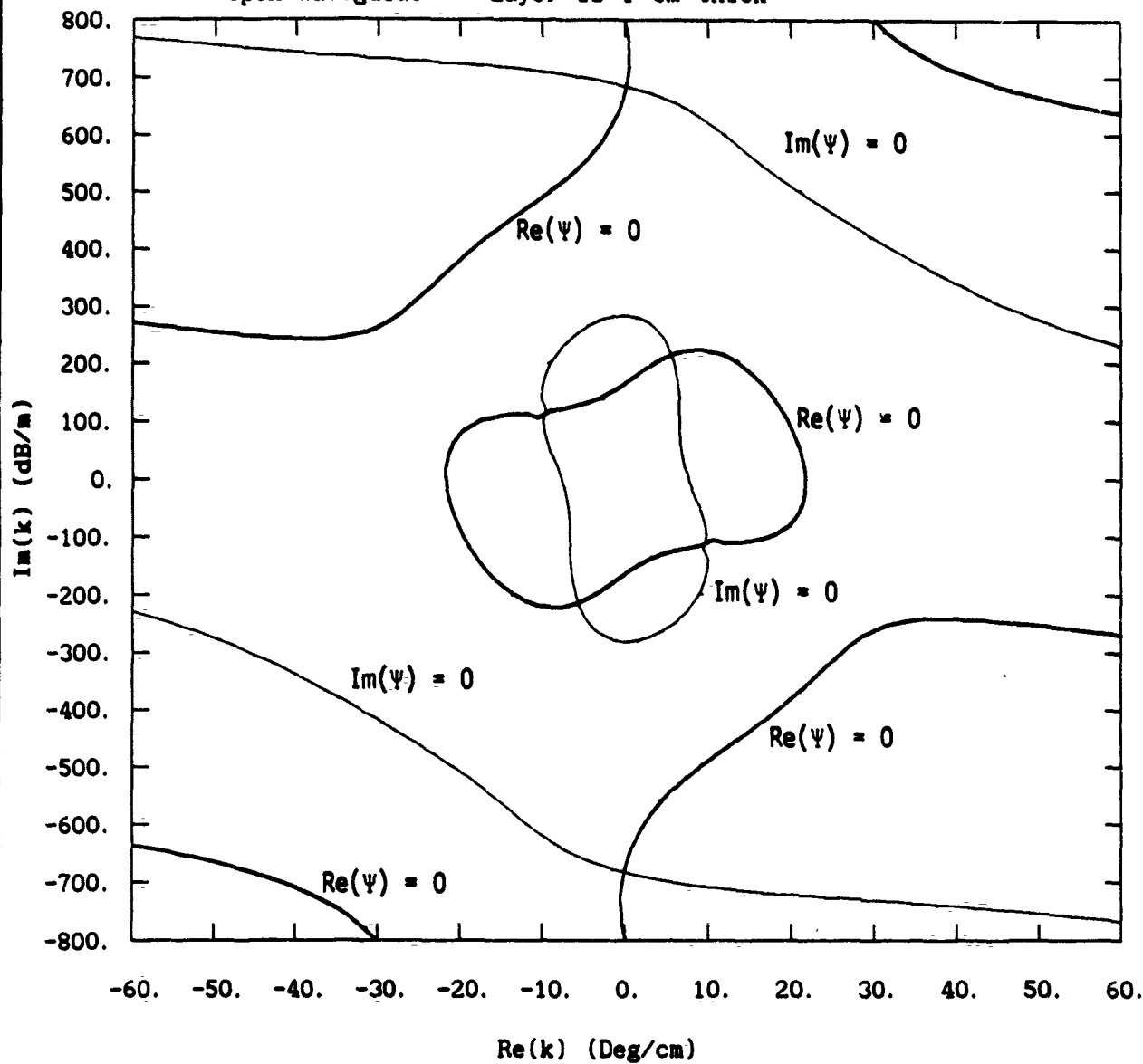
$$k = \alpha - i\beta \quad (5.17)$$

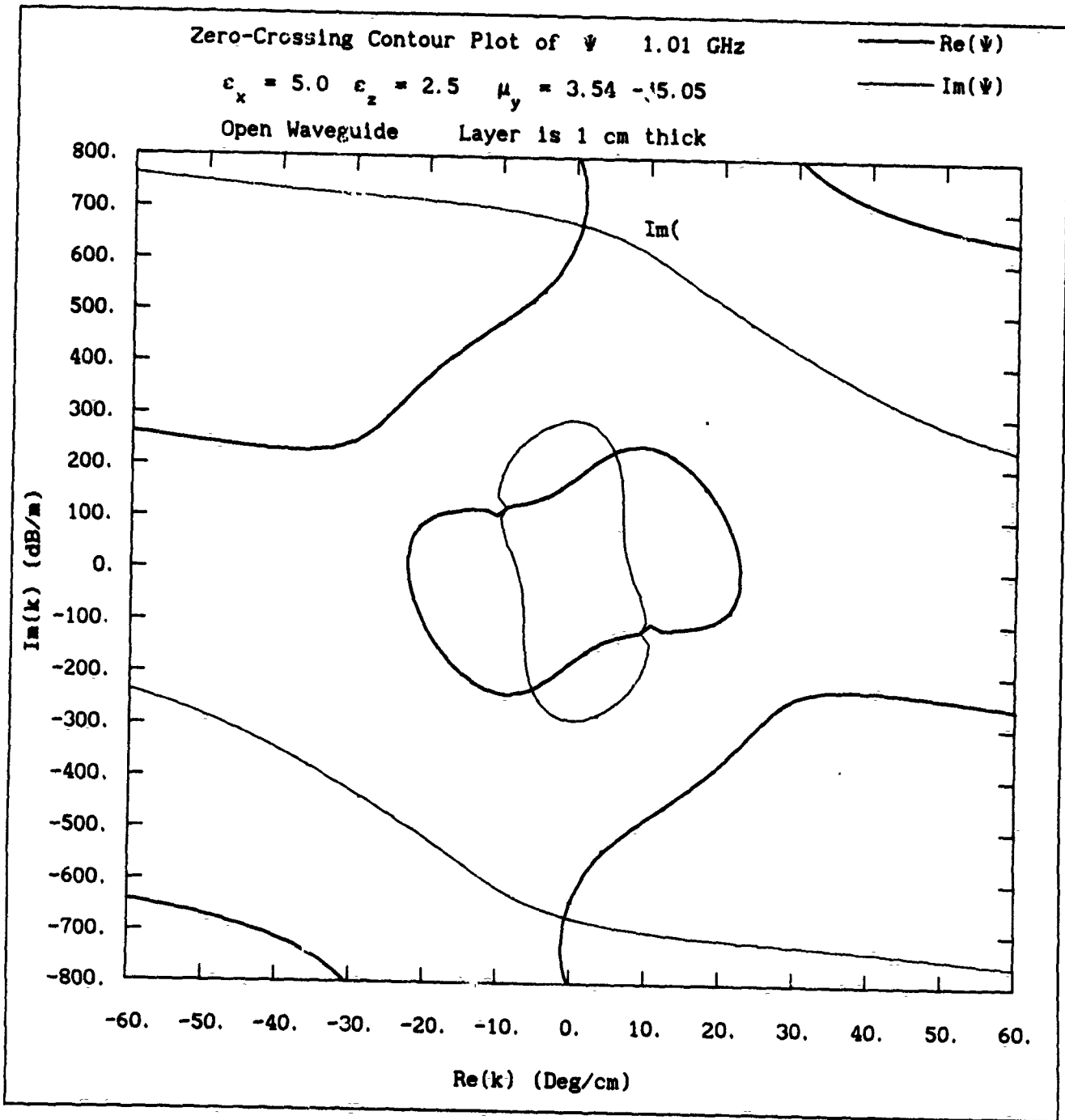
Zero-Crossing Contour Plot of ψ 1.00 GHz

$\epsilon_x = 5.0 \quad \epsilon_z = 2.5 \quad \mu_y = 3.50 - j5.0$

Open Waveguide Layer is 1 cm thick

— Re(ψ)
— Im(ψ)



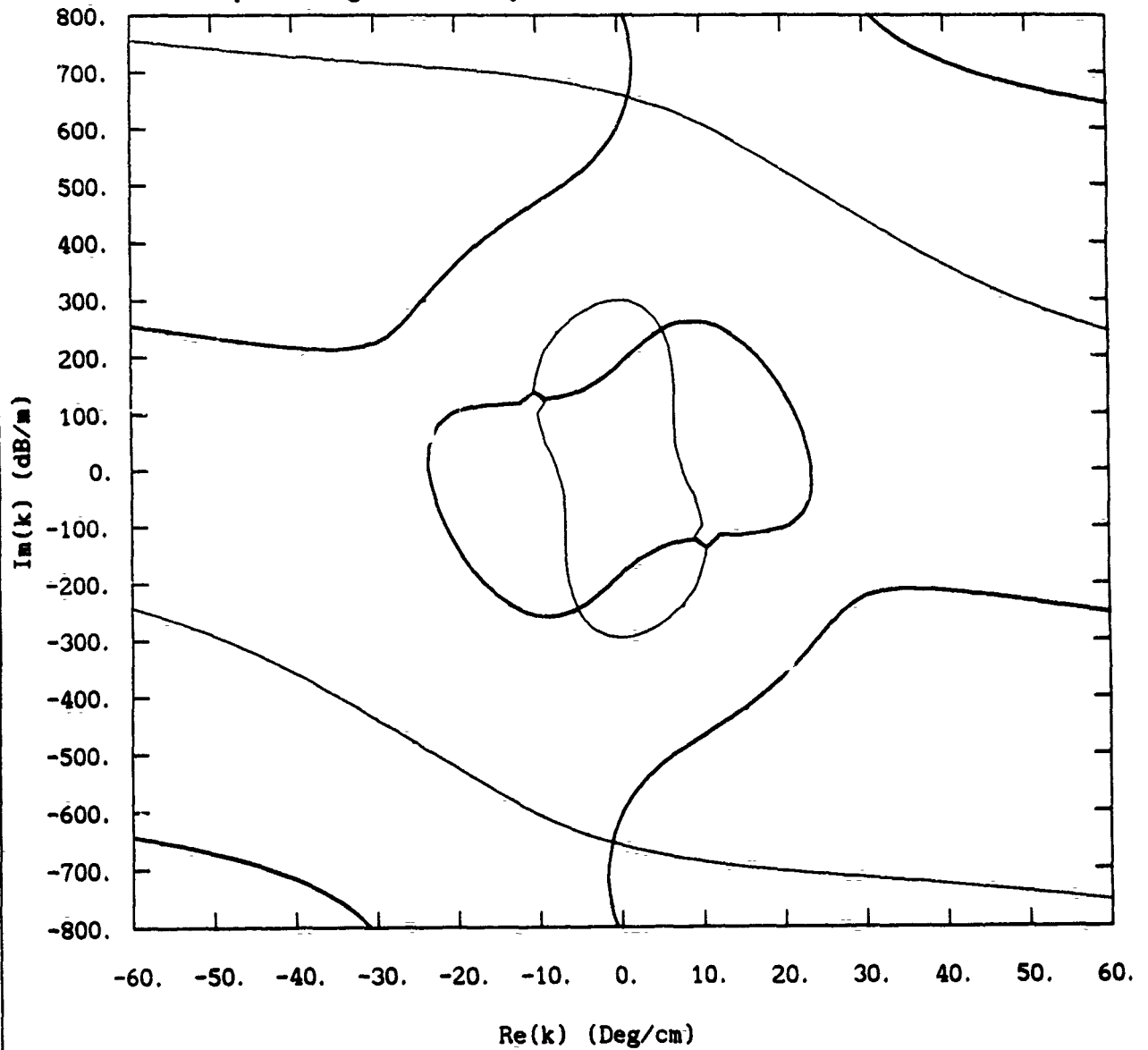


Zero-Crossing Contour Plot of Ψ 1.02 GHz

$\epsilon_x = 5.0 \quad \epsilon_z = 2.5 \quad \mu_y = 3.58 - j5.10$

Open Waveguide Layer is 1 cm thick

— Re(Ψ)
— Im(Ψ)



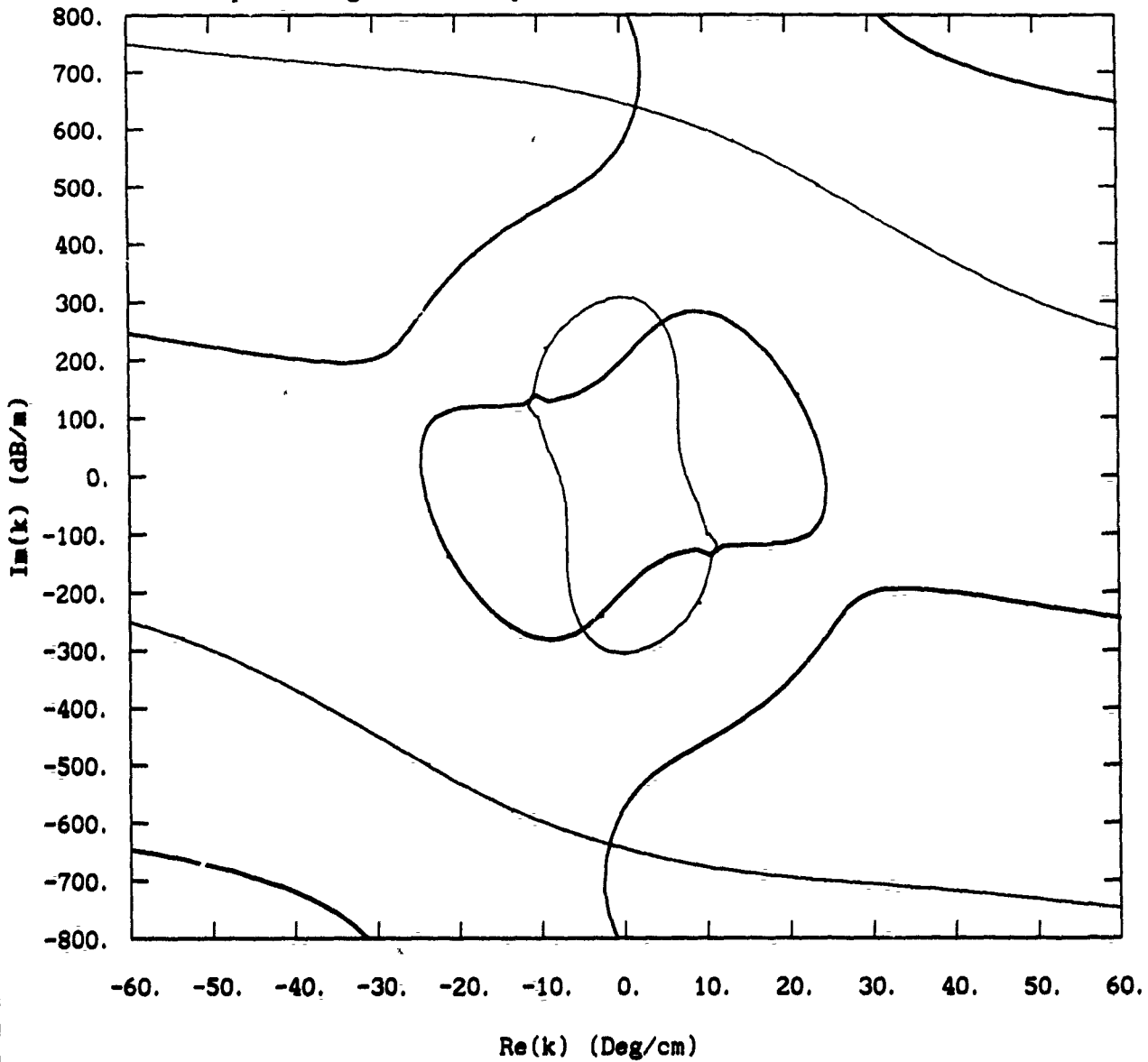
Zero-Crossing Contour Plot of Ψ 1.03 GHz

$\epsilon_x = 5.0 \quad \epsilon_z = 2.5 \quad \mu_y = 3.62 - j5.15$

Open Waveguide Layer is 1 cm thick

— Re(Ψ)

— Im(Ψ)



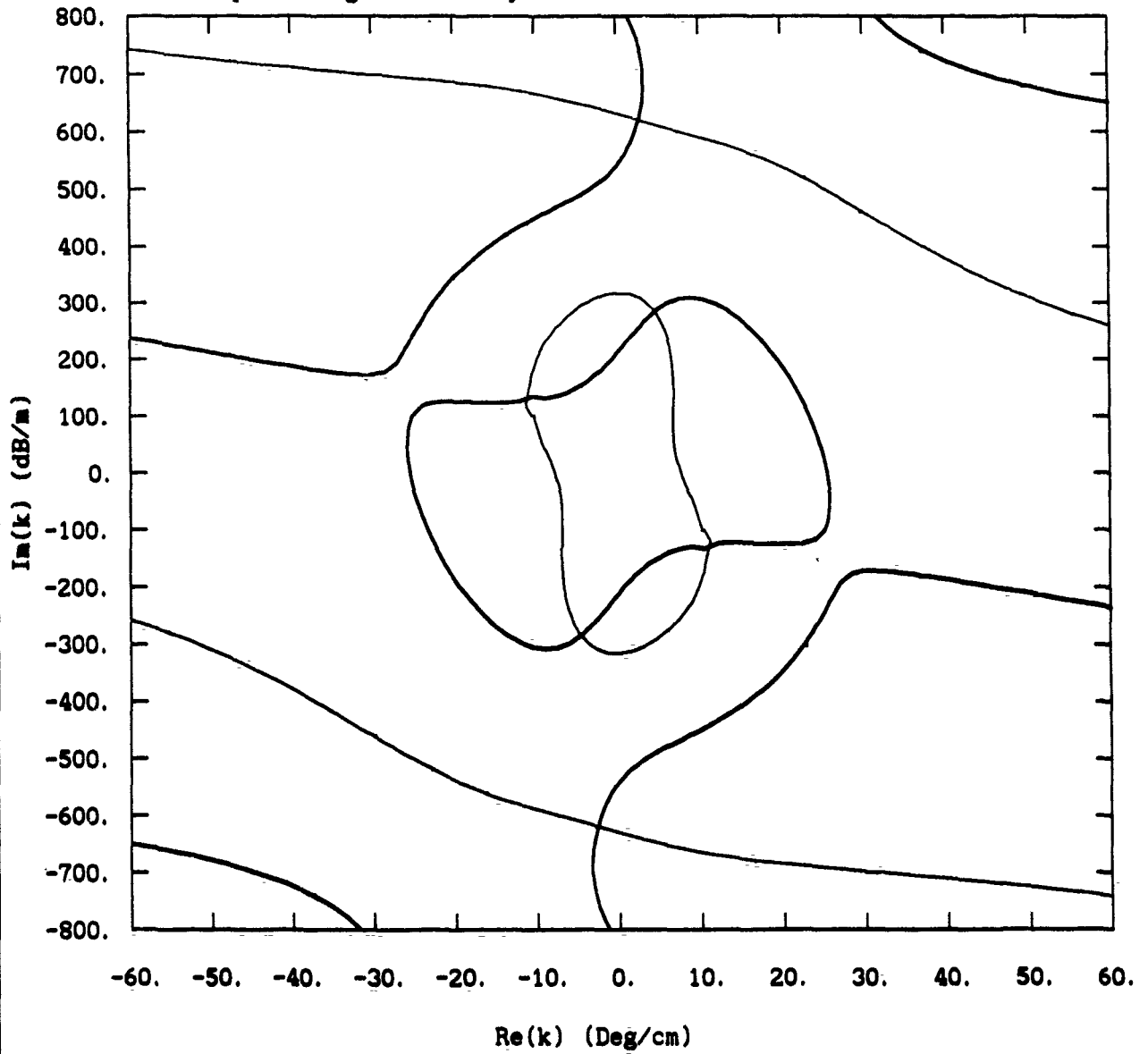
Zero-Crossing Contour Plot of Ψ 1.04 GHz

$\epsilon_x = 5.0$ $\epsilon_z = 2.5$ $\mu_y = 3.66 - j5.20$

Open Waveguide Layer is 1 cm thick

— $\text{Re}(\Psi)$

— $\text{Im}(\Psi)$



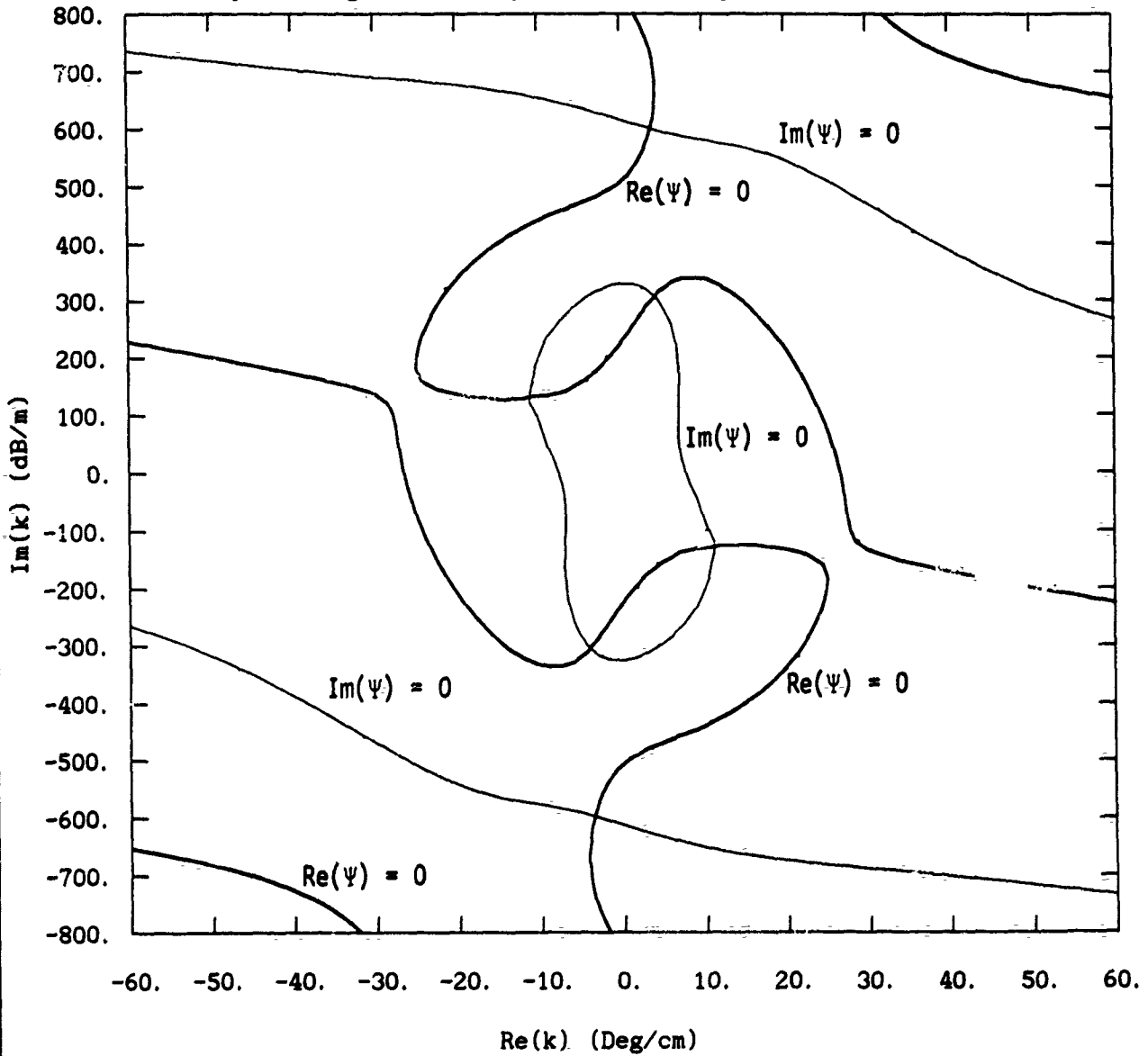
Zero-Crossing Contour Plot of Ψ 1.05 GHz

$\epsilon_x = 5.0 \quad \epsilon_z = 2.5 \quad \mu_y = 3.70 - j5.25$

Open Waveguide Layer is 1 cm thick

— Re(Ψ)

— Im(Ψ)



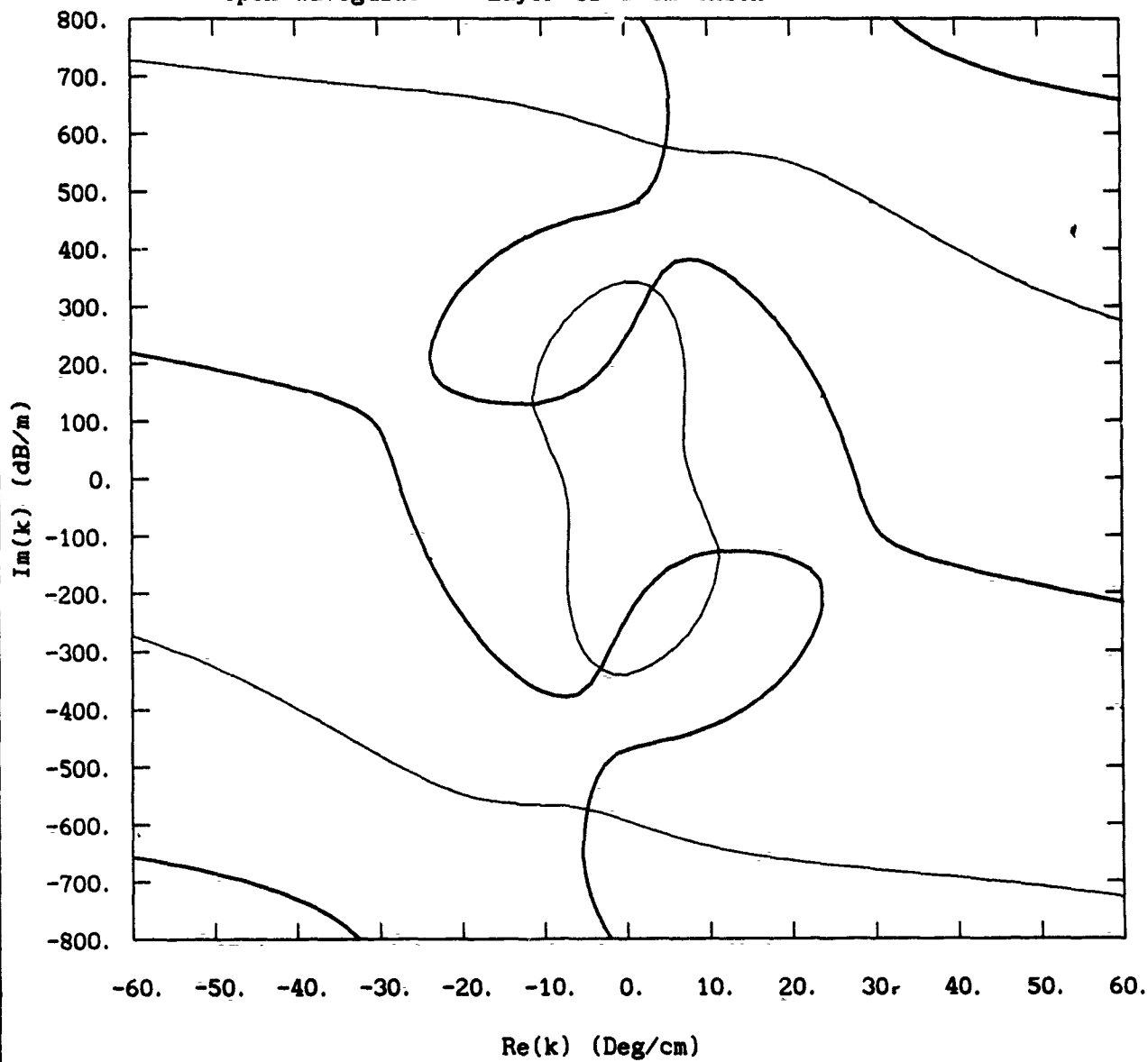
Zero-Crossing Contour Plot of Ψ 1.06 GHz

$\epsilon_x = 5.0$ $\epsilon_z = 2.5$ $\mu_y = 3.74 - j5.30$

Open Waveguide Layer is 1 cm thick

— Re(Ψ)

— Im(Ψ)



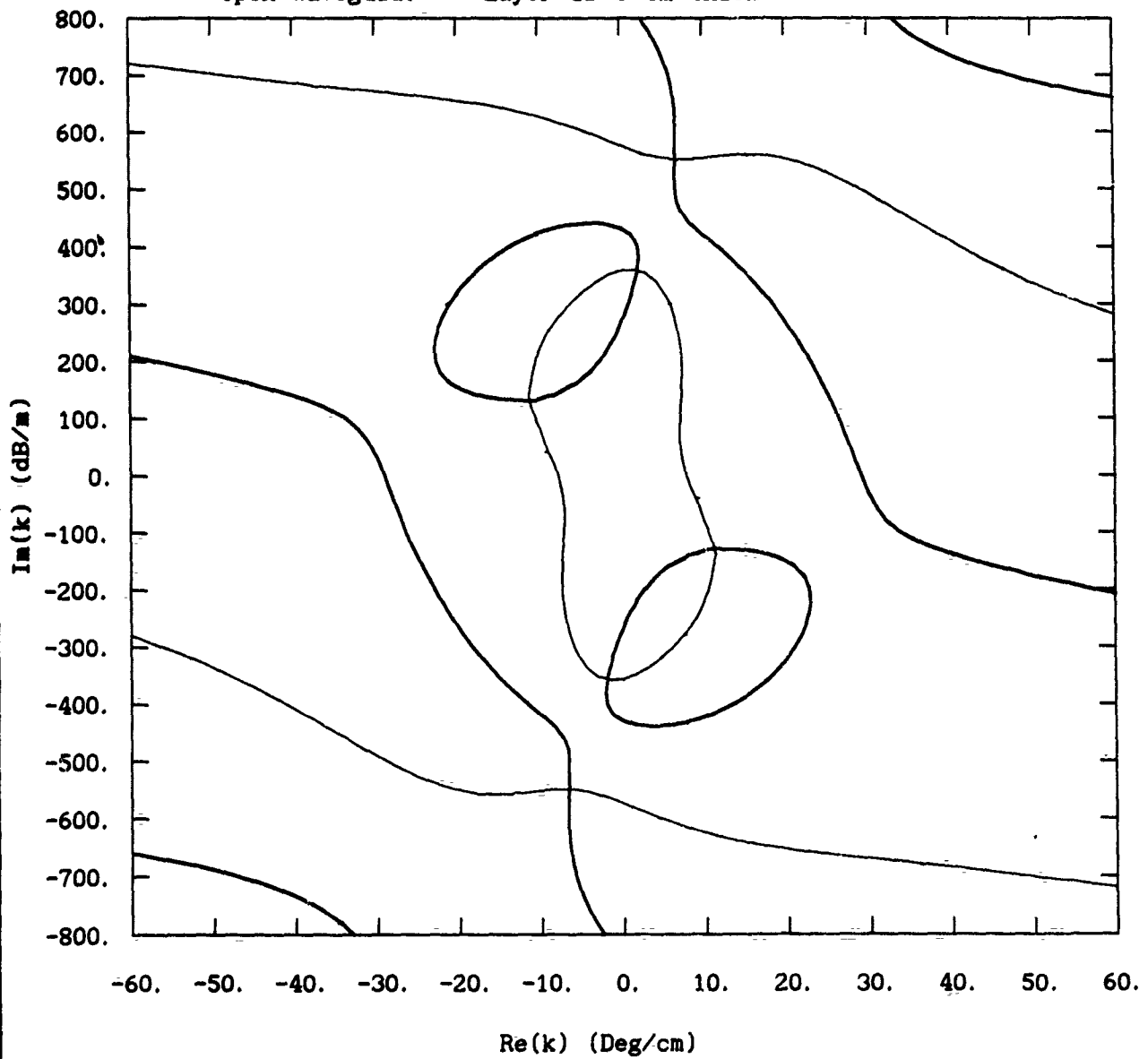
Zero-Crossing Contour Plot of Ψ 1.07 GHz

$\epsilon_x = 5.0$ $\epsilon_z = 2.5$ $\mu_y = 3.78 - j5.35$

Open Waveguide Layer is 1 cm thick

— Re(Ψ)

— Im(Ψ)



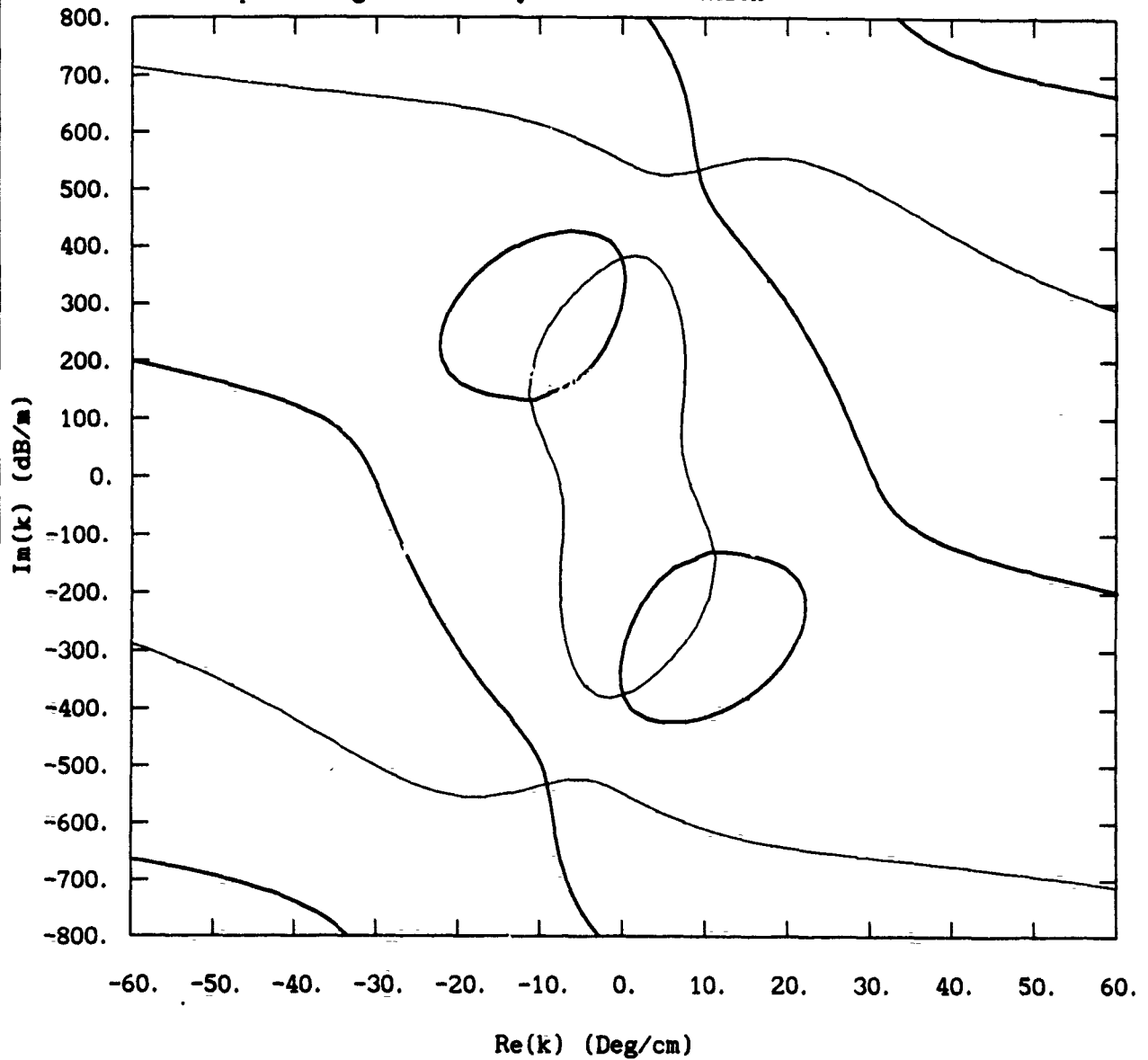
Zero-Crossing Contour Plot of Ψ 1.08 GHz

$\epsilon_x = 5.0 \quad \epsilon_z = 2.5 \quad \mu_y = 3.82 - j5.40$

Open Waveguide Layer is 1 cm thick

— Re(Ψ)

— Im(Ψ)



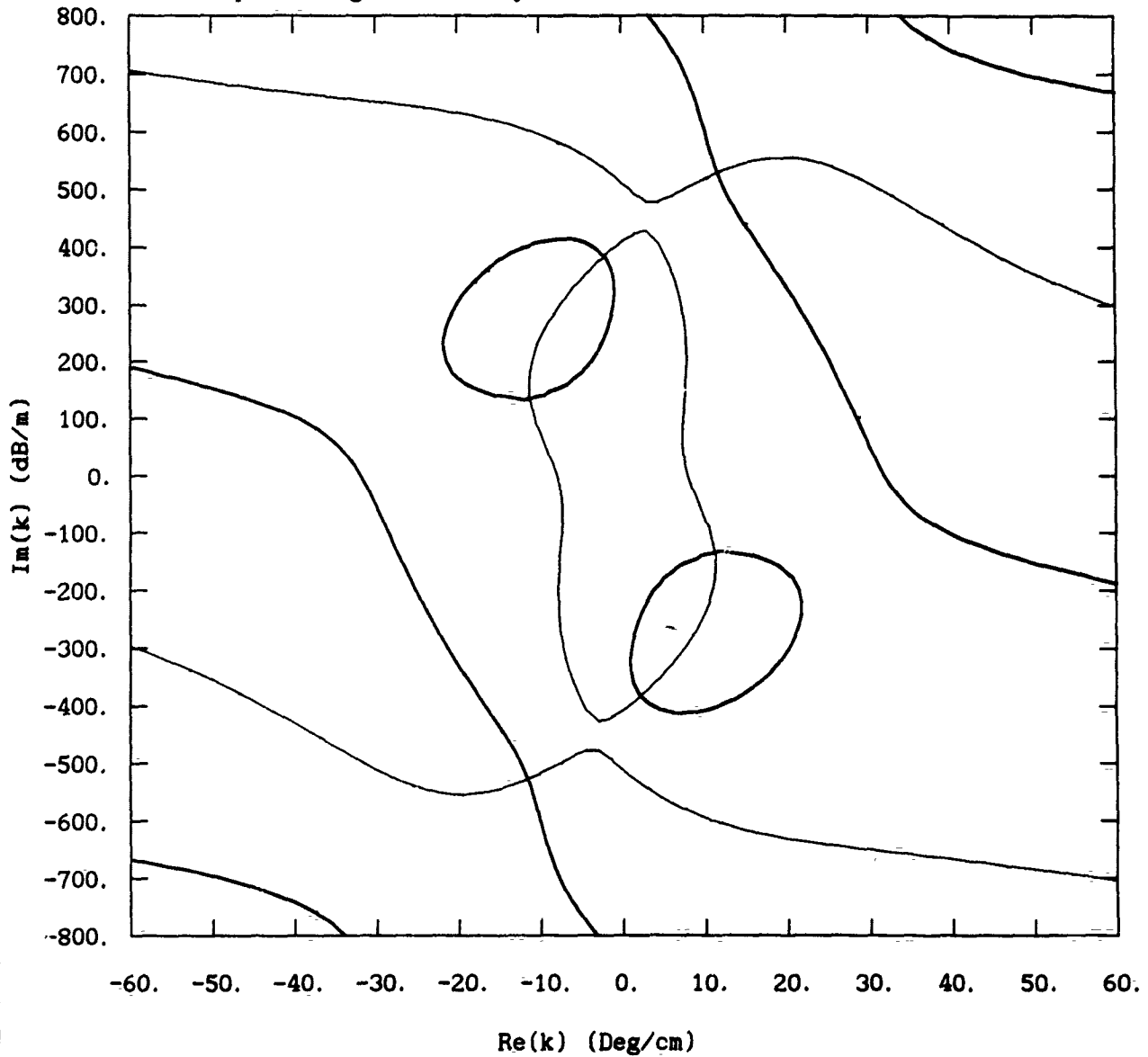
Zero-Crossing Contour Plot of Ψ 1.09 GHz

$\epsilon_x = 5.0 \quad \epsilon_z = 2.5 \quad \mu_y = 3.86 - j5.45$

Open Waveguide Layer is 1 cm thick

— Re(Ψ)

— Im(Ψ)



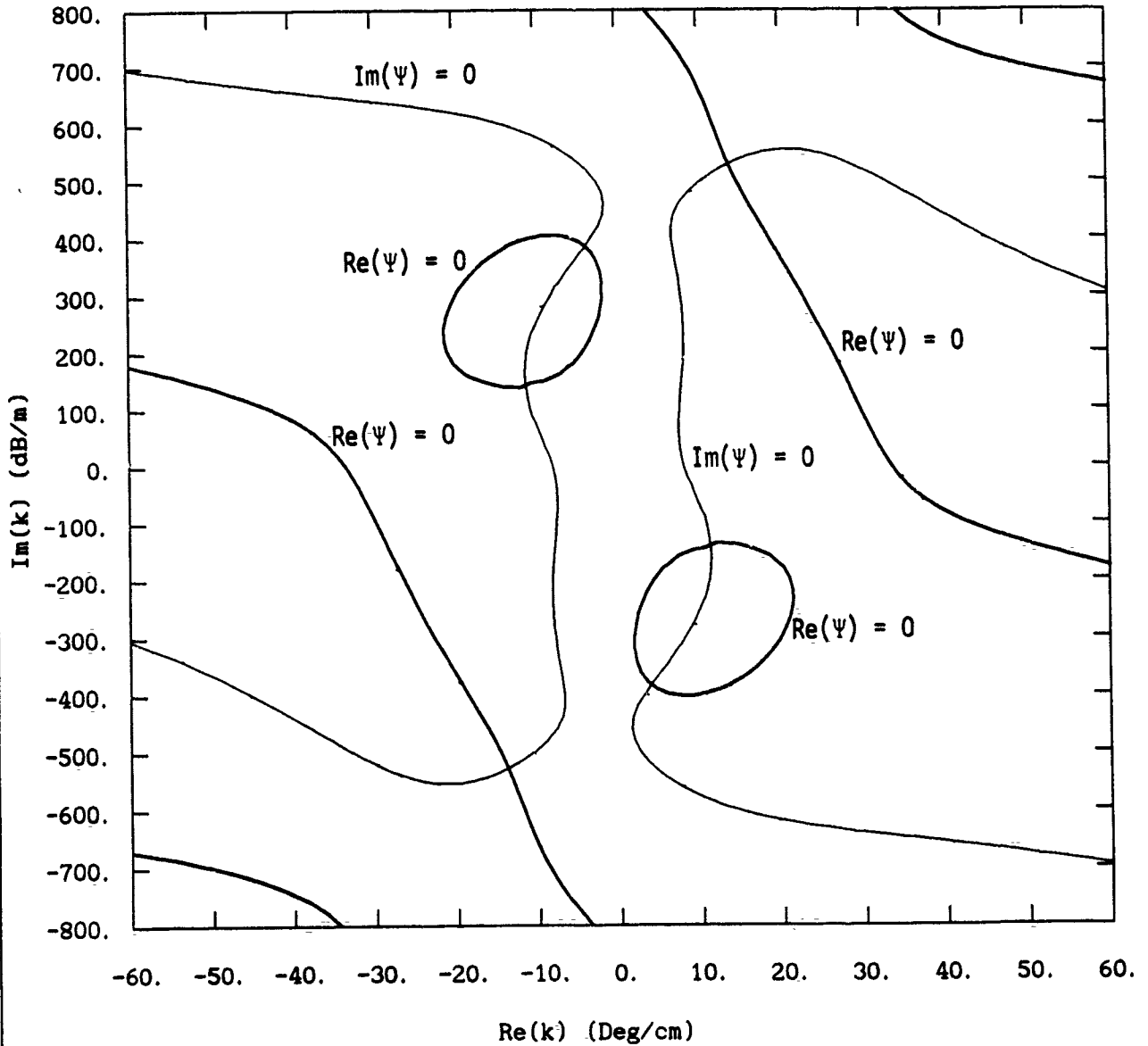
Zero-Crossing Contour Plot of Ψ 1.10 GHz

$\epsilon_x = 5.0 \quad \epsilon_z = 2.5 \quad \mu_y = 3.90 - j5.50$

Open Waveguide Layer is 1 cm thick

— Re(Ψ)

— Im(Ψ)



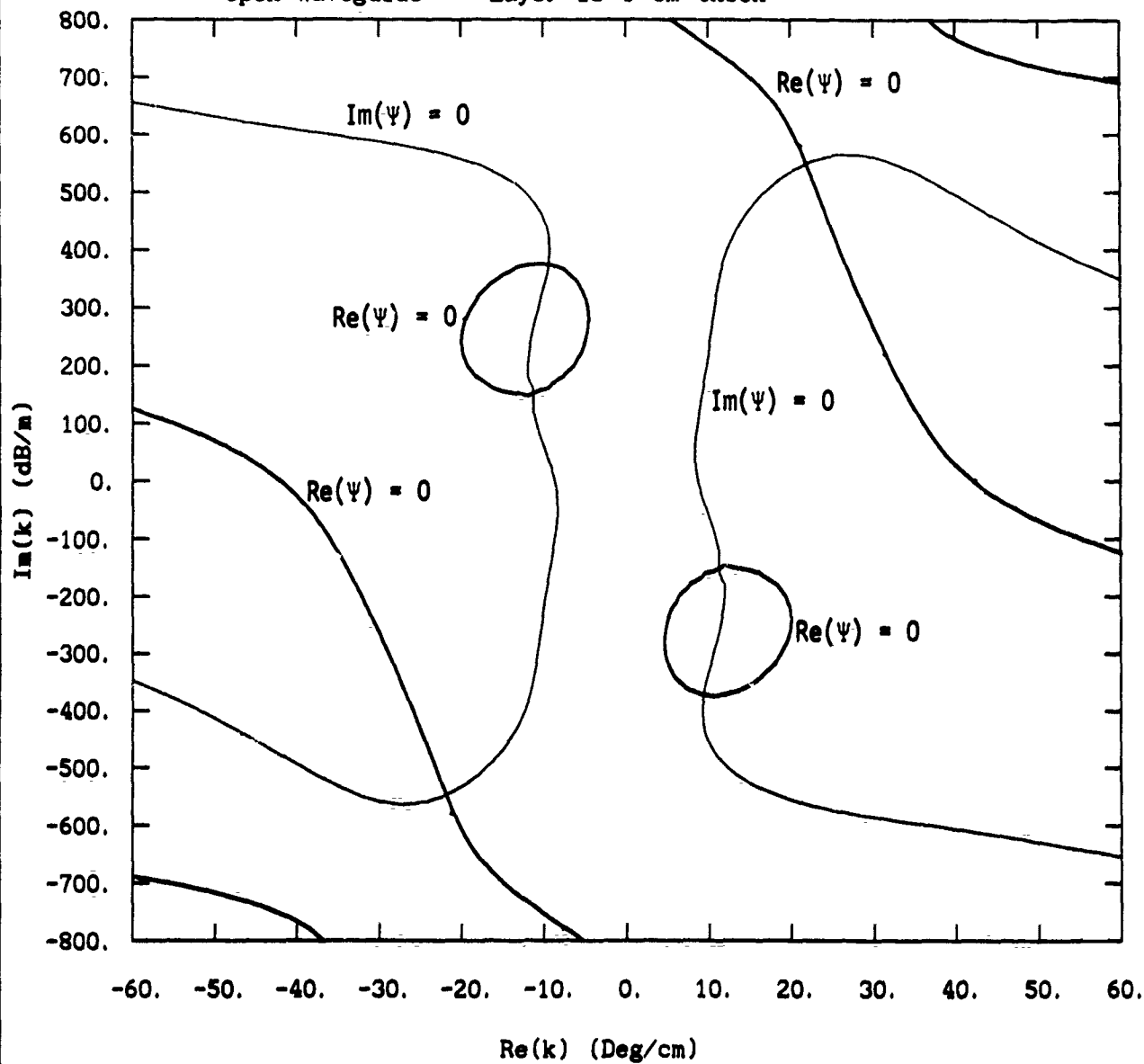
Zero-Crossing Contour Plot of Ψ 1.15 GHz

$\epsilon_x = 5.0 \quad \epsilon_z = 2.5 \quad \mu_y = 4.10 - j5.75$

Open Waveguide Layer is 1 cm thick

— Re(Ψ)

— Im(Ψ)

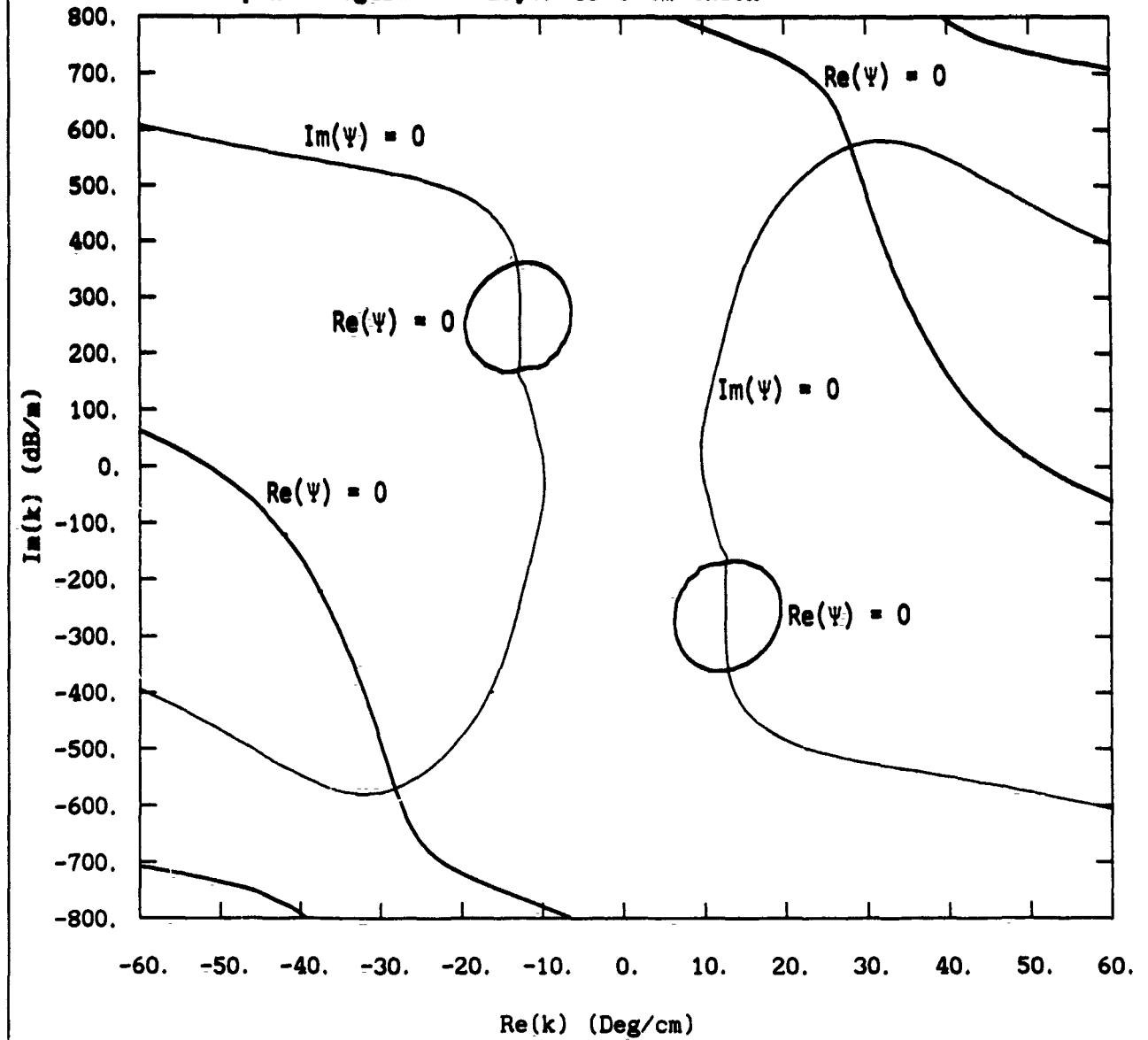


Zero-Crossing Contour Plot of Ψ 1.20 GHz

$\epsilon_x = 5.0 \quad \epsilon_z = 2.5 \quad \mu_y = 4.30 - j6.00$

Open Waveguide Layer is 1 cm thick

— $\text{Re}(\Psi)$
 - - $\text{Im}(\Psi)$

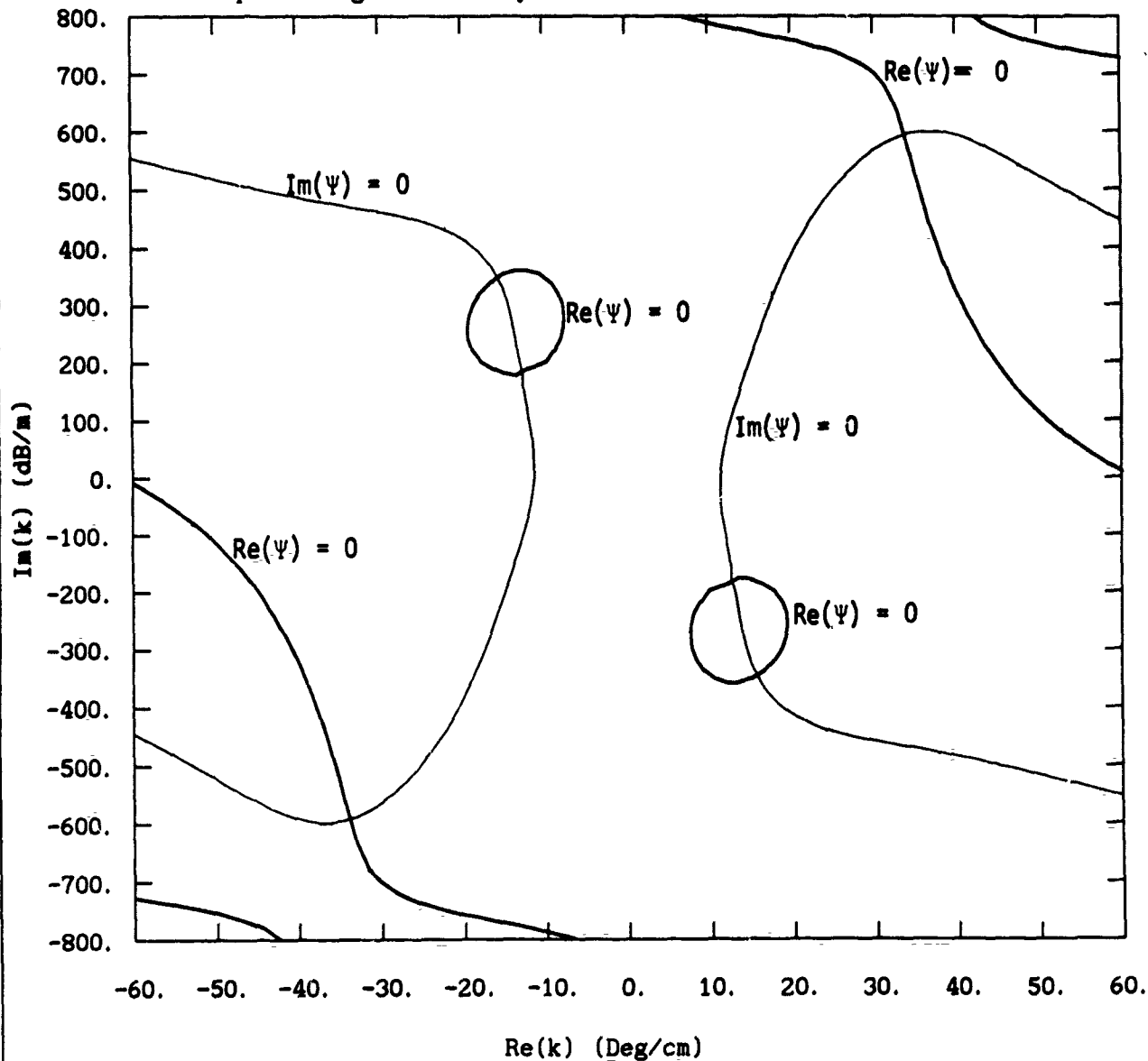


Zero-Crossing Contour Plot of Ψ 1.25 GHz

$\epsilon_x = 5.0 \quad \epsilon_z = 2.5 \quad \mu_y = 4.50 - j6.25$

Open Waveguide Layer is 1 cm thick

— Re(Ψ)
— Im(Ψ)

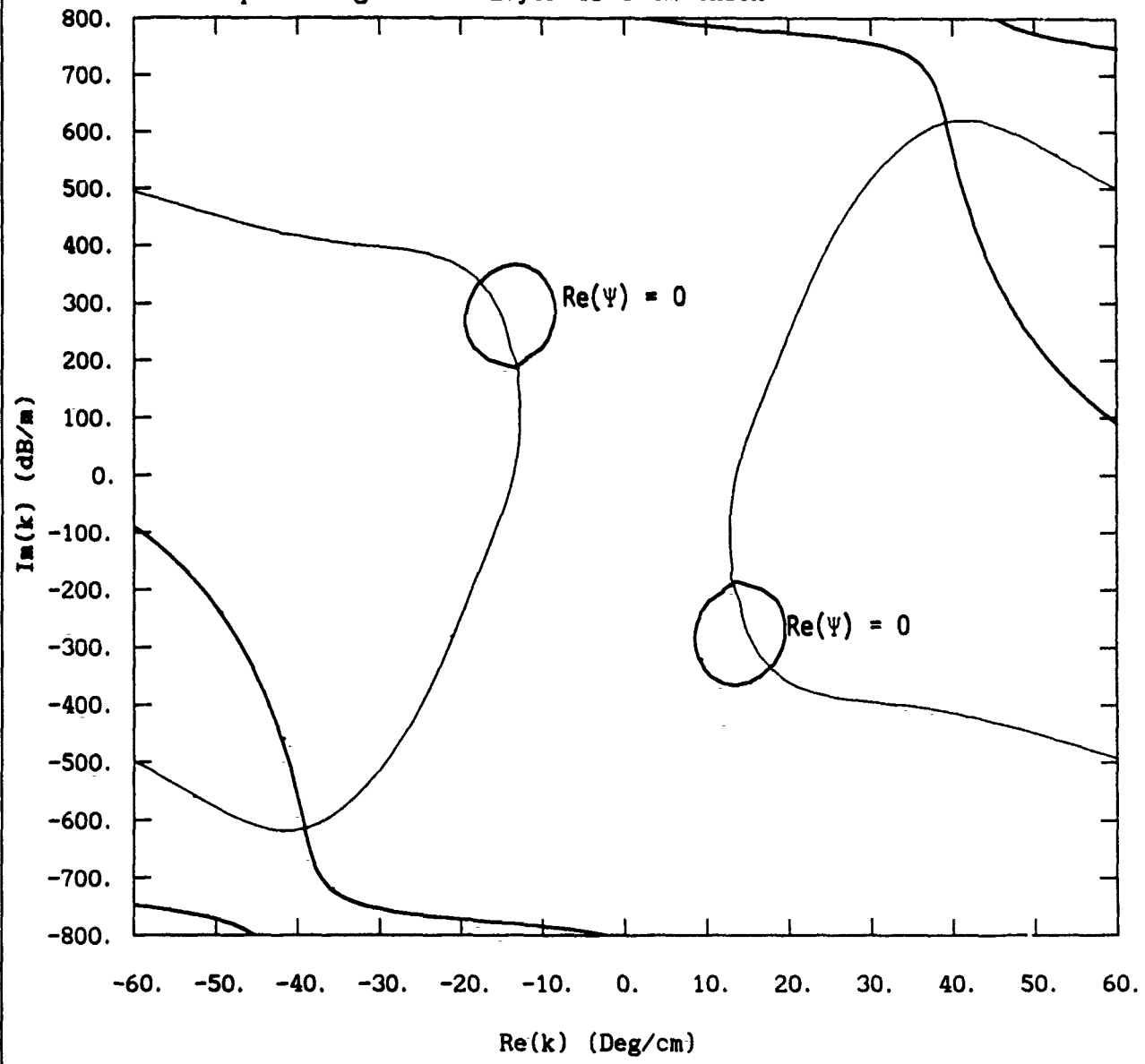


Zero-Crossing Contour Plot of Ψ 1.30 GHz

$\epsilon_x = 5.0$ $\epsilon_z = 2.5$ $\mu_y = 4.70 - j6.50$

Open Waveguide Layer is 1 cm thick

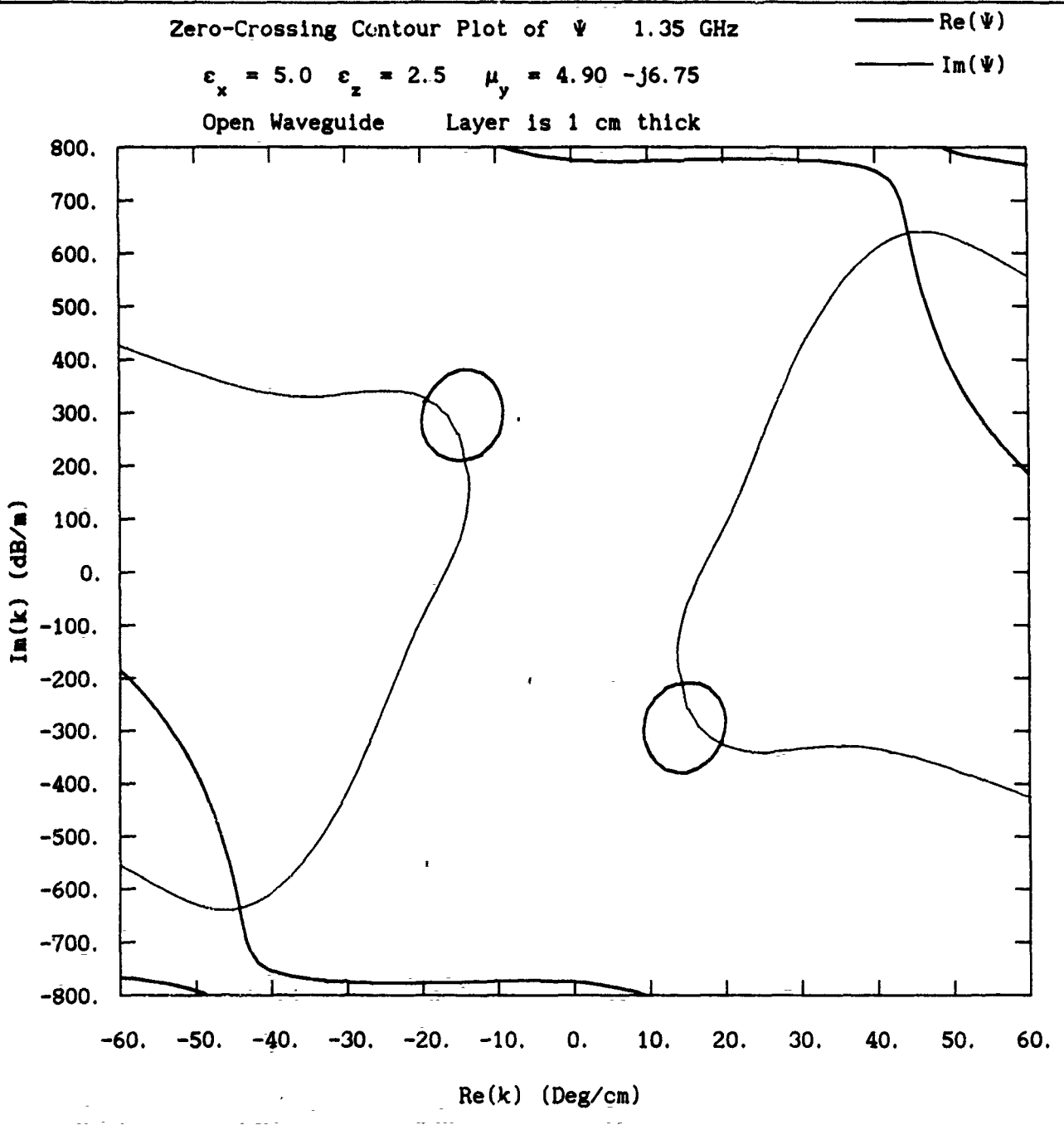
— $\text{Re}(\Psi)$
— $\text{Im}(\Psi)$



Zero-Crossing Contour Plot of Ψ 1.35 GHz

$\epsilon_x = 5.0 \quad \epsilon_z = 2.5 \quad \mu_y = 4.90 - j6.75$

Open Waveguide Layer is 1 cm thick



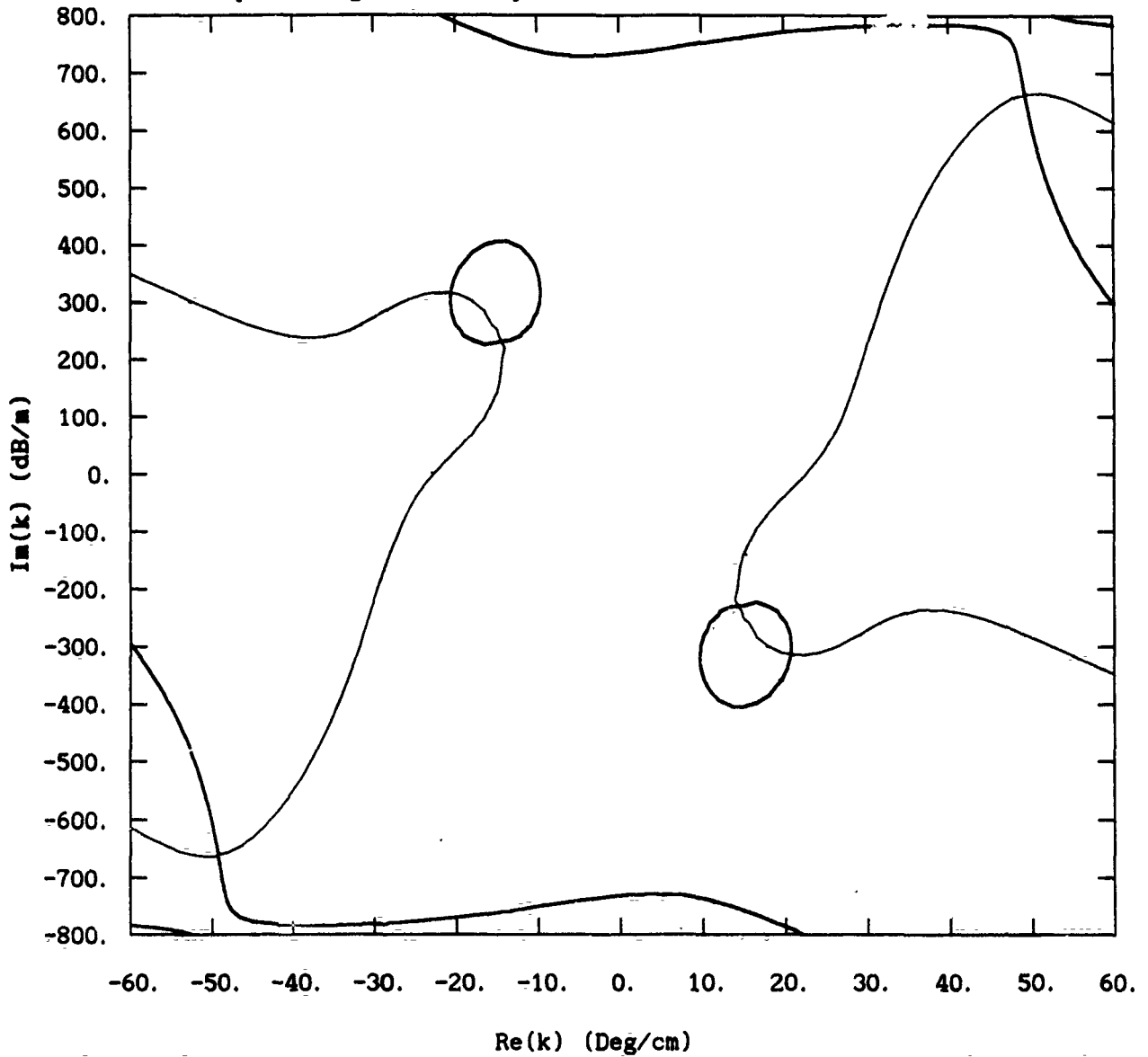
Zero-Crossing Contour Plot of Ψ 1.40 GHz

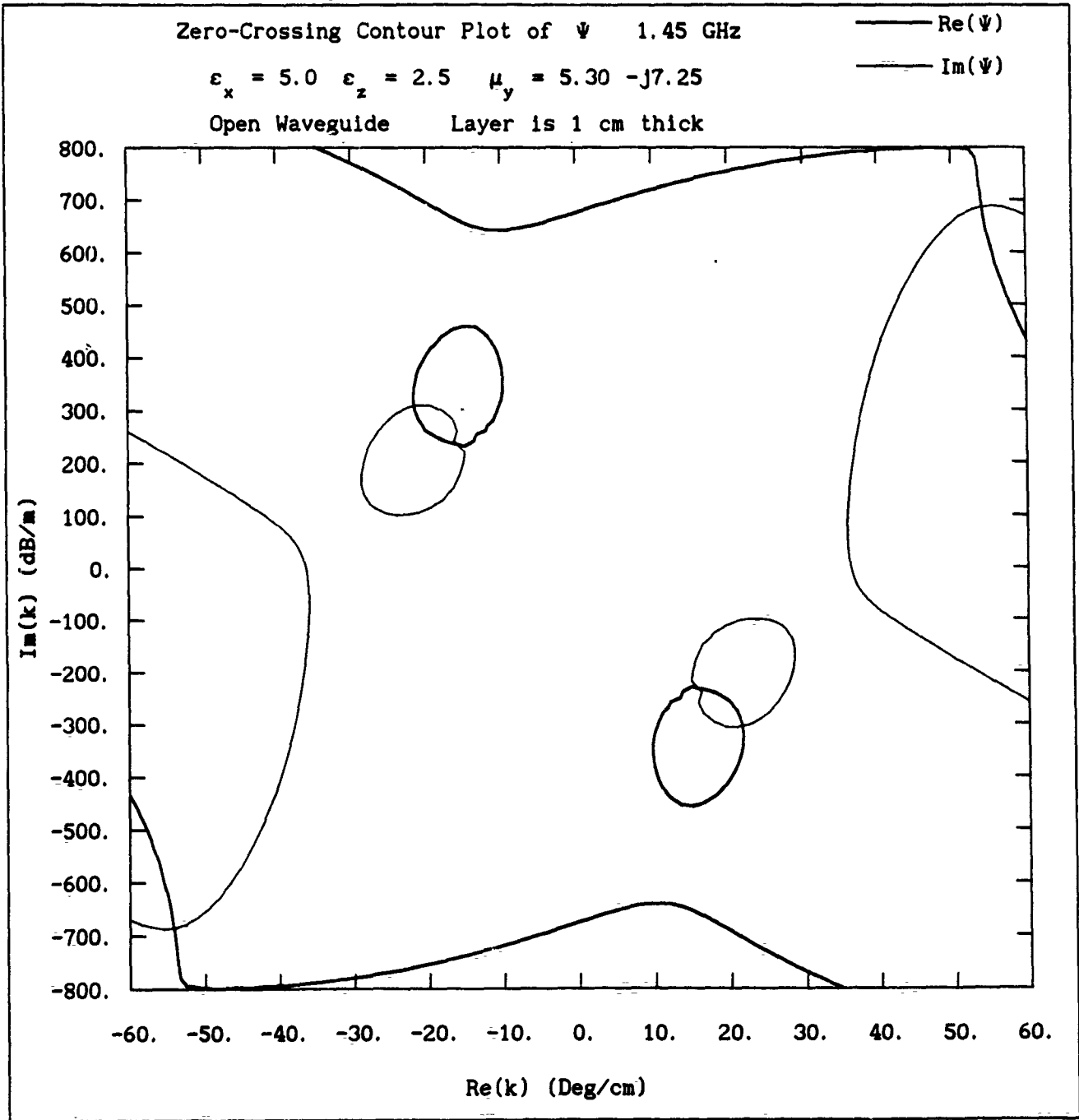
$\epsilon_x = 5.0 \quad \epsilon_z = 2.5 \quad \mu_y = 5.10 - j7.00$

Open Waveguide Layer is 1 cm thick

— Re(Ψ)

— Im(Ψ)





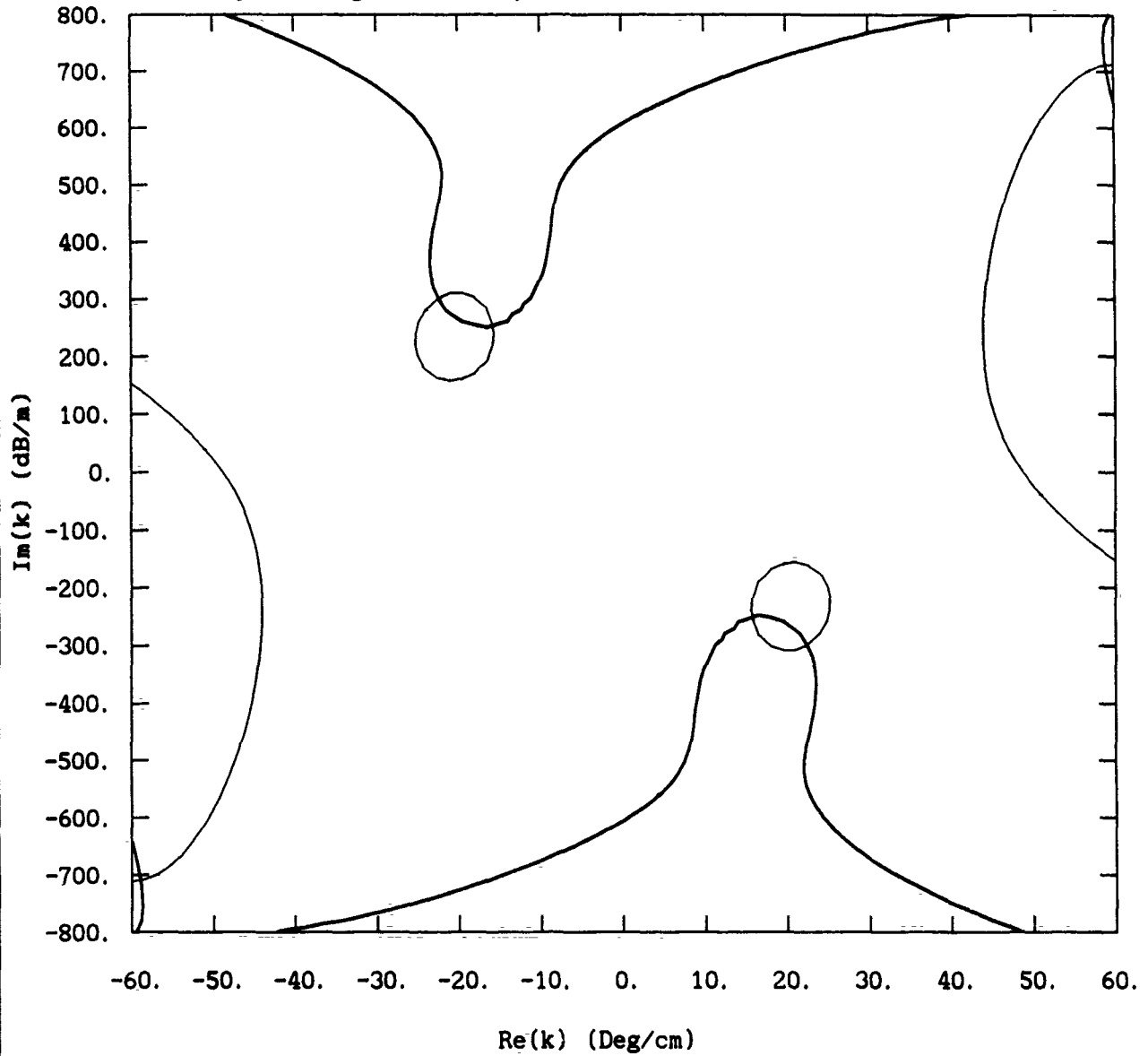
Zero-Crossing Contour Plot of Ψ 1.50 GHz

$\epsilon_x = 5.0$ $\epsilon_z = 2.5$ $\mu_y = 5.50 - j7.50$

Open Waveguide Layer is 1 cm thick

— Re(Ψ)

— Im(Ψ)



References

- [1] Garcia, C. B. and W. I. Zangwill. *Pathways to Solutions, Fixed Points, and Equilibria*. Englewood Cliffs, NJ: Prentice Hall(1981)
- [2] Hochstadt, Harry. *The Functions of Mathematical Physics*. New York: Dover(1986).
- [3] Hörmander, Lars. *Linear Partial Differential Operators* New York: Academic Press (1963)
- [4] Whittaker, E. T. and G. N. Watson. *A Course of Modern Analysis* London: Cambridge University Press (1986).

**MORPHOLOGY DEPENDENT RESONANCES OF TWO DISSIMILAR
COOPERATIVELY SCATTERING SPHERES**

K. A. Fuller
Atmospheric Sciences Laboratory
SLCAS-AR-A
WSMR, NM 88002

**RECENT PUBLICATIONS, SUBMITTALS FOR PUBLICATION,
AND PRESENTATIONS:**

- (A) K. A. Fuller and G. W. Kattawar, "A Consummate Solution to the Problem of Classical EM Scattering by an Ensemble of Spheres Part I: Linear Chains," *Opt. Lett.* **13**, 90(1988).
- (B) K. A. Fuller, "The Effects of Cooperative Scattering on Morphology Dependent Resonances of Bispheres," in *Proceedings of the 1988 CRDEC Scientific Conference on Obscuration and Aerosol Research*.
- (C) K. A. Fuller, "Internal Fields of Two Cooperatively Scattering Spheres," presented to the Optical Society of America 1988 Annual Meeting, Santa Clara, CA, Nov. 2.
- (D) K. A. Fuller and G. W. Kattawar, "A Consummate Solution to the Problem of Classical EM Scattering by an Ensemble of Spheres Part II: Clusters," *Opt. Lett.* **13**, 1063(1988).
- (E) K. A. Fuller, "Some Novel Features of Morphology Dependent Resonances of Bispheres," *Appl. Opt.* **28**, 3788(1989).

ABSTRACT

Recent calculations have shown that, on aggregation, two identical spheres can produce split resonance structures so broadened as to be observable even if their (single) progenitor resonances are narrow beyond detectability. Furthermore, it is well known that high Q morphology dependent resonances (MDRs) of single spheres are very sensitive to small variations in size and refractive index. Any attempt to observe the splitting effects that are induced by electromagnetic coupling of two dielectric spheres must concern itself with the practical matter of whether or not slight variations in the size and refractive index between the monomers will tend to obscure this phenomenon. In the following it is shown that realistic variations of about one part in 10^4 in the size and/or refractive index of the constituent spheres will still allow such resonance splitting to be observed. Effects of 'contamination' of a resonating sphere by a smaller sphere on its surface are studied as well.

DISCUSSION

Parameters of the form $kx = 2\pi x/\lambda$, where λ is the wavelength of the incident radiation, will be used henceforth to describe the dimensions of the system. The refractive indices of the spheres are denoted as $\mathcal{N}(\ell)$, where ℓ ($= 1$ or 2) identifies a specific constituent of the pair. Linearly polarized plane wave radiation with wave vector \mathbf{k}_0 impinges on these bispheres, with the angle between \mathbf{k}_0 and the common axis of the two spheres (designated as the z -axis) specified by α .

Theory predicts that, as two optically resonating spheres of identical size and composition are brought into close proximity of one another, electromagnetic coupling between the morphology dependent resonances (MDRs) of the monomers will cause the resonance structure of the system to split. Indications are that interactions between normal modes *other* than those responsible for the singlet resonances will enhance this splitting and, more importantly, broaden the resonance features by several orders of magnitude.¹

Under realistic laboratory conditions, the possibility of obtaining truly identical spheres is remote at best. The main question here is, 'Can the splitting survive if the constituents of the bisphere are slightly dissimilar?' Another experimental consideration is how the resonance spectrum of the bisphere in endfire illumination, where coupling between the spheres is strongest, will differ from that in broadside, where the coupling can be almost negligible.

Finally, it is of interest to see how the aggregation of a small contaminant sphere onto a larger, resonating sphere will affect that resonance.

MDRs correspond to isolated singularities in the coefficients of the multipole expansion of the scattered fields. In what follows, these normal modes are denoted according to their transverse electric ($TE_n^{(j)}$) and transverse magnetic ($TM_n^{(j)}$) nature, where the indices n and j denote the mode and resonance orders, respectively.² Fig. 1 shows the resonance spectra of two interacting spheres for varying separations and contrasts them with the spectrum of an isolated sphere. (It should be noted that if the separation is increased to 100 radii then the forward scattered intensity of the two spheres is almost four times the intensity scattered by a singlet, as expected.) A detailed discussion of the features appearing in Fig. 1 is given in Ref. 1. Briefly, the spectrum of the isolated sphere contains two prominent resonances, $TM_{39}^{(1)}$ and $TE_{35}^{(2)}$, which are located at $ka \approx 30.22$ and 30.30 , respectively. As a second sphere is brought into contact with the first the $TM_{39}^{(1)}$ resonance is split into two extrema: In the spectrum of the touching spheres, these appear as a maximum near 30.13 and a minimum at just below 30.26 . An important consequence of dependent scattering is that the 1st-order resonance in this bisphere spectrum can be as much as 1000 times as broad as the progenitor resonance. The two peaks in the bisphere spectrum at ≈ 30.23 and 30.38 are generated by the $TE_{35}^{(2)}$ resonance in the monomer and the peak at 30.39 is part of the $TE_{40}^{(1)}$ signature associated with a progenitor resonance near 30.459 .

Fig. 2 displays the effect that fluctuations in the size and/or refractive index of one sphere relative to the other have on the resonance spectrum of the system. As can be seen, the characteristic features of the split bisphere resonance are essentially unchanged even when both the size and refractive index of one sphere are about 0.07% lower than those of the other.

Figs. 3-5 offer comparisons between the spectra of a monomer, a scatterer composed of two such monomers, and systems constituted from this principal sphere being in close proximity to other spheres of a wide variety of sizes and refractive indices.

All of the above calculations have involved endfire incidence only. When radiation is

incident on a two-sphere system at angles other than endfire the lack of symmetry leads to a dramatic increase in the time required to calculate the resonance spectra of those bispheres considered above. One such run was made, however, and the results are shown in Fig. 6. Interestingly, at broadside incidence, the coupling between a large sphere and a relatively small carbon sphere which has adhered to its surface is too weak to significantly alter the resonance spectrum of the larger monomer. This observation also prompts one to ask whether or not splitting can be observed for orientations other than endfire incidence. To address this concern, the refractive index of the principal monomer was increased to 2.0, thus allowing sharp resonances to appear at around $ka = 10.0$, and bringing the length of the computations back into a more manageable range. It was found that splitting could be observed at shallow angles of incidence (say from $0 - 10^\circ$) even if dissimilarities between the spheres (relative fluctuations such as those discussed above) were introduced and the constituents were slightly separated.

In conclusion, it has been found that one need not have two perfectly identical spheres in order to observe the phenomenon of resonance splitting. Rather, the sizes and refractive indices of the two constituent spheres can differ by amounts that are within the limits imposed by current experimental methods. One is also allowed some latitude in the selection of the scattering geometry employed.

This work was conducted while the author was on a postdoctoral research associateship administered by the National Research Council and hosted by the U. S. Army Atmospheric Sciences Laboratory.

REFERENCES

1. K. A. Fuller, "Some Novel Features of Morphology Dependent Resonances of Bispheres," *Appl. Opt.* **28**, 3788(1989).
2. G. J. Rosasco and J. H. Bennett, "Internal field resonance structure: Implications for optical absorption and scattering by microscopic particles," *J. Opt. Soc. Am.* **68**, 1242(1978).

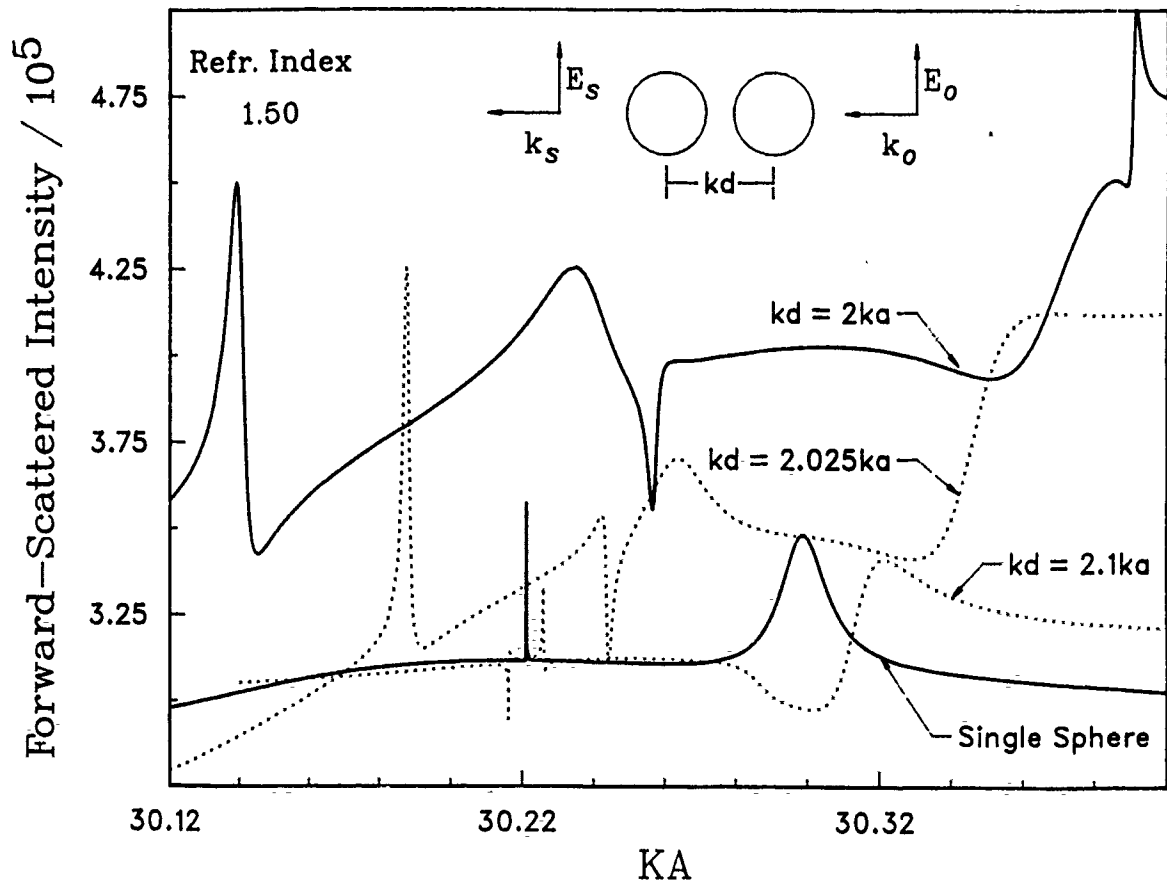


Fig. 1 Comparison of the resonance spectrum of two cooperatively scattering spheres with that of a single sphere.

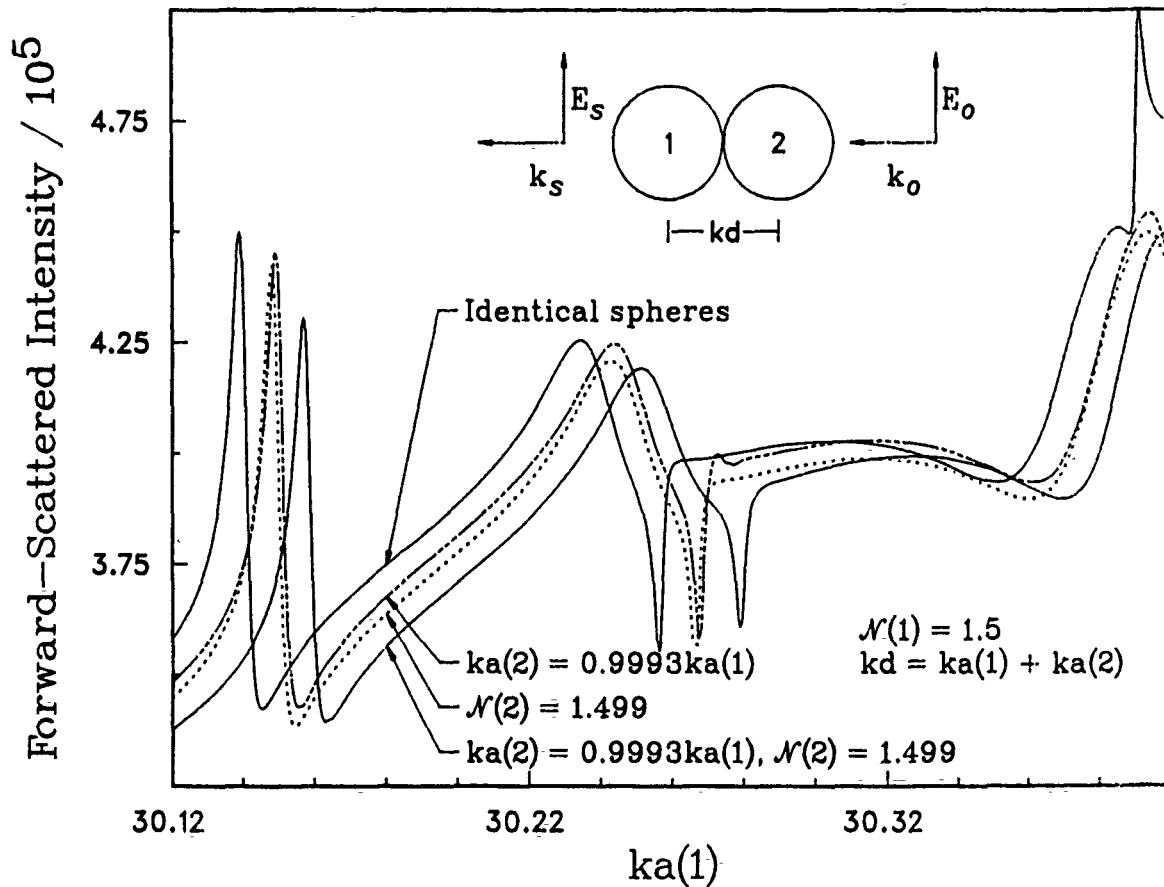


Fig. 2 Comparison of the resonance spectrum of two identical spheres with the spectra of bi-spheres with slightly dissimilar constituents. The two spheres are in contact in all cases.

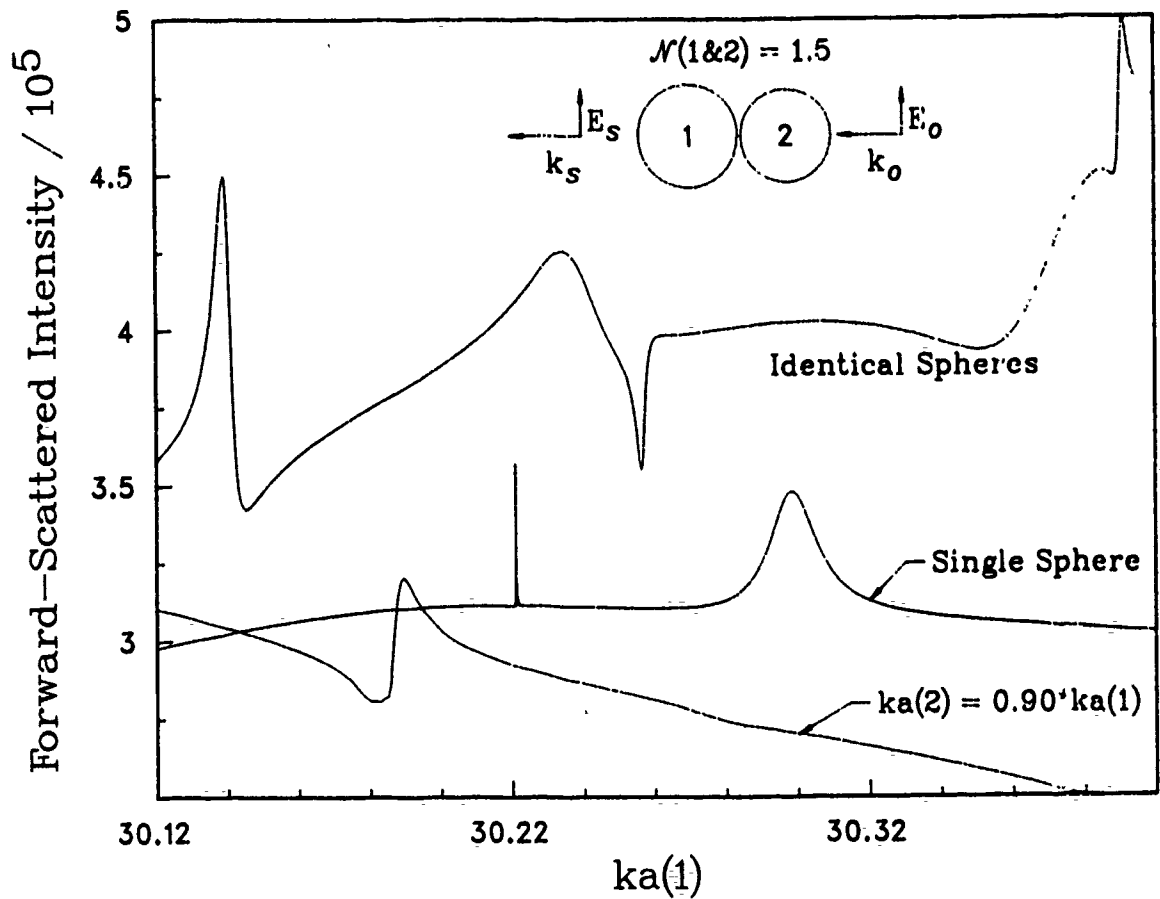


Fig. 3 Comparison of the resonance spectrum of two identical spheres with the spectrum of a system in which the size parameter of one of the spheres is 10% smaller than that of the other.

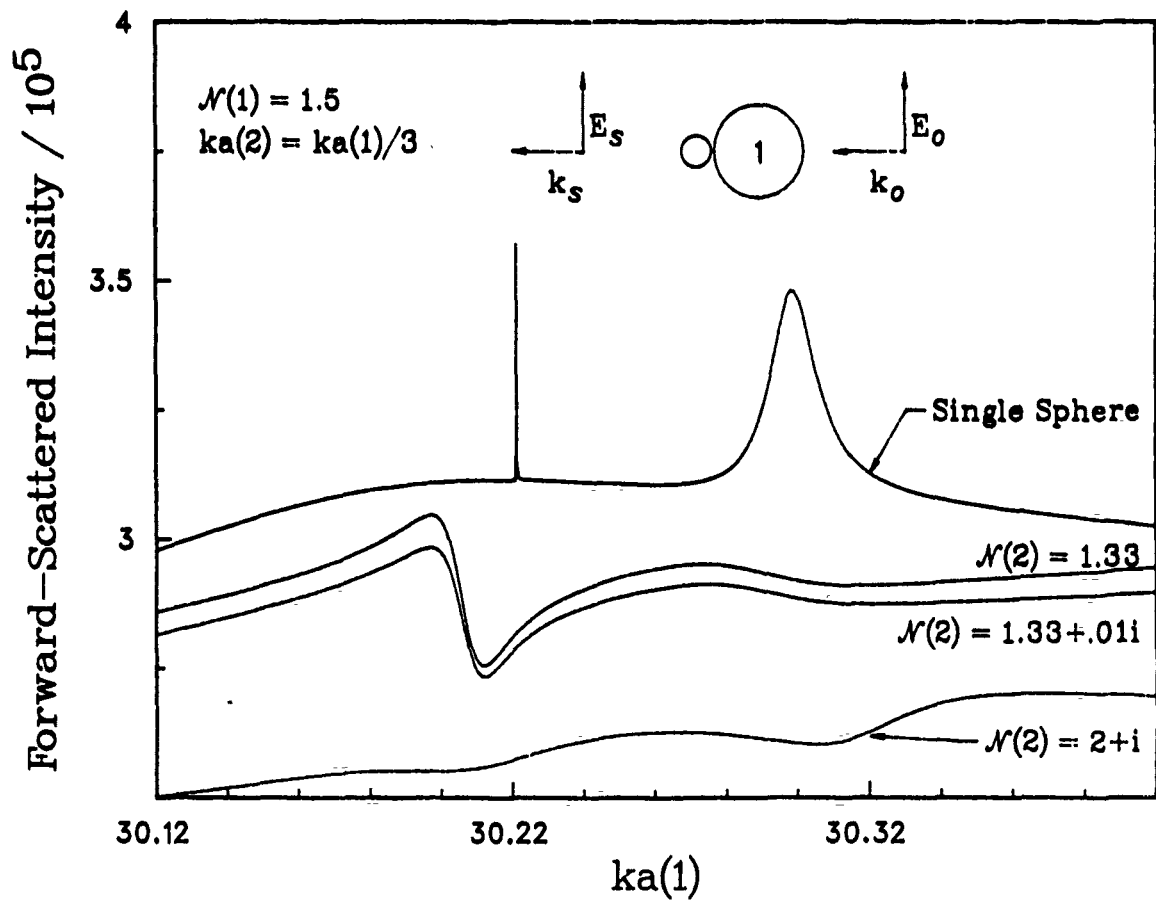


Fig. 4 The effect of a relatively small 'contaminants' of various refractive indices on the resonance spectrum of the principal sphere.

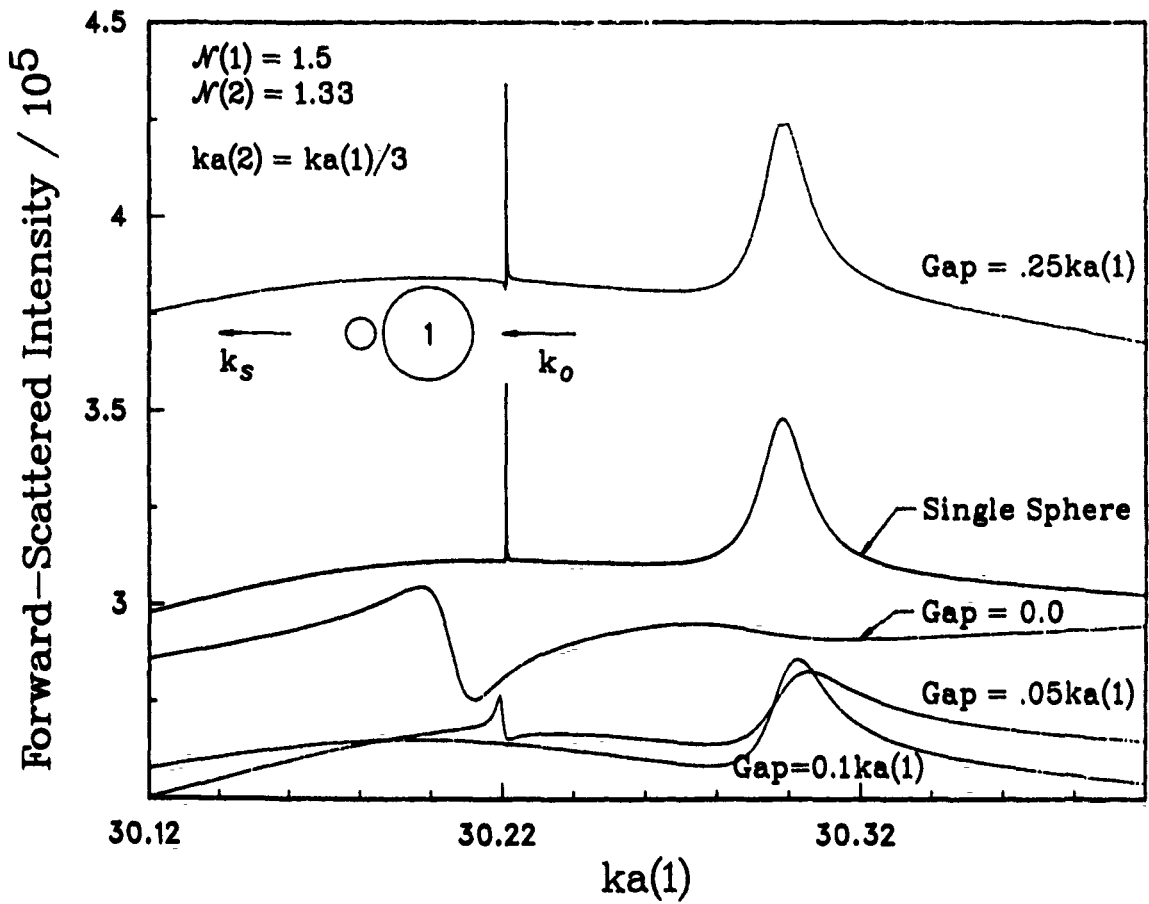


Fig. 5 The effects on the resonance spectrum of the principal sphere induced by a relatively small contaminant at various distances from its surface.

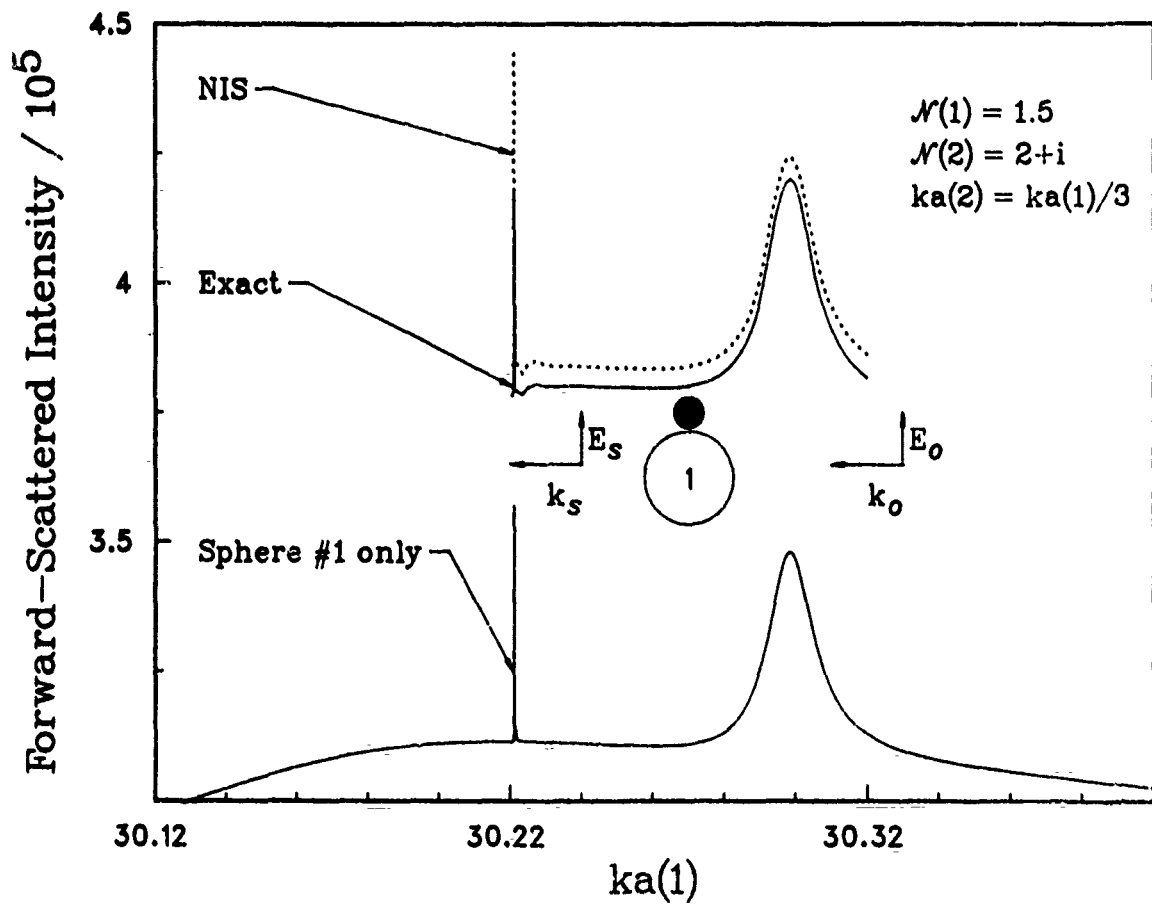


Fig. 6 The spectrum of a resonating sphere in contact with a relatively small, highly absorbing particle. In contrast to previous figures, the radiation impinges at broadside incidence. The case marked NIS is an approximation wherein dependent scattering is ignored. In the case of forward scattering, this quantity is independent of the incident angle. The NIS intensity of forward scattered radiation from identical bispheres is four times that of the radiation scattered by an isolated sphere.

Scattering of Femtosecond Laser Pulses

W. E. White, C. Wang, and E. S. Fry
Physics Department, Texas A&M University
College Station, Texas 77843

Recent Publications and Submittals for Publication:

1. "Colliding-Pulse Phase Modulation and Chirping of Ultrashort Optical Pulses in Thin Slabs of Nonresonant and of Saturable Media", K. L. Schehrer and E. S. Fry, *Optical Society of America B*, **6**, 1182 (1989).
2. "Consummate Solution to the Problem of Electromagnetic Scattering by an Ensemble of Spheres. I: Linear Chains", K. A. Fuller and G. W. Kattawar, *Optics Letters*, **13**, 90 (1988).
3. "Consummate Solution to the Problem of Classical Electromagnetic Scattering by an Ensemble of Spheres. II: Clusters of Arbitrary Configuration", K. A. Fuller and G. W. Kattawar, *Optics Letters*, **13**, 1063 (1988).
4. "Colliding Pulse Mode-Locked Dye Laser Stabilization Using an Intracavity Spectral Filter". K. L. Schehrer, E. S. Fry and G. T. Bennett, *Appl. Opt.* **27**, 1908 (1988).
5. "Time Averaged Scattering of Femtosecond Laser Pulses", W. E. White, C. Wang, and E. S. Fry, Submitted to *Appl. Opt.*, December, 1989.
6. "Calculation of Time-Resolved Scattering of Femtosecond Light Pulses from Dielectric Spheres" C.-R. Hu, G. H. Rose and G. W. Kattawar, Submitted to the Proceedings of the 1988 CRDEC Scientific Conference on Obscuration and Aerosol Research.
7. "Time Resolved Measurements of the Scattering of Femtosecond Laser Pulses", W. E. White, C. Wang, and E. S. Fry, Submitted to the Proceedings of the 1988 CRDEC Scientific Conference on Obscuration and Aerosol Research.

8. "Scattering of Femtosecond Laser Pulses", W. E. White, C. Wang, and E. S. Fry, Submitted to the Proceedings of the 1989 CRDEC Scientific Conference on Obscuration and Aerosol Research (**This paper**).
9. "Absorption Measurements Using an Integrating Cavity", R. M. Pope, E. S. Fry, and R. L. Montgomery, Submitted to the Proceedings of the 1989 CRDEC Scientific Conference on Obscuration and Aerosol Research(**These Proceedings**).

Recent Theses:

10. "Scattering of Femtosecond Laser Pulses", William E. White, Phd. Thesis, December, 1989.
11. "Intracavity Evolution of Ultrashort Optical Pulses in a Colliding Pulse Mode-Locked Laser", Kevin L. Schehrer, PhD. Thesis, May, 1989.

Recent Presentations:

12. "Analysis of Time-Resolved Scattering of Femtosecond Light Pulses from a Dielectric Sphere", G. H. Rose, C.-R. Hu, and G. W. Kattawar, presented at the 1989 CRDEC Scientific Conference on Obscuration and Aerosol Research, Aberdeen Proving Grounds, Maryland, 1989.
13. "Recent Femtosecond Scattering Results", C. Wang, W. E. White, and E. S. Fry, presented at the 1989 CRDEC Scientific Conference on Obscuration and Aerosol Research, Aberdeen Proving Grounds, Maryland, 1989.
14. "Precision Absorption Measurements in a Highly Scattering Medium", R. M. Pope, R. L. Montgomery, and E. S. Fry, presented at the 1989 CRDEC Scientific Conference on Obscuration and Aerosol Research, Aberdeen Proving Grounds, Maryland, 1989.
15. "Scattering from Sphere Doublets", K. L. Thieme, W. E. White, and E. S. Fry, presented at the 1989 CRDEC Scientific Conference on Obscuration and Aerosol Research, Aberdeen Proving Grounds, Maryland, 1989.
16. "Scattering by a Single Sphere at an Angle of Zero Degrees", D. F. McCoy, and E. S. Fry, presented at the 1989 CRDEC Scientific

Conference on Obscuration and Aerosol Research, Aberdeen Proving Grounds, Maryland, 1989.

17. "Integrating Cavity Absorption Meter", E. S. Fry, G. W. Kattawar, R. M. Pope, R. L. Montgomery, and J. S. Cleveland, **invited** paper at the Annual Meeting of the Am. Optical Society, Orlando, FL 1989.

ABSTRACT

Both time averaged and time resolved scattering of femtosecond laser pulses from small dielectric spheres has been studied under this contract, and initial results were presented in recent CRDEC Proceedings. This report describes recent and significantly improved data on the time averaged scattering. Measurements have been made for pulses that have spatial lengths ranging from smaller through larger than the dimensions of the scatterer. Our experimental data are in good agreement with theoretical predictions.

Improvements in time resolved scattering data for both single spheres and cubes are underway. Other future work includes: (1) time resolved measurements of frustrated total internal reflection and thus the first measurement of time delays associated with quantum mechanical tunneling; (2) measurement of the amplitude and phase of light scattering at an angle of zero degrees and the first study of the Optical Theorem in the visible; (3) measurement of the Mueller matrix for sphere doublets and triplets in various orientations; and (4) some studies of time resolved coherent back scattering.

INTRODUCTION

With the recent development of lasers capable of producing pulses with duration of the order of femtoseconds¹, an entirely new class of optical scattering problem has evolved. Even at 300 million meters per second, light can travel but a very short distance during one of these pulses. Thus, investigation of the scattering of pulses that are spatially shorter than the 5 - 50 μm dimensions of Mie sized scatterers is now experimentally feasible. This case is fundamentally different from previous scattering experiments in which a primary assumption is typically that the entire scatterer is exposed to a uniform

optical radiation field. For these ultrashort pulses, the front and back sides of the scatterer will interact with entirely different radiation fields. Figure 1 demonstrates this situation graphically by superimposing a scaled $20\ \mu\text{m}$ (diameter) sphere and a 33 femtosecond (FWHM) pulse. The 33 femtosecond pulse has a spatial length of $10\ \mu\text{m}$ and is therefore unable to interact with the front and back of the sphere simultaneously.

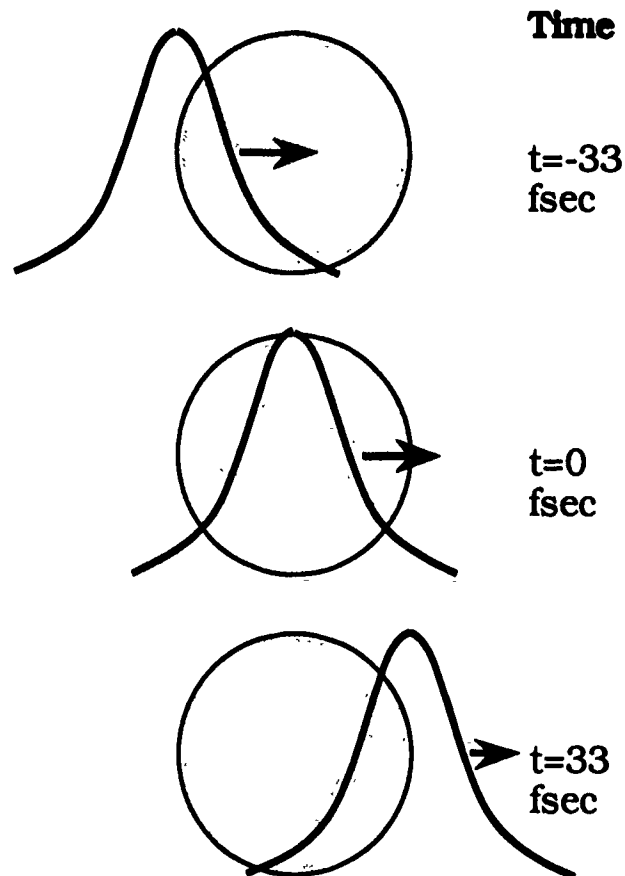


Figure 1. Interaction of a 33 femtosecond pulse with a $20\ \mu\text{m}$ (diameter) sphere taken at three consecutive times separated by 33 femtoseconds

EXPERIMENTAL

A block diagram of the experiment is presented in Figure 2. This entire system is mounted on a Newport Research Corp. optical table which is isolated from floor vibrations by Newport Research pneumatic isolation legs.

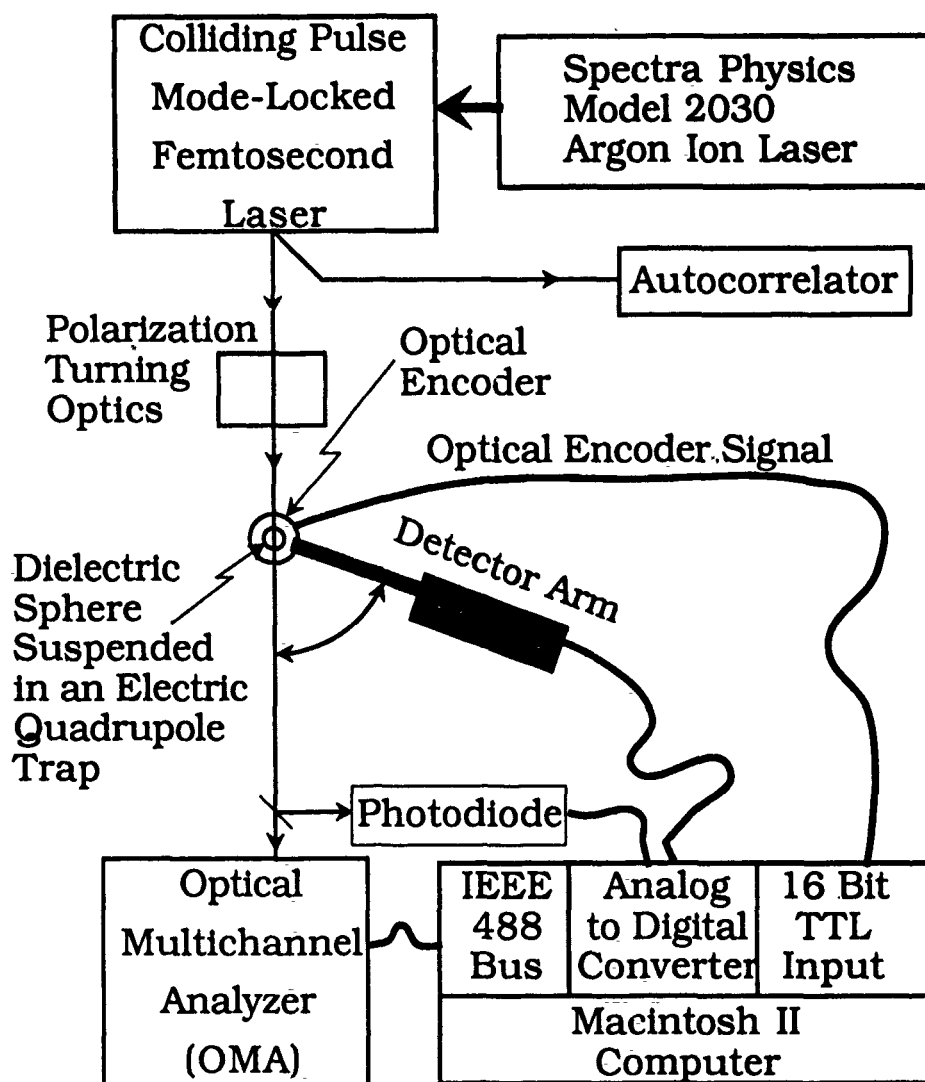


Figure 2. Overview of the experimental apparatus designed for measuring the time averaged scattering of femtosecond pulses from a single Mie sized dielectric sphere.

The apparatus is composed of four major components; the CPM laser, the detector arm, the quadrupole trap, and the data gathering computer.

The CPM laser

A Spectra Physics model 2030 argon ion laser provides the pump energy for the CPM laser and its typical operating parameters are shown in Table I. While the laser is capable of operating with pulse

widths as short as 28 fsec, and as long as 500 fsec; for the long term stability required for this research, the laser is operated between 75 fsec and 200 fsec. The measured bandwidth is the full width half maximum (FWHM) bandwidth measured from the actual output of the laser. Expected bandwidth is based on the Fourier transform limit assuming a Gaussian pulse envelope.

Table I. Typical operating characteristics of the CPM femtosecond laser used in this research.

Short term minimum pulse width	28 fsec
Short term maximum pulse width	500 fsec
Long term minimum pulse width	75 fsec
Long term maximum pulse width	250 fsec
Pulse repetition rate	83 MHz
Average output power	40 mW
Peak power (75 fsec sech ² pulse)	8.5 kW
Pulse energy	.5 nJ
Bandwidth at 75 fsec (measured)	5.5 nm
Bandwidth at 75 fsec (expected for Gaussian)	5.5 nm

Because the spectrum of the pulses is important in understanding the scattering, any experiment designed to provide insight into these scattering processes must include provisions for measurement of the pulse spectrum, along with pulse width and angular scattering. Since the CPM laser has two identical output beams, one beam is used for scattering and the other is simultaneously autocorrelated in order to monitor pulse width. The fact that only a minute percentage of the incident beam is actually scattered permits

simultaneous measurement of the pulse spectrum and average power by the OMA and photodiode, respectively. The average power measurement is used to constantly normalize the angular scattering measurements to laser power, thus eliminating the effect of laser power fluctuation on the scattering data.

The CPM laser ring is oriented in the horizontal plane and, since the intracavity prism sequence and dye jets are oriented at Brewster's angle, the output of the laser is polarized horizontally. However, more pronounced scattering features are observed when the light is polarized perpendicular to the scattering plane. Consequently, the incident beam is steered onto the scattering sphere by a pair of mirrors in a configuration designed to rotate the polarization to the perpendicular state.

The detector arm

The detector arm is motor driven and swings through a scattering angular range of 20° to 175° ; it is outlined in Figure 3. A lens with a 15 cm focal length is placed 15 cm from the levitated sphere, thus the light that is scattered by the sphere is collected and turned parallel by the lens. The pinhole assembly then determines the angular resolution of the system. In this case, the .008" pinhole used sets the upper limit on angular resolution to $\sim .155^\circ$. Because only light that is highly parallel can get through the double pinhole, this system also drastically reduces the amount of stray light getting to the PMT (mainly from scattering by the quadrupole trap structure). This is necessary in order to extract the maximum available dynamic range from the PMT and to ensure that the measured light was actually scattered from the sphere.

The motor speed and wheel diameter are chosen so that the sweep rate is approximately .25 degrees per second. This allows the time constant on the current to voltage amplifier to be as large as .62 seconds with no adverse effect on the angular resolution of the system. To insure that the time constant is not the limiting factor in angular resolution, a time constant of .5 sec is used in this experiment. Because of the slow rate at which the arm is swept, a measurement from 20° to 170° typically takes ~ 10 minutes.

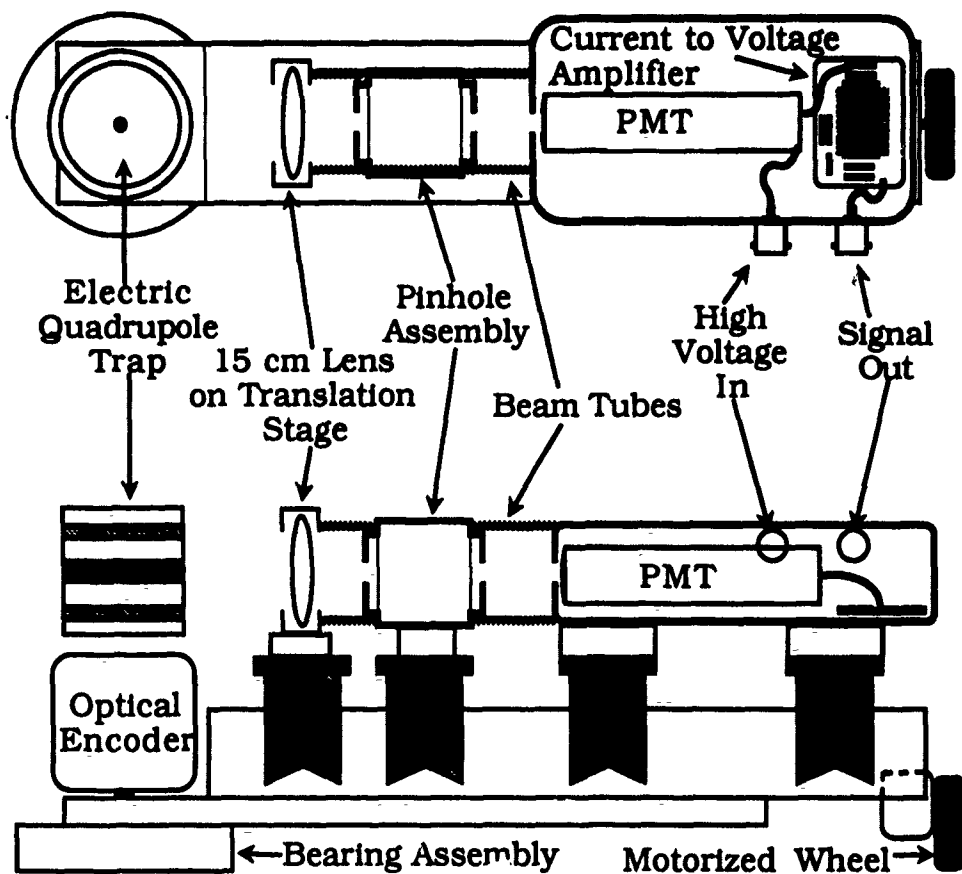


Figure 3. Top and side view of the detector arm assembly, and electric quadrupole trap.

Generally, several separate measurements are made and later averaged together. Consequently, the laser output must be stable throughout the time it takes to make all of the measurements to be averaged. If an average of four measurements is desired, the laser must then be stable for a period of approximately 40 minutes. It is this restriction that limits the pulse width to approximately 75 fsec in this experiment. While the laser is capable of providing pulses as short as 28 fsec, it will not operate below 75 fsec for a period of 30 to 40 minutes without significant pulsewidth or bandwidth changes.

The PMT is an RCA model 8644, which has particularly good response down into the red (630 nm) region of the spectrum. A two stage current to voltage amplifier is mounted inside the same shielded

case as the PMT. The first stage of the current to voltage amplifier provides a low impedance load for the current producing PMT. This stage of the amplifier forces a current equal to the current from the PMT through the feedback resistor, thus converting the input current to a voltage while at the same time keeping the load on the PMT to a minimum. The output voltage of the first stage is then further amplified and integrated by the second stage of the amplifier. The low output impedance of this stage allows the signal to be transmitted through several meters of coaxial cable to the GW Instruments analog to digital converter board in the Macintosh II computer, with minimum signal degradation.

The angle of the detector arm is monitored by a BEI model 8192 optical encoder. This encoder provides a measure of the absolute angle of the arm with a precision of 13 bits in 360 degrees or 43.95 millidegrees. The 13 bits of encoder information is input into a 16 bit TTL daughterboard that is mounted on the GW Instruments A/D-D/A card in the computer.

The electric quadrupole trap

Single micron sized spheres must be obtained and stably levitated for the scattering measurements. Electron microscopy reveals that the glass and polystyrene spheres which are purchased from companies such as Saragen Diagnostics are not perfect spheres, therefore a droplet of high viscosity, low vapor pressure oil is used. The vapor pressure must be low to prevent significant change in sphere size due to evaporation. An index matching oil produced by Cargille Laboratories (stock number #1160) was specifically chosen because it not only has a high vapor pressure, but the optical properties such as dispersion are characterized to 5 digit precision by the company.

The containment/levitation system was an electrodynamic trap similar to the design of Wuerker et al² Because the dynamics of this design are similar to those present in an electric quadrupole mass filter described by Paul and Raether³ in 1955, it is often referred to as an electric quadrupole trap. In 1980, Davis and Ray⁴ demonstrated that this type of charged particle trap is capable of stably suspending a

single liquid droplet at atmospheric pressure for extended periods of time.

The data gathering computer system

This experiment is controlled by an Apple Macintosh II personal computer which is responsible for gathering the experimental data, reducing it, and then presenting it in a useful format. Labview, a programming environment developed by National Instruments was used to develop the program responsible for gathering all of the pertinent information, and providing a user interface suitable for controlling this experiment. One Labview program is designed to control a Tracor Northern diode array interface, thus acting as an OMA. Another Labview program is responsible for measuring the normalized intensity scattered as a function of detector arm angle.

During the actual data gathering process, the pulse spectrum is measured before and after the scattering measurement, and the average is assumed to be a good representation of the spectrum during the scattering measurement. This is a very good assumption considering that prior to measurement, the laser is adjusted to provide a very stable spectrum. The spectra measured before and after the scattering measurement are typically indistinguishable. A more accurate method involving measurement of the pulse spectrum for each angular intensity measurement could be used. However, the volume of data gathered, and the computer time necessary to analyze the immense amount of data is for all practical purposes prohibitive.

THEORETICAL

For plane wave scattering, Mie demonstrated that by expanding the incident plane wave in terms of vector spherical harmonics and imposing the proper boundary conditions, the elements of the scattering matrix that relates the scattered fields to the incident fields can be calculated⁵. For the results presented here, the Mie calculations are performed by a FORTRAN program which was originally designed by Prof. George Kattawar⁶ and later modified to operate interactively on the Macintosh II computer. The bulk of this

lengthy program is contained in the subroutines that calculate the special functions.

The time averaged scattering of femtosecond pulses from a single sphere is expected to be equivalent to the superposition of the scattered intensity of each of the plane wave Fourier components of the pulse; these plane wave scattered intensities are calculated using Mie theory. Thus, in order to calculate the expected scattering of femtosecond pulses from a sphere, the Mie solution for each Fourier component must first be calculated; then, for each angular position, all of the Mie solutions are weighted according to relative spectral intensity, and added incoherently. This can be expressed mathematically as

$$I_{pulse}(\theta) = \sum_{\lambda} I(\lambda, \theta) G(\lambda)$$

where $I_{pulse}(\theta)$ is the time averaged intensity of the scattered pulse, $I(\lambda, \theta)$ is the plane wave scattered intensity at wavelength λ , and $G(\lambda)$ is the spectral intensity at λ . Experimentally, $G(\lambda)$ is measured directly by the OMA for each data set and is stored on the computer hard disk.

RESULTS

First, the size of the sphere must be accurately determined. The scattering of light by spheres produces scattering patterns that are rich in detail and strongly dependent on the index of refraction and the size parameter x . Thus, measured plane wave scattering patterns can be compared to the predictions of Mie theory, to determine the sphere radius a . In this case, the index of refraction of the oil is known to be 1.48218 at the 632.8 nm wavelength of the Helium-Neon laser used for the sizing measurements.

The measured scattering from a sphere, along with the results of the Mie calculation for a 32.615 μm sphere are shown in Figure 4. In this case the fitting was done by manually comparing the calculated and measured results, and looking for the best match. For the case of a sphere this large, the scattering patterns change enough to resolve the difference between, for example 32.610 μm and 32.615 μm ; thus the resolution of the fit is $\approx .005 \mu\text{m}$.

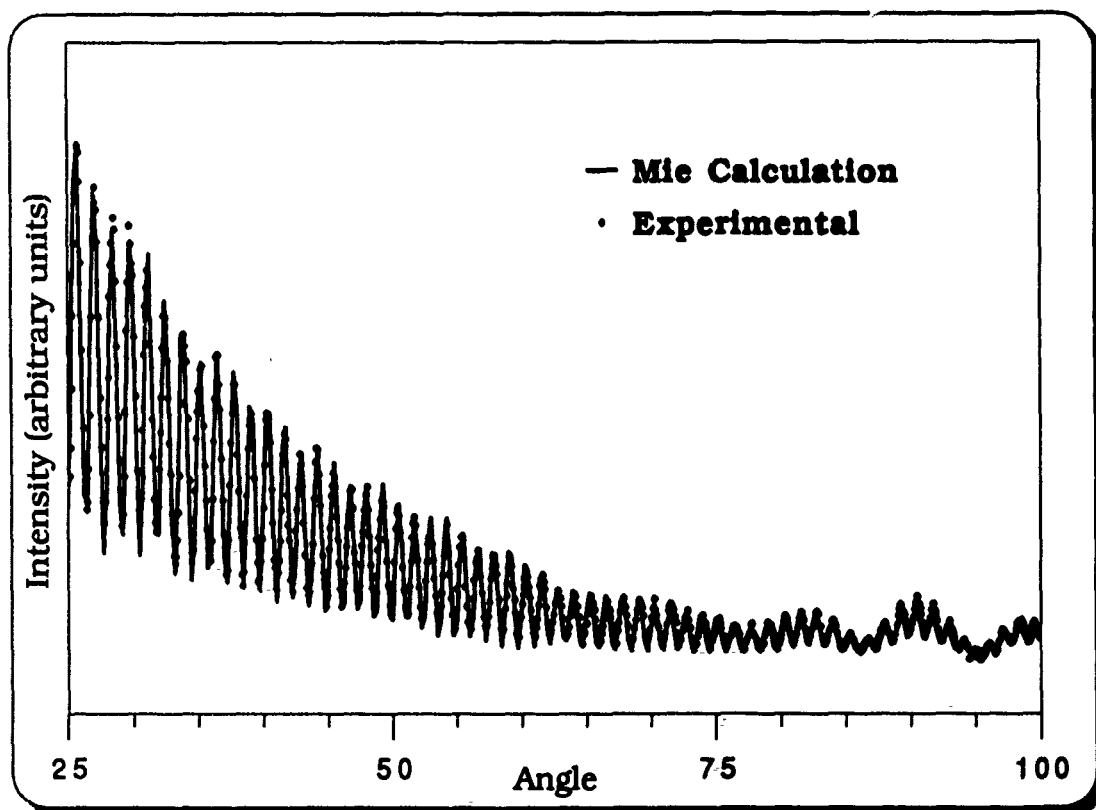


Figure 4. A comparison of the measured (dots) and calculated (line) intensity scattered by a $32.615\ \mu\text{m}$ sphere as a function of scattering angle. The wavelength of the cw incident beam is $\lambda = 632.8\ \text{nm}$.

Along with determination of sphere size, a comparison of measured and calculated scattering patterns allows an upper limit to be set on the absorption of the sphere. By running the Mie routine for this size sphere, with various values for the complex part of the index of refraction, the modulations in the envelope that begin to appear above 85° are heavily damped by any absorption. Comparison of these calculations with measured results shows that the upper limit for the complex part of the index of refraction is $\approx .001$.

Figures 5 and 6 are plots comparing the measured and calculated scattering of 75 and 188 femtosecond pulses from a $32.615\ \mu\text{m}$ sphere. This corresponds to pulses whose spatial lengths are $23\ \mu\text{m}$ and $56\ \mu\text{m}$, respectively; thus covering the range of smaller than, to larger than the sphere diameter. Each figure also includes a plot of the

corresponding measured spectral intensity which is used in the calculation of the theoretical scattering. Figure 7 is an expanded plot of the 75 femtosecond data over a narrower angular range that allows the results to be seen more clearly.

As seen in Figures 5-7, the calculated and the measured results are in excellent agreement; verifying that the scattering of femtosecond pulses is properly described as a superposition of the scattering of the Fourier components of the pulse. The effect seen in both these results, and by comparison with the cw data shown in Figure 4, is that as the bandwidth of the laser increases, the relative amplitude of peaks in the time averaged angular scattering is decreased. This is expected in view of the fact that as wavelength changes, the peaks shift in angle; therefore, a superposition of many wavelengths would "wash out" the peaks. It should also be noted that the spectral intensity of the pulses (shown in the inset on each figure) does not change appreciably between these two extreme pulse width cases. This is simply due to the fact that the laser does not always produce Fourier transform limited pulses; the same bandwidth can always have a temporal width greater than the Fourier transform minimum. These results clearly show that the time averaged scattering of femtosecond pulses is dependent only on pulse spectrum and not pulse width. One implication of this is that a cw laser with a spectral intensity identical to that of an ultra short pulse laser, would have angular scattering dependences identical to those of the ultra short pulse laser.

While the comparison above shows an excellent agreement between theory and experiment out to a scattering angle of 100° , a plot of the same data extended to 175° reveals significant discrepancies. Figure 8 shows these discrepancies at large scattering angles for incident 75 fsec pulses; however the discrepancies are identical for all pulse widths, and are also present in the cw scattering data. Because there is such excellent agreement over most of the angular range, this discrepancy is surprising. After all, any systematic problems in the experimental design capable of producing this disagreement between theory and experiment would be expected to have some effects at other scattering angles.

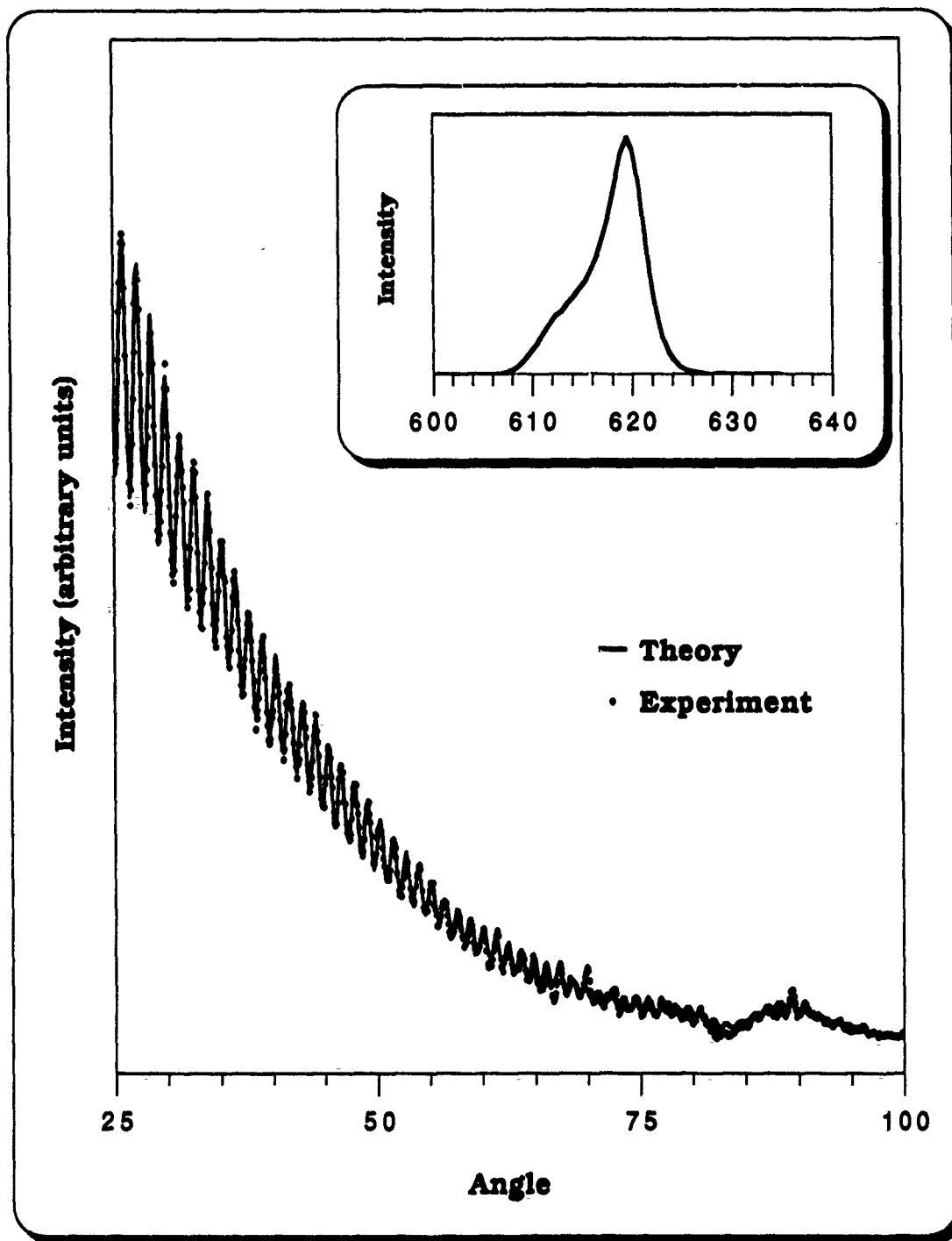


Figure 5. Comparison of experimental (points) and theoretical (line) time averaged angular scattering results for scattering of 75 fsec pulses from a 32.615 μm sphere. Inset shows spectral intensity of the laser during the scattering measurement.

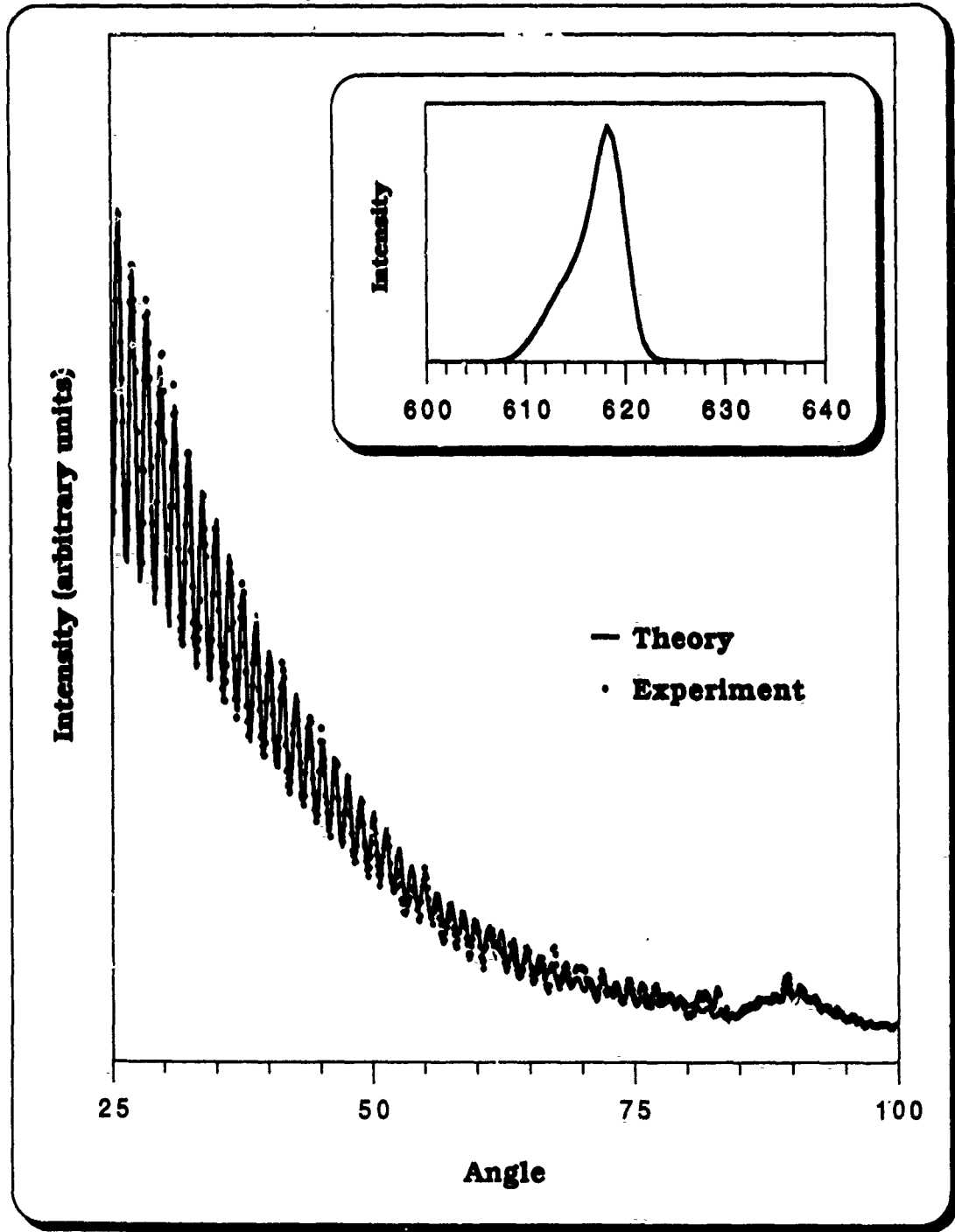


Figure 6. Comparison of experimental (points) and theoretical (line) time averaged angular scattering results for scattering of 188 fsec pulses from a 32.615 μm sphere. Inset shows spectral intensity of the laser during the scattering measurement.

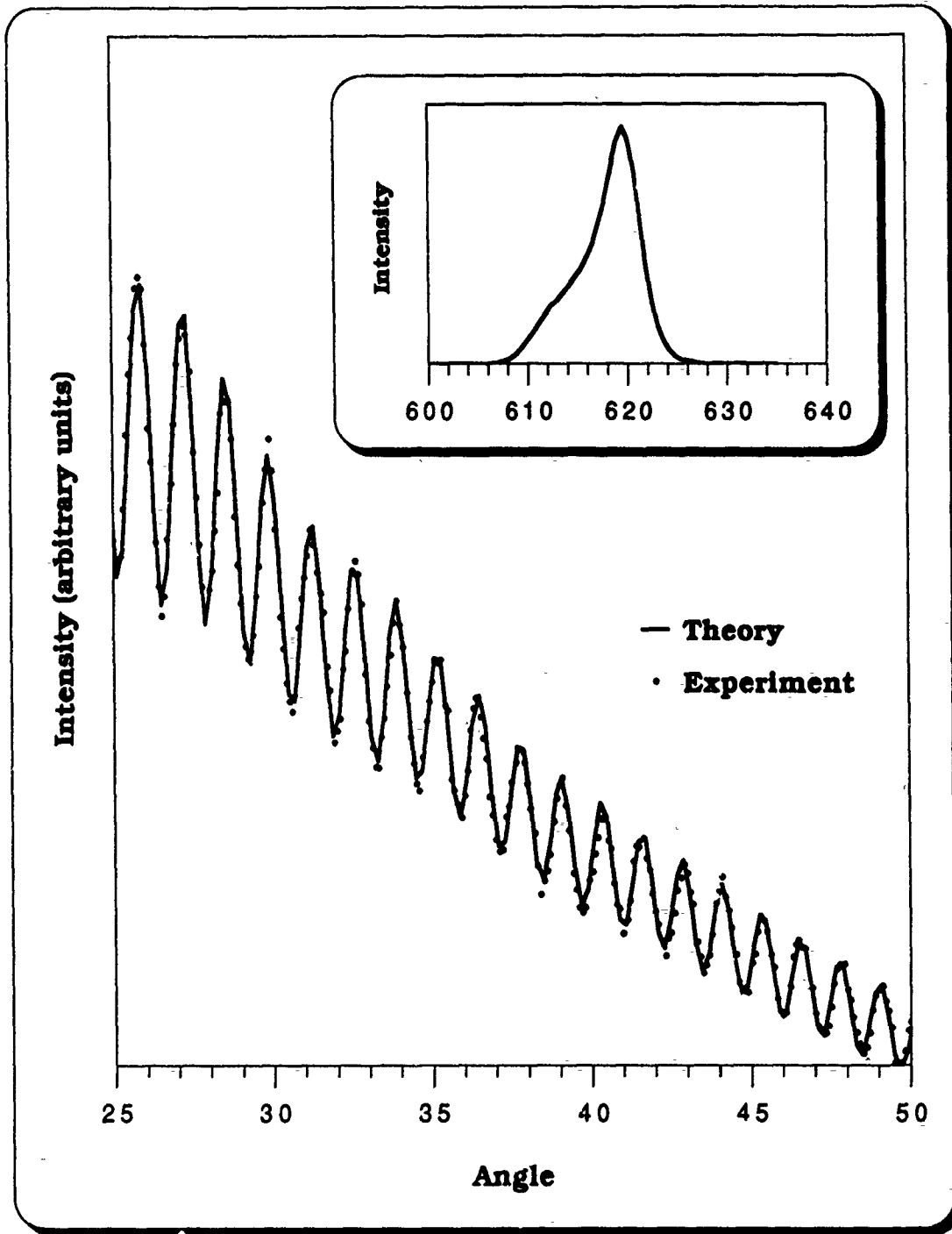


Figure 7. High resolution comparison of experimental (points) and theoretical (line) time averaged angular scattering results for scattering of 75 fsec pulses from a 32.615 μm sphere. Inset shows spectral intensity of the laser during the scattering measurement.

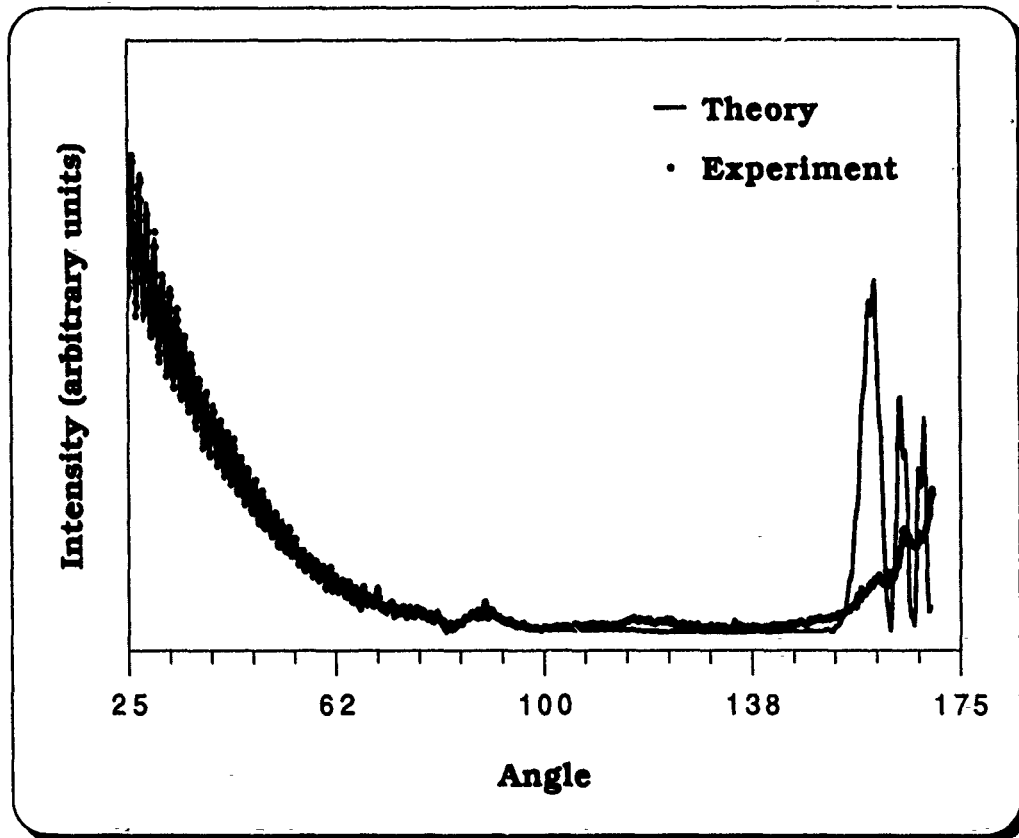


Figure 8. A comparison of experimental and theoretical scattering results showing the discrepancy at $\approx 155^\circ$.

The Mie code is not in error either since these calculated results have been carefully compared with results obtained from other researchers in this field with excellent agreement. The peak in the theoretical data at $\approx 155^\circ$ is in fact due to the geometric scattering phenomenon known as the rainbow, and is reproduced by the Mie code at the same angular position that can be calculated using only geometric optics techniques. Thus the lack of the rainbow at 155° in experimental data must be due to some experimental effect. A large (.006) imaginary part of the index of refraction (absorption) of the sphere would decrease the amplitude of the rainbow peak enough to resemble the measured scattering. However, as discussed earlier, the procedure used to determine the size of the sphere also set an upper limit on the imaginary part of the index of refraction at $\approx .001$. Thus, absorption cannot be considered the cause for the discrepancy.

The most likely cause is a deviation in the sphericity of the sphere. Because the droplet in the quadrupole trap is liquid, and is exposed to static and dynamic forces from both the trap and gravity, it is reasonable to expect that the particle might exhibit slight deviations from sphericity. In particular, the electrostrictive forces applied to the sphere by the large AC fields in the trap could couple to certain "capillary modes" of the sphere, in which the restoring force is the surface tension of the liquid⁷. Marston demonstrated in 1980 that when these type of oscillations are driven in liquid spheres, the rainbow rays undergo angular oscillations⁸. This type of behavior would explain the washed out rainbow; nevertheless, the effect is being investigated further to precisely confirm its origins.

BIBLIOGRAPHY

1. R. L. Fork, C. H. B. Cruz, P. C. Becker, and C. V. Shank., *Opt. Lett.*, 12, 483 (1987).
2. R. F. Wuerker, H. Shelton, and R. V. Langmuir., *J. Appl. Phys.*, 30, 342 (1959).
3. W. Paul, and M. Raether., *Z. Physik*, 140, 262 (1955).
4. E. J. Davis, and A. K. Ray., *J. Colloid Interface Sci.*, 75, 566 (1980).
5. C. F. Bohren, and D. R. Huffman., *Absorption and Scattering of Light by Small Particles* (John Wiley and Sons, New York, 1983).
6. G. W. Kattawar, and G. N. Plass., *Appl. Opt.*, 6, 1377 (1967).
7. P. L. Marston., private communication (1989).
8. P. L. Marston., *Appl. Opt.*, 19, 680 (1980).

UNIQUENESS OF SOLUTIONS OF
ELECTROMAGNETIC INTERACTION
PROBLEMS
ASSOCIATED WITH SCATTERING BY
A BIANISOTROPIC BODIES
COVERED WITH
IMPEDANCE SHEETS AND
HOMOTOPY

Dr. David Cohoon
West Chester University
Department of Mathematics
and Computer Science
West Chester, PA 19383

ABSTRACT

Bianisotropic materials are more general than either anisotropic or chiral materials. We write down the frequency domain Maxwell equations for a bianisotropic material and develop conditions on tensors appearing in these equations which guarantee uniqueness of the solution of the electromagnetic interaction problem. The primary tools here are the use of Silver Mueller radiation conditions and integral inequalities involving integrals of field quantities over the interior and surface of the scattering body derived from impedance sheet boundary conditions. The integral equation formulation of the electromagnetic interaction problem is provided.

1 INTRODUCTION

Bianisotropic materials, because of their greater complexity, have greater potential for creating materials with prescribed or desired absorption, transmission, and reflection properties. Chiral properties are a special case of bianisotropic materials. With chiral materials there is a special scalar ξ_c (Jaggard and Engheta, p 173) such that

$$\vec{D} = \epsilon \vec{E} + i\xi_c \vec{B} \quad (1.1)$$

and

$$\vec{B} = \mu \vec{H} - i\xi_c \mu \vec{E} \quad (1.2)$$

With the more general bianisotropic materials there are tensors α and β with the property that

$$\vec{D} = \epsilon \vec{E} + \alpha \vec{H} / (i\omega) \quad (1.3)$$

and

$$\vec{B} = \mu \vec{H} + \beta \vec{E} / (i\omega) \quad (1.4)$$

where ϵ and μ are tensors. Here Maxwell's equations have the form

$$\text{curl}(\vec{E}) = -i\omega \vec{B} \quad (1.5)$$

and

$$\text{curl}(\vec{H}) = i\omega \vec{D} + \sigma \vec{E} \quad (1.6)$$

Using these notions we make Maxwell's equations look like the standard Maxwell equations with complex sources by introducing the generalized electric and magnetic current densities by the relations,

$$\text{curl}(\vec{E}) = i\omega \mu_0 \vec{H} - \vec{J}_m \quad (1.7)$$

and

$$\text{curl}(\vec{H}) = i\omega \epsilon_0 \vec{E} + \vec{J}_e \quad (1.8)$$

where

$$\vec{J}_e = i\omega \epsilon \vec{E} + \alpha \vec{H} - i\omega \epsilon_0 \vec{E} \quad (1.9)$$

and

$$\vec{J}_m = i\omega \mu \vec{H} + \beta \vec{E} - i\omega \mu_0 \vec{H} \quad (1.10)$$

We also assume that there is an impedance sheet current density given by

$$\vec{J}_s = \sigma_s (\vec{E} - (\vec{n} \cdot \vec{E}) \vec{n}) \quad (1.11)$$

where σ_s is a tensor acting on the tangent plane of the boundary $\partial\Omega$ of the scattering body Ω . The formulation of integral equations for bianisotropic materials, therefore, is carried out by the analysis of the following coupled system of integral equations based on the notion of electric and magnetic charges defined by the two continuity equations

$$\operatorname{div}(\vec{J}_e) + \frac{\partial \rho_e}{\partial t} \quad (1.12)$$

and

$$\operatorname{div}(\vec{J}_m) + \frac{\partial \rho_m}{\partial t} \quad (1.13)$$

Having developed this the coupled system of integral equations describing the interaction of electromagnetic radiation with a bounded *bianisotropic* body Ω is given by the following relations. The electric field integral equation is given by

$$\begin{aligned} \vec{E} - \vec{E}^i = & -\operatorname{grad} \left(\int_{\Omega} \frac{\operatorname{div}(\vec{J}_e)}{\omega \epsilon_0} G(r, s) dv(s) \right) \\ & + \frac{i}{\omega \epsilon_0} \operatorname{grad} \left(\int_{\partial\Omega} (\vec{J}_e \cdot \mathbf{n}) G(r, s) da(s) \right) \\ & + \left(\frac{-i}{\omega \epsilon_0} \right) \left(\int_{\partial\Omega} \left\{ k_0^2 (\vec{J}_s) G(r, s) + \operatorname{div}(\vec{J}_s) \operatorname{grad}(G(r, s)) \right\} da(s) \right) \\ & - i\omega \mu_0 \int_{\Omega} \vec{J}_e G(r, s) dv(s) + \\ & - \operatorname{curl} \left(\int_{\Omega} \vec{J}_m G(r, s) dv(s) \right) \end{aligned} \quad (1.14)$$

and the magnetic field integral equation may be expressed as

$$\begin{aligned}
\vec{H} - \vec{H}^i &= -grad \left(\int_{\Omega} \frac{div(\vec{J}_m)}{\omega\mu_0} G(r, s) dv(s) \right) \\
&\quad - \frac{i}{\omega\mu_0} grad \left(\int_{\partial\Omega} (\vec{J}_m \cdot \vec{n}) G(r, s) da(s) \right) \\
&\quad - \left(\int_{\partial\Omega} (\vec{J}_s \times (grad(G(r, s)))) da(s) \right) \\
&\quad - i\omega\epsilon_0 \int_{\Omega} \vec{J}_m G(r, s) dv(s) + \\
&\quad + curl \left(\int_{\Omega} \vec{J}_s G(r, s) dv(s) \right) \tag{1.15}
\end{aligned}$$

where $G(r, s)$ is the rotation invariant, temperate fundamental solution of the Helmholtz equation,

$$(\Delta + k_0^2)G = \delta \tag{1.16}$$

given by

$$G(r, s) = \frac{\exp(-ik_0 |r - s|)}{4\pi |r - s|} \tag{1.17}$$

Substituting (1.10) and (1.11) into equations (1.13) and (1.14) we obtain, the coupled integral equations for bianisotropic materials. The electric field integral equation for a bianisotropic material is given by,

$$\begin{aligned}
\vec{E} - \vec{E}^i &= -grad \left(\int_{\Omega} \frac{div(i\omega\epsilon\vec{E} + \alpha\vec{H} - i\omega\epsilon_0\vec{E})}{\omega\epsilon_0} G(r, s) dv(s) \right) \\
&\quad + \frac{i}{\omega\epsilon_0} grad \left(\int_{\partial\Omega} (i\omega\epsilon\vec{E} + \alpha\vec{H} - i\omega\epsilon_0\vec{E} \cdot \vec{n}) G(r, s) da(s) \right) \\
&\quad + \left(\frac{-i}{\omega\epsilon_0} \right) \left(\int_{\partial\Omega} \left\{ k_0^2 (\sigma_s (\vec{E} - (\vec{n} \cdot \vec{E})\vec{n})) G(r, s) + \right. \right. \\
&\quad \left. \left. div(\sigma_s (\vec{E} - (\vec{n} \cdot \vec{E})\vec{n})) grad(G(r, s)) \right\} da(s) \right) \\
&\quad - i\omega\mu_0 \int_{\Omega} i\omega\epsilon\vec{E} + \alpha\vec{H} - i\omega\epsilon_0\vec{E} G(r, s) dv(s) + \\
&\quad - curl \left(\int_{\Omega} i\omega\mu\vec{H} + \beta\vec{E} - i\omega\mu_0\vec{H} G(r, s) dv(s) \right) \tag{1.18}
\end{aligned}$$

The magnetic field integral equation for a bianisotropic material covered by an impedance sheet is given by

$$\begin{aligned}
 \vec{H} - \vec{H}^i = & -\text{grad} \left(\int_{\Omega} \frac{\text{div}(i\omega\mu\vec{H} + \beta\vec{E} - i\omega\mu_0\vec{H})}{\omega\mu_0} G(r, s) dv(s) \right) \\
 & - \frac{i}{\omega\mu_0} \text{grad} \int_{\partial\Omega} (i\omega\mu\vec{H} + \beta\vec{E} - i\omega\mu_0\vec{H} \cdot \vec{n}) G(r, s) da(s) \\
 & - \left(\int_{\partial\Omega} (\sigma_s (\vec{E} - (\vec{n} \cdot \vec{E})\vec{n}) \times (\text{grad}(G(r, s)))) da(s) \right) \\
 & - i\omega\epsilon_0 \int_{\Omega} (i\omega\mu\vec{H} + \beta\vec{E} - i\omega\mu_0\vec{H}) G(r, s) dv(s) + \\
 & + \text{curl} \left(\int_{\Omega} i\omega\epsilon\vec{E} + \alpha\vec{H} - i\omega\epsilon_0\vec{E} G(r, s) dv(s) \right) \quad (1.19)
 \end{aligned}$$

While we have obtained exact solutions for layered materials, most of the problems are so complex that one must formulate the interaction problems using integral equations. The primary focus of this paper is to demonstrate the equivalence of integral equation and Maxwell equation formulations of the problem for suitable function spaces by demonstrating uniqueness. Then we can carry out the design of complex materials using an improvement of classical spline methods (Tsai, Massoudi, Durney, and Iskander, pp 1131-1139). The Tsai, Massoudi, Durney, and Iskander paper is unusual in that comparisons are made between internal fields predicted from moment method computations and Mie solution computations. Successful comparisons have been made for linear basis functions without enhancement by EFRIE theory. However, as the scattering bodies become more complex the computational requirements become larger and larger. With EFRIE theory if one has a discretization that enables one to closely approximate the solution, then refinements can be made by a convergent iterative process based on the concept that the norm of the difference between an approximate integral operator and the actual integral operator is simply smaller than one, not necessarily close enough to give answers of acceptable accuracy. Then the answer is improved by an iterative process to any desired precision without the use of additional computer memory.

We have formulated some one dimensional scattering problems associated with magnetic materials, and solutions obtained from the differential

equation formulations have been substituted into the integral equations and have been shown to satisfy them exactly. For magnetic materials, a single integral equation was obtained and the significance of surface values of the derivative of the electric vector were shown to be important. For higher order splines all terms arising in a matrix representation of the integral equation formulation of the problem, and all iterates of the integrals could be computed exactly.

2 UNIQUENESS

If \vec{E} and \vec{H} are electric and magnetic fields in a bianisotropic material, then there exist tensors μ , ϵ , α , and β such that

$$\text{curl}(\vec{E}) = -i\omega\mu\vec{H} - \beta\vec{H} \quad (2.1)$$

and

$$\text{curl}(\vec{H}) = (i\omega\epsilon + \sigma)\vec{E} + \alpha\vec{E} \quad (2.2)$$

We assume that if α is a complex tensor that α^* denotes its complex conjugate. We assume that a bounded bianisotropic body Ω with a smooth normal is embedded in three dimensional free space and is subjected to a remote source of radiation whose electric field is \vec{E}^i and whose magnetic field is \vec{H}^i . If \vec{E} denotes the difference between two solutions of the form $\vec{E}^i + \vec{E}^s$, where \vec{E}^s denotes the scattered radiation, in the exterior of Ω , or simply the difference of two solutions in the interior of Ω , then the solution is unique if we can prove that \vec{E} is identically zero in the exterior of Ω or everywhere inside Ω .

The starting point for proofs of uniqueness of solutions of electromagnetic scattering problems is the Silver Mueller radiation conditions which demand that if C_R is a sphere of radius R centered at a point in the scattering body, that then

$$\lim_{R \rightarrow \infty} \int_{C_R} (\vec{n} \times \text{curl}(\vec{E}) - ik_0\vec{E}) \cdot (\vec{n} \times \text{curl}(\vec{E}^*) + ik_0\vec{E}^*) da = 0 \quad (2.3)$$

Thus, we note that

$$\begin{aligned}
& \int_{C_R} |\vec{n} \times \text{curl}(\vec{E}) - ik_0 \vec{E}|^2 da = \\
& \int_{C_R} (|\vec{n} \times \text{curl}(\vec{E})|^2 + k_0^2 |\vec{E}|^2) da + \\
& ik_0 \int_{C_R} ((\vec{n} \times \text{curl}(\vec{E})) \cdot \vec{E}^*) da \\
& - ik_0 \int_{C_R} \vec{E} \cdot (\vec{n} \times \text{curl}(\vec{E}^*)) da \tag{2.4}
\end{aligned}$$

Focusing our attention on the last two terms in this equation, we see that

$$\begin{aligned}
& ik_0 \int_{C_R} (\vec{n} \times \text{curl}(\vec{E})) \cdot \vec{E}^* da = \\
& ik_0 \int_{C_R} \vec{n} \cdot (\text{curl}(\vec{E}) \times \vec{E}^*) dv \\
& = ik_0 \int_{V_1} \text{div}(\text{curl}(\vec{E}) \times \vec{E}^*) dv + \\
& + (ik_0) \int_{S_2} \vec{n} \cdot (\text{curl}(\vec{E}) \times \vec{E}^*) da \tag{2.5}
\end{aligned}$$

In the previous equation S_2 is the surface bounding the bianisotropic body and V_1 is the region between the bounded bianisotropic body and the sphere C_R centered at a point in the bianisotropic material. We will assume that V_2 represents the bounded bianisotropic body covered by an impedance sheet. Continuing our analysis, and replacing $\text{curl}(\vec{E})$ by $-i\omega\mu_0\vec{H}$ we find that

$$\begin{aligned}
& ik_0 \int_{C_R} (\vec{n} \times \text{curl}(\vec{E})) \cdot \vec{E}^* da = \\
& ik_0 \int_{C_R} \text{div}(\text{curl}(\vec{E}) \times \vec{E}^*) dv + \\
& k_0\omega\mu_0 \int_{S_2} \vec{n} \cdot (\vec{H} \times \vec{E}^*) da. \tag{2.6}
\end{aligned}$$

Thus, making use of the impedance sheet boundary condition which states that

$$\vec{n} \times \vec{H} = \vec{n} \times \vec{H}_2 + \sigma_s(\vec{E} - (\vec{n} \cdot \vec{E})\vec{n}) \tag{2.7}$$

we find that

$$\begin{aligned}
& ik_0 \int_{C_R} (\vec{n} \times \text{curl}(\vec{E})) \cdot \vec{E}^* da = \\
& ik_0 \int_{C_R} \text{div}(\text{curl}(\vec{E}) \times \vec{E}^*) dv + \\
& k_0 \omega \mu_0 \int_{S_2} \vec{n} \cdot (\vec{H}_2 \times \vec{E}_2^*) da + \\
& k_0 \omega \mu_0 \int_{S_2} \{(\sigma_s(\vec{E}_2 - (\vec{E}_2 \cdot \vec{n})\vec{n})) \cdot \vec{E}_2^*\} da \quad (2.8)
\end{aligned}$$

where \vec{H}_2 and \vec{E}_2 are the electric and magnetic fields just inside of the impedance sheet on the surface S_2 . First using the Gauss divergence theorem we find that

$$\begin{aligned}
& ik_0 \int_{C_R} (\vec{n} \times \text{curl}(\vec{E})) \cdot \vec{E}^* da = \\
& ik_0 \int_{C_R} \text{div}(\text{curl}(\vec{E}) \times \vec{E}^*) dv + \\
& k_0 \omega \mu_0 \int_{V_2} \text{div}(\vec{H}_2 \times \vec{E}_2^*) dv + \\
& k_0 \omega \mu_0 \int_{S_2} \{(\sigma_s(\vec{E}_2 - (\vec{E}_2 \cdot \vec{n})\vec{n})) \cdot \vec{E}_2^*\} da \quad (2.9)
\end{aligned}$$

We now make use of the vector calculus identity,

$$\text{div}(\vec{A} \times \vec{B}) = \vec{B} \cdot (\text{curl}(\vec{A})) - \vec{A} \cdot (\text{curl}(\vec{B})) \quad (2.10)$$

We find that

$$\begin{aligned}
& ik_0 \int_{C_R} (\vec{n} \times \text{curl}(\vec{E})) \cdot \vec{E}^* da = \\
& ik_0 \int_{V_1} (\vec{E}^* \cdot (\text{curl}(\text{curl}(\vec{E}))) - \text{curl}(\vec{E}) \cdot \text{curl}(\vec{E}^*)) dv + \\
& k_0 \omega \mu_0 \int_{V_2} (\vec{E}_2^* \cdot \text{curl}(\vec{H}_2) - \vec{H}_2 \cdot \text{curl}(\vec{E}_2^*)) dv + \\
& k_0 \omega \mu_0 \int_{S_2} \{(\sigma_s(\vec{E}_2 - (\vec{E}_2 \cdot \vec{n})\vec{n})) \cdot \vec{E}_2^*\} da \quad (2.11)
\end{aligned}$$

Substituting in the constitutive relations we find that

$$\begin{aligned}
ik_0 \int_{C_R} (\vec{n} \times \text{curl}(\vec{E})) \cdot \vec{E}^* da &= -ik_0 \int_{V_1} \{ \vec{E}^* \cdot \Delta \vec{E} + |\text{curl}(\vec{E})|^2 \} dv \\
&+ k_0 \omega \mu_0 \int_{V_2} \vec{E}_2^* \cdot \{ (i\omega\epsilon + \sigma) \vec{E}_2 + \alpha \vec{H}_2 \} dv \\
&- k_0 \omega \mu_0 \int_{V_2} \vec{H}_2 \cdot (i\omega \mu^* \vec{H}_2^* - \beta^* \vec{E}_2^*) dv + \\
&k_0 \omega \mu_0 \int_{S_2} \{ (\sigma_s (\vec{E}_2 - (\vec{E}_2 \cdot \vec{n}) \vec{n})) \cdot \vec{E}_2^* \} da \quad (2.12)
\end{aligned}$$

Considering the conjugate term of this form we observe that

$$\begin{aligned}
-ik_0 \int_{C_R} (\vec{n} \times \text{curl}(\vec{E}^*)) \cdot \vec{E} da &= ik_0 \int_{V_1} \{ \vec{E} \cdot \Delta \vec{E}^* + |\text{curl}(\vec{E})|^2 \} dv \\
&+ k_0 \omega \mu_0 \int_{V_2} \vec{E}_2 \cdot \{ (-i\omega\epsilon^* + \sigma^*) \vec{E}_2^* + \alpha^* \vec{H}_2^* \} dv \\
&- k_0 \omega \mu_0 \int_{V_2} \vec{H}_2^* \cdot (-i\omega \mu \vec{H}_2 - \beta \vec{E}_2) dv + \\
&k_0 \omega \mu_0 \int_{S_2} \{ (\sigma_s^* (\vec{E}_2^* - (\vec{E}_2^* \cdot \vec{n}) \vec{n})) \cdot \vec{E}_2 \} da \quad (2.13)
\end{aligned}$$

Adding these equations we find that the solution is unique provided that either a quadratic form is positive definite or another form is either negative or positive definite. Indeed it may be easier to prove uniqueness for the more complex material than when the scatterer has a simpler form. We find that

$$\begin{aligned}
& 2\text{Re} \left(ik_0 \int_{C_R} (\vec{n} \times \text{curl}(\vec{E})) \cdot \vec{E}^* da \right) = \\
& k_0 \omega \mu_0 \int_{V_2} \left\{ (\vec{E}_2^* \cdot (i\omega\epsilon + \sigma)\vec{E}_2) + (\vec{E}_2 \cdot (-i\omega\epsilon^* + \sigma^*)\vec{E}_2^*) \right\} dv + \\
& k_0 \omega \mu_0 \int_{V_2} \left\{ (\vec{E}_2^* \cdot (\alpha)\vec{H}_2) + (\vec{E}_2 \cdot (\alpha^*)\vec{H}_2^*) \right\} dv + \\
& -k_0 \omega \mu_0 \int_{V_2} \left\{ (\vec{H}_2 \cdot (i\omega\mu^*\vec{H}_2^*) + (\vec{H}_2^* \cdot (-i\omega\mu\vec{H}_2)) \right\} dv + \\
& k_0 \omega \mu_0 \int_{V_2} \left\{ (\vec{H}_2 \cdot \beta^* \vec{E}_2^*) + (\vec{H}_2^* \cdot \beta \vec{E}_2) \right\} + \\
& 2\text{Re} \left[k_0 \omega \mu_0 \int_{S_2} \left\{ (\sigma_s (\vec{E}_2 - (\vec{E}_2 \cdot \vec{n})\vec{n})) \cdot \vec{E}_2^* \right\} da \right] \quad (2.14)
\end{aligned}$$

Note that if the permeability, μ , the permittivity, ϵ , and the tensors α and β are scalars times the identity matrix then sufficient conditions for uniqueness are that the real part of σ is positive and the imaginary parts of ϵ and μ are negative and that the real part of σ_s is positive and that the quadratic form associated with the matrix Q defined by

$$\begin{aligned}
& Q = \\
& \begin{pmatrix} A_\epsilon & 0 & 0 & \text{Re}(\alpha) & 0 & 0 \\ 0 & A_\epsilon & 0 & 0 & \text{Re}(\alpha) & 0 \\ 0 & 0 & A_\epsilon & 0 & 0 & \text{Re}(\alpha) \\ \text{Re}(\beta) & 0 & 0 & \omega \text{Im}(\mu) & 0 & 0 \\ 0 & \text{Re}(\beta) & 0 & 0 & \omega \text{Im}(\mu) & 0 \\ 0 & 0 & \text{Re}(\beta) & 0 & 0 & \omega \text{Im}(\mu) \end{pmatrix} \quad (2.15)
\end{aligned}$$

where

$$A_\epsilon = \omega \text{Im}(\epsilon) + \text{Re}(\sigma), \quad (2.16)$$

is positive definite. Thus, in particular, if there is enough domination of the α and β terms by the positive diagonal terms, then this form is positive definite and we do indeed have a unique solution of the electromagnetic interaction problem in a variety of naturally arising function spaces if the impedance sheet conductivity σ_s is positive.

The general uniqueness result is therefore derived by observing that

$$\begin{aligned}
& \lim_{R \rightarrow \infty} \int_{C_R} (\vec{n} \times \text{curl}(\vec{E}) - ik_0 \vec{E}) \cdot (\vec{n} \times \text{curl}(\vec{E}^*) + ik_0 \vec{E}^*) da = \\
& \lim_{R \rightarrow \infty} \int_{C_R} (|\vec{n} \times \text{curl}(\vec{E})|^2 + k_0^2 |E|^2) da + \\
& k_0 \omega \mu_0 \int_{V_2} \{(\vec{E}_2^* \cdot (i\omega \epsilon + \sigma) \vec{E}_2) + (\vec{E}_2 \cdot (-i\omega \epsilon^* + \sigma^*) \vec{E}_2^*)\} dv + \\
& k_0 \omega \mu_0 \int_{V_2} \{(\vec{E}_2^* \cdot (\alpha) \vec{H}_2) + (\vec{E}_2 \cdot (\alpha^*) \vec{H}_2^*)\} dv + \\
& -k_0 \omega \mu_0 \int_{V_2} \{(\vec{H}_2 \cdot (i\omega \mu^* \vec{H}_2^*) + (\vec{H}_2^* \cdot (-i\omega \mu \vec{H}_2))\} dv + \\
& k_0 \omega \mu_0 \int_{V_2} \{(\vec{H}_2 \cdot \beta^* \vec{E}_2^*) + (\vec{H}_2^* \cdot \beta \vec{E}_2)\} + \\
& 2\text{Re} \left[k_0 \omega \mu_0 \int_{S_2} \{(\sigma_s (\vec{E}_2 - (\vec{E}_2 \cdot \vec{n}) \vec{n})) \cdot \vec{E}_2^*\} da \right] \quad (2.17)
\end{aligned}$$

The uniqueness is established by observing that upon taking the limit of all terms as the radius R of C_R becomes infinite that if the difference \vec{E} between two solutions were a nonzero function, then we would get effectively two equations by taking the real and imaginary parts of both sides of the relationship

$$\begin{aligned}
& 0 = C^2 + \\
& k_0 \omega \mu_0 \int_{V_2} \{(\vec{E}_2^* \cdot (i\omega \epsilon + \sigma) \vec{E}_2) + (\vec{E}_2 \cdot (-i\omega \epsilon^* + \sigma^*) \vec{E}_2^*)\} dv + \\
& k_0 \omega \mu_0 \int_{V_2} \{(\vec{E}_2^* \cdot (\alpha) \vec{H}_2) + (\vec{E}_2 \cdot (\alpha^*) \vec{H}_2^*)\} dv + \\
& -k_0 \omega \mu_0 \int_{V_2} \{(\vec{H}_2 \cdot (i\omega \mu^* \vec{H}_2^*) + (\vec{H}_2^* \cdot (-i\omega \mu \vec{H}_2))\} dv + \\
& k_0 \omega \mu_0 \int_{V_2} \{(\vec{H}_2 \cdot \beta^* \vec{E}_2^*) + (\vec{H}_2^* \cdot \beta \vec{E}_2)\} + \\
& 2\text{Re} \left[k_0 \omega \mu_0 \int_{S_2} \{(\sigma_s (\vec{E}_2 - (\vec{E}_2 \cdot \vec{n}) \vec{n})) \cdot \vec{E}_2^*\} da \right] \quad (2.18)
\end{aligned}$$

where C^2 is the real number given by

$$C^2 = \lim_{R \rightarrow \infty} \int_{C_R} (|\vec{n} \times \text{curl}(\vec{E})|^2 + k_0^2 |E|^2) da \quad (2.19)$$

Since this is not possible if the electromagnetic parameters are such that the body is dissipative in the sense that the bilinear form acting on the function (\vec{E}, \vec{H}) that is defined by

$$\begin{aligned} b(\vec{E}, \vec{H}) = & \\ & k_0 \omega \mu_0 \int_{V_2} \{ (\vec{E}_2^* \cdot (i\omega\epsilon + \sigma)\vec{E}_2) + (\vec{E}_2 \cdot (-i\omega\epsilon^* + \sigma^*)\vec{E}_2^*) \} dv + \\ & k_0 \omega \mu_0 \int_{V_2} \{ (\vec{E}_2^* \cdot (\alpha)\vec{H}_2) + (\vec{E}_2 \cdot (\alpha^*)\vec{H}_2^*) \} dv + \\ & -k_0 \omega \mu_0 \int_{V_2} \{ (\vec{H}_2 \cdot (i\omega\mu^*)\vec{H}_2^*) + (\vec{H}_2^* \cdot (-i\omega\mu)\vec{H}_2) \} dv + \\ & k_0 \omega \mu_0 \int_{V_2} \{ (\vec{H}_2 \cdot \beta^* \vec{E}_2^*) + (\vec{H}_2^* \cdot \beta \vec{E}_2) \} + \\ & k_0 \omega \mu_0 \int_{S_2} (\sigma_s^* + \sigma_s) \{ (\vec{E}_2 \cdot \vec{E}_2^*) - (\vec{E}_2 \cdot \vec{n})(\vec{E}_2^* \cdot \vec{n}) \} da \quad (2.20) \end{aligned}$$

is positive definite.

3 HOMOTOPY

We have developed a variety of homotopy methods for solving electromagnetic interaction problems. The basic idea of homotopy is to start with an easy problem such as scattering by an N layer bianisotropic sphere, and use this exact solution to move via a dynamical system defined by a system of ordinary differential equations along a homotopy path. We pick a discretization of the scattering body and locally represent the fields using a spline approximation in each scatterer subunit. If for example, we were considering a dielectric body with a nonspherical shape, we would represent this shape locally as a smooth function of the spatial variables. We could assume that there is a transformation T which takes the original spherical

body Ω_0 into a complex shape Ω_1 . We suppose that there is a cellular decomposition of Ω_0 which transforms under T into a cellular decomposition of Ω_1 . If C_i is the i th cell of the cellular decomposition of Ω_0 , then

$$C_{(\lambda,s)} = \lambda T(C_i) + (1 - \lambda)C_i \quad (3.1)$$

By assuming that there is a one parameter family of coefficients used to represent the fields which satisfy, as closely as possible, the integral equations, (1.18) and (1.19), we see that we can obtain the representation of the field in the interior of the complex shape using N^2 operations. We treat λ , and the expansion coefficients of the induced electric and magnetic fields as dependent variables in a system of ordinary differential equations involving the homotopy parameter s as the independent variable. Because the initial conditions for the easy problem can be obtained in N steps times a constant which is independent of N , we know the starting values of the derivatives of the expansion coefficients and the parameter λ . We halt the solution of the system of differential equations as soon as λ becomes equal to 1 and we are solving the integral equations (1.18) and (1.19) for

$$\Omega = \Omega_1 \quad (3.2)$$

The basis of our method concerns tracking a homotopy path using the fact that if on the curve

$$(\lambda(s), \vec{X}(s)) \in [0, 1] \times \mathbb{R}^n \quad (3.3)$$

we define for each $\vec{X}(s)$ the parameterized function,

$$\vec{\rho}_x(\lambda, \vec{X}) = \lambda \vec{F}(\vec{X}) + (1 - \lambda)(\vec{X} - \vec{a}) \quad (3.4)$$

and ask that it take on values in \mathbb{R}^n , then if it were true that a path were chosen such that

$$\vec{\rho}_x(\lambda(s), \vec{X}(s)) = \vec{0} \quad (3.5)$$

that then we would have

$$\begin{pmatrix} T_{(1,1)} & T_{(1,2)} & \cdots & T_{(1,n+1)} \\ T_{(2,1)} & T_{(2,2)} & \cdots & T_{(2,n+1)} \\ \vdots & \vdots & \ddots & \vdots \\ T_{(n,1)} & T_{(n,2)} & \cdots & T_{(n,n+1)} \end{pmatrix} \begin{pmatrix} \lambda^{(1)}(s) \\ X_1^{(1)}(s) \\ \vdots \\ X_n^{(1)}(s) \end{pmatrix} = \begin{pmatrix} 0 \\ 0 \\ \vdots \\ 0 \end{pmatrix} \quad (3.6)$$

where the coefficient matrix T is essentially the Jacobian of the vector valued function $\bar{\rho}_g$. The entries of the coefficient matrix T are given specifically by

$$T_{(1,1)} = \frac{\partial \rho(\bar{x},1)}{\partial \lambda}, \quad (3.7)$$

$$T_{(1,2)} = \frac{\partial \rho(\bar{x},1)}{\partial X_1}, \quad (3.8)$$

$$T_{(1,n+1)} = \frac{\partial \rho(\bar{x},1)}{\partial X_n}, \quad (3.9)$$

$$T_{(n,1)} = \frac{\partial \rho(\bar{x},n)}{\partial \lambda}, \quad (3.10)$$

$$T_{(n,2)} = \frac{\partial \rho(\bar{x},n)}{\partial X_1}, \text{ and} \quad (3.11)$$

$$T_{(n,n+1)} = \frac{\partial \rho(\bar{x},n)}{\partial X_n} \quad (3.12)$$

If along the path satisfying these equations, the Jacobian were full then its kernel would be one dimensional and we would have a nontrivial solution of the above linear system which would give us formulas for the derivatives with respect to the parameter s of the variables λ , X_1 , ..., and X_n . By solving this system of differential equations we move from the solution of an easy problem

$$\vec{X} - \vec{a} = \vec{0} \quad (3.13)$$

to the solution of the more difficult constrained optimization problem which has been made equivalent to the solving of the nonlinear equation,

$$\vec{F}(\vec{X}) = \vec{0}. \quad (3.14)$$

References

- [1] Burr, John G., David K. Cohoon, Earl L. Bell, and John W. Penn. Thermal response model of a Simulated Cranial Structure Exposed to Radiofrequency Radiation. *IEEE Transactions on Biomedical Engineering*. Volume BME-27, No. 8 (August, 1980) pp 452-460.
- [2] Cohoon, D. K., J. W. Penn, E. L. Bell, D. R. Lyons, and A. G. Cryer. *A Computer Model Predicting the Thermal Response to Microwave Radiation SAM-TR-82-22* Brooks AFB, Tx 78235: USAF School of Aerospace Medicine. (RZ) Aerospace Medical Division (AFSC) (December, 1982).
- [3] Cohoon, D. K. An Exact Formula for the Accuracy of a Class of Computer Solutions of Integral Equation Formulations of Electromagnetic Scattering Problems. *Electromagnetics, Volume 7, Number 2* (1987) pp 153-165
- [4] Hochstadt, Harry. *The Functions of Mathematical Physics*. New York: Dover(1986).
- [5] Jaggard, D. L. and N. Engheta. *ChirosorbTM* as an invisible medium. *Electronic Letters*. Volume 25, Number 3 (February 2, 1989) pp 173-174.
- [6] Li, Shu Chen. Interaction of Electromagnetic Fields with Simulated Biological Structures. Ph.D. Thesis(Temple University, Department of Mathematics 038-16, Philadelphia, Pa 19122) (1986). 454 pages
- [7] Tsai, Chi-Taou, Habib Massoudi, Carl H. Durney, and Magdy F. Iskander. A Procedure for Calculating Fields Inside Arbitrarily Shaped, Inhomogeneous Dielectric Bodies Using Linear Basis Functions with the Moment Method. *IEEE Transactions on Microwave Theory and Techniques, Volume MTT-34, Number 11* (November, 1986) pp 1131-1139.
- [8] Whittaker, E. T. and G. N. Watson. *A Course of Modern Analysis* London: Cambridge University Press (1986).

BLANK

INDEX A
Index of Authors

- D.R. ALEXANDER, 121, 175
R.L. ARMSTRONG, 107, 135
S. ARNOLD, 35, 45
E. BAHAR, 199
J.P. BARTON, 121, 175
A. BISWAS, 107, 135
H. BRENNER, 15
J. BROCK, 51, 97, 115, 143
B.V. BRONK, 45, 87
J. CARLS, 97
J.E. CERMAK, 9
D.K. COHOON, 159, 211, 277
R.A. FARRELL, 57
G. FERNANDEZ, 107
R.C. FLAGAN, 25
L.M. FOLAN, 35
D.E. FREUND, 57
E.S. FRY, 149, 259
K.A. FULLER, 249
A. HADAD, 9
G. HOLTMEIER, 121
G. HUANG, 199
D.R. HUFFMAN, 87
S.G. JENNINGS, 107
B. JURCIK, 51
H. LATIFI, 135
L. LIEBMAN, 143
R.L. McCALLY, 57
R.L. MONTGOMERY, 149
B.S. PARK, 107
J.D. PENDLETON, 107
R.G. PINNICK, 107, 135
R.M. POPE, 149
M. POREH, 9
R.M. PURCELL, 211
J.M. RAMSEY, 45
S.A. SCHAUB, 121, 175
Y. SEO, 115
M. SHAPIRO, 15
M. STANLEY, 87
W.P. VAN DE MERWE, 87
C. WANG, 259
W.E. WHITE, 259
W.B. WHITTEN, 45

BLANK

INDEX B

Index of Authors' Organizations

California Institute of Technology Division of Engineering and Applied Science	25
Colorado State University Engineering Research Center	9
Israel Institute of Technology - Technion Faculty of Mechanical Engineering	9, 15
Massachusetts Institute of Technology Department of Chemical Engineering	15
New Mexico State University Physics Department	107, 135
Oak Ridge National Laboratory	45
Polytechnic Institute of New York Department of Physics	35, 45
Texas A&M University Department of Physics	149, 259
The Johns Hopkins University Applied Physics Laboratory Milton S. Eisenhower Research Center	57
Uniformed Services University of the Health Sciences	87
University of Arizona Department of Physics	87
University of Nebraska-Lincoln College of Engineering Center for Electro-Optics	121, 175
Department of Electrical Engineering	199
University of Texas Chemical Engineering Department	51, 97, 115, 143
U.S. Army Chemical Research, Development and Engineering Center	45, 87

**West Chester University
Department of Mathematics and Computer
Science**

159, 211, 277

**White Sands Missile Range
Atmospheric Sciences Laboratory**

107, 135, 249

INDEX B

APPENDIX A

PHOTOGRAPH OF 1989 CONFERENCE ATTENDEES



1989 CRDEC Scientific Conference
on Obscuration and Aerosol Research

Pictured left to right are:

First Row

David McCoy

Jerold Bottiger

John Barton

Steve Arnold

Willem Van De Merwe

Rick Flagan

Howard Littman

Gary Salzman

Craig Bohren

Horn-Bond Lin

Second Row

Mark Seaver

Sam Wozniak

Robert Armstrong

Bill Whitten

Burt Bronk

Thomas R. Lettieri

Donald Hagen

Robert Fricke

Cliff Dungey

Chia Ben Hu

Third Row

Bill Whitten

Kirk Fuller

Barton Dahneke

Ed Stuebing

Walter Back

Dennis Alexander

Marc Stanley

Tracy Morre

John R. White

Robin M. Pope

Fourth Row

Orazio Sindoni

Lorcan Folan

Gregory Rose

Donald Huffman

David Krueger

Howard Brenner

Edwin Dauber

Tony Campillo

Morris Morgan

Ching Wang

Fifth Row

Edward Fry

Jay Eversole

Marek Sitarski

Keng Leong

Photograph taken Wednesday, June 28, 1989

APPENDIX B

LIST OF 1989 ATTENDEES

ACKERMAN, THOMAS
(814) 865-2915
Pennsylvania State University
Dept. of Meteorology
University Park, CA 16802

BARTON, JOHN P.
(402) 472-5081
Dept. of Mechanical Engineering
255 WSEC
University of Nebraska-Lincoln
Lincoln, NE 68588-0525

ALEXANDER, DENNIS
(402) 472-5080
Mechanical Engineering Dept.
255 WSEC
University of Nebraska-Lincoln
Lincoln, NE 68588-0525

BIRENZVIGE, AMMON
(301) 671-3321
Commander
US Army CRDEC
SMCCR-RSP-P
Aberdeen Proving Ground, MD 21010

ARMSTRONG, ROBERT L.
(505) 646-3838
New Mexico State University
Dept. of Physics, 3D
Las Cruces, NM 88003

BISWAS, ABHIJT
(505) 646-5199
New Mexico State University
College of Arts and Sciences
Dept. of Physics
Box 3D

ARNOLD, STEPHEN
(718) 643-3245
Department of Physics
Polytechnic Institute of New York
333 Jay St.
Brooklyn, NY 11201

BOHREN, CRAIG
(814) 865-2951
Dept of Meteorology
Penn State University
University Park, PA 16802

BACH, WALTER
(919) 549-0641
US Army Research Office
P.O. Box 12211
Research Triangle Park, NC 27709

BOTTIGER, JEROLD
(301) 671-2395
Commander
US Army CRDEC
ATTN:SMCCR-RSP-B/J. BOTTIGER
Aberdeen Proving Ground, MD 21010-5423

BAHAR, EZEKIEL
(402) 472-1966
Dept. of Electrical Engineering
209N WSEC
University of Nebraska-Lincoln
Lincoln, NE 68588-0511

BOWEN, TRACEY
(301) 278-7072
BRL
SLCBR-IB-I
Aberdeen Proving Ground, MD 21005-5066

BRADLEY, MIKE
(415) 422-1835
Lawrence Livermore National Lab
P.O. Box 808
Livermore, CA 94550

CAPASSO, NICHOLAS
(301) 838-5282
605 Shamrock Rd
Bel Air, MD 21014

BRENNER, HOWARD
(617) 253-6687
Department of Chemical Engineering
Mass. Inst. of Technology
Cambridge, MA 02139

CARPIN, JOHN
(301) 671-4716
Commander
US Army CRDEC
ATTN: SMCCR-RST-E
Aberdeen Proving Ground, MD 21010-5423

BROCK, JAMES R.
(512) 471-3348
Department of Chemical Engineering
University of Texas
Austin, TX 78712

CHANG, YU-CHEN
(301) 454-4742
University of Maryland College Park
Dept. of Chemical & Nuclear Engineering
College Park, MD 20742

BRONK, BURT
(301) 671-2326
Commander
US Army CRDEC
ATTN: SMCCR-RSP-B/B. BRONK
Aberdeen Proving Ground, MD 21010-5423

COHEN, LEN
(215) 895-2710
Department of Physics & Atmospheric
Sciences
Drexel University
Philadelphia, PA 19104

BRUNO, JOHN
(703) 448-6317
SAIC
1710 Goodridge Dr.
McClellan, VA 22180

COHOON, DAVID
(215) 358-0200
Damaskos, Inc.
43 Skyline Drive
Glenn Mills, PA 19342

CAMPILLO, ANTHONY
(202) 767-2057
Code 65F46
Naval Research Lab
Washington, D.C. 20375

COTTON, WILLIAM
(303) 491-8593
P.O. Box 74
Bellvue, CO 80512

DAHNEKE, BART
(315) 597-5846
Particle Measurement Research
930 Johnsen Road
Palmyra, NY 14522

FLAGAN, RICHARD
(818) 356-4383
California Inst. of Technology
Mail Stop # 138-78
Pasadena, CA 91125

DAUBER, EDWIN
(301) 392-3300
W.L. Gore & Associates
P.O. Box 1100
Elkton, MD 21921

FLANNIGAN, DENNIS
(301) 671-2395
Commander
US Army CRDEC
ATTN: SMCCR-RSP-B/D. FLANNIGAN
Aberdeen Proving Ground, MD 21010-5423

DUNGEY, CLIFF
(814) 865-3239
Penn State Univ.
Meteorology Dept.
University Park, PA 16802

FOLAN, LORCAN M.
Physics Dept.
University of New York
333 Jay Street
Brooklyn, NY 11201

EVANS, KENNETH
(301) 671-3079
13 Melanie Court
Baltimore, MD 21234

FREUND, DAVID
(301) 792-6260
Johns Hopkins
Applied Physics Lab
Johns Hopkins Rd.
Laurel, MD 20707

EVERSOLE, JAY
(202) 767-2057
Commander Naval Research Lab
Attn: Code 6546 / J. Eversol
Washington, DC 20375

FRICKEL, ROBERT
(301) 671-2395
Commander
US Army CRDEC
ATTN: SMCCR-RSP-B/R. FRICKEL
Aberdeen Proving Ground, MD 21010-5423

FARRELL, RICHARD
(301) 953-6229
Johns Hopkins University
Applied Physics Lab
Johns Hopkins Road
Laurel, MD 20707

FRY, EDWARD
(409) 845-7717
Dept. of Physics
Texas A&M University
College Station, TX 77843

FULLER, KIRK
(505) 678-5634
US Army Atmospheric Sciences Lab
ATTN: SLCAS-AR-A/DR. Kirk Fuller
White Sands Missile Range, NM 88002

HUNT, ARLON
(415) 486-5370
Lawrence Berkeley Lab
90-2024
Berkeley, CA 94720

GLATZMAIER, GARY A.
(505) 667-7647
Los Alamos National Laboratory
ESS-5, Mail Stop F665
Los Alamos, NM 87545

KOSKI, WALTER
(301) 338-7418
Johns Hopkins University
Dept. of Chemistry
Balto., MD 21218

HARTLEY, RICHARD S.
(202) 325-7744
Defense Nuclear Agency
6801 Telegraph Rd.
Alexandria, VA 22310

KRUEGER, DAVID
(303) 491-7381
Colorado State Univ.
Ft. Collins, CO 80523

HU, PO
(212) 690-6864
City College of New York
Physics Dept.
Convent Ave & 137 Street
New York, NY 10031

KWOK, ALFRED
(203) 432-4231
Yale University
Applied Physics
P.O. Box 2157, Yale Station
New Haven, CT 06520

HU, CHIA-REN
(409) 845-3531
Department of Physics
Texas A&M University
College Station, TX 77843

LAWLESS, PHIL A.
(919) 541-6782
Research Triangle Institute
P.O. Box 12194
Research Triangle Park, NC 27709

HUFFMAN, DONALD R.
(602) 621-4804
Dept. of Physics
University of Arizona
Tuscon, AZ 85721

LAX, MELVIN
(212) 690-6864
City College Of New York
Physics Dept.
New York, NY 10031

LEACH, DAVID
(203) 432-4234
Yale University
Applied Physics
P.O. Box 2157, Yale Station
New Haven, CT 06520

LEONG, KENG H.
(312) 972-3254
Argonne National Lab
ENG Bldg 207
9700 S. Cass Ave.
Argonne, IL 60439-4841

LETTIERI, THOMAS R.
(301) 975-3496
National Institute of Standards and Tech
Met-A117
Gaithersburg, MD 20899

LIMM, WILLIAM
(301) 671-4297
Commander
US Army CRDEC
SMCCR-RSCA
Aberdeen Proving Ground, MD 21010-4297

LIN, H.B.
(202) 767-2057
National Research Lab
Code 6546
Washington, DC 20375-5000

LIPOWICZ, PETER
(804) 274-4705
Philip Morris Research Center
P.O. Box 26583
Richmond, VA 23261

LITTMAN, HOWARD
(518) 276-6039
Rensselaer Polytechnical Institute
Dept. of Chemical Engineering
123 Ricketts Building
Troy, NY 12180-3590

LOCHNER, J.M.
(301) 671-2116
Commander
US Army CRDEC
ATTN: SMCCR-RSL/J.M. LOCHNER
Aberdeen Proving Ground, MD 21010-5423

MA, YUSHIEH
(814) 865-0178
Pennsylvania State University
Dept. of Engineering Science & Mechanics
227 Hammond Building
University Park, PA 16802

MCCALLY, RUSSELL
(301) 792-6201
Johns Hopkins University
Applied Physics Lab
Laurel, MD 20707

MCCOY, DAVID
(409) 845-7906
Texas A&M University
Physics Dept.
College Station, TX 77843

MILHAM, MERRILL
(301) 671-3854
Commander
US Army CRDEC
SMCCR-RSP-B
Aberdeen Proving Ground, MD 21010

MORGAN, MORRIS H.
(518) 276-6059
Dept. of Chemical Engineering
Rensselaer Polytechnic Institute
Troy, NY 12180-3590

POPE, R.
(409) 845-7906
Dept of Physics
Texas A&M
College Station, TX 77843

MORRE, TRACY
(814) 865-3239
Penn State Univ.
Meteorology Dept.
University Park, PA 16802

RADKE, LAWRENCE
University of Washington
Dept. of Atmospheric Sciences
Mail Stop AK 40
Seattle, WA 98195

PAO, JUNG-RERN
(301) 454-4742
University of Maryland College Park
Dept. of Chemical & Nuclear Engineering
College Park, MD 20742

RAY, ASIT
(606) 257-7999
University of Kentucky
161 Anderson Hall, Chemical Engineering
Lexington, KY 40506-0046

PARSONS, JOHN
(301) 671-2416
Geo-Centers Inc.
3808 Washington Ave.
Abingdon, MD 21009

ROGERS, C. WILLIAM
(716) 631-6808
Calspan Corp
4455 Genesee ST.
Buffalo, NY 14225

PATERNO, DOROTHEA
(301) 671-4466
Commander
US Army CRDEC
ATTN: SMCCR-RSL/D. PATERNO
Aberdeen Proving Ground, MD 21010-5423

ROSE, G.H.
(409) 845-7018
Texas A&M University
Dept. of Physics
College Station, TX 77843

PILIE, ROLAND J.
(716) 632-7500
Calspan Corporation
P.O. Box 400
Buffalo, NY 14225

RUBEL, GLENN
(301) 671-2395
Commander
US Army CRDEC
ATTN: SMCCR-RSP-B/G. RUBEL
Aberdeen Proving Ground, MD 21010-5423

SALZMAN, GARY
(505) 667-5503
Los Alamos National Lab
P.O. Box 1663
MS M880
Los Alamos, NM 87545

SEAVER, MARK
Naval Research Lab
Code 6540
Washington, D.C. 20375

SINDONI, ORAZIO
(301) 671-2395
Commander
US Army CRDEC
SMCCR-RSP-B/O. Sindoni
Aberdeen Proving Ground, MD 21010

SITARSKI, MAREK
(304) 291-4834
US Department of Energy
Morgantown Energy Technology Center
PO Box 880
Collins Ferry Road
Morgantown, WV 26505

SMALL, RICHARD D.
(213) 820-2200
Pacific Sierra Research Corp
12340 Santa Monica Blvd
Los Angeles, CA 90025

STANLEY, MARC
(301) 295-5674
Laser Bio Physics Center
Jones Bridge Rd
Bethesda, MD 20814

STOYANOV, BASIL
(301) 453-6261
The Johns Hopkins Univ./APG
Johns Hopkins Road
Laurel, MD 20707

STUEBING, ED
(301) 671-3089
Commander
US Army CRDEC
SMCCR-RSP-B/E. Stuebing
Aberdeen Proving Ground, MD 21010-5423

STUEMPFLE, ART
(301) 671-2651
Commander
US Army CRDEC
SMCCR-RSP
Aberdeen Proving Ground, MD 21010

TSANG, TATE H.
(606) 257-2825
Dept. of Chemical Engineering
University of Kentucky
Lexington, KY 40506-0046

VAN DE MERWE, W.
(301) 295-5674
Laser Bio Physics
Uniform Services of the Health Science
4301 Jones Bridge Rd
Bethesda, MD 20814-4799

WANG, CHING
(409) 846-0052
Texas A&M Univ.
Physics Dept.
College Station, TX 77840

WEINMAN, JIM
(301) 459-8442
ARC
8201 Corporate Dr. #920
Landover, MD 20785

WOZNIAK, SAM
(213) 414-2057
Rockwell International
P.O. Box 92098
Los Angeles, CA 90009

WHITE, W.E.
Texas A&M University
Dept. of Physics
College Station, TX 77843-4242

ZEROKA, DANIEL
(215) 758-3479
Dept. of Chemistry #6
Lehigh University
Bethlehem, PA 18015

WHITE, JOHN R.
(301) 671-2395
Commander
US Army CRDEC
ATTN: SMCCR-RSP-B/J.R. WHITE
Aberdeen Proving Ground, Md 21010-5423

WHITTEN, BILL
(615) 574-4921
Oak Ridge National Lab
Oak Ridge, TN37830

WILSEY, EDWARD
(301) 278-6332
BRL-VLD
SLC BR-IB-I
Aberdeen Proving Ground, MD 21005

WITRIOL, NORMAN
(318) 257-4670
Dept. of Physics
Louisiana Tech University
Ruston, LA 71272

APPENDIX C
CONFERENCE AGENDA

CONFERENCE AGENDA

AGENDA

1988 ORDEO SCIENTIFICO CONFERENCE

ON

OILSUCRATION AND AEROSOL RESEARCH II

27-30 JUNE 1988

Bldg. E4810 (Conference Center/Post Theater) Edgewood Area

TUESDAY, 27 JUNE

8:00 Registration Opens

8:45 Opening of Conference

Edward W. Swobbing, Aerosol Science Coordinator

Welcome

Joseph J. Vervier, Technical Director, ORDEO

Administrative Announcements

Elmer Engquist, Conferences Administrator

I. AEROSOL DYNAMICS

Moderator: Glenn Rubel

A. Fundamental Physicochemical Properties of Aerosols

9:10 Glenn Rubel (ORDEO), Measurement of the Absorption of Partially Soluble Alcohol Vapors by Aqueous Droplets [15]

9:30 Asit Roy and James Huckaby (Univ. of KY), Structural Resonances in Raman-Mie Scattering [15]

9:50 Asit Roy and A. Souyri (Univ. of KY), Dynamic Behavior of Layered Droplets [15]

10:10 BREAK

10:35 Richard Flagan (Cal. Tech.), Experimental Studies of Nucleation and Growth of Aerosols and Reacting Systems [20]

B. Transport and Dispersion of Aerosols

11:00 Tso Tsang (Univ. of KY), Second Order Closure Turbulence Modelling on the Dispersion of Smoke [15]

11:30 Bruce Jerich and James Brock (Univ. of Texas), Aerosol Plumes: Dispersion and Characterization [20]

1:45 J. Michael Shapiro, David Edwards, and Howard Brenner (Cal. Tech. & MIT), Modeling of Aerosol Filtration and Fibrous Filters [20]

12:10 LUNCH

II. WORKSHOP

NUCLEAR WINTER - Aerosol Source, Transport, and Effects

Moderator: Edward W. Swobbing

1:50 R. D. Small (Pacific-Sierra Research Corp.), Introduction to Nuclear Winter Research [15]

1:55 R. D. Small (Pacific-Sierra Research Corp.), Aerosol Source and Turbulent Injection into the Atmosphere [15]

1:55 L. Radke (University of Washington), Smoke Generation by Large Fires and Interaction with Cloud Layers [15]

2:15 W. C. Cotton and Craig Tomback (Colo. State Univ.) and Greg Tripoli (Univ. of Wisconsin), Mesoscale Transport of Water Substance and Aerosol, and their Interactions [15]

2:35 BREAK

- Consequent Bacterial Size to the S24 Scattering Pattern of a Suspension [15]
- 10:50 D. Huffman (University of Arizona); Polarized Modulated IR and Visible Light Scattering from Individual Particles on a Surface [15]
- 11:10 R. Farrell, R. McCally, and D. Freund (Johns Hopkins Applied Physics Lab.); Probing the Corneal Structure of the Eye with Light Scattering [40]
- 11:50 LUNCHEON
- 1:15 G. Salzman, R. Johnston, J. Siskamp, and A. Stevenson (Los Alamos Natl. Lab.); Flow Cytometry and its Application to Particle Classification [15]
- 1:35 C. Bohren (Pennsylvania State University); Overview on Applications of the Coupled Dipole Approximation [30]

IV. POSTER PROGRAM

- Posters are identified by proper session topic symbol (I, II, III, IV, V, VI) and in sequence of preview presentations.
- A. Poster Previews (2:10 - 2:30)
- III H. B. Lin, J. D. Eversole, and A. J. Campillo (NRL); Multi-order Morphology Dependent Resonances Observed in Lasing Droplets
- III H. B. Lin, J. D. Eversole, and A. J. Campillo (NRL); Observation of Mie Resonances in Layered Microspheres
- V A. Biswas, B. S. Park, and R. L. Armstrong (NMSU); and R. G. Finnick (ASL); Optical Effects in Laser Irradiated Droplets
- VI K. A. Fuller (ASL); Energy Distribution Inside and Near Sphere Doublets

- 3:15 R. C. Schnell (Univ. of Colo.) and J. F. Bestgen (NOAA); Transport of Highly Absorbing and Scattering Aerosols in the Arctic Troposphere [16]
- 3:35 T. Ackerman (Penn State Univ.); Radiative Effects of Nuclear Winter Aerosols [16]
- 3:55 G. A. Glatzmaier, R. C. McFerson, and J. Kee (Los Alamos Natl. Lab.); Global Numerical Simulations of the Climatic Effects Caused by Large Scale Smoke Injection [30]
- 4:25 GENERAL DISCUSSION

WEDNESDAY, 28 JUNE

III. AEROSOL CHARACTERIZATION

Moderators Jerry R. Böttiger and Durt V. Breenk

- 8:30 R. B. Mädhav, Y. C. Chang and J. W. Gentry (University of Maryland); Representative Sampling and Transport of Concentrated Aerosols. [16]
- 8:50 W. Whittier, M. Ramsey, S. Arnold, and B. Breenk (Oak Ridge National Laboratory) Approach to the Ultimate Detection Limit by Fluorescence in Microparticles [16]
- 9:10 S. Arnold, L. Folan and B. Breenk, (Polytechnic University of New York and ORDEC) Detection of the Molecular Density of an Absorber at the Surface of an Aerosol Particle [16]
- 9:30 L. Folan, and S. Arnold, (Polytechnic University) Microparticle Electrometer for Determination of Charge Exchange between a Particle and a Surface [16]
- 9:50 BREAK
- 10:30 B. Breenk, W. Van de Merwe and D. Hoffmann (ORDEC, USUHS, and U. of AZ); Relationship of Growth Conditions and

- VI K. Thieme, B. White, and E. Fry (Texas A&M), Scattering from Doublets
- VI D. McCoy and E. Fry (Texas A&M), Scattering by a Single Sphere at an Angle of Zero Degree
- VI R. H. Fricke (ORDEC), Charges on a Sphere in a Uniform Field
- VI R. W. Alexander, R. J. Dell, and L. Newquist (Univ. of Missouri-Rolla), Optical Properties of Aerosol Materials at Submillimeter Wavelengths
- VI D. K. Coheon (Penn. State Delaware County Campus), Precise Formulation of the Problem of Scattering by Finite Length Anisotropic Cylinders. & Exact Solution for Scattering by N-Layer Anisotropic Cylinders - A Computer Implementation

II. Poster Session

2:30 --- 4:30 Posters Open (Seminar Center)

THURSDAY, 29 JUNE

V. NONLINEAR EFFECTS AT HIGH ENERGY

Moderator: John R. White

- 08:30 D. R. Alexander, J. P. Barton, S. A. Schaub (University of Nebraska - Lincoln), Laser Induced Breakdown of H_2O Droplets and Solid Wires at 0.248 μm [15]
- 08:50 A. Kwok, R. K. Chang (Yale University), Fluorescence Imaging of CO_2 Laser Heated Droplets [15]
- 09:10 R. G. Pinnick, A. Biswas, R. L. Armstrong, J. D. Pendleton, G. Fernandez, E. Creagan, and P. Shah (ASL and NMSU), Micron-

Sized Droplets Irradiated With A Pulsed CO_2 Laser: Measurement of Explosion and Breakdown Thresholds [15]

09:30 J. R. White (ORDEC) High Energy Laser Interaction with Vacuum Clouds [15]

09:50 BREAK

10:20 R. L. Armstrong, A. Biswas, R. Pinnick, and H. Latiifi (New Mexico State University - Las Cruces), Nonlinear Laser-Droplet Interactions: Stimulated Raman Scattering and Explosive Dynamics [15]

10:40 J. R. Brock, Y. Seo, and J. C. Corde (University of Texas - Austin), Studies in Nonlinear Response of Microparticles to Laser Radiation [15]

11:00 M. A. Sitarshi (Clarkson University c/o DOE/METC), Feasibility of Superheating and Disruptive Boiling of a Small Multiphase Droplet in a Hot and Radiant Environment [15]

11:20 F. P. Matar (NYU), Transverse Effects in Raman Solitons: Propagational Effects [15]

NOTE See also 10:30 AM Friday

11:40 LUNCHEON

OVERVIEW AND DISCUSSION

1:00 Edward W. Stuebing (ORDEC), Overview of Aerosol Research Program and Discussion of Directions for Future Research in the ORDEC Aerosol Science Program

2:35 BREAK

VI. OPTICAL PROPERTIES OF AEROSOLS

A. Scattering by Single Particles and Small Aggregates

Moderator: *Orazio J Sindoni*

- 3:30 C. Wang, B. White, and E. Fry (Texas A&M), Recent Femtosecond Scattering Results [15]
- 3:35 G. H. Rose, Chie-Ren Ho, and G. W. Kalkauer (Texas A&M), A Study of Time-Resolved Scattering of Femtosecond Light Pulses from a Dielectric Sphere [15]
- 3:55 D. K. Cohen (Penn State Delaware County Campus), A Computer Code to Determine by Exact Formulae the Thermal Response of an N Layer Electromagnetically and Thermally Anisotropic Spherically Symmetric Structure to Electromagnetic Radiation [15]
- 4:15 L. Cohen, R. D. Harees, A. Cohen (Drexel University), Convergence Criteria for Evaluating the Polarization Matrix for Scattering from a Dielectric Target [15]

FRIDAY, 30 JUNE

VI. OPTICAL PROPERTIES OF AEROSOLS (Continued)

A. Scattering by Single Particles and Small Aggregates

Moderator: *Orazio J Sindoni*

- 8:30 J. P. Barton, D. R. Alexander, and S. A. Schaub (University of Nebraska, Lincoln), Electromagnetic Field Calculations for a Tightly-Focused Laser Beam Incident upon a Spherical Particle [15]
- 8:50 L. Liebman, J. R. Brock (University of Texas - Austin), A Finite Element Approach to Laser/Droplet Interactions [15]

9:10 K. Fuller (U. S. Army Atmospheric Sciences Lab), Morphology-Dependent Resonances of Two Dissimilar, Cooperatively Scattering Spheres [15]

9:30 R. Pope, R. Montgomery, D. White, and E. Fry (Texas A&M), Precision Absorption Measurements in a Highly Scattering Medium [15]

9:50 BREAK

10:30 Session V - ITEL - insert

M. Lee, B. Yadenin, P. Ho, and A. Zardochi, S. Chikensis (UNY and IANL), Shock Wave Calculations with GA VEAT, Godunov and POST [15]

C. Multiple Scattering and Radiative Transfer

Moderator: *Robert H. Fricke*

10:50 Ezetel Bahar and Guorong Huang (University of Nebraska - Lincoln), Transmission Scattering and Depolarisation across Rough Surfaces --- Full Wave Solutions [15]

11:10 Yeshiel Ma (The Pennsylvania State University), Pulse Propagation in Discrete Random Media [15]

11:30 D. K. Cohen (Penn. State Delaware County Campus), Multiple Scattering from Clusters of Anisotropic Spherical Aerosol Particles [15]

11:50 ADJOURN